DISSERTATION

submitted
to the
Combined Faculties for Natural Sciences and for Mathematics
of the
Ruperto-Carola University Heidelberg, Germany

for the degree of
Doctor of Natural Sciences

put forward by
Dipl.-Phys. Stephan General
born in Ahlen, Germany
Oral examination: 23.07.2014

Development of the Heidelberg Airborne Imaging DOAS Instrument (HAIDI)

A novel remote sensing device for the investigation of two- and three-dimensional trace gas distributions in the troposphere

Referees: Prof. Dr. Ulrich Platt
Prof. Dr. Thomas Wagner

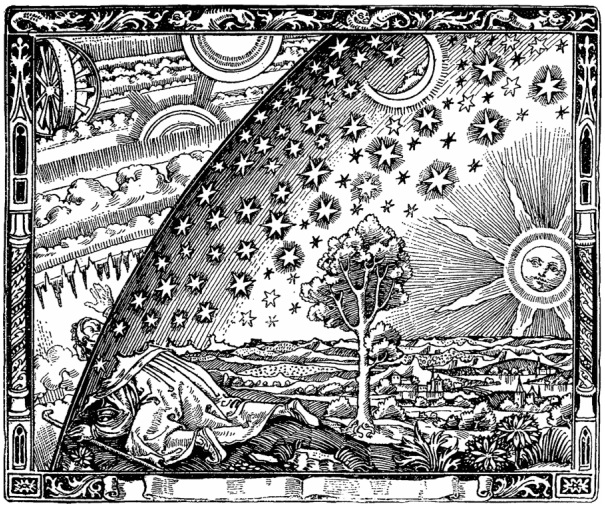

A man is peering beyond the place where heaven and Earth meet, beyond current knowledge, to discover what lies behind. Wood engraving by an unknown artist, taken from *Camille Flammarion, L'atmosphère: météorologie populaire, 1888*.

Abstract

The investigation of trace gases and related chemical processes in the atmosphere on local and regional scales requires measurement techniques with high spatial resolution and coverage. In the context of this thesis a novel remote sensing device, the Heidelberg Airborne Imaging DOAS Instrument (HAIDI), was developed. HAIDI works on the basis of the well established DOAS method and has the ability to determine horizontal and vertical distributions of several important atmospheric species with a resolution of better than 100 m at high sensitivity. The thesis gives a detailed overview on the operating principle of the instrument and its characteristics. In addition, measurement results of several field campaigns with this instrument are presented, which yielded interesting findings. For instance, BrO/SO_2 ratios were measured at Mt. Etna (Italy), showing constant values of 1.4×10^{-4} and 2.0×10^{-4}, respectively, along the plume's centerline on both measurement days (observed plume ages: 2–34 min), but an increase by a factor of two to three towards the edges of the plume. Moreover, a temporal change in the BrO/SO_2 ratio was observed prior to the culmination of a paroxysm. The measurements are also one of the first to show spatial resolved $OClO/SO_2$ and OClO/BrO ratios in the plume of Mt. Etna. Further measurements were performed near Indianapolis (Indiana, USA) and Barrow (Alaska, USA) to investigate the spatial distribution of NO_2 over polluted urban areas as well as the occurrence of "bromine explosion" events during boundary layer ozone depletion in polar regions. The data allow to characterize the spatial distribution of BrO and thus give insight into possible bromine sources.

Zusammenfassung

Die Untersuchung von Spurenstoffen und damit zusammenhängenden chemischen Reaktionen in der Atmosphäre auf lokalen und regionalen Skalen erfordert Messtechniken mit hoher räumlicher Auflösung und Abdeckung. Im Rahmen dieser Arbeit wurde ein neuartiges Fernerkundungsinstrument, das „Heidelberg Airborne Imaging DOAS Instrument“ (HAIDI), entwickelt. HAIDI ist in der Lage sowohl horizontale als auch vertikale Verteilungen einer Vielzahl wichtiger atmosphärischer Spurenstoffe mit einer Auflösung besser als 100 m und hoher Sensitivität zu bestimmen. Die Arbeit gibt einen detailierten Überblick über die Funktionsweise des Gerätes und seine Eigenschaften. Zudem werden Messergebnisse von verschiedenen Kampagnen mit dem Gerät präsentiert, die interessante Resultate ergaben. Beispielsweise wurden BrO/SO_2 Verhältnisse am Ätna (Italien) gemessen, die an beiden Messtagen konstante Werte von 1.4×10^{-4} bzw. 2.0×10^{-4} entlang der Mittelachse der Fahne aufweisen (untersuchte Fahnenalter: 2–34 min), aber einen Anstieg um einen Faktor von zwei bis drei zu den Rändern der Fahne hin. Zudem konnte eine zeitliche Änderung im BrO/SO_2 Verhältnis kurz vor dem Höhepunkt eines Ausbruchs beobachtet werden. Die Messungen sind darüber hinaus eine der ersten, die räumlich aufgelöste $OClO/SO_2$ und OClO/BrO Verhältnisse in der Emissionsfahne des Ätnas zeigen. Weitere Messungen wurden in der Nähe von Indianapolis (Indiana, USA) und Barrow (Alaska, USA) durchgeführt, um die räumliche Verteilung von NO_2 über verschmutzten städtischen Gebieten zu untersuchen, sowie das Auftreten von „Bromexplosionen“ während der Ozonzerstörung in der planetaren Grenzschicht polarer Gebiete. Die Daten ermöglichen eine Charakterisierung der räumlichen Verteilung von BrO und gewähren somit einen Einblick in dessen mögliche Quellen.

Contents

Introduction

Despite their small contribution to earth's atmospheric composition, many trace gases play an important role in atmospheric chemistry and global climate. Methods for determining their spatial and temporal distribution are therefore of great scientific interest. Two-dimensional trace gas distribution patterns with almost daily global coverage can be obtained from modern satellite instruments like e. g. GOME, GOME-2, OMI or SCIAMACHY. Based on such satellite observations (TOMS on NIMBUS-7) the true extend of the Antarctic ozone hole could be revealed in the mid-1980s, for example (Bhartia, 2009). However, the spatial resolution that is currently achieved by satellite instruments is of the order of several tens of km, while many relevant processes in tropospheric chemistry take place on scales of tens to hundred of meters. In contrast, ground-based measurements offer a high spatial resolution, but are often not mobile or have only a restricted mobility. Observations are thus limited to a relatively small area. The resolution of tomographic inversion methods like LP-DOAS (Laepple et al., 2004; Pöhler, 2010) furthermore depends on the number of light paths. This means that a high spatial resolution requires a large number of instruments and therefore high instrumental effort (Hartl et al., 2006). Airborne DOAS-measurements are able to fill the existing gap between local ground-based measurements and global satellite observations. They offer a sufficiently high spatial resolution and can cover large areas in short time.

During the last decades it has been reported from an increasing number of airborne DOAS-measurements (e. g. Wahner et al., 1990; Pfeilsticker and Platt, 1994; McElroy et al., 1999; Petritoli et al., 2002; Melamed et al., 2003; Bruns et al., 2004; Heue et al., 2005; Wang et al., 2005; Bruns et al., 2006; Wang et al., 2006; Heue et al., 2008; Dix et al., 2009; Merlaud et al., 2011; Prados-Roman et al., 2011; Merlaud et al., 2012; Baidar et al., 2013). These measurements pursued very different scientific objectives, ranging from studies of stratospheric chemistry to tropospheric point source emissions, and were thus conducted at various flight altitudes and regions of the world. However, to date only a few airborne measurements were performed with imaging instrumentation able to acquire two-dimensional spatially resolved distributions of trace gases (e. g. Heue et al., 2008; Kowalewski and Janz, 2009; Popp et al., 2012). To address this shortcoming, a novel remote sensing device, the **H**eidelberg **A**irborne **I**maging **D**OAS **I**nstrument (HAIDI), was developed and tested in the context of this thesis.

HAIDI is capable of measuring trace gas distributions with a horizontal resolution of better than 100 m (for flight altitudes below 4000 m) and high sensitivity. What distinguishes the system from previous airborne DOAS instruments, however, is the possibility to operate up to

three independent entrance optics, each with imaging capabilities. In this way, HAIDI can not only measure the two-dimensional horizontal distribution of trace gases, but also their vertical profile, which finally allows for a three-dimensional reconstruction of the original trace gas distribution via tomographic inversion methods. It thus combines the functionality of airborne multi-axis DOAS (AMAX-DOAS) instruments, having multiple simultaneous viewing elevations, with airborne imaging DOAS instruments. The imaging spectrographs applied by the system are custom-built and use a wavelength range from 300 to 407 nm (shiftable to 343–450 nm), which enables the simultaneous observation of several important species with the DOAS method, e. g. NO_2, SO_2, BrO, IO, HCHO, $C_2H_2O_2$, H_2O, O_3 and O_4. Based on the observed patterns of trace gas distributions, sources and sinks of these species can be quantified and chemical processes including conversion rates and atmospheric lifetimes may be analyzed. The high spatial resolution of the HAIDI system thereby ensures that closely spaced sources can be resolved and quantified separately. The results can be used for the validation of chemical transport models, for instance. In addition, the variability of trace gas concentrations within a satellite pixel is one of the major issues that can be addressed with the new imaging DOAS instrument.

The general operating principle of the HAIDI system is explained in detail in Chap. 3 of this thesis. Followed by a description of the main components of the system, e. g. entrance optics, spectrographs and CCD cameras. Furthermore, different configurations of the system are shown. Each configuration was optimized for the operation on a particular aircraft. Up to now HAIDI was applied on two smaller aircraft (ultralight and twin-engine propeller plane) for a total of 18 measurement flights, during three campaigns. The first campaign was conducted in July 2011 on Sicily, Italy. Here, spatial distributions of SO_2, BrO and OClO could be measured in the emission plume of Mt. Etna. As a result, the BrO/SO_2 ratio could be determined along several traverses of the plume and for different plume ages, showing increasing ratios towards the edges of the plume and a possible correlation to the volcanic activity. The next campaign was in October 2011 and focused on the distribution of NO_2 over the metropolitan area of Indianapolis (Indiana, USA). Traverses flown downwind of the city clearly showed the emission plume originating from Indianapolis. Furthermore, the measurements could be used to calculate the approximate NO_2 emission flux of the urban area. The last campaign up to now was carried out at Barrow (Alaska, USA), where the HAIDI system participated in the **BR**omine, **O**zone, and **M**ercury **EX**periment (BROMEX). The campaign focused on the improvement of knowledge about polar ozone depletion events and HAIDI contributed to this by measuring the spatial distribution of BrO and NO_2 in the polar boundary layer. The obtained results could reveal strong gradients in the BrO distribution and generally a good agreement with simultaneous satellite measurements. A detailed consideration of all measurement results can be found at the end of this thesis.

1. Atmospheric Chemistry of the Troposphere

In the context of this thesis a number of measurement campaigns were conducted to verify the systems functionality under real measurement conditions. These campaigns took place at very different regions in the world. The first airborne measurements with the HAIDI system were undertaken with a small ultralight aircraft on Sicily, Italy, in summer of 2011, for example. Here, several flights to Mt. Etna and Mt. Stromboli were performed in order to investigate the volcanic plume chemistry (see Chap. 5.1 for details). In October of the same year also a campaign to Indiana, USA, was arranged in cooperation with Purdue University. This time the metropolitan area of Indianapolis was the destination of the measurement flights. Indianapolis has lots of air pollution due to its industry and the influence of nearby Chicago (Chap. 5.2). The polluted air causes high concentrations of nitrogen oxides and ozone in the lower troposphere, which were subject to examination. While the former two campaigns were carried out in the temperate zone of the northern hemisphere, the last one took place in Barrow, Alaska, in spring of 2012. Barrow is the northernmost city of the United States and located beyond the arctic circle (Chap. 5.3). Every year during springtime large ozone depletion events, initiated by the release of reactive bromine species into the gas phase, can be observed here. Hence, each of these regions exhibited unique conditions in terms of atmospheric chemistry and the conducted measurements therefore focused on different trace gases. The following sections should give an overview of the most important chemical processes for each of the measurement locations.

1.1. Volcanic Emissions

Volcanic emissions are of high scientific interest, especially for two reasons. On the one hand, the chemical composition of volcanic plumes can give an insight into the underlying volcanic processes, which in turn could help to improve the prediction of volcanic eruptions (e. g. Oppenheimer, 2003). On the other hand, active volcanoes emit gases and aerosols in such enormous quantity, that they can have significant impact on global atmospheric chemistry and climate (e. g. Robock, 2000). The most prevalent gas in volcanic emissions is water vapor (H_2O). Typically followed by CO_2, SO_2, H_2S and HCl (e. g. Carroll and Holloway, 1994). Further emitted compounds in much lower abundances include CS_2, COS, CO, HF, HBr and a number of volatile metal chlorides as well as heavy metals like mercury (see e. g. Buat-Ménard and Arnold, 1978; Carroll and Holloway, 1994; Hinkley et al., 1999). A table with average percentages of emitted species and estimated global flux can be found in Tab. 1.1. Beside gases

Table 1.1.: Typical composition of volcanic plumes directly after the emission and estimated global flux (Textor et al., 2004).

Species	H_2O	CO_2	SO_2	H_2S	HCl	CS_2	COS	HBr	HF
Composition in % Vol.	50..90	1..40	1..25	1..10	1..10	$10^{-4}..10^{-2}$	$10^{-4}..10^{-2}$	n/a	$< 10^{-3}$
Global flux in Tg/a	n/a	75	1.5..50	1..2.8	0.4..11	0.007..0.096	0.006..0.1	0.0078..0.1	0.06..6

also aerosols are highly abundant in volcanic plumes and due to the high amount of water vapor often condensation takes place, providing even more surface for heterogeneous reactions. The following sections focus primarily on emitted sulfur and halogen compounds as they play an important role in volcanic plume chemistry.

1.1.1. Sulfur Compounds

The following section is based on the work of Zielcke (2010). It discusses the importance of volcanic sulfur emissions for global environment and climate as well as its usefulness for the investigation of reactive halogen species in the plume.

Sulfur is one of the most common elements on Earth ($\sim 0.46\,\%$ of Earth's mass, Allègre et al. (2001)) and essential for all life as it is required by a number of biochemical processes. In its elemental form sulfur can be found mainly near volcanically active areas. The predominant part, however, exists in the form of sulfur compounds. These are widely distributed in Earth's lithosphere as well as in the hydrosphere, biosphere and atmosphere. Between all spheres of the earth system a continuous exchange of sulfur takes place, which is called the sulfur cycle. The relevant exchange processes for the atmosphere are illustrated in Fig. 1.1. One of the major natural sources for the release of sulfur compounds to the atmosphere are volcanoes. According to Brasseur et al. (1999), volcanoes are responsible for approximately 10 % of the global SO_2 emission. The only natural source which emits more sulfur to the atmosphere are the oceans, where dimethyl sulfide (DMS) is emitted by phytoplankton (Schmidt et al., 2012).

As mentioned previously, volcanic emissions contain many different sulfur compounds. For instance, sulfur dioxide (SO_2), hydrogen sulfide (H_2S), carbon disulfide (CS_2) and carbonyl sulfide (COS). Even though the exact composition of the emissions varies, SO_2 is typically the most abundant sulfur compound emitted by volcanoes. In addition, most other emitted sulfur compounds are rapidly oxidized to SO_2 by the hydroxyl radical (OH) or ozone (O_3), which are both available as oxidizing agents in the troposphere. The SO_2 then has a typical lifetime of at least several hours (McGonigle et al., 2004). Some sources also report lifetimes of a few days in the troposphere (e. g. Berresheim et al., 1995; Oppenheimer et al., 1998; von Glasow et al.,

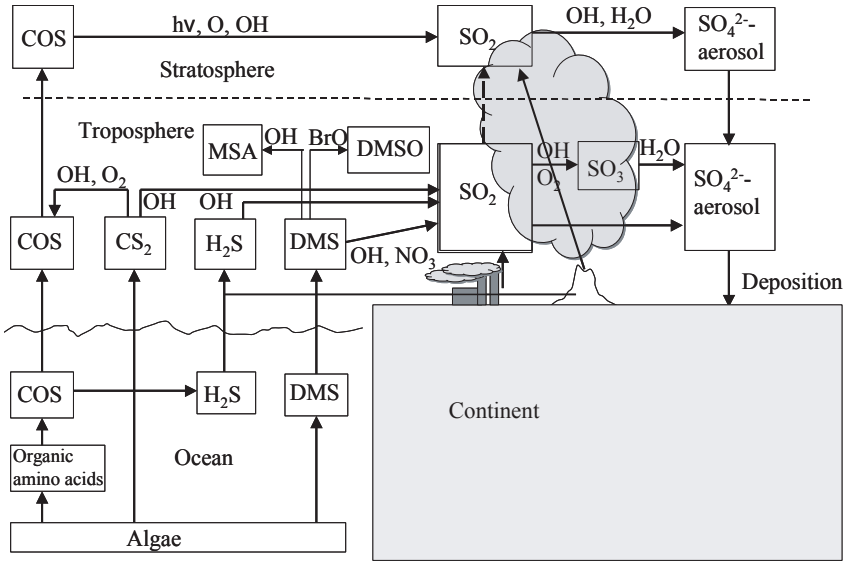

Figure 1.1.: The sulfur cycle of the atmosphere. Adapted from a lecture by *U. Platt*.

2009). It is finally removed from the troposphere by dry and wet deposition. Because of this inertness SO_2 is often used as a tracer for the dilution of volcanic plumes. The evolution of reactive species like BrO or OClO in the plume can thus be investigated by looking at the ratio of their concentrations with that of SO_2.

However, SO_2 is not only important as a tracer. It can also have significant impact on the environment and human health. One the one hand, it contributes to the formation of acid rain by forming sulfuric acid (H_2SO_4) in the atmosphere. Sulfuric acid can seriously damage forests, waters and building materials, for example. On the other hand, sulfate aerosols can alter Earth's radiation budget in a direct and indirect manner. Directly by scattering sunlight back into space and indirectly by serving as cloud condensation nuclei (CCN). CCNs can influence Earth's total albedo by affecting cloud formation as well as lifetimes and radiative properties of clouds (Schmidt et al., 2012).

1.1.2. Halogen Compounds

Volcanic halogen emissions are thought to be degassed predominantly as hydrogen halides (see e. g. Carroll and Holloway, 1994), which should be thermodynamically favored over other halogen species as equilibrium model data suggest (e. g. Gerlach, 2004). However measurements and laboratory kinetic data show that the transformation - at least of HBr to other bromine molecules - can be relatively fast. Already at the crater rim volcanic gases are usually diluted by factors of more than 1000 with the surrounding atmosphere. As a result of model studies von Glasow (2010) found that the contribution of HBr to total bromine can fall below 50 % at plume ages < 2 min.

1.1.2.1. Bromine Chemistry

The BrO/SO_2 ratio in plumes generally increases with distance from the emission source (e. g. Oppenheimer et al., 2006a; Bobrowski et al., 2007; von Glasow, 2010) indicating a chemical production of BrO in the volcanic plume. New enhanced data sets (e. g. Vogel, 2011; Bobrowski and Giuffrida, 2012; Platt and Bobrowski, 2014) show that after an initial increase the BrO/SO_2 ratio reaches a quasi-equilibrium state for a certain - still to be determined - period of time. The formation of BrO in volcanic plumes is currently explained by an autocatalytic photo-chemical reaction cycle (the so-called "bromine explosion" mechanism, see Platt and Lehrer (1997)), which was first proposed for polar regions and involves multi-phase chemistry. An essential step for the "bromine explosion" mechanism is the uptake of gas phase HOBr and HBr into aerosol particles:

$$HOBr_{(g)} \longrightarrow HOBr_{(aq)} \tag{1.1a}$$

$$HBr_{(g)} \longrightarrow HBr_{(aq)} \tag{1.1b}$$

$$HBr_{(g)} \longrightarrow Br^-_{(aq)} + H^+_{(aq)}\,. \tag{1.1c}$$

When a sufficient acidity is given (pH < 6.5, Fickert et al. (1999)), the following acid-catalyzed reaction can take place and Br_2 is released to the gas phase:

$$HOBr_{(g)} + Br^-_{(aq)} + H^+_{(aq)} \longrightarrow Br_{2(g)} + H_2O\,. \tag{1.2}$$

As soon as the Br_2 is released, it is rapidly photolysed to Br atoms during the day:

$$Br_2 + h\nu \longrightarrow 2Br\,. \tag{1.3}$$

The thus generated Br radicals can then react with O_3, forming BrO:

$$Br + O_3 \longrightarrow BrO + O_2\,. \tag{1.4}$$

In a next step, bromine atoms can be recycled from BrO via self-reaction, for example:

$$BrO + BrO \longrightarrow 2Br + O_2 \tag{1.5a}$$

$$BrO + BrO \longrightarrow Br_2 + O_2\,. \tag{1.5b}$$

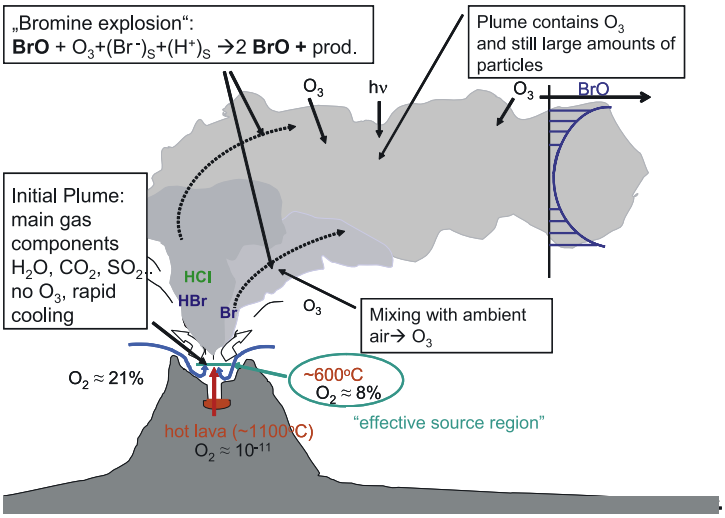

Figure 1.2.: Schematic progress of bromine in volcanic plumes. See text for explanations. Adapted from Bobrowski et al. (2007).

As the Br atoms can again react with O_3 according to reaction (1.4), this leads to a rapid destruction of ozone in the volcanic plume. Moreover, the reaction of BrO with hydrogen peroxy radicals leads to the formation of HOBr:

$$\mathrm{BrO} + \mathrm{HO_2} \longrightarrow \mathrm{HOBr} + \mathrm{O_2}\,, \tag{1.6}$$

which can then react according to the reactions (1.1a), (1.2), (1.3) and (1.4), closing the reaction cycle. Because the uptake of each HOBr molecule by aerosols leads to the release of two Br atoms to the gas phase, which in turn can form two HOBr molecules, this is an autocatalytic cycle. Hence the name “bromine explosion”. The atmospheric oxidants O_3 and HO_2 are required for the above described chemical mechanism. Thermodynamical model studies show that HO_2 may additionally be formed in the effective source region (see Fig. 1.2) with mixing ratios $> 10\,\mathrm{ppb}$ (e. g. Gerlach, 2004; von Glasow, 2010). Because O_3 is neither emitted from the volcano nor produced in the plume, it will be mixed into the plume while it expands into the ambient atmosphere. Therefore oxidation of halogenides should be more effective at the plume edge resulting in BrO enhancement at the edge. This has been shown already by Bobrowski et al. (2007) and Louban et al. (2009), and is again observed in the measurements presented in Sec. 6.

1.1.2.2. Chlorine Chemistry

The chemistry of chlorine is quite different from that of bromine in some important regards: No “chlorine explosion” is expected nor could it be observed in the field as the reactions (1.2), (1.5a) and (1.5b) are slower for chlorine than for bromine and as chlorine reacts with hydrocarbons

like methane, which is highly abundant in the atmosphere. Most of the emitted HCl either stays as HCl in the gas phase or is taken up into aerosol and cloud particles. This difference in the reactivity of hydrogen halides also leads to modeled decreases in HBr/SO_2 downwind of volcanoes, whereas the HCl/SO_2 ratio seems to stay fairly constant (e. g. Horrocks et al., 2003; Voigt et al., 2014). On the other hand changes in HCl/SO_2 ratios were already detected by Burton et al. (2001) and Mather et al. (2003) in condensing plumes, but might be only the consequence of extreme conditions (RH $> 80\,\%$, Martin et al. (2012)).

To date, only few investigations of chlorine oxides (ClO, OClO) and Cl_2 have been carried out at volcanoes - e. g. at Mt. Sakurajima, Japan (Lee et al., 2005), at Mt. Etna, Italy (Bobrowski et al., 2007; Gliß, 2013) and at the Tolbachik volcanic complex, Russia (Zelenski and Taran, 2012). The measurements presented in Chap. 6 of this thesis are thus one of the first to show the spatially resolved distribution of OClO within volcanic emissions. The predominant source of OClO in volcanic plumes is thought to be the following reaction:

$$\mathrm{BrO} + \mathrm{ClO} \longrightarrow \mathrm{OClO} + \mathrm{Br}\,. \tag{1.7}$$

Reaction (1.7) is much faster than the further possible production of OClO from ClO and ozone or from the ClO self reaction (Sander et al., 2006). However, reaction (1.7) has two further pathways:

$$\mathrm{BrO} + \mathrm{ClO} \longrightarrow \mathrm{ClOO} + \mathrm{Br} \tag{1.8a}$$

$$\mathrm{BrO} + \mathrm{ClO} \longrightarrow \mathrm{BrCl} + \mathrm{O_2}\,. \tag{1.8b}$$

The distribution of the reaction products thereby depends on the temperature, showing similar reaction rates for (1.7) and (1.8a) at 300 K and a much lower reaction rate for (1.8b). During daytime the main sink for OClO is its photolytic destruction:

$$\mathrm{OClO} + h\nu \longrightarrow \mathrm{ClO} + \mathrm{O}\,. \tag{1.9}$$

In contrast to OClO the direct detection of ClO by UV-spectroscopy requires measurements at wavelengths near 300 nm, where the solar radiation intensity is very low. Therefore passive DOAS measurements of ClO are not very reliable and the data available today could be considerably overestimated. However, since OClO is in a photo-stationary state with ClO via reactions (1.7) and (1.9), the approximate ClO concentration in the plume can also be calculated by the following equation:

$$[\mathrm{ClO}] = \frac{J_{OClO}}{k_{(1.7)}} \times \frac{[\mathrm{OClO}]}{[\mathrm{BrO}]} \,. \tag{1.10}$$

The ClO concentration can thus be determined on the basis of measured OClO and BrO slant column densities. An important quantity is the photolysis rate of OClO, J_{OClO}, which strongly depends on the solar zenith angle (SZA). Simulations performed by E. Jäkel (Leipzig Institute for Meteorology) using the 1-D radiative transfer model libRadtran (Mayer and Killing, 2005), yielded a photolysis rate of $J_{OClO} = 5.1 \times 10^{-2}/\mathrm{s}$ for the prevailing conditions during our measurements (low SZA, clear sky). Beside this value, a rate constant $k = 6.0 \times 10^{-12}\,\mathrm{cm}^3/\mathrm{s}$ was assumed for reaction (1.17) at 298 K (Sander et al., 2006) to calculate the ClO concentrations. In fact, the conducted DOAS measurements of OClO (see Chap. 6) indicate much lower ClO levels, more in line with the model calculations (e. g. Roberts et al., 2009).

1.2. Urban Air Pollution

The increased burning of fossil fuels since the beginning of the Industrial Revolution in the 18$^{\mathrm{th}}$ century has caused an obvious reduction of the local air quality over larger urban areas. Especially the emission of nitrogen oxides (NO and NO_2, together referred to as NO_x), which are formed in most combustion processes using air as the oxidant have a noticeable impact on human health and also on tropospheric chemistry. They play, for example, a key role in the photochemically induced catalytic production of ozone. This process has effected continuously increasing ozone levels in the lower troposphere over parts of North America, Europe and Asia during the past decades (Volz and Kley, 1988; Richter et al., 2005). Particularly in summer, when it is warm and sunny, high ozone concentrations lead to the so-called summer smog (also known as "Los Angeles smog") over heavily polluted areas. Beside this, nitrogen oxides influence the availability of hydroxyl radicals (OH) in the atmosphere and are furthermore responsible for acid rain.

The following sections are based on the work of Sihler (2007) and Horbanski (2010). They should give an overview of the most important sources and sinks for tropospheric NO_x as well as the processes that are responsible for the formation of summer smog.

1.2.1. Sources and Sinks of Nitrogen Oxides in the Troposphere

Nitrogen oxides are released to the troposphere by a variety of different sources. These are of both natural and anthropogenic origin and contribute to the total emission in different extent. Approximate values for the global emission strength of the individual sources can be found in Tab. 1.2. Such emission estimates are usually based on "bottom-up" inventories, which means that the calculations rest upon statistical data about the considered region (e. g. fuel and land

Table 1.2.: Estimated global emission strength for the major anthropogenic and natural sources of tropospheric NO_x (Lee et al., 1997).

Source	Emission in Tg N/a	Uncertainty in Tg N/a
Fossil fuel combustion	22	13..31
Biomass burning	7.9	3..15
Soil microbial production	7.0	4..12
Lightning	5.0	2..20
Aircraft	0.8	0.59..0.95
Stratospheric	0.64	0.4..1
Total	44	23..81

use). Satellite measurements of NO_2 can provide additional "top-down" constraints to improve these emission inventories (Martin et al., 2006). Modern satellite instruments like OMI (Aura) are capable of mapping NO_2 distributions with high spatial resolution and daily global coverage. A map generated from SCIAMACHY (Envisat) measurements that shows the global mean distribution of NO_2 in the months between January 2003 and June 2004 is illustrated in Fig. 1.3. As can be seen here, there is clearly a positive correlation between NO_2 vertical column densities and the population density in the respective areas. In fact, anthropogenic sources are responsible for more than half of the global NO_x emission (see also Tab. 1.2). About 90 % of the anthropogenic NO_x emissions are thereby released in the form of NO, which results from the combustion of fossil fuels. The dominant mechanism for the formation of NO is the "Zel'dovich mechanism" (Zel'dovich, 1946):

$$O_2 + M \rightleftharpoons O + O + M \tag{1.11a}$$

$$O + N_2 \rightleftharpoons NO + N \tag{1.11b}$$

$$N + O_2 \rightleftharpoons NO + O\,, \tag{1.11c}$$

where M is an inert molecule that is required to conserve energy and momentum (e. g. N_2 or O_2). Due to the strong N_2 triple bond, reaction (1.11b) has an activation energy of about 320 kJ/mol (Gardiner, 2000) and is therefore only efficient at temperatures above ~ 2000 K. The equilibrium concentration of NO then increases with temperature during combustion. If the gas is subsequently cooled at a rapid rate (e. g. by expansion), the NO concentration cannot follow the equilibrium concentration and is thus "frozen out". This is the case, for example, in lightnings or during the combustion in engines. Another important source of NO_x are microbiological processes in soil. This contributes with approximately 16 % to the global emission (Yienger and Levy, 1995).

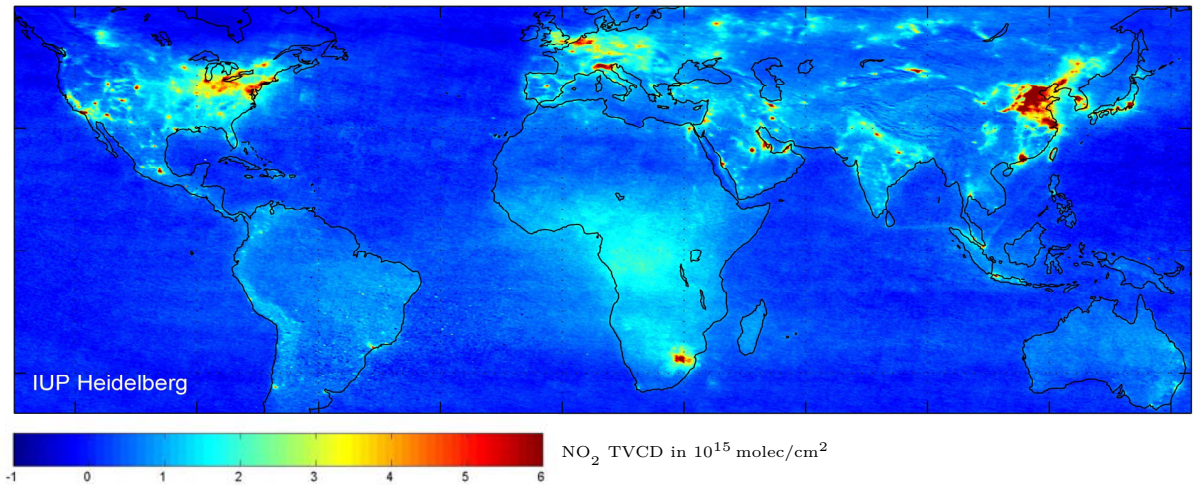

Figure 1.3.: Global mean distribution of tropospheric NO_2, measured by SCIAMACHY (Envisat) in the period between January 2003 and June 2004 (Beirle, 2004). Larger urban agglomerations like New York, Chicago or Johannesburg can clearly be identified by their strong NO_2 emissions.

The main sink of nitrogen oxides is the further oxidation in the atmosphere. During daytime, NO_2 is oxidized to nitric acid (HNO_3) by hydroxyl radicals:

$$NO_2 + OH + M \longrightarrow HNO_3 + M \tag{1.12}$$

Furthermore, NO_2 can react with O_3:

$$NO_2 + O_3 \longrightarrow NO_3 + O_2\,. \tag{1.13}$$

Because of the low rate coefficient, reaction (1.13) plays only a minor role as long as sunlight is available. Moreover, NO_3 is rapidly photolyzed in this case, which could otherwise further react with NO_2. At nighttime, however, NO_2 can form N_2O_5 by reacting with NO_3:

$$NO_2 + NO_3 + M \rightleftharpoons N_2O_5 + M\,. \tag{1.14}$$

N_2O_5 is then removed from the troposphere by hydrolysis and subsequent dry or wet deposition (e. g. Mentel et al., 1996):

$$N_2O_{5(g)} + H_2O_{(g)} \longrightarrow 2\,HNO_{3(g)} \tag{1.15a}$$

$$N_2O_{5(g)} + H_2O_{(l)} \longrightarrow 2\,HNO_{3(aq)} \tag{1.15b}$$

Model calculations by Dentener and Crutzen (1993) suggest that up to 90 % of the HNO_3 formation in the northern hemisphere occurs via reaction (1.15b).

1.2.2. The Photostationary State of NO_x

In the absence of volatile organic compounds (VOCs), the following reactions involving NO, NO_2 and O_3 form a self-contained cycle (e. g. Seinfeld, 1986):

$$NO_2 + h\nu \xrightarrow{j_{NO_2}} NO + O(^3P) \qquad (\lambda < 420\,\text{nm}) \tag{1.16a}$$

$$O(^3P) + O_2 + M \longrightarrow O_3 + M \tag{1.16b}$$

$$O_3 + NO \xrightarrow{k} NO_2 + O_2\,. \tag{1.16c}$$

Reaction (1.16a) requires light with a wavelength shorter than 420 nm in order to occur. At higher wavelengths the photon energy is insufficient to promote band cleavage. Because there is no net production nor net loss of NO, NO_2 or O_3 in reaction scheme (1.16), the concentrations of these species are in a steady state. The relation between them can then be expressed by the following equation, which is also known as the Leighton Relationship or photostationary state (Leighton, 1961):

$$\frac{[NO_2]}{[NO]} = [O_3]\frac{k_{(1.16c)}}{j_{NO_2}}\,, \tag{1.17}$$

where k is the rate constant for reaction (1.16c) and j_{NO_2} the photolysis rate of NO_2. The rate constant could be determined to $k = 1.8 \times 10^{-14}\,\text{cm}^3\,\text{molec}^{-1}\,\text{s}^{-1}$ on the basis of laboratory measurements by Atkinson et al. (2004). The exact photolysis rate, however, depends on the solar zenith angle. It is therefore expected, that the Leighton Ratio also changes in the course of the day. At noon time the photolysis rate reaches its maximum of about $j_{NO_2} = 8 \times 10^{-3}\,\text{s}^{-1}$ for clear sky conditions (e. g. Junkermann et al., 1989). This results in a NO_2 lifetime of the order of two minutes.

1.2.3. Deviation from the Photostationary State

When significant amounts of VOCs are available in the atmosphere, an additional reaction path for the conversion of NO to NO_2 is created. This reaction allows to oxidize NO without the involvement of ozone and thus leads to a deviation from the photostationary state. However, before the reaction can take place, the VOCs have to be oxidized. This is typically done by OH

radicals, which are mainly formed by the photolysis of ozone:

$$O_3 + h\nu \longrightarrow O(^1D) + O_2 \qquad (\lambda < 320\,\text{nm}) \tag{1.18a}$$

$$O(^1D) + H_2O \longrightarrow 2\,OH\,. \tag{1.18b}$$

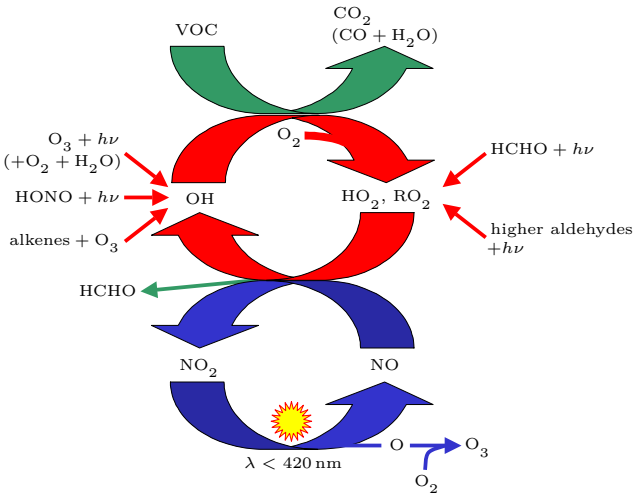

Figure 1.4.: Schematic illustration of the reaction cycles that are responsible for a net production of tropospheric ozones in a polluted atmosphere. The blue cycle represents the photostationary state of NO_x, which is disrupted by the presence of VOCs. Adapted from Trick (2004).

In a first step of the reaction chain, hydrocarbons (RH) may be oxidized by the hydroxyl radicals:

$$RH + OH \longrightarrow R + H_2O \tag{1.19a}$$

$$R + O_2 \longrightarrow RO_2\,. \tag{1.19b}$$

Subsequently, NO_2 can be formed by the reaction of peroxy radicals (RO_2 and HO_2) with NO (Crutzen, 1970; Parrish et al., 1986; Carroll and Thompson, 1995):

$$RO_2 + NO \longrightarrow NO_2 + RO \tag{1.20a}$$

$$RO + O_2 \longrightarrow R'CHO + HO_2 \tag{1.20b}$$

$$HO_2 + NO \longrightarrow NO_2 + OH\,. \tag{1.20c}$$

The reactions (1.20a) and (1.20c) produce NO_2 without destroying ozone and have a rate constant which is nearly 1000 times faster than that of reaction (1.16c) (Thornton et al., 2002). By applying the above reaction scheme several times, the original VOC is finally converted to

CO_2 or CO and H_2O. In combination with reaction scheme (1.16), this results in the following net reaction:

$$\mathrm{RH} + 4\,\mathrm{O_2} + 2h\nu \longrightarrow \mathrm{R'CHO} + \mathrm{H_2O} + 2\,\mathrm{O_3} \qquad (\lambda < 420\,\mathrm{nm})\,. \tag{1.21}$$

This obviously represents a source of tropospheric ozone. The total reaction scheme, which is responsible for the ozone production, is also illustrated in Fig. 1.4 together with the most important sources of OH and peroxy radicals.

1.3. Ozone Depletion Events in Polar Regions

Despite its perceived remoteness, especially the Arctic is strongly influenced by pollution from highly industrialized countries of the Northern Hemisphere (Simpson et al., 2007b). The pollutants reach the Arctic region mainly via air mass transport or ocean currents and result in an increased contamination by heavy metals, such as mercury, or other persistent toxic substances (PTS) like PCBs[1], γ-HCH[2] and DDT[3] (Schroeder et al., 1998; Hung et al., 2005; Su et al., 2006). Together with the prevailing tropospheric chemistry in polar regions, this can have serious health consequences to the indigenous population. Thus, for example, tropospheric ozone levels are periodically depleted to near zero over huge areas (up to several thousand square kilometers, Sihler et al. (2011)) of the Arctic, similar to the annual appearance of the stratospheric ozone hole over the Antarctic. These events temporary alter the oxidation potential of the atmosphere and lead to a deposition of gas-phase mercury to the snow, allowing it to be absorbed into the food chain (Lindberg et al., 2002).

Tropospheric ozone depletion events (ODEs) were first observed close to Barrow, Alaska, in the early 1980s by Oltmans (1981). Since then, there have been extensive research efforts to investigate tropospheric ODEs, which most commonly occur from March to May in the Arctic and from August to October in the Antarctic, respectively (e. g. Mickle et al., 1989; Sumner and Shepson, 1999; Frieß et al., 2001; Bottenheim et al., 2002). Thereby a correlation between ozone depletion and enhanced atmospheric bromine in the boundary layer has been found (Mickle et al., 1989).

1.3.1. Bromine Explosions

The found negative correlation between bromine and ozone during tropospheric ODEs strengthened the hypothesis that a bromine-catalyzed chain reaction was responsible for the destruction of ozone (Barrie et al., 1988). Later measurements and studies could confirm that BrO plays a

[1] Polychlorinated biphenyl (formerly used dielectric and coolant fluid)
[2] γ-Hexachlorcyclohexan (insecticide)
[3] Dichlorodiphenyltrichloroethane (insecticide)

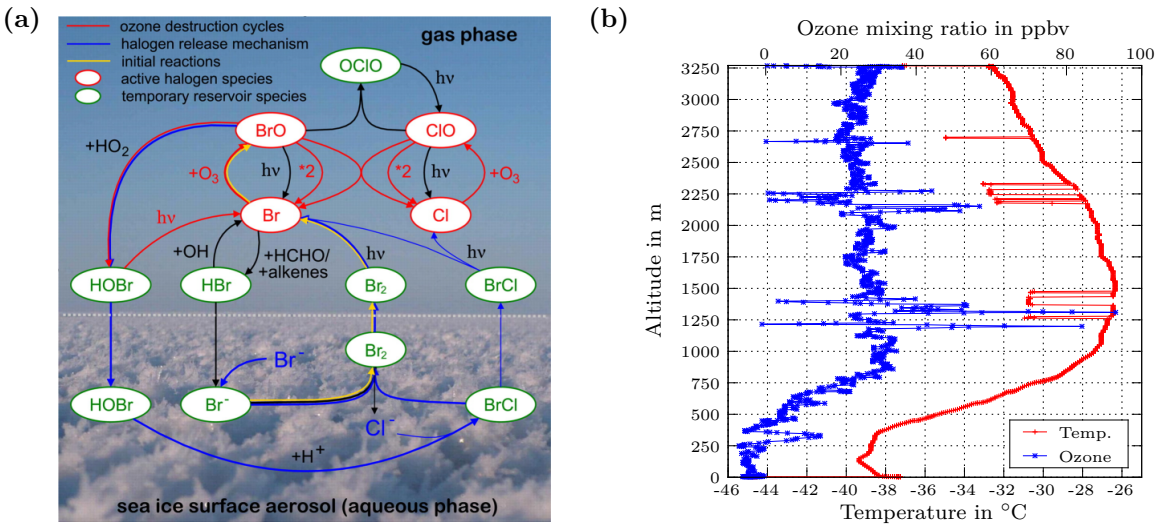

Figure 1.5.: Tropospheric ozone depletion events in the Arctic: (a) Schematic showing the simplified chemical mechanisms leading to bromine explosion and ozone destruction in polar regions (Pöhler et al., 2009). (b) Temperature and ozone mixing ratio measured by the instruments on ALAR during a flight on 15th March 2012. The temperature trend shows an inversion layer between a height of about 350 and 1000 m. Ozone is depleted in the planetary boundary layer due to the release of reactive halogen species.

key role in ODEs (e. g. Hausmann and Platt, 1994; Tuckermann et al., 1997; Martinez et al., 1999; Hönninger et al., 2004) and that bromine is most likely released from sea salt to the gas phase in an autocatalytic process (Fan and Jacob, 1992; Vogt et al., 1996). The involved reactions are basically identical to those occurring in volcanic emission plumes. However, the occurrence of bromine explosion events also in volcanic plumes was discovered much later (Bobrowski et al., 2003; Oppenheimer et al., 2006b; Bobrowski et al., 2007). A detailed description of the bromine explosion reaction cycle can be found in Sec. 1.1.2.1 of this chapter. The most important reactions for bromine release and ozone destruction are furthermore illustrated in Fig. 1.5a.

For the reasons mentioned earlier, a chlorine explosion is not expected as the conversion of Cl to HOCl is very inefficient in the gas phase and typical chlorine concentrations found during ODEs in the Arctic are also very low. Reported ratios of [Br]/[Cl] are about 800:1 (Boudries and Bottenheim, 2000; Keil and Shepson, 2006). Hence, the fraction of ozone depletion due to atomic chlorine would only be around 2 % (Simpson et al., 2007b). In contrast, IO concentrations found particularly in the Antarctic seem to be substantial. Saiz-Lopez et al. (2007) reported similar mixing ratios of BrO and IO (up to $\sim$ 6 pmol/mol) from active DOAS measurements during the CHABLIS campaign in Halley, Antarctica. Therefore, iodine chemistry may play an important role in ODEs within such regions. Even though there is no chlorine or iodine explosion, the availability of halogen compounds like ClO or IO can enhance the recycling of BrO and thus support the catalytic destruction of ozone via cross-reaction (Solomon et al., 1994; Bras and

Platt, 1995):

$$\mathrm{BrO + YO} \longrightarrow \mathrm{Br + Y + O_2} \tag{1.22a}$$
$$\longrightarrow \mathrm{BrY + O_2} \tag{1.22b}$$
$$\longrightarrow \mathrm{Br + OYO}\,, \qquad \text{with } \mathrm{Y = Cl, I}\,. \tag{1.22c}$$

An important prerequisite for the autocatalytic bromine release to occur is the availability of sunlight, as can be seen from reaction (1.3). Furthermore, special meteorological conditions are needed, to accumulate the released reactive halogen species (RHS) close to the surface. Due to the high albedo of snow and ice, air masses close to the surface are often cooler than the ones above, when sunlight returns to the Arctic region in March (1.5b). Thus, strong temperature inversion layers are formed in the lowermost 100 to 1000 m of the polar troposphere (Frieß et al., 2004). These inversion layers acts as a barrier between boundary layer and free troposphere, so that RHS-enriched air is confined to the ground. For these reasons tropospheric ODEs are predominantly observed during polar springtime, when all necessary conditions coincidence. Although the chemical processes involved in tropospheric ODEs seem to be understood, there are still a lot of open questions:

- how exactly is active bromine released from the sea salt to the gas phase?
- which are the necessary meteorological conditions?
- what is the vertical distribution of the reactive halogens?
- is the appearance of ODEs influenced by the extent and age of the Arctic sea ice?

Some of these points should be addressed briefly in the following. For a more detailed consideration of these questions, please refer to Simpson et al. (2007b).

1.3.2. Sources of RHS

Sea salt is available over wide areas in polar regions and contains a large percentage of halogens by weight, especially chlorine (55.7 %), but also bromine (0.19 %) and iodine (0.000 02 %) (Lehrer et al., 2004). Therefore, it is very likely that the reactive halogen species, which are responsible for tropospheric ozone depletion events, are released from sea salt reservoirs by the autocatalytic reaction scheme described in Sec. 1.1.2.1. However, it is still unclear from which kind of substrate Arctic halogen activation mainly arises. Proposed substrates include e. g. surface snow, blowing snow, sea ice, sea salt aerosols, sea spray, brine and frost flowers. Particularly frost flowers, which are ice crystals that grow on newly forming sea ice (Fig. 1.5a), seem to play an important role here. Thus, for example, satellite observations from GOME showed a good agreement between areas potentially covered by frost flowers and enhanced levels of BrO in the Arctic

and Antarctic (Kaleschke et al., 2004). Since frost flowers usually grow on a thin layer of high salinity brine they can have bromide ion concentrations which are about three times higher than that of sea water (Rankin et al., 2002). In addition they could efficiently release RHS to the gas phase, thanks to their relatively large surface area. Whether frost flowers directly release bromine to the atmosphere or spread sea salt aerosols by wind, which could then undergo halogen activation, is still subject to investigations. Another possibility is that sea salt aerosols are initially deposited in acidic surface snow over first-year sea ice or tundra, where bromine is then activated and released to the atmosphere by wind pumping (Pratt et al., 2013).

1.3.3. Influence of Arctic Sea Ice Extent

During the last decades an increasing decline in Arctic sea ice extent could be observed for the summer months (see Fig. 1.6). In contrast to that, the mean extent in winter remained almost the same. This means that there is now significantly more first-year ice (FYI) in the Arctic during winter and spring than 30 years before. Satellite observations of both hemispheres made by GOME (ERS-2) in 1997 showed that air masses with enhanced BrO levels were mainly present over young sea ice ($\leq$ 1 year) or in its direct vicinity (Wagner et al., 2001). Similar results were also reported by Frieß et al. (2004) and Simpson et al. (2007a) using back-trajectory calculations of BrO enriched air masses. This agreement between tropospheric BrO features and areas of first-year sea ice may be due to a higher salinity of first-year ice in comparison to multi-year ice, or because of the potential appearance of frost flowers in these regions. For these reasons, it should be expected that the frequency of tropospheric ODEs in the Arctic will increase in the future and with it possibly also negative impacts on the Arctic biosphere by the deposition of mercury.

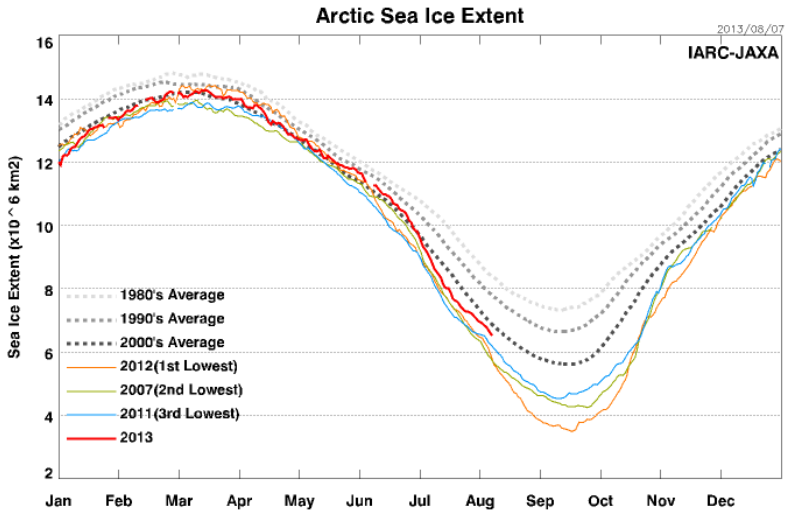

Figure 1.6.: Comparison of Arctic sea ice extent over the last three decades, showing a continuously shrinking extent during the summer months (IJIS, 2013).

2. Differential Optical Absorption Spectroscopy

The differential optical absorption spectroscopy (DOAS) is an atmospheric measurement technique that relies on characteristic narrowband absorption structures shown by several trace gas molecules in order to quantify their concentration along an observed light path. It was first applied in the late 1970's and considerably contributed to the discovery and quantification of OH and NO_3 radicals in the atmosphere (Perner et al., 1976; Platt et al., 1979). Since then it has become a widely used method to detect a variety of UV/vis absorbing species, including NO_2, HCHO, $C_2H_2O_2$, H_2O, O_3, O_4, SO_2, IO, OClO and BrO. For instance, DOAS instruments are often used aboard of Earth observation satellites like ERS-2 (GOME), MetOp (GOME-2), Aura (OMI) or Envisat (SCIAMACHY) to monitor global distributions of key air quality components such as ozone, nitrogen dioxide and sulfur dioxide (e. g. Beirle et al., 2004; Veefkind et al., 2006). The remote sensing capabilities of the DOAS method also make it a particular useful tool for the investigation of highly reactive species (e. g. halogen compounds in volcanic plumes).

In principle DOAS instruments can be subdivided in two types: active ones and passive ones. While active DOAS instruments use artificial light sources like xenon arc lamps or light-emitting diodes (LEDs), passive DOAS instruments use already existing light sources in nature (e. g. sun, moon or stars). For details about the different types of DOAS instruments and their application, please refer to Platt and Stutz (2008). In the following the main focus is set on describing the fundamentals of the DOAS method.

2.1. Absorption Spectroscopy

When light passes through an absorber (e. g. gases or liquids), its intensity is reduced due to photon-matter interactions. Such interactions are, for example, the excitation of molecular electronic, vibrational or rotational states. Since molecular excitation states have discrete energy levels, each absorber shows a specific absorption structure in a continuous energy spectrum. In absorption spectroscopy transmitted light is analyzed for these characteristic structures in order to identify and quantify the involved substances. Figure 2.1 shows some literature absorption cross-sections of species which can be detected with the DOAS technique.

The basic equation in absorption spectroscopy is the Beer-Lambert law, which quantitatively describes the absorption of light by matter:

$$I(\lambda) = I_0(\lambda) \cdot \exp\left(-L \cdot \sigma(\lambda) \cdot c\right) , \tag{2.1}$$

where $I_0(\lambda)$ is the initial intensity of the light beam, L the length of the light path within the absorber, c the concentration (number density) of the absorber, $\sigma(\lambda)$ the absorption cross-section at the wavelength λ and $I(\lambda)$ the remaining light intensity after passing the absorber. (see also Fig. 2.2).

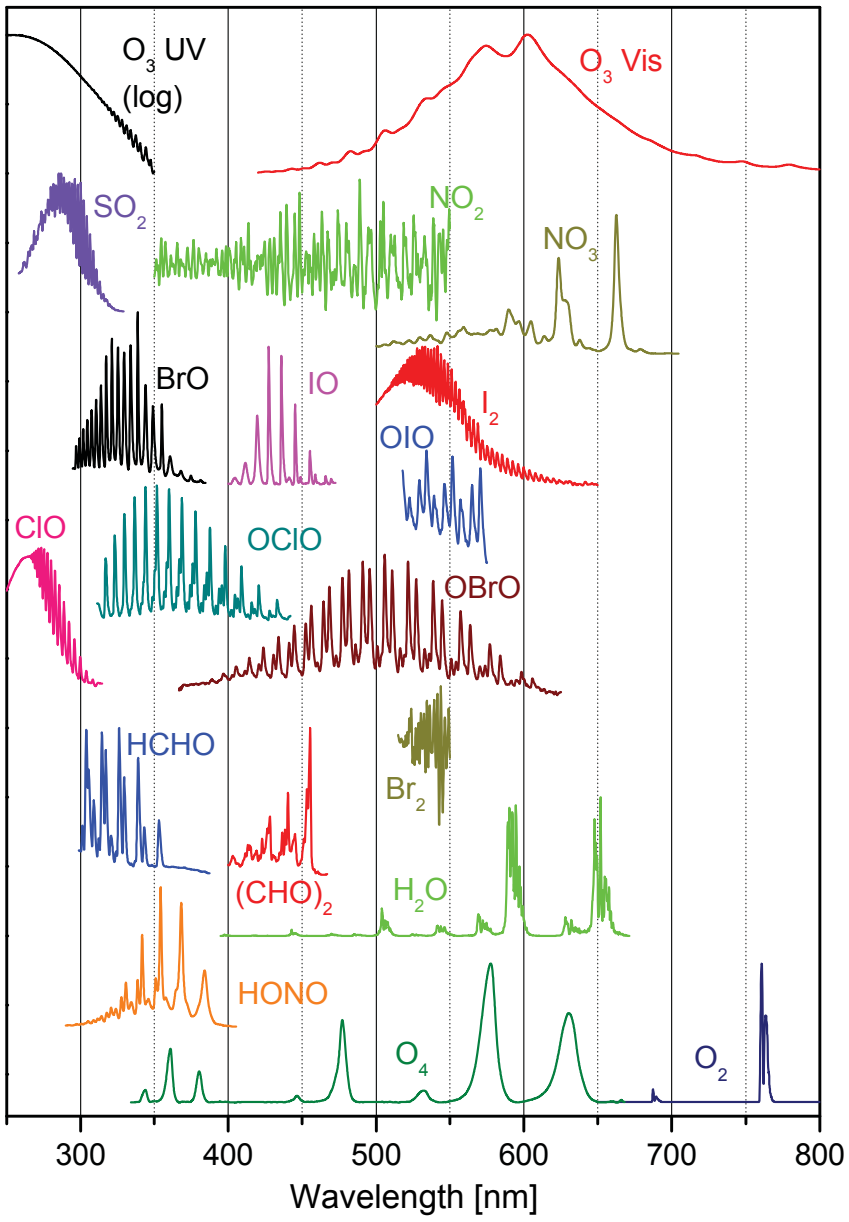

Figure 2.1.: Literature cross-sections with arbitrary scaling for detectable species in the UV-vis range. (U. Frieß, personal communication, 2010)

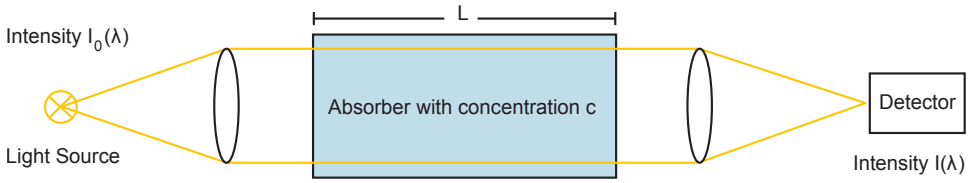

Figure 2.2.: Basic principle of the absorption spectroscopy: Light is emitted with the initial intensity $I_0(\lambda)$ from a light source and subsequently passes an absorber with the concentration c. The remaining intensity $I(\lambda)$ is then measured by a detector. Adapted from Sebastián Müller de Vries (2004).

Thus, when the cross-section $\sigma(\lambda)$ and the length L are known, the concentration c of the absorber can be calculated from the measured ratio of $I_0(\lambda)$ and $I(\lambda)$:

$$c = \frac{\ln \frac{I_0(\lambda)}{I(\lambda)}}{\sigma(\lambda) \cdot L} = \frac{\tau(\lambda)}{\sigma(\lambda) \cdot L} \,. \tag{2.2}$$

In the above equation the "optical density" $\tau(\lambda)$ was introduced, which is defined as the negative exponent in Eq. 2.1:

$$\tau(\lambda) \coloneqq \ln \frac{I_0(\lambda)}{I(\lambda)} \,. \tag{2.3}$$

However, Eq. (2.1) is only valid for the simple case of a single, homogeneously distributed absorber. The Beer-Lambert law has thus to be extended when multiple absorbers are present at the same time. Also the absorption cross-section σ not only depends on the wavelength of the incident light but also on pressure and temperature. Furthermore, the extinction of light due to scattering has to be considered for atmospheric measurements. Especially the elastic scattering processes of Rayleigh and Mie scattering have to be taken into account. Then Eq. (2.1) becomes:

$$I(\lambda) = I_0(\lambda) \cdot \exp\left(- \int_0^L \left(\epsilon_R(\lambda, l) + \epsilon_M(\lambda, l) + \sum_i \sigma_i(\lambda, p, T) \cdot c_i(l) \right) \mathrm{d}l \right) , \tag{2.4}$$

with the extinction coefficients ϵ_R and ϵ_M for Rayleigh and Mie scattering as well as the concentration c_i and the cross-section σ_i of the i-th absorber. Equation 2.4 now adequately describes the extinction of light due to absorption and scattering in the atmosphere. Nonetheless, some serious problems arise when applying this approach to atmospheric measurements. So, for example, it is almost impossible for ground-based or airborne instruments to measure the initial intensity $I_0(\lambda)$ of the used light source, because this would require to remove the atmosphere from the observed light path (i. e. measure in space for passive DOAS). Moreover it is very

difficult to distinguish between broadband absorption structures due to scattering processes or molecular absorption. In the differential optical absorption spectroscopy such difficulties are avoided.

2.2. The DOAS Principle

Many factors that reduce the initial light intensity $I_0(\lambda)$ during atmospheric measurements (e. g. scattering processes or the transmittance of the instrument's optics) show broadband absorption structures, but certain trace gases also exhibit narrowband (or "differential") spectral characteristics. The basic idea of the DOAS method is thus to separate broad- and narrowband spectral structures and use only the latter ones for spectral analysis. Accordingly, the absorption cross-section can be split in two parts and written as follows:

$$\sigma(\lambda, p, T) = \sigma_B(\lambda, p, T) + \sigma'(\lambda, p, T)\,. \tag{2.5}$$

The principle of this separation is illustrated in Fig. 2.3. When inserting Eq. 2.5 in Eq. 2.4, one obtains:

$$\begin{aligned} I(\lambda) = I_0(\lambda) \cdot \exp\left(-\int_0^L \left(\epsilon_R(\lambda, l) + \epsilon_M(\lambda, l) + \sum_i \sigma_{B,i}(\lambda) \cdot c_i(l)\right) \mathrm{d}l\right) \\ \cdot \exp\left(-\int_0^L \left(\sum_i \sigma'_i(\lambda) \cdot c_i(l)\right) \mathrm{d}l\right) \end{aligned} \tag{2.6}$$

The first two factors in Eq. 2.6 vary only slowly with wavelength and are combined in the intensity I'_0 below:

$$I'_0(\lambda) = I_0(\lambda) \cdot \exp\left(-\int_0^L \left(\epsilon_R(\lambda, l) + \epsilon_M(\lambda, l) + \sum_i \sigma_{B,i}(\lambda, p, T) \cdot c_i(l)\right) \mathrm{d}l\right)\,. \tag{2.7}$$

Analogue to Eq. 2.3 then a differential optical density can be defined:

$$\tau'(\lambda) := \ln \frac{I'_0(\lambda)}{I(\lambda)} = \int_0^L \sum_i \sigma'_i(\lambda, p, T) \cdot c_i(l)\,\mathrm{d}l \tag{2.8}$$

The concentration c_i of an atmospheric absorber can therefore be calculated via Eq. 2.2, when substituting $\tau(\lambda)$ and $\sigma(\lambda)$ with the differential quantities $\tau'(\lambda)$ and $\sigma'_i(\lambda, p, T)$. A useful quantity to be introduced here is the slant column density (SCD), S, which is the concentration of a certain absorber integrated along the observed light path and the result of a DOAS retrieval:

$$S_i := \int_0^L c_i(l)\,\mathrm{d}l \tag{2.9}$$

In this way the DOAS method allows to detected several trace gas species simultaneously, because each absorber has a unique absorption structure. For ground-based or airborne passive DOAS measurements, the reference $I'_0(\lambda)$ is usually obtained by recording a spectrum in an area which is presumably free of the investigated trace gases (e. g. luv side of a volcano). However, the presence of the observed species in the reference spectrum can not be excluded by this approach and cause an offset in the measured slant column densities. The results of such passive DOAS measurements are therefore referred to as differential slant column densities (dSCDs), which give the concentration of the observed trace gases integrated along a particular light path through the atmosphere minus the integrated concentration already existing in the reference spectrum $I'_0(\lambda)$.

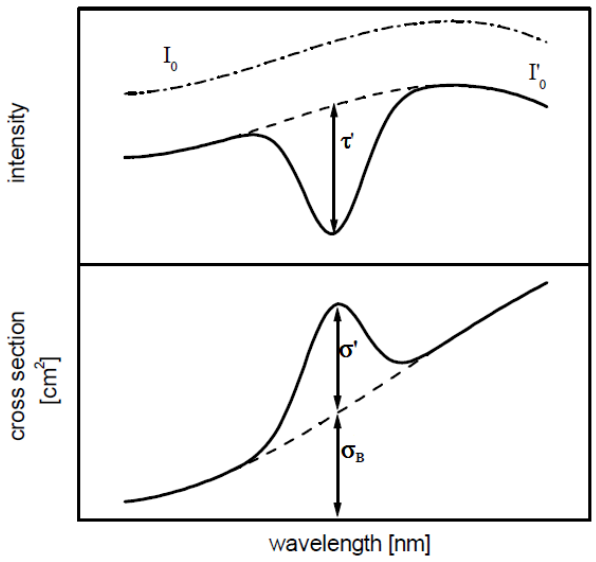

Figure 2.3.: Illustration of the basic DOAS principle: The measured light intensity and literature absorption cross-sections are split into broadband (I'_0 and σ_B) and narrow parts (τ' and σ'). Adapted from Platt and Stutz (2008)

2.3. The Measurement Process

When recording atmospheric absorption spectra one has to consider, that the width of many absorption features is well below the spectral resolution of a typical spectrograph ($\sim 0.1-1.0\,\mathrm{nm}$). Especially the finite width of the entrance slit and the sampling of the used detector limit the spectral resolution of a spectrograph, but it is also degraded by aberration effects of the optics (e. g. grating, collimators). Mathematically the degradation of the spectral resolution can be

described by the convolution of the incident light intensity $I(\lambda)$ with an instrument function $H(\lambda)$:

$$I^*(\lambda) = I(\lambda) * H(\lambda) \coloneqq \int I(\lambda') \cdot H(\lambda - \lambda') \, \mathrm{d}\lambda' \,, \tag{2.10}$$

where $I^*(\lambda)$ is the light intensity, that impacts on the detector. The instrument function $H(\lambda)$ is usually determined by recording single atomic emission lines with the instrument (e. g. mercury emission lines in the UV range). Since the natural line width of such emission lines is only of the order of 10 pm (Platt and Stutz, 2008), the measured response of the spectrograph is a good approximation for $H(\lambda)$. The discretization of the spectrum due to the size of the individual detector elements is then given by the following equation:

$$I^+(j) = \int_{\lambda(j)}^{\lambda(j+1)} I^*(\lambda') \, \mathrm{d}\lambda' \,. \tag{2.11}$$

Here, j is the channel number of the particular detector element (e. g. CCD pixel), which typically ranges from 1 to 1024. The wavelength-to-pixel mapping $\lambda(j)$ depends on the dispersion of the spectrograph along the spectral axis of the detector and can usually be approximated by a polynomial of second or third degree ($q = 2, 3$):

$$\lambda(j) = \sum_{k=0}^{q} a_k \cdot j^k \tag{2.12}$$

Aside from discretizing the incident light spectrum, the detector also adds two different offsets to the output signal $I^+(j)$:

$$S(j) = I^+(j) + O(j) + D(j) \tag{2.13}$$

The first one is the electronic offset $O(j)$, which is added to the signal in order to assure that the ADC of the detector does not receive negative values (see Sec. 3.7.2.1). Because the electronic offset is added during every readout process, its value is proportional to the number of co-added scans. The second one is the dark current $D(j)$, which is due to the thermal excitations of electrons in the detector material (see Sec. 3.7.2.1) and thus proportional to the exposure time and the Boltzmann-factor $e^{-\Delta E/kT}$. Both offsets have to be subtracted from the received signal $S(j)$ prior to the DOAS evaluation procedure. An overview to the general DOAS measurement process can be found in Fig. 2.4.

Not only the incident light spectrum, but also the literature absorption cross-sections σ_i

typically have a much higher spectral resolution than achievable with spectrographs used in the field. Hence, their resolution has to be degraded to match the one of the instrument in preparation for the DOAS analysis. For this reason the cross-sections are likewise convolved with the instrument function $H(\lambda)$:

$$\sigma_i^*(\lambda) = \sigma_i(\lambda) * H(\lambda) = \int \sigma_i(\lambda') \cdot H(\lambda - \lambda')\,\mathrm{d}\lambda' \,. \tag{2.14}$$

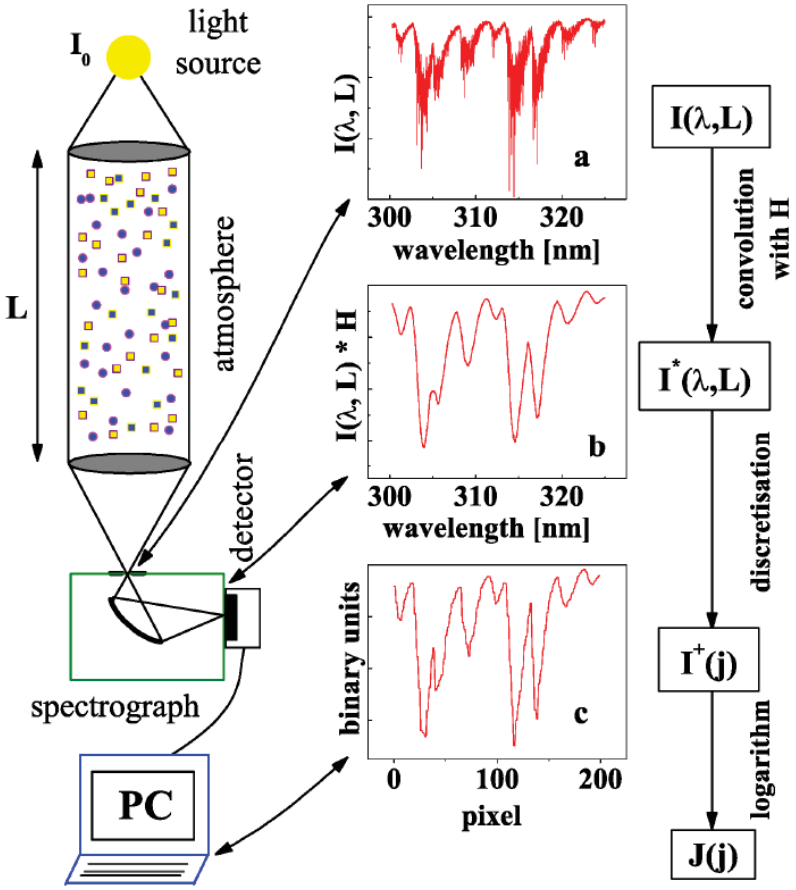

Figure 2.4.: The general measurement process of a DOAS instrument: Light with the initial intensity I_0 passes an absorber (here: HCHO) and enters a spectrograph. Due to the finite spectral resolution of the spectrograph, the incident spectrum I_0 is convolved with the instrument function H. The resulting intensity I^* is then discretized by the detector of the instrument to I^+. Adapted from Platt and Stutz (2008).

2.4. The DOAS Analysis

In the following, all intensity spectra are considered to be already corrected for electronic offset and dark current signal. They can then be evaluated for trace gas absorptions by a suitable software. For the evaluation of the data presented in Chaps. 6 to 8 the software DOASIS (Kraus, 2006) for Windows operating systems was used, which works according to the principle below.

First of all Eq. 2.4 has to be rewritten in order to introduce the polynomial $P(\lambda)$:

$$\begin{aligned} \ln(I(\lambda)) &= \ln(I_0(\lambda)) + P(\lambda) - \int_0^L \sum_i \sigma_i(\lambda, p, T) \cdot c_i(l)\, \mathrm{d}l \\ &= \ln(I_0(\lambda)) + P(\lambda) - \sum_i \sigma_i(\lambda, p, T) \cdot S_i\,. \end{aligned} \tag{2.15}$$

$P(\lambda)$ thereby expresses the differences in the broadband absorption between the reference spectrum $I_0(\lambda)$ and the measurement spectrum $I(\lambda)$. The degree of the polynomial is set prior to the evaluation process and depends on the considered wavelength range as well as the expected amount of absorbers. Usually a polynomial of second to fifth degree is applied. The DOAS fit algorithm then creates a model function $F(\lambda)$:

$$F(\lambda) = \ln(I_0(\lambda)) + P(\lambda) - \sum_i (\sigma_i(\lambda) \cdot S_i) \tag{2.16}$$

and varies the linear combination of the absorption cross-sections σ_i and the slant column densities S_i as long as χ^2 becomes minimal. In this case, χ^2 is the sum of the squared differences between the logarithm of the measured light intensity $\ln(I(l))$ and the model function $F(l)$:

$$\chi^2 = \sum_{l=\lambda_1}^{\lambda_2} (\ln(I(l)) - F(i))^2\,, \tag{2.17}$$

where λ_1 and λ_2 are the limits of the chosen evaluation wavelength range. For minimizing χ^2, DOASIS uses a combination of a linear least-squares fit and a non-linear Levenberg-Marquardt algorithm (Levenberg, 1944; Marquardt, 1963), which is required for the calculation of spectral shift and squeeze parameters.

2.5. The Ring Effect

When comparing spectra of atmospheric scattered sunlight taken at different solar zenith angles (SZAs), one can observe a “filling-in” of the Fraunhofer lines with increasing light path through

the atmosphere. This is the so-called "Ring effect", which was first described by Shefov (1959) and Grainger and Ring (1962). Today, it is known that the Ring effect is primary caused by rotational Raman scattering on O_2 and N_2 molecules in the atmosphere (e. g. Bussemer, 1993; Joiner and Bhartia, 1995; Vountas et al., 1998). The inelastic scattering processes change the energy and thus the wavelength of incident photons. Since more photons are available at wavelength regions with higher light intensity, the Fraunhofer lines become filled up in total. The typical reduction in optical density due to the Ring effect is only of the order of a few percent (Platt and Stutz, 2008). However, the absorption by trace gases like BrO and OClO can be more than an order of magnitude smaller. For this reason it is essential to correct for the Ring effect when weak atmospheric absorbers should be detected with high accuracy.

In order to correct for the Ring effect, Solomon et al. (1987) suggested to consider an additional spectrum, the so-called Ring spectrum, in the DOAS analysis process. Knowing the rotational Raman spectra of O_2 and N_2 as well as their concentration in the atmosphere, the Ring spectrum can be computed from the reference spectrum I_0 (Chance and Spurr, 1997). The DOASIS software (Kraus, 2006) offers a function for this calculation, which was used for the spectral retrieval in this work. Because the amplitude of the Ring spectrum can have different wavelength dependencies due to e. g. multiple Rayleigh scattering or strong contributions of surface reflection, in some cases also a second Ring spectrum is included in the DOAS analysis (Wagner et al., 2009). This additional Ring spectrum can be calculated from the original one by multiplication with a polynomial of fourth degree.

2.6. The Solar I_0 Effect

Another effect that is related to the Fraunhofer lines is the so-called I_0 effect. It arises due to the fact, that the literature absorption cross-sections for the DOAS analysis are typically recorded in a laboratory with a nearly smooth reference spectrum I_0, whereas in passive DOAS measurements that use the sun as light source I_0 is the highly structured solar Fraunhofer spectrum (Aliwell et al., 2002). If now the optical density τ^* is determined from passive DOAS measurements, the Fraunhofer lines do not completely cancel out because I_0 and I are both convolved with the instrument function $H(\lambda)$ before their ratio is calculated (see Eq. (2.18)). The remaining absorption structures thus slightly differ from the literature cross-sections $\sigma^*(\lambda)$ that were convolved with the instrument function $H(\lambda)$. Mathematically, this can be explained by the non-commutativity of ratioing and convolution.

$$\begin{aligned} \tau^* = \ln \frac{I_0^*(\lambda)}{I^*(\lambda)} &= \ln \frac{I_0(\lambda) * H(\lambda)}{(I_0(\lambda) \cdot \exp(-\sigma \cdot S)) * H(\lambda)} \\ &\neq \ln \frac{I_0(\lambda)}{I_0(\lambda) \cdot \exp(-\sigma \cdot S)} * H(\lambda) = \sigma^*(\lambda) \cdot S \end{aligned} \tag{2.18}$$

Especially for strong absorbers like O_3 in the UV range, the I_0 effect can lead to significant errors in the spectral retrieval and has thus to be corrected for. This can be achieved by calculating an I_0-corrected absorption cross-section:

$$\sigma^*_{I_0}(\lambda) = \ln \frac{I^*_{0,K}(\lambda)}{I^*_K(\lambda)} \cdot \frac{1}{S}\,, \tag{2.19}$$

where $I^*_{0,K}(\lambda)$ is a high resolution Fraunhofer spectrum (Chance and Kurucz, 2010) that is convolved with the instrument function $H(\lambda)$:

$$I^*_{0,K}(\lambda) = I_K(\lambda) * H(\lambda) \tag{2.20}$$

and $I^*_K(\lambda)$ additionally includes absorption, using the literature cross-section $\sigma(\lambda)$ of the considered species:

$$I^*_K(\lambda) = (I_K(\lambda) \cdot \exp(-\sigma(\lambda) \cdot S)) * H(\lambda) \tag{2.21}$$

As can be seen from Eq. (2.21), the calculation of an I_0-corrected cross-section also requires the slant column density S of the absorber. For that purpose, the following approach was used in this work: First of all, the column density was calculated using the standard convolution for the literature cross-sections (Eq. (2.14)). The retrieved value was then used as input parameter for Eq. (2.19). In order to minimize the additional computational effort, the I_0-corrected cross-section was only recalculated when the column density changed by more than a given factor (20 % for O_3) during the evaluation of multiple spectra.

3. Instrument Description

3.1. The Heidelberg Airborne Imaging DOAS Instrument (HAIDI)

The HAIDI system was built with the intention to take hyperspectral images (images with two or three spatial dimensions, where each pixel contains additional spectral information) of large areas with high spatial resolution and in the shortest possible time, to capture also high dynamic processes. Therefore the requirements to an instrument carrier are best fulfilled by an aircraft, which is not bound to roads and not restricted by physical features of the ground, like woods, rivers or hills. It can cover large distances in relatively short time and its high flight altitude allows to overview greater areas at once. At the same time the flight altitude is still low enough to achieve a high spatial resolution compared to satellite measurements. By using the DOAS method (Platt and Stutz, 2008), the spectral information within each pixel of the hyperspectral images can be translated into the column density of one or several trace gases. This data can subsequently be assembled into maps to reveal the spatial distribution of the trace gases along various dimensions in space, depending on the choice of the instrument's viewing geometry.

3.2. Remote Sensing Techniques

Today, various methods exist to acquire hyperspectral images from remote sensing observations via satellites or aircraft. Two commonly used are the "whiskbroom" and the "pushbroom" scanning technique (Schowengerdt, 2006). Both techniques are based on the detection of light dispersed by a prism or grating in order to obtain the spectral information of the images. However, the usage of the detector and the way images are acquired is very different. A simple method to illustrate the basic differences in the recording of hyperspectral images between the two techniques is the so-called hyperspectral cube (Fig. 3.1). Since each pixel of a hyperspectral image is in principle a 3-dimensional dataset with two spatial dimensions and a third spectral one, the information contained in such images can be represented by a 3-dimensional space, the hyperspectral cube. The hyperspectral cube is thus spanned by two spatial axes (x, y) and an additional spectral one ($I(\lambda)$). Now, in order to acquire a hyperspectral image the entire cube has to be scanned by the instrument, i. e. information about each element in the 3-dimensional space has to be collected. The approaches followed by whiskbroom and pushbroom scanning techniques for that purpose are discussed below.

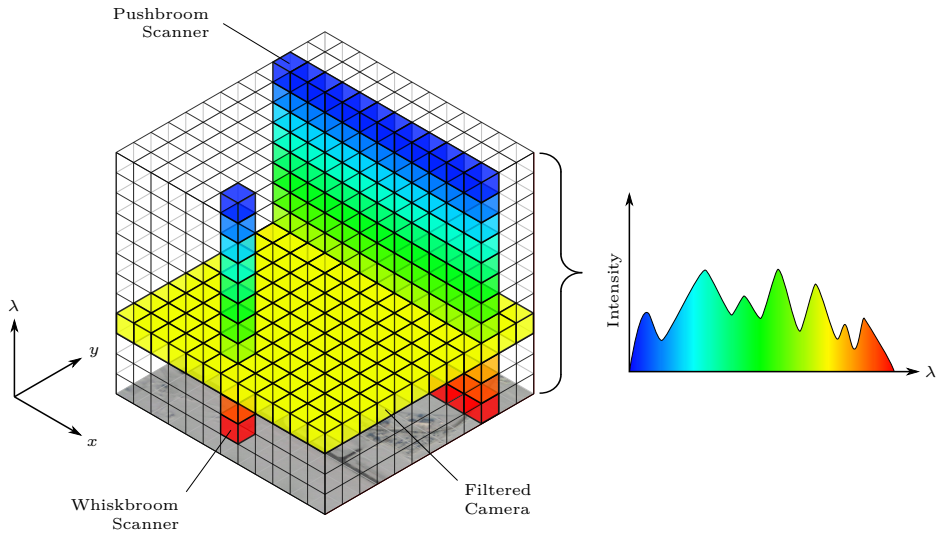

Figure 3.1.: The hyperspectral cube is an often used schematic to visualize the different recoding techniques in hyperspectral imaging. Two dimensions of the cube represent the spatial dimensions of the image (x, y), while the third axis represents the spectral dimension (i. e. the wavelength λ). For spectral images the whole cube has to be scanned. As can be seen, the whiskbroom technique can only acquire one pixel at a time with spectral information. So, scanning in two spatial dimensions is necessary to take spectral images. The pushbroom technique records a whole swath with spectral information at once and needs only scanning in one spatial dimension. A camera equipped with band-pass filters can take both spatial dimensions at once but will only contain spectral information from one narrow wavelength range.

3.2.1. Whiskbroom Scanning Method

Whiskbroom scanners (sometimes also referred to as across track scanners) are often used in air- and satellite-borne instruments (e. g. Landsat 1–7 or MODIS on Terra/Aqua, Kramer (2001)). The name thereby derives from the fact that such a system uses a scanning prism or mirror to redirect incident light into the instrument (see Fig. 3.2a), which is similar to the motion of a whisk broom. A scanning optics is necessary in this case, because the detector of a whiskbroom system records only spectral information and no information along the x or y axis. Therefore, only a one-dimensional detector is required by the whiskbroom scanner. However, a two-dimensional detector normally offers a larger area to collect incident light and can thus achieve a better signal-to-noise ratio.

The restriction on spectral information means that only one ground element (pixel) can be observed at a time. So, in order to get a hyperspectral image of the overflown area the missing spatial dimensions have to be acquired via scanning. While scanning in one dimension is usually achieved by the motion of the instrument carrier (aircraft, satellite, etc.), the other dimension is acquired by the scanning prism or mirror that changes the instrument's viewing direction perpendicular to the flight track. The nadir viewing directions of the HAIDI system operate according to the principle of the whiskbroom technique (Fig. 3.3).

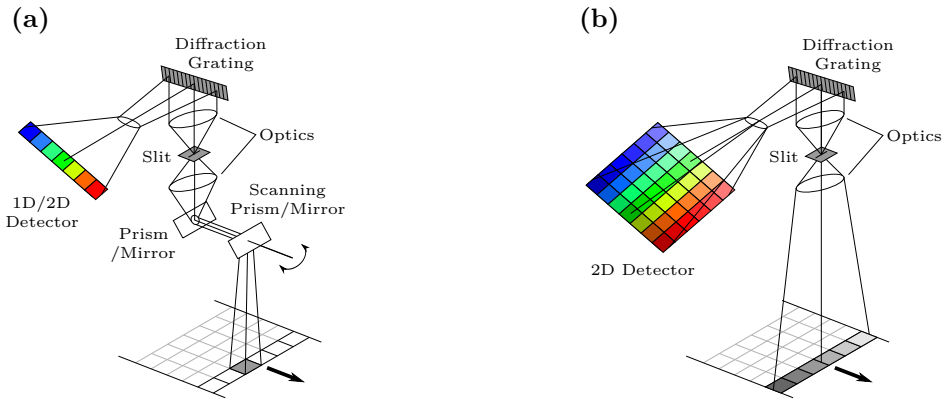

Figure 3.2.: Basic principle of operation for common remote sensing techniques: (a) Whiskbroom scanner (b) Pushbroom scanner.

3.2.2. Pushbroom Scanning Method

Also pushbroom scanners (or along track scanners) are used by a number of satellites to acquire hyperspectral images (e. g. Landsat 8, Roy et al. (2014)). In contrast to the whiskbroom technique, the pushbroom technique mandatorily requires a two-dimensional detector (e. g. CCD-Array) and an imaging spectrograph, because in this case the detector records spectral information and one spatial dimension (x or y) simultaneously. This means that spectral information is stored along the rows of the CCD detector, where different rows can belong to different pixels on the ground (see Fig. 3.2b). For this reason, pushbroom scanners can take a whole row of pixel, also called a swath, at once. Analogue to the whiskbroom technique, the remaining spatial dimension is then also acquired by the motion of the instrument platform. The movement of the instrument's field of view (FOV) therefore resembles more that of a push broom. Due to this approach the pushbroom technique does not require any movable parts. When HAIDI uses an instrument in limb geometry, the pushbroom technique is applied (Fig. 3.3).

3.3. Operating Principle of HAIDI

In practical terms, both scanning techniques described in the previous sections have their advantages and disadvantages (see Tab. 3.1). Therefore it depends on the particular application and possible restrictions which of these techniques is suited best for the measurement of trace gas distributions. HAIDI is designed in such a way that it can be used with both techniques. This allows to reach a maximum of flexibility. In total HAIDI can operate up to three fully independent passive DOAS instruments working with either the whiskbroom or the pushbroom technique. Each instrument features a telescope system to analyze scattered solar radiation between 300 nm and 407 nm (shiftable to 343 nm − 450 nm) with a spectral resolution of about

0.5 nm. To cover a preferably large area with one overflight the HAIDI system always uses a whiskbroom scanner in nadir direction, as the scanning prism can cover a very wide field of view (FOV) across track without requiring a large or complex entrance optics. Moreover, the field of view can be easily changed by software according to the requirements of a particular mission (see Sec. 3.4). A drawback of the whiskbroom technique is that the spatial resolution varies with the scan angle of the system. This is caused by an increasing distance between entrance optics and ground towards the ends of a swath. Because of the resulting shape of the swath this is called the bow tie effect. The pushbroom technique does not suffer from this effect (other than caused by the curvature of the Earth) because here the varying distance is compensated by a likewise changing distance between the optical center of the lens and the individual fibers in the fiber column on the telescope side (see Fig. 3.20).

With the whiskbroom scanner applied in nadir direction the horizontal distribution of trace gases can be determined. To obtain also the vertical profile of tropospheric absorbers, one of the following approaches can be used:

- **Multiple Downward Scanners:** The installation of HAIDI aboard the HALO research aircraft (see Sec. 3.11.3) is intended to use a set of three whiskbroom scanners pointed to different downward directions (Fig. 3.63) and thus to retrieve the vertical trace gas distribution by tomographic inversion methods applied to the different lines of sight (e. g. Laepple et al., 2004; Heue, 2005). Because HALO typically flies at high altitude (∼10–15 km), above the investigated air masses, this setup is most suitable to obtain vertical profile information. Whiskbroom scanners have furthermore the advantage of a constant spectral property for all viewing directions. Since it is not necessary to operate the CCD detector in imaging mode, a whiskbroom scanner does not need a mechanical shutter or equivalent techniques as in Interline-Transfer CCDs, which effectively reduce the light sensitive area of the detector.
- **Forward Scanner:** Vertical profile information of trace gases and aerosols at, or close to, the flight altitude can be obtained with high vertical resolution by a system looking in forward direction and covering a range of elevation angles around 0°. For this purpose, a "pushbroom" scanner is applied in limb geometry. In principle also a whiskbroom scanner can be used for the limb direction, but this has so far not been implemented because of space restrictions. A pushbroom scanner can be more compact due to the lack of motorized optics and in addition it is beneficial for the later profile retrieval that it measures all elevation angles at the same time (no need to compensate for different aircraft positions and orientations). However, since the detector of a pushbroom scanner records spectral and spatial information simultaneously it takes much longer (up to 300 ms) to read out the CCD compared to a whiskbroom scanner. During this time the shutter has to be closed and the detector is therefore not sensitive to incident light, which reduces the achievable signal-to-noise ratio of the instrument.

Table 3.1.: Advantages and disadvantages of the different remote sensing techniques used by the HAIDI system.

Advantages	Disadvantages
Whiskbroom Scanner	
• can cover a very wide swath without complex entrance optics • swath can easily be changed by software • no mechanical shutter required • system has the same spectral slit function for all viewing directions	• requires moving parts (scanner) • pixel distortion (bow tie effect) • requires more space for installation (motorized optics) • movement of instrument and optics during integration time makes viewing geometry more complex
Pushbroom Scanner	
• all pixel of a swath are taken at the same time and under same conditions • no pixel distortion • narrow swath can be realized with very simple and compact entrance optics • no moving parts (scanner)	• typically requires mechanical shutter • readout time (closed shutter) is lost for recording signal • separate slit function for each viewing direction • change of swath only possible with change of optics

The general measurement principle and geometry of the HAIDI system is illustrated in Fig. 3.3. In this example, both scanning techniques (one whiskbroom scanner in nadir direction and one pushbroom scanner in forward direction) are used. It is especially suited to smaller, low flying aircraft. An overview to the different instrumental setups of the HAIDI system can be found in Sec. 3.11. Independent of the used scanning technique, all setups are working on the same principle. Solar radiation with the intensity $I_0(\lambda)$ is passing Earth's atmosphere and is thereby partly absorbed by different trace gases and aerosols. This light is then reflected on the ground or scattered in the atmosphere by Rayleigh and Mie scattering before it is collected by HAIDI's telescopes with the remaining intensity $I(\lambda)$. As can be seen in Fig. 3.3, the instantaneous field of view (IFOV) of the telescopes differs for the two scanning techniques. Due to the reasons discussed above, the whiskbroom scanner has to record all pixel sequentially in order to obtain hyperspectral images. Because of the aircraft's motion during the scan this leads to a diagonal strip pattern of the observed area which is typical for the whiskbroom technique. Each strip is called a swath and currently consists of up to 128 scans which are taken while the whiskbroom scanner moves the viewing direction of the telescope along one swath. The IFOV of the forward-looking telescope covers all viewing directions at the same time instead, but has only a narrow total FOV due to the restrictions of the pushbroom technique. In case of the

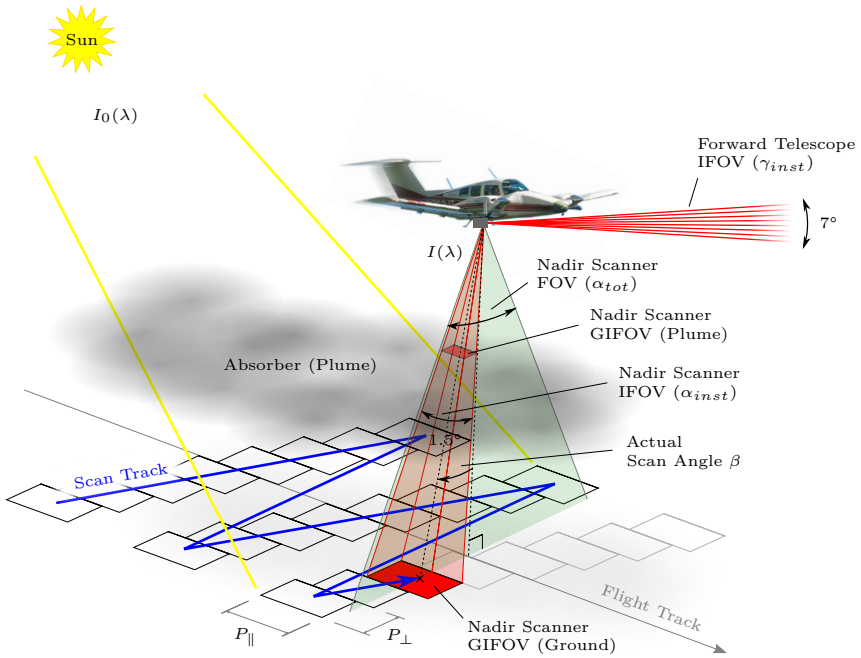

Figure 3.3.: Schematic showing the general measurement principle of the HAIDI system using a whiskbroom scanner in nadir direction and a pushbroom scanner in forward direction. The instantaneous field of view of the two telescopes (α_{inst}, γ_{inst}) is marked in red. While the whiskbroom scanner uses a sweeping prism to rotate the viewing direction of the nadir telescope by angle β across track direction, resulting in the total FOV α_{tot} (green), the forward-looking telescope observes multiple viewing angles at once.

nadir observations the results from the following DOAS analysis (Sec. 4) can then be plotted into spatial maps by reconstructing the path taken by the light from the sun to the telescopes (Sec. 4.2).

In order to disperse and detect the light gathered with the different entrance optics, HAIDI features a set of custom-built spectrograph and CCD detector for each applied whiskbroom or pushbroom scanner. The spectrographs and detectors are stored in a special instrument rack inside the aircraft and are connected to the entrance optics by a fiber-optical system of several meter length. In the following sections the different components of the HAIDI system are described in detail, beginning with an overview of the overall instrumental setups used for the whiskbroom and pushbroom scanners.

3.4. The Nadir Scanner (Whiskbroom)

As mentioned before, the entrance optics of HAIDI's whiskbroom scanners are usually pointed to the downward direction of the aircraft in order to scan the ground beneath. In the following, HAIDI's whiskbroom scanners are thus referred to as nadir scanners. The overall technical setup used for a nadir scanner can be seen in Fig. 3.4. The first part, when following the path

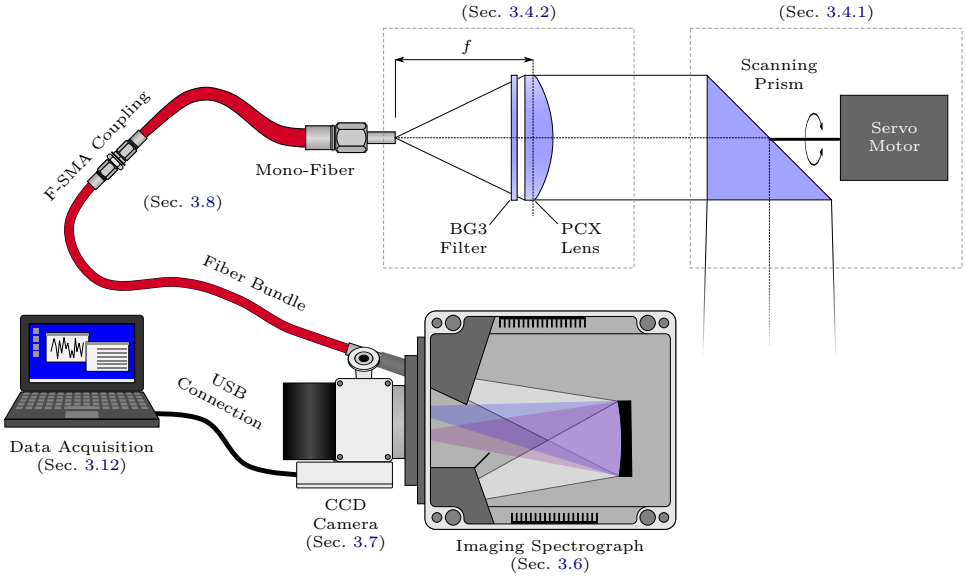

Figure 3.4.: Setup of HAIDI's nadir scanner (whiskbroom scanner). A sweeping prism guides the light from different viewing directions to the telescope of the system. From there the light passes through a fiber optic cable to the spectrograph. Hardware control and data acquisition is done by a computer which is connected via USB.

of light through the instrument, is the entrance optics. It essentially consists of a telescope whose viewing direction can be changed perpendicular to the flight direction by a servo actuated right angle quartz prism. A detailed description on how the servo is controlled can be found in Sec. 3.4.1. The quartz prism is used here instead of a mirror to redirect incident light into the telescope, because the reflectivity of metallic surfaces (mirror) depends not only on the angle of incident but also on the polarization direction (Williams, 1982). As the sunlight becomes partly polarized by scattering in the atmosphere (Liou, 2002), a mirror can act as a polarization filter and thus affect the sensitivity of the system to different components in the incident radiation. The total internal reflection of a prism instead is polarization-independent. Only the reflectivity of the prism surfaces varies slightly with polarization direction due to Fresnel reflection. However, for almost normally incident light, like in case of the nadir scanner prism, the polarization dependence of the Fresnel reflection vanishes.

The entrance optics is intended to be placed over an aperture in the fuselage of an aircraft or alternatively in an external housing with a clear view to the ground. Since available space is usually very rare at such positions, the entrance optics of HAIDI's nadir scanner is separated from the rest of the instrument. This is achieved by using a system of optical fibers. Viewed from the telescope side, the first part of the fiber optics cable consist of a mono fiber (single optical fiber) with a core diameter of 1250 µm. Together with the focal length of the telescope (48.1 mm at 350 nm, see Sec. 3.4.2), this yields an instantaneous field of view (IFOV) of $\alpha_{inst} = 1.5°$ (see Fig. 3.3). Thus, for an assumed flight altitude of 1500 m, the ground projected instantaneous field of view (GIFOV) of the telescope would be about 40×40 m. However, because of the

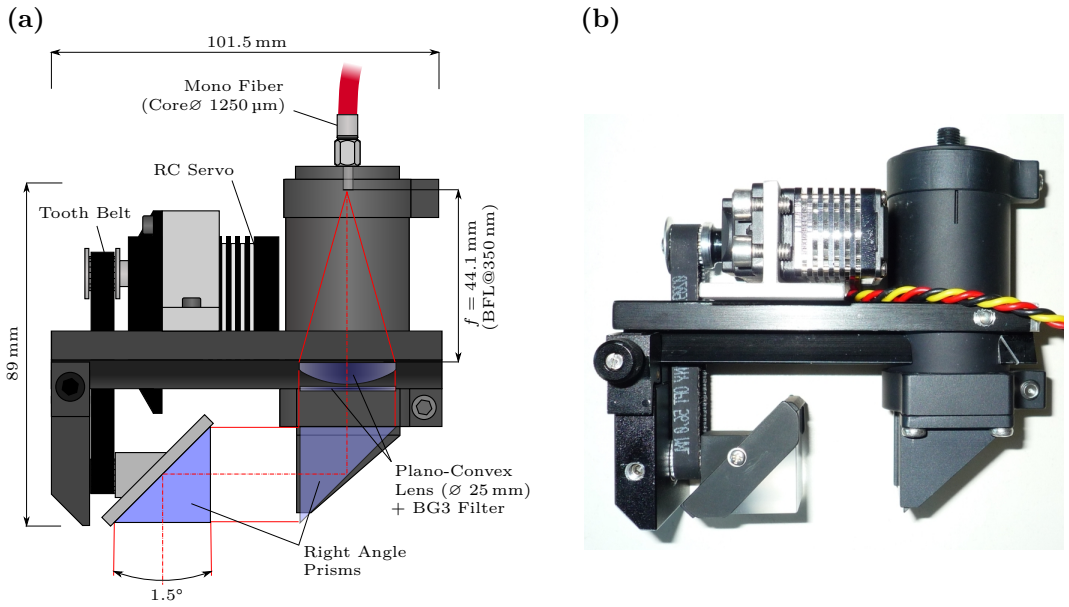

Figure 3.5.: Entrance optics of HAIDI's nadir scanner (whiskbroom): (a) Illustration showing the optical components used in the entrance optics and approximate dimensions. (b) Photo of the completed entrance optics, which is build up on a SYS 40 optical rail system from Owis.

motion of the aircraft and the prism during a scan, the actual spatial resolution achieved by the instrument depends on several factors, like integration time, aircraft speed, prism rotation speed and number of co-added scans. The influence of these parameters on the spatial resolution of the nadir scanner and other related considerations are discussed in Sec. 3.4.3.

The mono fiber coming from the telescope is then attached to a fiber bundle with a length of 5 m via standard F-SMA (SMA 905) fiber optic connector. This bundle consists of 31 individual fibers with a core diameter of 150 µm. While the fibers of the bundle are arranged as the smallest possible circle at the coupling to maximize the light throughput, they are arranged as a column at the spectrograph side, directly forming its entrance slit. For further information about HAIDI's fiber optical system, please refer to Sec. 3.8.

After passing the fiber optics, the light enters one of HAIDI's imaging spectrographs. The spectrographs were developed in-house in order to adapt them to the special requirements of airborne imaging DOAS measurements. They are temperature stabilized and have an instantaneous spectral coverage of 107 nm. Usually the wavelength region of the spectrographs is set to 300 nm–407 nm, which is the wavelength region the diffraction grating is optimized for, but they can also be operated from 343 nm–450 nm to allow the detection of species like IO, for example. The CCD cameras attached to the spectrographs are custom-built as well in cooperation with khs-instruments from Munich, Germany. Overall, the system reaches a spectral resolution of approximately 0.5 nm. More details about the imaging spectrographs and CCD cameras can be found in Sec. 3.6 and 3.7, respectively.

For security reasons and for easy access, spectrographs and CCD cameras are housed in HAIDI's instrument rack (see Sec. 3.9). The instrument rack is a modified 19-inch aluminum rack with a height of 6 rack units ($19 \times 20 \times 10.5$ in). In addition to spectrograph mountings that withstand load factors of at least 9 times the acceleration due to gravity, the instrument rack also features a temperature-stabilized section for the spectrographs and DC-to-DC converters to power the nadir scanner servo motors. The instrument rack moreover supplies the netbooks with power, which store the acquired data from the CCD cameras and furthermore run the software to control the entire instrument (see Sec. 3.12).

3.4.1. Servo Motor Control

As mentioned in Sec. 3.3, the nadir scanner uses a scanning prism that sweeps back and forth in order to span the spacial dimension of the hyperspectral image perpendicular to the flight direction. Because information is only collected during the forward scan, the time needed for the back scan should be kept as small as possible. For this reason, the actuation of the prism is realized by a digital RC servo motor (HS-7940TH from HiTEC), which offers high speed, high torque and high angular resolution (measured repositioning accuracy: 0.08°) at the same time. Technical details on the servo motor can be found in Tab. 3.2. In the current instrumental setup, the servo motors are supplied with an operating voltage of 6.0 V and are connected to the prism over a tooth belt with a gear ratio of 1:1 (Fig. 3.5b), so that the servo motion is directly transfered to the scanning prism.

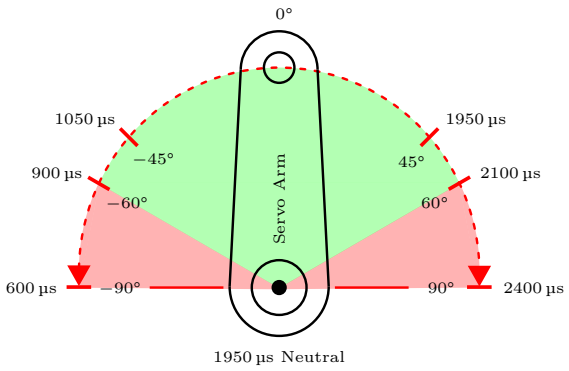

Figure 3.6.: Pulse width of the PWM signal with corresponding angular deflection of the servo arm.

RC servo motors are typically controlled by a PWM[1] signal whose pulse width is between 1 ms and 2 ms. The pulse width of the signal is thereby linearly correlated to the angular position of the servo arm, or in this case, the orientation of the gearwheel. For a standard servo motor this means that, for example, a pulse width of 1 ms causes a full-scale deflection in one direction, while a pulse width of 2 ms causes a full-scale deflection in the opposite direction. A pulse width of 1.5 ms usually gives the neutral (center) position of a servo motor. However,

[1] Pulse-width modulation

Table 3.2.: Technical specifications of the HiTEC HS-7940TH digital servo (HiTEC, 2014).

	Operating Voltage	
	6.0 V	7.4 V
Operating Speed (no Load)	0.07 s/60°	0.06 s/60°
Stall Torque	1.3 N m	1.6 N m
Idle Current	10 mA	10 mA
Running Current (no Load)	390 mA	500 mA
Stall Current	4800 mA	6200 mA
Control System	Pulse-Width Modulation	
Dead Band Width	1 µs	
Weight	68 g	
Dimensions	40 × 20 × 38 mm	

the here applied servo motor uses a wider pulse width range than standard servos (HiTEC, 2014). In the default (high-resolution) mode, the servo accepts pulse widths between 900 µs and 2100 µs, which corresponds to a angular range of 120° (see also Fig. 3.6). This pulse width range is quantized into 2048 (11-bit) different output levels, or "steps", by the ADC of the servo, resulting in a theoretical resolution of 0.06° per step. The servo also features a mode which allows a pulse width range from 600 µs to 2400 µs (180°) with a resolution of 10-bit. However, as an angular range of 100° is entirely sufficient for the scanning prism, the pulse width range of the servo motor is limited to the standard range of 1–2 ms by the controller.

The PWM signal that controls the motion of the nadir scanner servo motor is generated by the CCD camera electronics with a period of 10 ms. Accordingly, the target position of the servo motor is transmitted 100 times per second, which allows to synchronize the motion of the scanning prism to the recording of spectra with high temporal accuracy. Synchronization means in this context that the PWM signal starts from an initial value (usually a pulse width of 1250 ms $\widehat{=}$ −25°) every time a new swath is recorded. In between, the prism should move at uniform speed to the end position (usually a pulse width of 1750 ms $\widehat{=}$ +25°), before it returns to the initial position for the next swath. In order to obtain a smooth prism movement at a given speed, the pulse width of the PWM signal has to be increased continuously. This is achieved by a PWM ramp. As the camera electronics offers a resolution of 9-bit (512 steps) for the pulse width range between 1 ms and 2 ms, each step Δ_{PWM} in the PWM ramp corresponds to a change of 2 µs in pulse width or a prism rotation of 0.2°, respectively. Figure 3.7 shows an illustration of the generated signal together with the respective servo position. As can be seen, the PWM cycle is divided into two parts, which are described in the following:

- **Forward Scan:** The forward scan is the part of the scan, where data is collected. Directly before the start of the forward scan, the PWM signal is set to its initial value to ensures that the prism orientation is always the same at the beginning of the forward scan. The

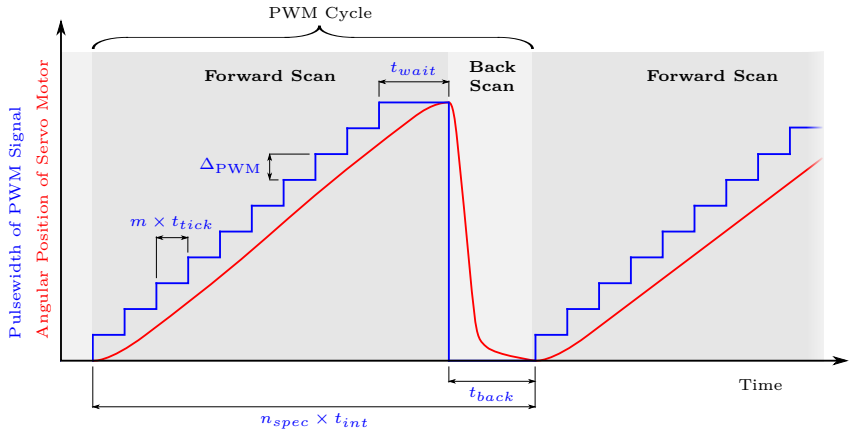

Figure 3.7.: Illustration of the PWM ramp used to control the servo motor of the nadir scanner.

pulse width then starts to increase as soon as the integration time of the first spectrum of the forward scan begins. Subsequently, the pulse width increases at a constant rate until the end value is reached. At this value, the pulse width is held constant for a short period of time t_{wait}, to compensate for the lag between signal and actual servo angle. As t_{wait} is only of the order of some milliseconds, it is neglected in the following.

- **Back Scan:** Once the prism has reached its end position, the back scan begins. In order to move the scanning prism back to the starting position as fast as possible, the pulse width is directly set to its initial value. However, the servo needs some time for this. Measurements with a laser beam projected through the prism to a distant wall and a high speed camera yield a back scan time t_{back} of about 250 ms for a scan range of $\beta_{range,scan} = 50°$. Because most of the time during the back scan is needed to decelerate the prism when approaching the initial position, the back scan time $t_{back} = 250\,\mathrm{ms}$ is also valid for similar scan ranges ($\pm 10°$). After the back scan is complete, the next swath can be recorded.

Since parameters like Δ_{PWM}, t_{wait} or t_{back} are fixed, the slope and duration of the PWM ramp are given by the number of PWM steps n_{step} and the time between them $m \times t_{tick}$. The former depends on the angle $\beta_{range,scan}$ that is to be covered by the scanning prism:

$$n_{step} = \frac{n_{step,max} \cdot \beta_{range,scan}}{\beta_{range,max}}\,, \tag{3.1}$$

where $n_{step,max} = 512$ is the maximum number of steps and $\beta_{range,max} = 100°$ the maximum angle that can be covered by the scanning prism. So, for example, when the nadir scanner is intended to cover an angle $\beta_{range,scan}$ of 50° the number of steps n_{step} is 256. The time between these steps consists of multiples of a CPU clock tick t_{tick}, which correspond to a time of 1 µs. The factor m, which is the number of CPU clock ticks between two PWM steps, can then be calculated by the following equation:

$$m = \frac{n_{spec} \cdot t_{int} - t_{back}}{n_{step} \cdot t_{tick}}\,, \tag{3.2}$$

where n_{spec} is the total number of spectra taken during the forward and back scan and t_{int} the integration time of a single spectrum. Thus, for 128 spectra with an integration time of 50 ms, m would be 24023. When the necessary parameters $\beta_{range,scan}$, n_{spec} and t_{int} are entered into the measurement software (Sec. 3.12), n_{step} and m are calculated automatically.

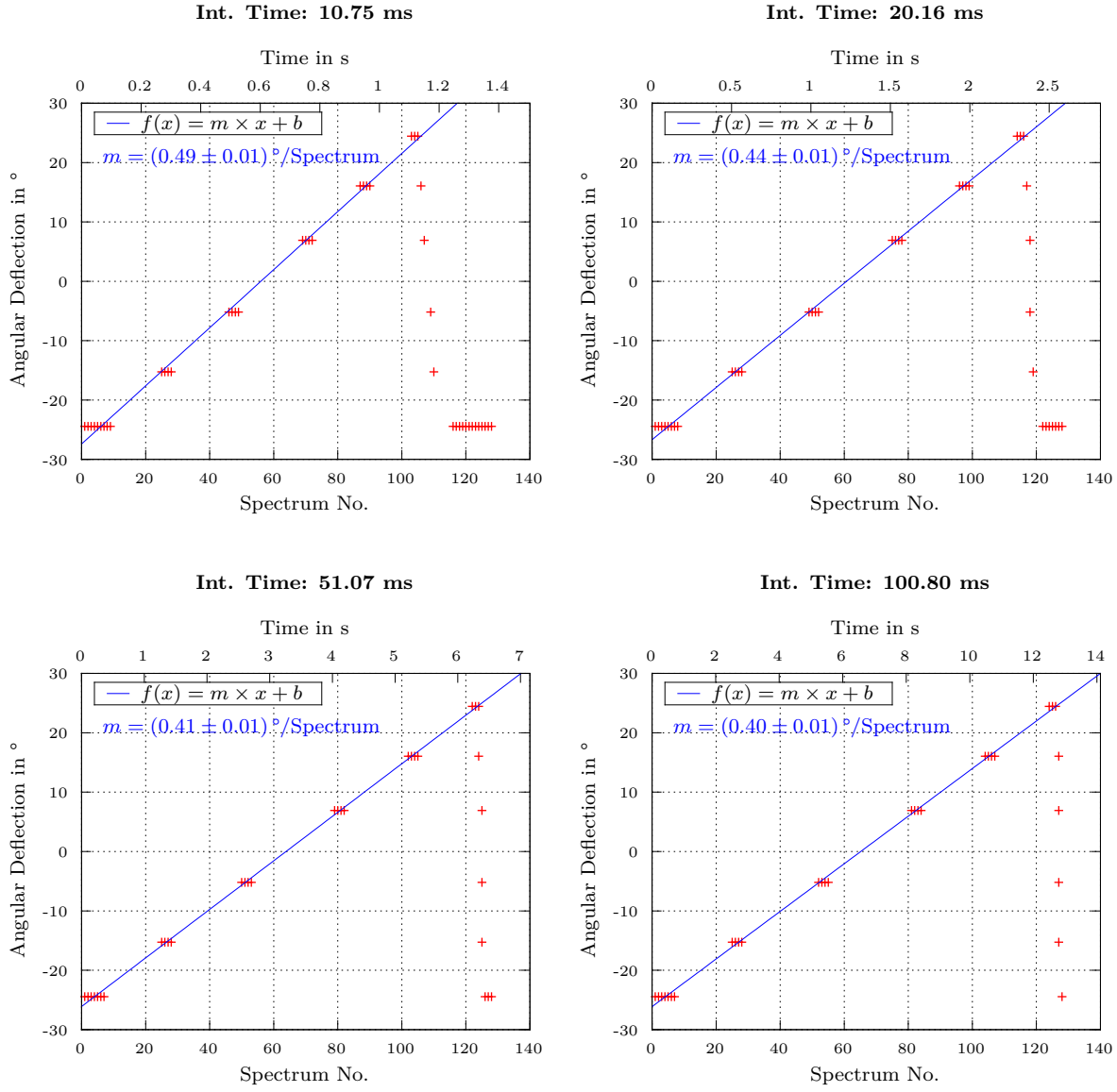

Figure 3.8.: Test of the nadir scanner prism movement for four different integration times. As can be seen by the linear fits, the angular deflection of the prism is almost linear with time during the forward scan. The increasing scan speed (in °/Spectrum) with shorter integration times comes from the fact that a larger number of spectra is required for the back scan.

An important characteristic of the nadir scanner is the scanning speed of the prism. This information is especially required for the later plotting of the collected hyperspectral data into geographical maps. Since the integration time of spectra does not change while recording a swath, the scanning speed can also be expressed as the angular range that is covered by the scanning prism during the recording of each spectrum. Theoretically, the angular movement of the prism should be linear with time, so that a specific deflection angle can be assigned to each spectrum, when the scanning speed is known. For a scanning prism that moves with constant speed between starting and end position, the scanning speed v_{scan} in °/Spectrum is given by the following equation:

$$v_{scan} = \frac{\beta_{range,scan}}{n_{spec} - \frac{t_{back}}{t_{int}}} \tag{3.3}$$

In order to check to what extent the calculated prism speed is consistent with real world measurements, a test setup was used. In this setup the nadir scanner was directed to an inspection lamp in a distance of a few meter. The inspection lamp was mounted to a rail, so that it could be moved along the scanning direction of the nadir scanner. In the following, the lamp was placed at different locations within the scan range and the spectrum numbers where light from the lamp was seen by the nadir scanner were recorded. With this method it could be determined, at which time the prism pointed to a specific direction. The results of the measurements can be seen in Fig. 3.8. Here, the lamp was placed at six different positions that were later converted to the corresponding deflection angles. Two of the lamp positions were thereby located at the start and end positions of the scan. To achieve the best temporal resolution, the number of spectra n_{spec} was set to the maximum of 128. Furthermore the standard scan range of $\beta_{range,scan} = 50°$ was applied. As can be seen from Fig. 3.9, the measured

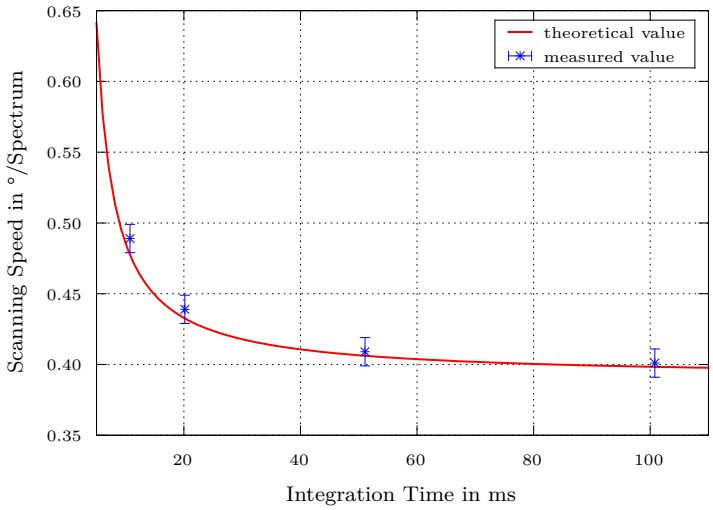

Figure 3.9.: Comparison of measured scanning speeds with theoretically calculated values.

values for the scanning speed of the nadir scanner are in good agreement with the theoretical ones, which were calculated via Eq. (3.3). Thus, for the scanning geometry discussed in Sec. 3.4.3 the actual deflection angle of the scanning prism was derived from the calculated values.

3.4.2. Telescope Field of View

The instantaneous field of view (IFOV) is defined as the angular extend of the world seen by a telescope at a moment and is therefore an important measure for the spatial resolution of an instrument. In order to determine the IFOV of HAIDI's telescopes, one first has to know the focal length of the applied lenses. HAIDI's entrance optics use plano-convex lenses, which have less spherical aberration compared to biconvex lenses when the convex surface is oriented towards the parallel incident light (see Fig. 3.5a and 3.21a). The back focal length (f_{BFL}) of these lenses is specified by the manufacturer with 46 mm at a wavelength of 587.6 nm (Fraunhofer d-line). Back focal length here means the distance between the last optical surface and the rear focal point of the lens (see figure in Tab. 3.4). However, due to the fact that the refractive index of a medium changes as a function of wavelength, the focal length in the UV spectral region will significantly differ from the specified value. This effect is also known as chromatic aberration. For an accurate calculation of the IFOV the focal length has thus to be determined for the used wavelength range from 300 to 400 nanometer. As a first step, the corresponding refractive indices of the lens material (fused silica) are calculated. The refractive index of a medium at a certain wavelength λ is given by the Sellmeier equation:

$$n^2 = 1 + \frac{B_1\lambda^2}{\lambda^2 - C_1^2} + \frac{B_2\lambda^2}{\lambda^2 - C_2^2} + \frac{B_3\lambda^2}{\lambda^2 - C_3^2}\,, \tag{3.4}$$

where the Sellmeier coefficients $B_{1,2,3}$ and $C_{1,2,3}$ are experimental determined quantities. For fused silica the Sellmeier coefficients are as follows:

Table 3.3.: Sellmeier coefficients for fused silica at 20 °C (Malitson, 1965).

Coefficient	Value
B_1	0.696 166 3
B_2	0.407 942 6
B_3	0.897 479 4
C_1	0.068 404 3 µm
C_2	0.116 241 4 µm
C_3	9.896 161 0 µm

Computation of equation 3.4 with the above parameters yields the graph displayed in Fig. 3.10. As can be seen, the refractive index of fused silica varies from 1.48779 to 1.47012 between 300 and 400 nanometers. What this means for the focal length f_{EFL} of the plano-convex lenses can now be calculated with the Lensmaker's equation:

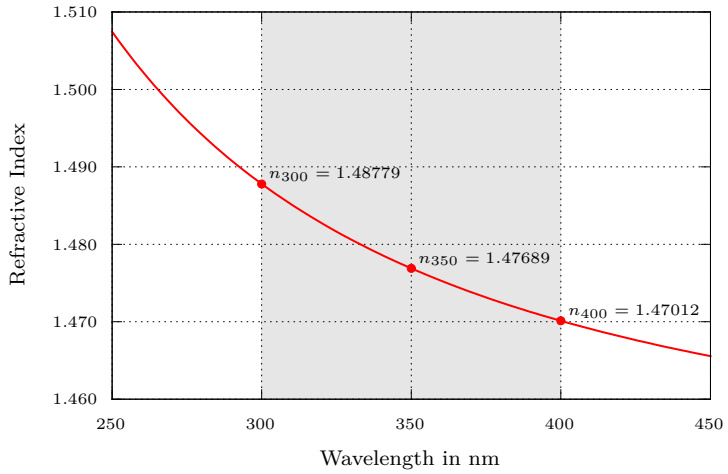

Figure 3.10.: Refractive index of fused silica as a function of wavelength. The typically wavelength range used by HAIDI's imaging spectrographs is indicated by the gray shaded section.

$$\frac{1}{f_{EFL}} = \frac{n - n_0}{n_0}\left(\frac{1}{R_{S1}} - \frac{1}{R_{S2}} + \frac{(n - n_0)w_{lens}}{nR_{S1}R_{S2}}\right), \tag{3.5}$$

where n is the refractive index of the lens material, n_0 the refractive index of the surrounding medium (in this case, air), $R_{S1,S2}$ the radii of curvature (RoC) of the corresponding optical surfaces and w_{lens} the thickness of the lens measured at the optical axis. It should be noted that Eq. (3.5) gives the effective focal length (f_{EFL}), which is the distance between the principal plane of the lens and its rear focal point (see figure in Tab. 3.4). All focal lengths f given in the following are thus effective focal lengths. The necessary specifications of the lenses to calculate the focal lengths can be found in Tab. 3.4. Since the lenses are plano-convex, the radius of curvature of one optical surface is infinite. Therefore, equation 3.5 is reduced to:

$$\frac{1}{f} = \frac{n - n_0}{n_0 R_{S1}} \tag{3.6}$$

Plugging in the radius of curvature $R_{S1} = 22.92\,\text{mm}$, the calculated refractive indices of fused silica and the refractive indices of dry air (15 °C, 101 325 Pa, 450 ppm CO_2, Ciddor (1996)) then yields the following focal lengths:

$$\begin{aligned}
n_{air,300} &= 1.00029157 \quad \Rightarrow \quad f_{300} = 47.0292\,\text{mm} \\
n_{air,350} &= 1.00028612 \quad \Rightarrow \quad f_{350} = 48.1040\,\text{mm} \\
n_{air,400} &= 1.00028276 \quad \Rightarrow \quad f_{400} = 48.7966\,\text{mm} \\
n_{air,587.6} &= 1.00027717 \quad \Rightarrow \quad f_{587.6} = 50.0332\,\text{mm}
\end{aligned}$$

To verify the above results, the effective focal length was also calculated for a wavelength of

587.6 nm. When comparing the obtained value with the one specified by the manufacturer (see Tab. 3.4), one can see that they are in very good agreement.

Table 3.4.: Specifications of the used plano-convex lenses from Edmund Optics (Edmund Optics, 2012). To minimize the reflection loss in the UV spectral region, the lenses feature a special anti-reflection coating.

Parameter	Value
RoC R_{S1}	22.92 mm
RoC R_{S2}	∞
Diameter d_{lens}	25.00 mm
Thickness w_{lens}	5.84 mm
f_{EFL} at 587.6 nm	50.00 mm
f_{BFL} at 587.6 nm	46.00 mm

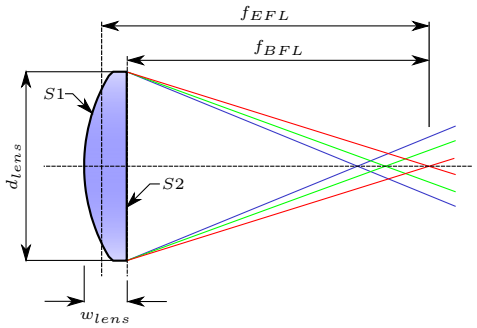

Now that the focal lengths of the telescope are known for the typical wavelength range of HAIDI's spectrographs, the instantaneous field of view can be calculated. When the entrance of the optical fiber is placed in a distance l_{fiber} to the principal plane of the lens (see Fig. 3.11), the telescope is focused to infinity for the wavelength λ at which the effective focal length f_λ corresponds to the distance l_{fiber}. In this case, the IFOV is given by the following equation:

$$\text{IFOV} = \alpha_{\lambda, f_\lambda = l_{fiber}} = 2 \tan^{-1} \left(\frac{d_{fiber}}{2 \cdot l_{fiber}} \right) , \tag{3.7}$$

where d_{fiber} is the diameter of the fiber core, or in case of a non-axially symmetric fiber entrance, the size of the entrance measured in the considered dimension. However, as stated previously, the focal length f_λ varies slightly within the used spectral region due to the wavelength dependency of the refractive index. For wavelengths with a focal length shorter ($f_\lambda < l_{fiber}$) or greater ($f_\lambda > l_{fiber}$) than the distance l_{fiber}, the telescope is not focused to infinity and the incoming rays, illustrated in red and blue in Fig. 3.11, are not parallel anymore. The above equation is therefore not valid for wavelengths where the focal length differs significantly from the distance l_{fiber}. Instead, the IFOV can be calculated by the following equations:

$$\alpha_{\lambda, f_\lambda < l_{fiber}} = 2 \tan^{-1} \left(\frac{(l_{fiber} - f_\lambda) \times \tan(\alpha_{NA}) + d_{fiber}/2}{f_\lambda} \right) \tag{3.8}$$

$$\alpha_{\lambda, f_\lambda > l_{fiber}} = 2 \tan^{-1} \left(\frac{(f_\lambda - l_{fiber}) \times \tan(\alpha_{NA}) + d_{fiber}/2}{f_\lambda} \right) , \tag{3.9}$$

where α_{NA} is the acceptance angle of the fiber (see also Sec. 3.8), which limits the seen part of the lens. HAIDI's nadir scanner uses a circular mono-fiber with an NA of 0.22 ($\Rightarrow \alpha_{NA} = 12.7°$)

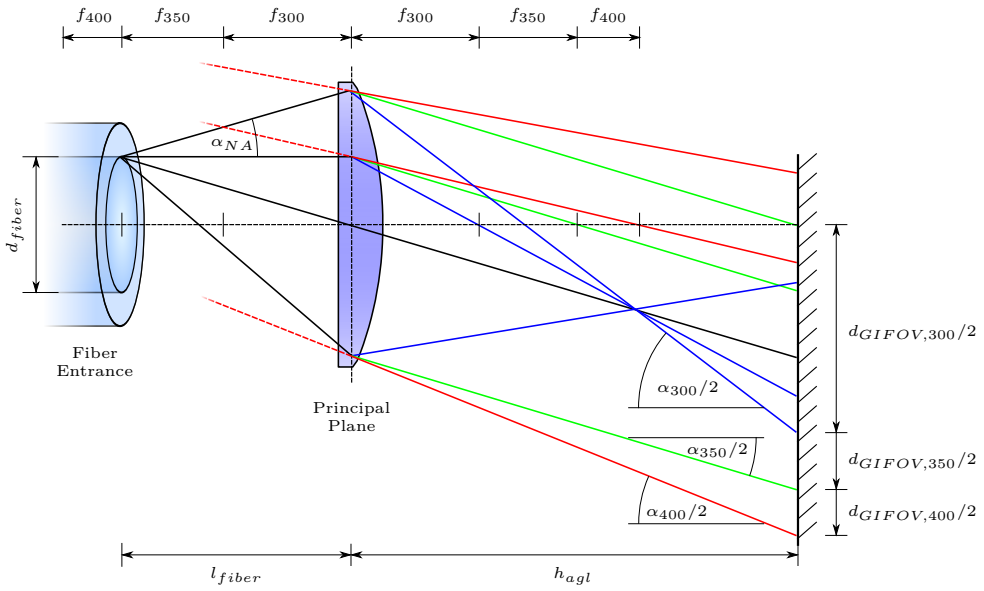

Figure 3.11.: The IFOV α_λ of HAIDI's telescopes varies slightly with wavelength due to chromatic aberration. In the illustrated case, the fiber entrance is placed at the distance $l_{fiber} = f_{350}$. Therefore, the telescope is focused to infinity for a wavelength of 350 nm (green), while shorter (blue) and longer (red) wavelengths are defocused.

and a core diameter of $d_{fiber} = 1250\,\mu m$. Plugging in these values yields the following IFOVs in dependency of the distance l_{fiber}:

Table 3.5.: The instantaneous field of view α_λ of HAIDI's nadir scanner, calculated for different fiber locations l_{fiber} and wavelengths λ. Values where l_{fiber} is equal to the focal length at the considered wavelength are displayed in red.

$l_{fiber} = f_{300}$	$l_{fiber} = f_{350}$	$l_{fiber} = f_{400}$
$\alpha_{300} = 1.52°$	$\alpha_{300} = 2.11°$	$\alpha_{300} = 2.49°$
$\alpha_{350} = 2.07°$	$\alpha_{350} = 1.49°$	$\alpha_{350} = 1.86°$
$\alpha_{400} = 2.40°$	$\alpha_{400} = 1.83°$	$\alpha_{400} = 1.47°$

As can be seen from these values, the IFOV changes only slightly over the considered spectral range as long as the fiber is placed at the focal length of the respective wavelength (red entries in Tab. 3.5). Noticeably larger are the variations of the IFOV due to chromatic aberration at a fixed fiber distance. They become greater with increasing difference between the distance l_{fiber} and the focal lengths of the considered wavelengths. A fiber which is placed at a focal length that approximately corresponds to the center wavelength of the considered spectral range therefore offers the smallest variation in the IFOV. For the typical spectral range of HAIDI's spectrographs this is a wavelength of about 350 nm. For this reason, the IFOV of HAIDI's entrance optics is calculated based on Eq. 3.7 and a fiber distance of $l_{fiber} = f_{350}$ by default,

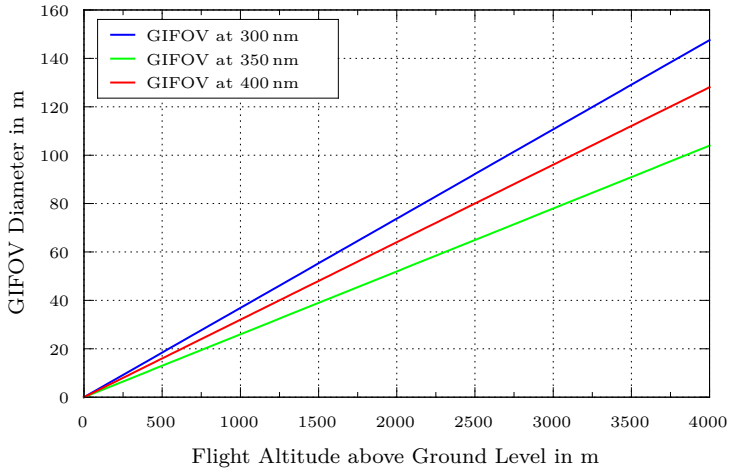

Figure 3.12.: The plot shows the GIFOV of the nadir scanner for different wavelengths as a function of the flight altitude above ground level (h_{agl}). As the calculation was performed with a fiber distance of $l_{fiber} = f_{350}$, a wavelength of 350 nm (green) shows the smallest GIFOV. Due to chromatic aberration the GIFOV increases for wavelengths of 300 nm (blue) and 400 nm (red).

referred to as α_{inst} throughout the thesis. However, it has to be noted that the calculation of the IFOV by Eqs. (3.7), (3.8) and (3.9) is only a rough estimate, as optical aberrations are not considered.

The observed area corresponding to the IFOV is called the ground projected instantaneous field of view (GIFOV). It depends on the distance between lens and object or the altitude h_{agl} of the instrument above ground level, respectively. The extent of the observed area for a certain wavelength λ, $d_{GIFOV,\lambda}$ (see Fig. 3.11), is therefore given by the equations below:

$$d_{GIFOV,\lambda,f_\lambda \geq l_{fiber}} = 2\left(\tan(\alpha_{NA}) \cdot l_{fiber} - \frac{d_{fiber}}{2} + \tan\left(\frac{\alpha_\lambda}{2}\right) \cdot h_{agl}\right) \tag{3.10}$$

$$d_{GIFOV,\lambda,f_\lambda < l_{fiber}} = 2\left(-\tan(\alpha_{NA}) \cdot l_{fiber} - \frac{d_{fiber}}{2} + \tan\left(\frac{\alpha_\lambda}{2}\right) \cdot h_{agl}\right). \tag{3.11}$$

The first two terms in the brackets are due to the size of the GIFOV at the location of the principal plane of the lens and can be neglected for typical flight altitudes of several thousand meter above ground level. Accordingly, Eqs. (3.10) and (3.11) are reduced to:

$$d_{GIFOV,\lambda} = 2\tan\left(\frac{\alpha_\lambda}{2}\right) \cdot h_{agl} \tag{3.12}$$

The typical GIFOV of the nadir scanner ($l_{fiber} = f_{350}$) can then be calculated by inserting the values from Tab. 3.5 in Eq. (3.12). Figure 3.12 shows the results plotted versus the flight altitude above ground level. As one can see, the GIFOV is about 104 m at 350 nm and a flight

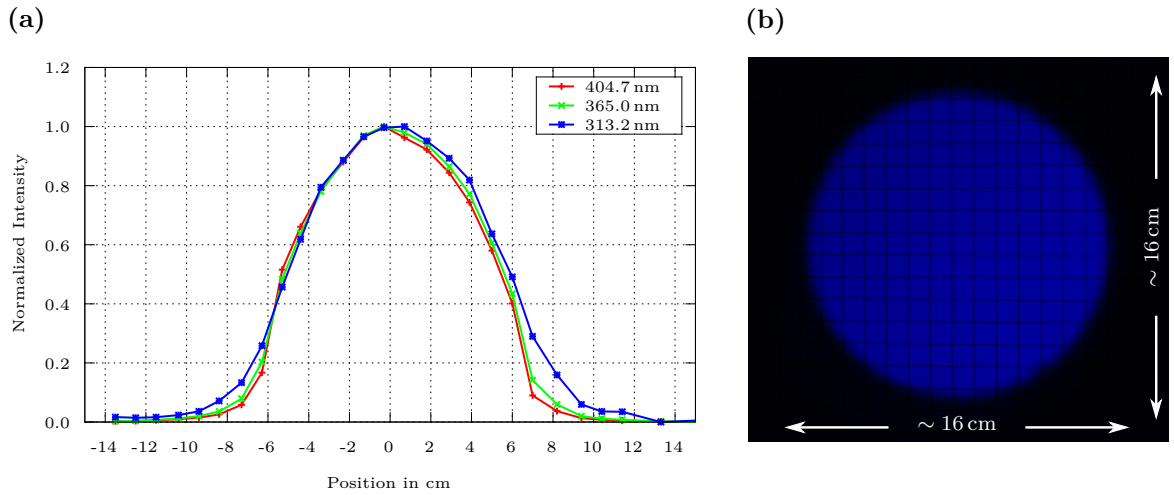

Figure 3.13.: Measurement of the nadir scanners GIFOV: (a) The plot shows the normalized measured intensity of the three mercury emission lines in dependency of the lamp position. (b) Prior to the measurement, the position of the optical fiber was adjusted by guiding light reversely through the optics. A sharp image of the fiber entrance for all distances h_{agl} then indicates that the fiber is located at the focal plane of the telescope. The raster seen in the image has a centimeter scale and the blue color comes from the BG3 filter in the telescope.

altitude of 4 km, when the viewing direction of the instrument is perpendicular to the ground. At a wavelength of 300 nm the diameter of the GIFOV is 148 m in contrast, which is an increase by 42 %. Due to pitch, roll and scanning angles, the viewing direction of the nadir scanner is usually not perpendicular to the ground, so that the actual GIFOV deviates from a circular shape (Sec. 3.4.3).

In order to check how well the calculated GIFOVs agree with measured ones, the nadir scanner was again pointed to an inspection lamp. Then, light was guided reversely through the entrance optics. In this way, the telescope can be focused to infinity relatively simple (see Fig. 3.13b). Subsequently, the lamp was moved stepwise through the instantaneous field of view of the instrument. Because the inspection lamp (fluorescent tube) was a low pressure mercury-vapor gas-discharge lamp, the lamp spectrum also contained some mercury emission lines. Therefore, the extent of the GIFOV could be determined for three different wavelengths simultaneously by measuring the intensity of the 404.7 nm, 365.0 nm and 313.2 nm emission lines at the different lamp positions. The result of the measurement is shown in Fig. 3.13a. As can be seen, the GIFOV has a diameter of about 16 cm for a distance of 5 m to the lamp. Assuming the fiber entrance of the telescope to be located at a distance of $l_{fiber} = f_{350}$, yields a theoretical GIFOV diameter of 15.0 cm for a wavelength of 350 nm (Eq. (3.10)) and a value of about 16.1 cm for 300 nm (Eq. (3.11)). Measured and calculated GIFOV thus show a good agreement.

HAIDI's forward-looking telescope uses multiple fibers arranged to a column, to cover several viewing directions simultaneously. The total instantaneous field of view of the instrument therefore differs in horizontal and vertical direction. In horizontal direction the IFOV corresponds

to that of a single fiber. Since fibers with a core diameter of $d_{fiber} = 150\,\mu m$ are used in the forward-looking telescope, the IFOV calculates to $\alpha_{inst,hor} = 0.18°$ (Eq. 3.7). In vertical direction the telescope uses 31 fibers. Here, one has to include the cladding of the fibers in the calculation. The diameter of the fibers with cladding is 190 µm. Thus, the total height of the fiber entrance is $d_{fiber} = 5.85\,mm$, which results in a vertical IFOV of $\alpha_{inst,vert} = 6.96°$.

3.4.3. Scanning Geometry

An important aspect in remote sensing applications is the scanning geometry used by the instrument. It determines the spatial resolution as well as the areal coverage that can be achieved with the system and it has furthermore to be known precisely in order to assemble the collected hyperspectral data into geographical maps. Therefore, the scanning geometry of HAIDI's nadir scanner will be described in more detail below.

As mentioned earlier, HAIDI's nadir telescope has an instantaneous field of view (IFOV) of $\alpha_{inst} = 1.5°$. In order to acquire the spatial dimension perpendicular to the flight direction, the telescope's IFOV is rotated by the scan angle β across track. Typically, β is set to a range of $-25°$ to $+25°$ relative to the yaw-axis of the aircraft (labeled z_a in Fig. 3.14). Since the scan angle β is defined to be positive in clockwise direction (looking in flight direction), similar to the roll angle of the aircraft, the forward scan of the system is from right to left. The total angle α_{tot} covered by the nadir scanner during one swath, also called its field of view (FOV), is then about 50°. This means, that the swath width approximately equals the flight altitude of the aircraft above ground level h_{agl}. A rough estimate of the spatial resolution that is achieved by the system in dependency of the flight altitude and the number of co-added scans can be given by the following equations:

$$P_{\parallel} = (n_{swath} - 1) \cdot t_{int} \cdot n_{scan,total} \cdot v_g + \tan\left(\frac{\alpha_{inst}}{2}\right) \cdot h_{agl} \cdot 2 \tag{3.13}$$

$$P_{\perp} = \left(\tan\left(\frac{\alpha_{tot}}{2}\right) \cdot \frac{n_{scan}}{n_{scan,total} - n_{scan,back}} + \tan\left(\frac{\alpha_{inst}}{2}\right)\right) \cdot h_{agl} \cdot 2 \tag{3.14}$$

where $P_{\parallel}$ is the resulting pixel size in flight direction (see Fig. 3.3), $P_{\perp}$ the pixel size perpendicular to the flight direction, n_{swath} the number of co-added swaths, n_{scan} the number of co-added scans within a swath, $n_{scan,total}$ the total amount of scans taken during one swath (typically 128), t_{int} the integration time of a single scan, $n_{scan,back}$ the quantity of scans taken during the back scan ($n_{scan,back} = {}^{t_{back}}/_{t_{int}}$, $t_{back} \approx 250\,ms$) and v_g the ground speed of the aircraft. However, the above equations are not suited to visualize the exact ground projected field of view (GFOV) of the nadir scanner. They neither give the position of the pixels relative to that of the aircraft nor do they consider the real shape of the instrument's ground projected instantaneous field of view (GIFOV), perspective distortion or flight parameters like pitch and

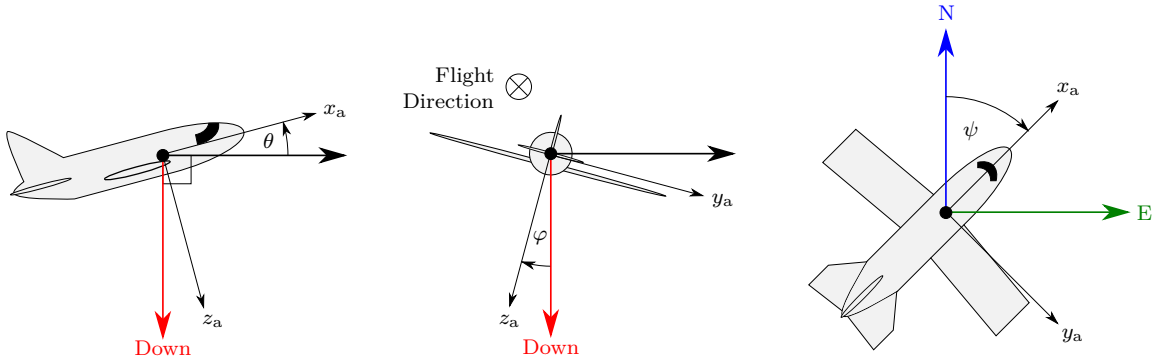

(a) Pitch **(b)** Roll **(c)** Heading

Figure 3.14.: Definition of pitch, roll and heading angles with reference to the aircraft's principal axes: (a) The pitch angle θ is specified as the angle between a horizontal plane, which goes through the aircraft's center of gravity, and the positive roll axis x_a. It is positive when the positive roll axis is above the horizontal plane. (b) The roll angle φ describes the rotation about the platform's roll axis x_a and is positive when the positive pitch axis y_a is below the horizontal plane. (c) The heading angle ψ is the horizontal angle between the north direction and the projection of the aircraft's positive roll axis x_a. It is measured clockwise, so for a heading of 0° the aircraft's nose points to the north and for a heading of 90° it points to the east.

roll. All of these parameters can have significant impact on the actual pixel size of the nadir scanner. The accurate calculation of the GFOV thus requires a much more complex algorithm. This algorithm is based on the analytical calculation of intersection points between a cone (IFOV of the telescope) and a plane (surface of the earth). The result of such a calculation for typical flight conditions on smaller aircraft is illustrated in Fig. 3.15. Each plot thereby contains two consecutive swaths, marked in red (1st swath) and blue (2nd swath) to show the areal coverage of the nadir scanner. In order to obtain the best areal coverage with the instrument, the gap between consecutive swaths should be kept as small as possible. In general, the distance covered by the aircraft during the time for one swath should be equal to the extend of the GIFOV in flight direction, d_{GIFOV}, in order to minimize the gap and avoid overlap:

$$v_g \cdot t_{int} \cdot n_{scan,total} \overset{!}{\approx} d_{GIFOV} \tag{3.15}$$

Although the distance between two swaths depends on many parameters, like e. g. flight altitude above ground level, aircraft speed, integration time and number of scans per swath, only few of them can be chosen freely. The aircraft speed, for example, usually cannot be influenced and the integration time per scan depends on the intensity of incident light. Thus, the distance between two swaths is typically adjusted by choosing a different number of scans per swath (Fig. 3.15).

The approach with determining the intersection points between the instrument's IFOV and the ground, however, is very CPU-intensive. Therefore, a simplified algorithm was used to calculate the pixel sizes and positions for the geographical maps in the result chapters (6–8).

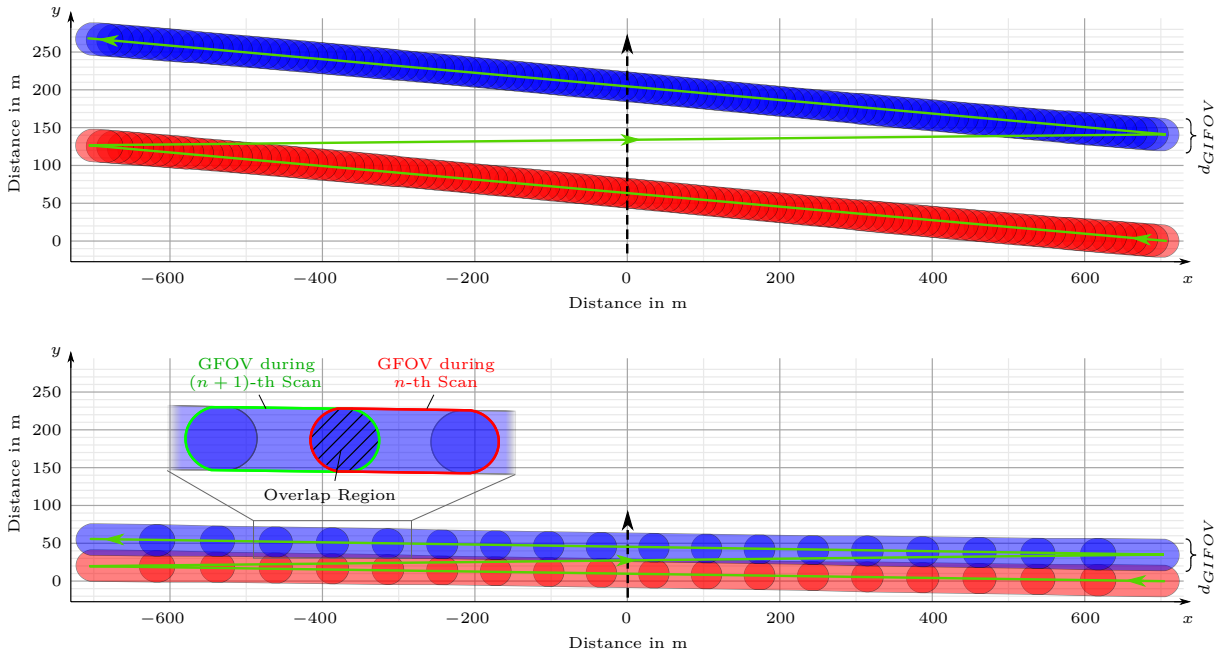

Figure 3.15.: Calculation of the nadir scanner's GFOV for two sequent swaths. The direction of the scan is from right to left (along the green line) while the aircraft travels in the direction of the positive y axis at $x = 0$ (dashed line). Each swath is subdivided into several segments, which indicate the area covered by the scanner's GIFOV during the integration time of a single scan (i. e. the GFOV during a single scan). As there is no delay between scans, the GFOV of sequent scans overlaps (see enlarged view). The areal coverage can be adapted to the flight conditions by altering the total number of scans per swath $n_{scan,total}$. The GFOV in the lower subfigure is calculated for a total number of 32 scans per swath while the upper one uses the maximum of 128 scans per swath. All remaining parameters are the same for both figures: $v_g = 55\,\mathrm{m/s}$, $h_{agl} = 1500\,\mathrm{m}$, $t_{back} = 250\,\mathrm{ms}$, $t_{int} = 20\,\mathrm{ms}$.

The simplified algorithm still considers roll and pitch angles of the aircraft as well as the bow tie effect, but uses quadrangles for the pixel shape instead of the actual GFOV. In a first step of the algorithm, the four corner point coordinates of a pixel in relation to the position of the aircraft have to be calculated. For this purpose, a Cartesian coordinate system is used, where the point of origin is the ground projected location of the aircraft A and the positive y-axis its heading direction (see Fig. 3.16). Then the x and y coordinates of the four corner points P_1–P_4 are as follows:

$$x_{P_1} = \frac{h_{agl,t_1}}{\cos\theta_{t_1}} \cdot \tan\left(\beta_{t_1} - \varphi_{t_1} + \frac{\alpha_{inst}}{2}\right), \quad y_{P_1} = h_{agl,t_1} \cdot \tan\left(\theta_{t_1} - \frac{\alpha_{inst}/2}{\cos\left(\beta_{t_1} - \varphi_{t_1}\right)}\right) \tag{3.16}$$

$$x_{P_2} = \frac{h_{agl,t_1}}{\cos\theta_{t_1}} \cdot \tan\left(\beta_{t_2} - \varphi_{t_1} - \frac{\alpha_{inst}}{2}\right), \quad y_{P_2} = h_{agl,t_1} \cdot \tan\left(\theta_{t_1} - \frac{\alpha_{inst}/2}{\cos\left(\beta_{t_2} - \varphi_{t_1}\right)}\right) \tag{3.17}$$

$$x_{P_3} = \frac{h_{agl,t_2}}{\cos\theta_{t_2}} \cdot \tan\left(\beta_{t_1} - \varphi_{t_2} + \frac{\alpha_{inst}}{2}\right), \quad y_{P_3} = h_{agl,t_2} \cdot \tan\left(\theta_{t_2} - \frac{\alpha_{inst}/2}{\cos\left(\beta_{t_1} - \varphi_{t_2}\right)}\right) \tag{3.18}$$

$$x_{P_4} = \frac{h_{agl,t_2}}{\cos\theta_{t_2}} \cdot \tan\left(\beta_{t_2} - \varphi_{t_2} - \frac{\alpha_{inst}}{2}\right), \quad y_{P_4} = h_{agl,t_2} \cdot \tan\left(\theta_{t_2} - \frac{\alpha_{inst}/2}{\cos\left(\beta_{t_2} - \varphi_{t_2}\right)}\right) \tag{3.19}$$

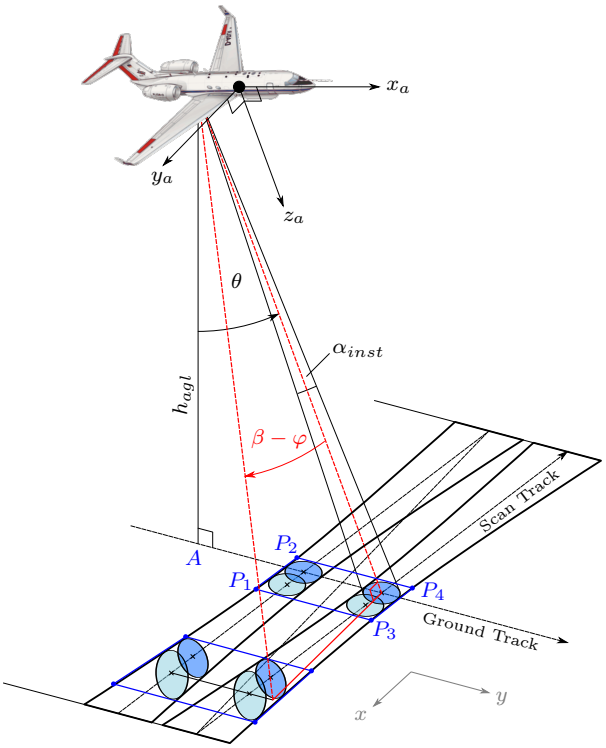

Figure 3.16.: Illustration of the scanning geometry used by HAIDI's nadir scanner. To obtain a better signal-to-noise ratio, usually several scans within a swath or also within multiple consecutive swath are co-added. The area covered during these scans is bounded by a quadrangle with the corner points P_1 to P_4 and represents a singe pixel in the hyperspectral image. Due to the bow tie effect the pixel size increases slightly towards the edges of a swath.

where the index t_1 denotes the starting time of the first scan that belongs to a pixel and t_2 the end of the exposure time of the last scan of a pixel. Next, the Cartesian coordinates have to be transformed to the geographic system. This requires the course ψ_P between the location of the aircraft A and the corner points P as well as the distance L_P between the points A and P in units of arc degree:

$$\psi_{P_1} = \mathrm{sgn}(x_{P_1}) \cdot \sphericalangle\left(\vec{e_y}, \overrightarrow{P_1}\right) + \psi_{t_1}\,, \qquad L_{P_1} = \frac{\left|\overrightarrow{P_1}\right|}{2\pi \cdot R_\oplus/360} \tag{3.20}$$

$$\psi_{P_2} = \mathrm{sgn}(x_{P_2}) \cdot \sphericalangle\left(\vec{e_y}, \overrightarrow{P_2}\right) + \psi_{t_1}\,, \qquad L_{P_2} = \frac{\left|\overrightarrow{P_2}\right|}{2\pi \cdot R_\oplus/360} \tag{3.21}$$

$$\psi_{P_3} = \mathrm{sgn}(x_{P_3}) \cdot \sphericalangle\left(\vec{e_y}, \overrightarrow{P_3}\right) + \psi_{t_2}\,, \qquad L_{P_3} = \frac{\left|\overrightarrow{P_3}\right|}{2\pi \cdot R_\oplus/360} \tag{3.22}$$

$$\psi_{P_4} = \mathrm{sgn}(x_{P_4}) \cdot \sphericalangle\left(\vec{e_y}, \overrightarrow{P_4}\right) + \psi_{t_2}\,, \qquad L_{P_4} = \frac{\left|\overrightarrow{P_4}\right|}{2\pi \cdot R_\oplus/360} \tag{3.23}$$

where sgn() is the signum function (with $\mathrm{sgn}(0) = +1$) and $R_\oplus \approx 6371\,\mathrm{km}$ the mean radius of the earth. Latitude and longitude of the pixel corner points can then be calculated by the equations below (Williams, 2012):

$$Lat_{P_1} = \arcsin\left(\sin Lat_{t_1} \cdot \cos L_{P_1} + \cos Lat_{t_1} \cdot \sin L_{P_1} \cdot \cos \psi_{P_1}\right) \tag{3.24}$$

$$Lat_{P_2} = \arcsin\left(\sin Lat_{t_1} \cdot \cos L_{P_2} + \cos Lat_{t_1} \cdot \sin L_{P_2} \cdot \cos \psi_{P_2}\right) \tag{3.25}$$

$$Lat_{P_3} = \arcsin\left(\sin Lat_{t_2} \cdot \cos L_{P_3} + \cos Lat_{t_2} \cdot \sin L_{P_3} \cdot \cos \psi_{P_3}\right) \tag{3.26}$$

$$Lat_{P_4} = \arcsin\left(\sin Lat_{t_2} \cdot \cos L_{P_4} + \cos Lat_{t_2} \cdot \sin L_{P_4} \cdot \cos \psi_{P_4}\right) \tag{3.27}$$

$$Lon_{P_1} = \left(Lon_{t_1} + \arcsin\left(\frac{\sin \psi_{P_1} \cdot \sin L_{P_1}}{\cos Lat_{P_1}}\right) + \pi\right) \bmod (2\pi) - \pi \tag{3.28}$$

$$Lon_{P_2} = \left(Lon_{t_1} + \arcsin\left(\frac{\sin \psi_{P_2} \cdot \sin L_{P_2}}{\cos Lat_{P_2}}\right) + \pi\right) \bmod (2\pi) - \pi \tag{3.29}$$

$$Lon_{P_3} = \left(Lon_{t_2} + \arcsin\left(\frac{\sin \psi_{P_3} \cdot \sin L_{P_3}}{\cos Lat_{P_3}}\right) + \pi\right) \bmod (2\pi) - \pi \tag{3.30}$$

$$Lon_{P_4} = \left(Lon_{t_2} + \arcsin\left(\frac{\sin \psi_{P_4} \cdot \sin L_{P_4}}{\cos Lat_{P_4}}\right) + \pi\right) \bmod (2\pi) - \pi \tag{3.31}$$

It must be taken into account that the equations (3.24) to (3.31) are only valid for distances smaller than $\pi/2$ in longitude and endpoints that do not coincident with either the north or south pole ($\cos Lat_P = 0$). In order to verify the accuracy of the corner point coordinates calculated by Eqs. (3.16)–(3.19), a comparison with the more realistic but slower algorithm was carried out for different aircraft orientations that can occur during flight (Fig. 3.17). In each case, the corner points were calculated by the simplified algorithm for the last pixel in the first swath, where perspective distortion is most evident. As can be seen, the resulting pixel (black quadrangle) agrees very well with the GFOV during the exposure time of a scan. Another proof for the correctness of the used algorithm and the servo motion control is represented in Fig. 3.18. It shows the measured light intensity in the wavelength range around 400 nm plotted on a georeferenced satellite image from that day. The transition between sea ice and open water can be seen clearly in the reconstructed hyperspectral image and its location is consistent with the satellite image. Also the runway of Barrow airport and some nearby roads can be identified in the image. For comparison, a picture of Barrow airport, taken by HAIDI's nadir webcam during the same overflight, is shown in Fig. 3.19.

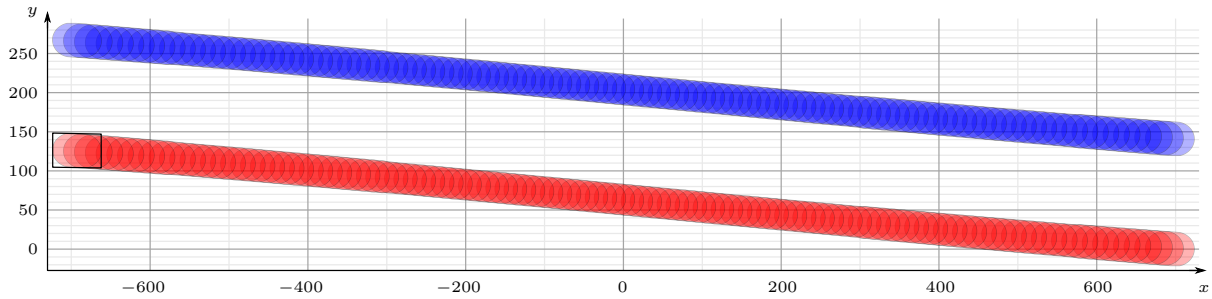

(a) pitch angle θ: 0°, roll angle φ: 0°

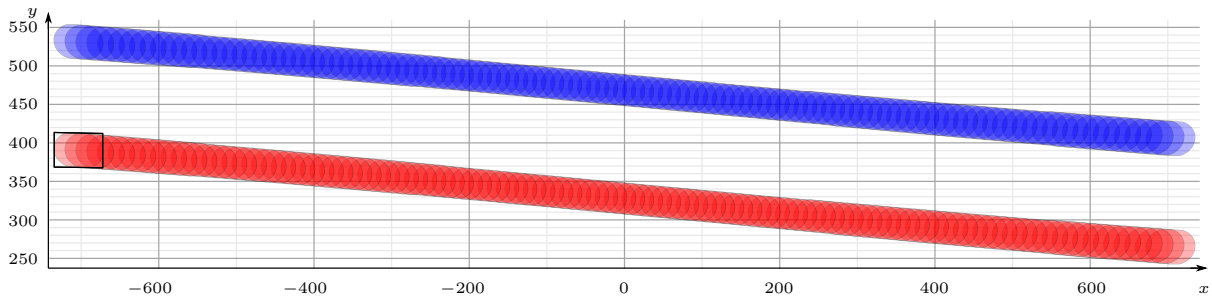

(b) pitch angle θ: 10°, roll angle φ: 0°

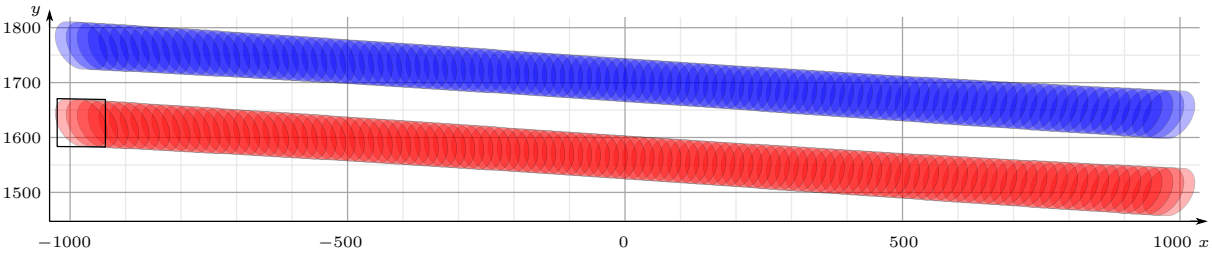

(c) pitch angle θ: 45°, roll angle φ: 0°

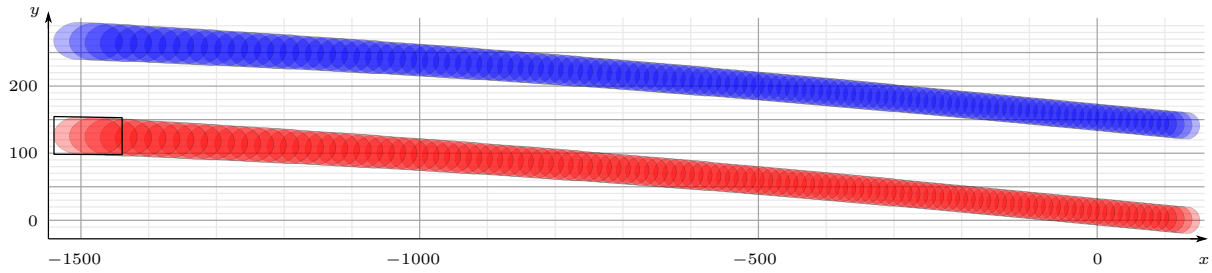

(d) pitch angle θ: 0°, roll angle φ: 20°

Figure 3.17.: Comparison of the algorithms used to calculate the nadir scanner's GFOV. Each plot shows two consecutive swaths (red, blue), calculated by the accurate but more complex algorithm for certain pitch and roll angles of the aircraft. The remaining parameters are identical in all plots: $n_{scan,total} = 128$, $v_g = 55\,\mathrm{m/s}$, $h_{agl} = 1500\,\mathrm{m}$, $t_{back} = 250\,\mathrm{ms}$, $t_{int} = 20\,\mathrm{ms}$. As can be seen, a higher pitch angle causes a shift of the GFOV in flight direction (compare (a) with (b) and (c)), while a change in roll angle causes a shift perpendicular to the flight direction (compare (a) with (d)). The black quadrangles show the pixels that were calculated with the simplified algorithm for the last scan of the first swath in each case. Even though the size and shape of the GFOV during a single scan changes as a function of pitch and roll angles, both algorithms show a good agreement.

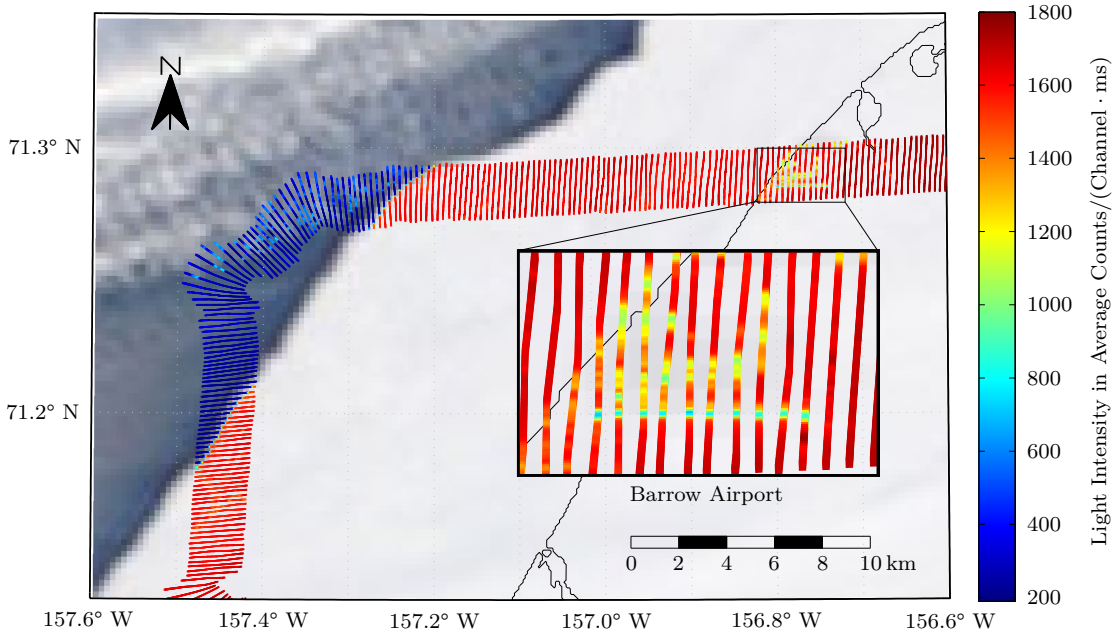

Figure 3.18.: This picture shows the light intensity around 400 nm measured during a flight on 24$^{\text{th}}$ March 2012 at Barrow, Alaska, to demonstrate the imaging capabilities of HAIDI's nadir scanner. The pixel corner point coordinates were calculated by the simplified algorithm and subsequently plotted on a georeferenced true color satellite image from MODIS (Terra), taken on the same day with a resolution of 250 m (NASA, 2012). The image also allows a rough estimate of the spatial resolution of the instrument, since the Barrow airport runway (width $\sim$ 50 m) is resolved by several pixels at a flight altitude of about 2500 m. A photo of the airport for comparison can be found in Fig. 3.19.

Figure 3.19.: Aerial photograph of the city of Barrow (Alaska, USA) with nearby airport, taken on 24$^{\text{th}}$ March 2012. The image was stitched together from multiple pictures of HAIDI's nadir webcam.

3.5. The Forward-Looking Telescope (Pushbroom)

In contrast to the conventional usage in nadir direction, HAIDI's pushbroom scanner is designed to be applied in limb geometry (see Fig. 3.3). The resulting hyperspectral images are thus not parallel to the ground but perpendicular, with one spatial dimension along the flight direction and the other one normal to the surface of the earth. Due to the viewing geometry, HAIDI's pushbroom scanner is usually referred to as forward-looking telescope, which is also the name used in the following. The overall technical setup for the forward-looking telescope can be seen in Fig. 3.20. Because the basic setup is relatively similar to that of the nadir scanner, only the differences will be discussed below.

The most obvious difference to the setup of the nadir scanner is the entrance optics of the forward-looking telescope. It collects scattered sunlight from multiple elevation angles close to the horizon. This viewing geometry yields very long absorption paths, giving the system a high sensitivity to absorbing trace gases, especially close to the flight altitude (see Sec. 4.2.3). For this reason, the forward-looking telescope is suited best for the profile retrieval of tropospheric absorbers on smaller, low flying aircraft. Due to space restrictions on these aircraft, the entrance optics of the forward-looking system had to be as compact and lightweight as possible. This could be achieved with the pushbroom technique, which does no require a motorized scanning mechanism (Sec. 3.2). Therefore, in principle, a lens would be sufficient to build up the entrance optics of the forward-looking telescope. However, as the spectrograph of the system is usually

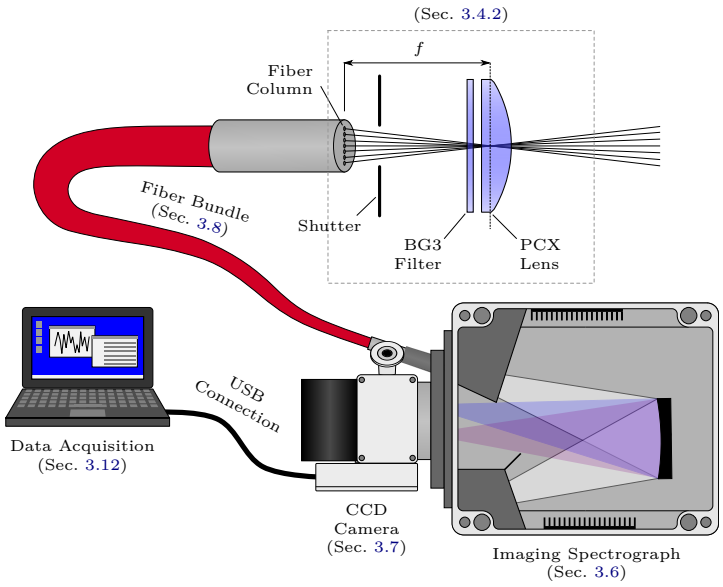

Figure 3.20.: Setup of HAIDI's forward-looking telescope (pushbroom scanner). The individual fibers of the fiber optics bundle, which connects the telescope with the imaging spectrograph, are arranged to a slit on both sides. This leads to 31 simultaneous viewing directions/elevation angles. A mechanical shutter protects the detector from incident light during the readout process. Hardware control and data acquisition is done by a computer which is connected via USB.

located above or sideways of the telescope, an additional right-angle prism is used to guide the fiber optics towards the spectrograph.

As mentioned in Sec. 3.2, the pushbroom technique uses the different dimensions of a CCD array to record spectral and spatial information at the same time. In case of the HAIDI system, the spectral dimension is along the rows of the CCD, while the column-direction of the detector is used to image the different elevation angles of the instrument simultaneously. As a consequence, the pushbroom technique requires a fiber optical cable that preserves spatial information and a spectrograph-detector unit with imaging capabilities. Therefore, the fibers of the fiber optics bundle are arranged into columns at both ends, with corresponding fiber ends having the same position in the column. A detailed description of the fiber optics for the forward-looking telescope can be found in Sec. 3.8. In the following only the most important key data of the fiber optics is briefly discussed. The fiber optics bundle has a length of 5 m and consists of 31 individual fibers with a core diameter of 150 µm each. Also in this case, the exit end of the fiber bundle directly acts as the entrance slit of the spectrograph. The other end is placed in the focal plane of the telescope. Due to the different distances of the fibers to the optical axis of the telescope, this results in 31 different elevation angles. As the height of the fiber columns is about 5.9 mm, the telescope yields a total vertical IFOV of about 7° (see also Sec. 3.4.2). The horizontal IFOV on the other hand is $\sim 0.2°$, which corresponds to the vertical IFOV of a single fiber.

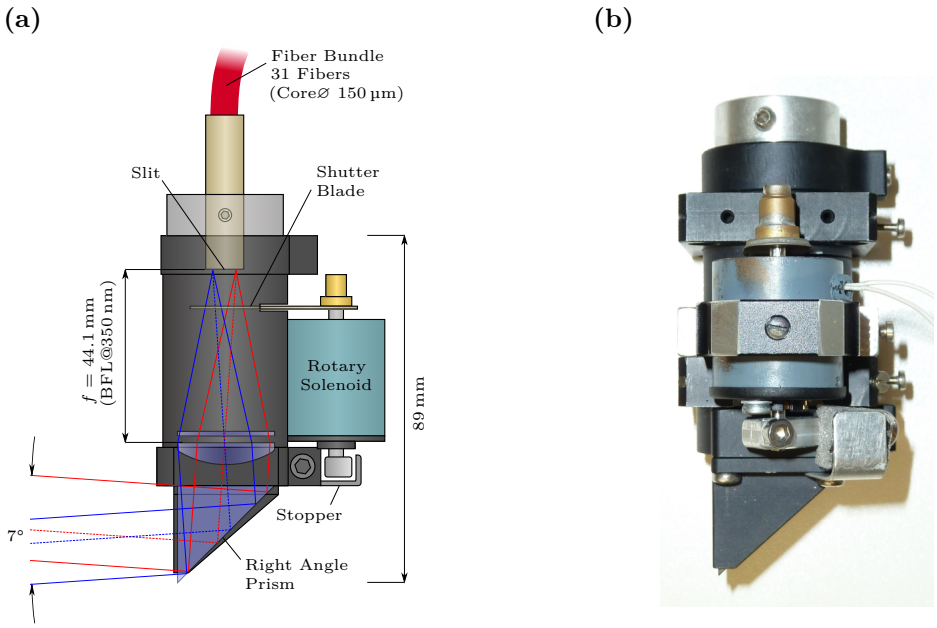

Figure 3.21.: Entrance optics of HAIDI's forward-looking telescope (pushbroom): (a) Schematic illustration showing the optical components used in the entrance optics and approximate dimensions. The rotary solenoid is shown displaced by 90° to give a clear view to the underlying components. (b) Picture of the finalized entrance optics.

The exact orientation of the instrument's entrance optics depends on the scientific question of the respective campaign. If trace gas plumes are investigated close to the flight altitude, as, for example, during the campaign on Sicily (campaign I in Tab. 5.1), the vertical IFOV of the forward-looking telescope is centered to the horizon for the expected average pitch angle during flight. For the campaigns in Indiana and Alaska (campaign II & III in Tab. 5.1) in contrast, more sensitivity at low altitudes was required and the vertical IFOV thus adjusted to an elevation angle range of $-5°$ to $+2°$.

3.5.1. Calibration of the Viewing Direction

Since the individual elevation angles of the forward-looking telescope are an important input parameter for the profile retrieval, the orientation of the instruments vertical IFOV has to be known precisely. One proven method to determine the actual orientation of the instrument's vertical IFOV is given below. First of all, a laser level has to be attached to the box which contains the entrance optics. Care must be taken to ensure that the laser level is located on the same height as the prism of the forward-looking telescope (see also Fig. 3.22). In this way an artificial horizon can be projected, which by definition corresponds to an elevation angle of 0°. Next, an inspection lamp is placed in front of the forward-looking telescope, in a distance of a few meter and on the height of the artificial horizon. Then, some spectra are taken with the instrument. By knowing the total vertical IFOV of the telescope (7°) and the CCD row number where the light from the inspection lamp can be seen in the image of the entrance slit, one can calculate the mean elevation angle of the forward-looking telescope. For example, when the entrance slit is imaged to the rows 20–240 of the CCD, each row would correspond to an IFOV of 0.032°. When the light from the lamp can be seen in row 120, it is 10 fibers away from the center of the entrance slit, which are about 0.32° in this case. Thus, there is an offset of 0.32° between the mean elevation angle and the artificial horizon. Simultaneously with these measurements the pitch angle from the aircraft's INS should be logged, because it has to be subtracted from the measured offset angle in order to obtain the offset angle relative to the pitch angle of the aircraft.

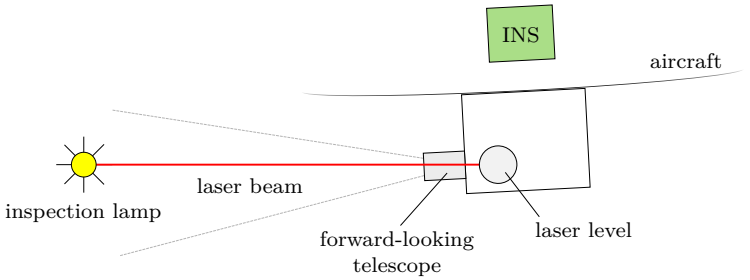

Figure 3.22.: Measurement setup used to determine the viewing direction of the forward-looking telescope.

3.6. Spectrographs

One of the main challenges in the development of the HAIDI system was to make it as compact and lightweight as possible, so that at least two of the imaging spectrographs and CCD cameras can also be installed on smaller aircraft (see Sec. 3.11). It quickly became clear that no commercial available system fulfills the requirements regarding weight, size, light throughput, spectral resolution and imaging capabilities at the same time. The Acton 300i spectrograph, for example, which was used for previous airborne imaging DOAS measurements (e. g. Heue et al., 2008), has dimensions of 34 × 25 × 20 cm and a weight of 16 kg. Solely due to the high weight, the spectrograph would be unsuitable for installation on ultralight aircraft. Therefore, we decided to design and built a new spectrograph, which is optimally adapted to the requirements of airborne imaging DOAS measurements. The HAIDI imaging spectrographs are based on a diecast aluminum box (BOPLA A140 SI) that was supplemented by a detector flange, a mount for the diffraction grating and some light traps (see Fig. 3.23).

The diffraction grating applied in the spectrographs is a type 523 00 080 grating (1200 lines/mm) from Jobin Yvon. This concave holographic grating has a focal length of 21 cm and a f-number of 3.2, which matches the f-numbers of the telescopes and the optical fibers quite well (Sec. 3.8). Due to the focusing properties of concave gratings, additional optical elements are not

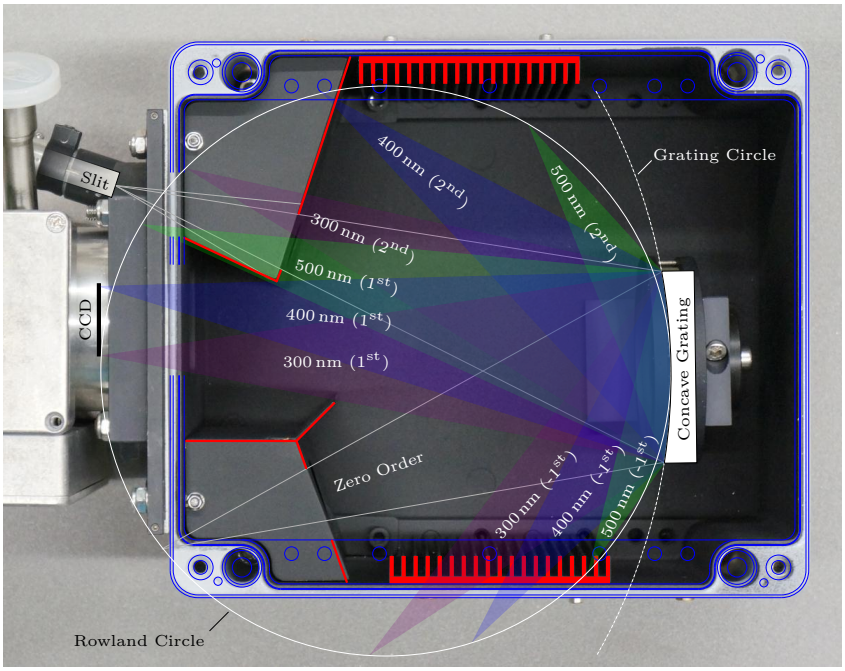

Figure 3.23.: Opened HAIDI imaging spectrograph showing the diffraction angles of the grating for different wavelengths (300 nm (violet), 400 nm (blue), 500 nm (green)) and orders. Due to the concave grating the spectrograph works on the basis of the Rowland circle. For an optimized imaging on flat surfaces (e. g. CCD) the shape of the Rowland circle is slightly altered by a special groove pattern of the grating (flat-field correction). This is why the entrance slit is not located exactly on the illustrated circle. Installed light traps are marked in red.

required by the spectrographs. This design has several advantages: On the one hand, it makes the spectrographs very easy to adjust in comparison to Czerny-Turner setups which have many more degrees of freedom for adjustment (Neumann, 2013). On the other hand, light loss due to additional optical surfaces is avoided and fewer optical compounds make the system also less sensitive to vibrations, which is an important advantage for airborne applications. Beside these mechanical advantages, concave holographic gratings offer some imaging properties which cannot be achieved with ruled ones. For example, most aberration effects like astigmatism are significantly reduced by a special groove pattern of the used holographic grating. In the same way a flat-field correction could be implemented. This improves the imaging on flat surfaces (e. g. CCD), resulting in an almost homogeneous imaging quality over the whole surface of the chip (see Fig. 3.32b). Concave holographic gratings have furthermore the advantage of producing less stray light than ruled ones (Palmer and Loewen, 2005) and that the zero order of the diffracted light can be easily guided to a light trap with small aperture, because it is also focused.

Usually the wavelength range of the spectrographs is set from 300 nm to 407 nm. However, the spectrographs also allow to rotate the grating to shift the observable wavelength range to 350 nm − 457 nm. The optical resolution achieved by the system within this range is about 0.5 nm (∼5 pixel), as can be seen in Fig. 3.32b. A list with the characteristics of the spectrographs can be found in Tab. 3.6.

Table 3.6.: Characteristics of HAIDI's imaging spectrographs.

Spectrograph characteristics	
Dimensions	24 × 20.5 × 9.5 cm
Weight	3.0 kg
Grating Type	flat field concave holographic
Configuration	quasi-Littrow
Grating Diameter	70 mm
Groove Density	1200 lines/mm
Spectral Range	300 nm to 407 nm (350 nm to 457 nm)
Dispersion	4 nm/mm
Focal length	21 cm
f-Number	3.2
typ. Resolution	∼ 0.5 nm

3.6.1. Operating Principle of Diffraction Gratings

An important decision in the design of a spectrograph is the choice of a suitable dispersive element. Prisms offer only a relatively low angular dispersion which is furthermore nonlinear with wavelength. As compactness was a crucial factor in the design of the spectrograph, a diffraction grating was used instead. Diffraction gratings are basically optical components with small

periodic structures on the surface (e. g. slits or reflecting grooves). When the mutual distance d of these structures (e. g. the distance between grooves) is of the order of the wavelength of the incident light, the light is dispersed into its spectrum. The reason for this effect becomes clear when regarding every groove of a reflection grating as slit-shaped source of outgoing elementary waves. The entire grating then acts as an array of coherent light sources interfering with each other. For a given distance d and wavelength λ there is only a set of discrete angles at which the light emitted by the grooves is in phase and constructive interference occurs.

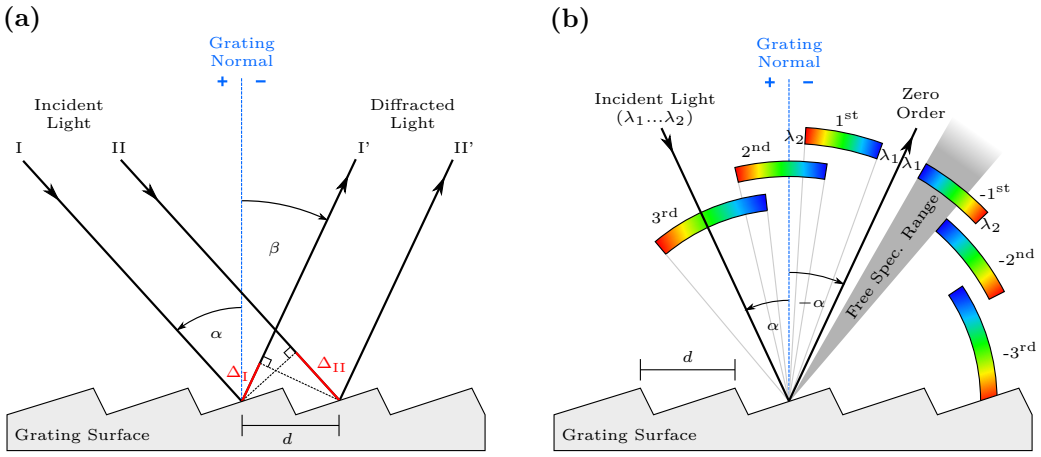

Figure 3.24.: Schematic illustration of a diffraction grating's operating principle: (a) The geometrical path difference ($\Delta_\mathrm{I} + \Delta_\mathrm{II}$) between two light beams leads to constructive interference at certain angles β. (b) The usable spectral range of a grating is limited by the existence of multiple diffraction orders.

The interference condition for a diffraction grating is illustrated in Fig. 3.24a. Two parallel light beams (I and II) of wavelength λ hitting the grating surface one groove spacing d away from each other under the angle of incidence α, measured from the grating normal. This angle and all other angles which are located on the same side of the grating normal as the incident light beams are positive by definition. The monochromatic light beams are then diffracted to an angle of β, which is in this case negative. As can be seen in the illustration, the geometrical path difference between the two beams after diffraction is as follows:

$$\Delta_\mathrm{I} + \Delta_\mathrm{II} = d \sin\beta + d \sin\alpha \tag{3.32}$$

Constructive interference can only occur when the phase shift after diffraction equals the wavelength λ of the incoming light, or an integral multiple m from that. This finally leads to the well-known grating equation:

$$m \cdot \lambda = d\,(\sin\alpha + \sin\beta)\ , \tag{3.33}$$

where the integer m is also called the diffraction order or spectral order of the diffracted light.

The usual sign convention for the spectral order is given below:

$$\begin{aligned} m > 0 \quad &\text{for} \quad \beta > -\alpha \\ m < 0 \quad &\text{for} \quad \beta < -\alpha \\ m = 0 \quad &\text{for} \quad \beta = -\alpha \end{aligned}$$

The existence of multiple diffraction orders is a disadvantage of diffraction gratings in comparison to prisms. As shown in Fig. 3.24b the diffraction orders can overlap each other, so that two or more different wavelengths are diffracted to the same angle. Thus, the usable wavelength region is restricted to the so-called *free spectral range* which can be modified by using suitable optical filters. Another consequence from this is that a fraction of the light is lost, because it is distributed to several spectral orders that do not contribute to the measured signal. For a holographic reflection grating this can be more than 50 % of the incident light (see Fig. 3.26), whereby most of the light is reflected to the zero order ($\beta = -\alpha$).

3.6.1.1. Blaze Angle

One possibility to reduce the light loss due to the distribution of incident light to multiple diffraction orders is to modify the grating setup in such a way that a large percentage of the incoming light is concentrated to one specific diffraction order. This process is called *blazing*. Blazed gratings show a significant higher efficiency when the *blaze condition* is satisfied:

$$m \cdot \lambda = 2d \sin \theta_B \,, \tag{3.34}$$

where θ_B is the *blaze angle*, which is the angle between the plane of the grating and the grating facets (see Fig. 3.25). This is the case when the facet normal bisects the angle between incident and diffracted light ($\alpha - \theta_B = \beta - \theta_B$).

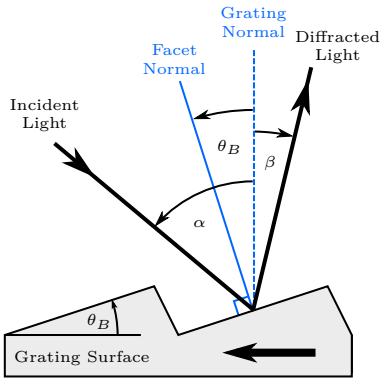

Figure 3.25.: Blazed gratings exhibit a particularly high diffraction efficiency when the blaze condition is fulfilled. For proper orientation, blazed gratings usually have a blaze arrow that points from the grating normal to the bisector between the incident and diffracted beams.

A blazed grating shows the highest efficiency when it is operated in the *Littrow configuration*, where $\alpha = \beta$. Even though the surface of a holographic gratings usually has a sinusoidal shape instead of the sawtooth profile of a ruled grating it can still have blazing characteristics. So, for example, the grating used by HAIDI's imaging spectrographs is optimized for the 1st diffraction order and is furthermore operated in a quasi-Littrow configuration ($\alpha \approx \beta$). The blaze characteristics of a holographic grating can be further improved by ion sputtering when needed. In this way the sinusoidal relief of a holographic grating can be altered towards a more triangular shape.

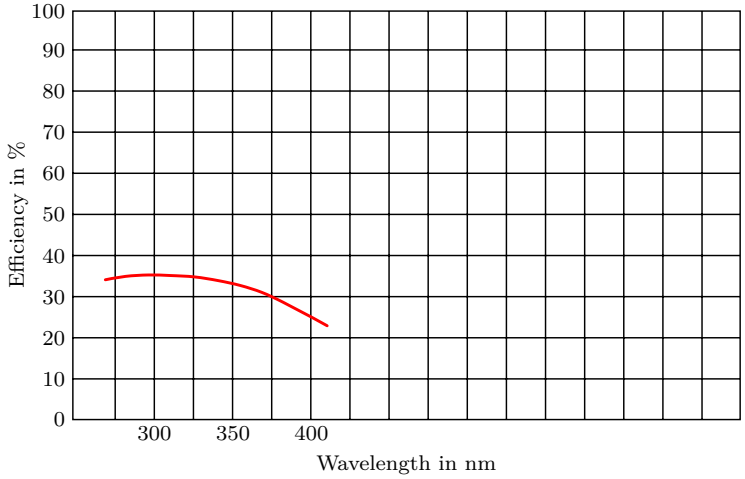

Figure 3.26.: Spectral efficiency curve of the used concave holographic grating (Type: 523 00 080) from HORIBA Jobin Yvon (Franz Josef Schäfer, Optical Components - Sales Manager HORIBA Jobin Yvon GmbH, pers. comm.).

3.6.1.2. Optical Layout of the Spectrographs

To use a diffraction grating for optical spectroscopy one also needs some collimating and/or focusing elements in addition to the dispersing one. The arrangement of these elements in relation to the entrance slit of the spectrograph and the image plane (i. e. the CCD) is usually referred to as the grating *mount*. There are a lot of different mounts for all kinds of gratings and applications. One very common mount, for example, is the Czerny-Turner mount. It uses a plane grating and at least two additional spherical mirrors to collimate and focus the incident light (Fig. 3.27a). However, due to the above mentioned advantages, HAIDI's spectrographs use a single concave holographic grating which combines dispersing and focusing properties. Concave diffraction gratings use a mount based on the Rowland circle. In a Rowland circle mount the entrance slit of the spectrograph and the tangential foci (focus in the xy-plane, see Fig. 3.28) of all wavelengths are located on the same circle, the so-called Rowland circle (Fig. 3.27b). For a grating with the radius of curvature $R_{grating}$, the Rowland circle has a radius of $R_{grating}/2$ and goes through the center of the grating surface, with the grating tangent to the circle and the grooves perpendicular to the plane of the circle (Kunze, 2009).

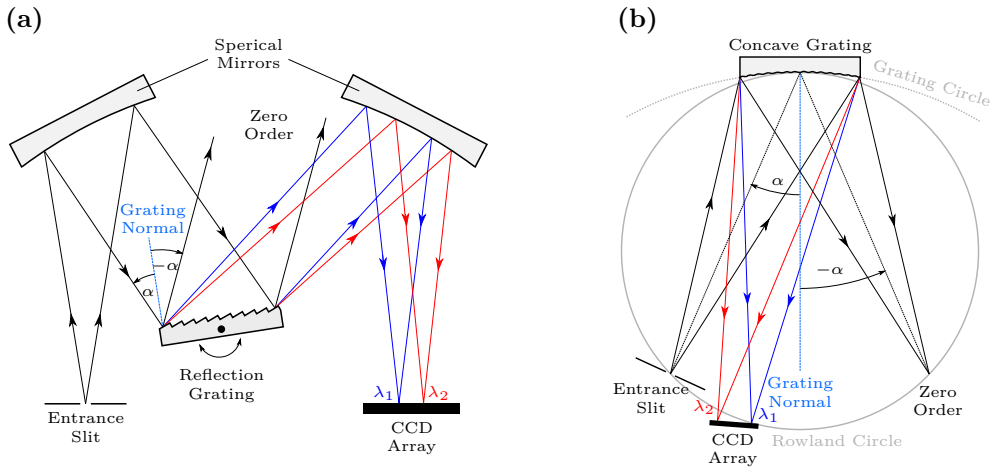

Figure 3.27.: Different types of diffraction grating mounts that are commonly used in spectrographs: (a) Czerny-Turner mount. (b) Rowland circle mount.

The disadvantage of the conventional Rowland circle mount is, that the sagittal focus for a certain wavelength λ does not coincide with the tangential one due to the off-axis usage of the grating (see Fig. 3.28). This effect is called astigmatism. In addition to that, tangential and sagittal foci are located on curved surfaces, making it impossible to bring the whole entrance slit of the spectrograph into focus on a flat image plane (i. e. the CCD). Both effects are significantly reduced in the applied diffraction gratings by a special groove pattern, which modifies the focal curves of the grating. The grooves of such aberration and flat-field corrected holographic gratings are neither parallel nor equally spaced. As a consequence of the modified focal curves, the distances between entrance slit, grating and CCD in HAIDI's spectrographs are not directly given by the Rowland circle anymore. From Tab. 3.7 it can be seen, for example, that the specified distance between entrance slit and center of the grating surface l_A is slightly greater than the grating's radius of curvature $R_{grating}$.

However, the diffraction angles β, which are required to calculate the location of the CCD,

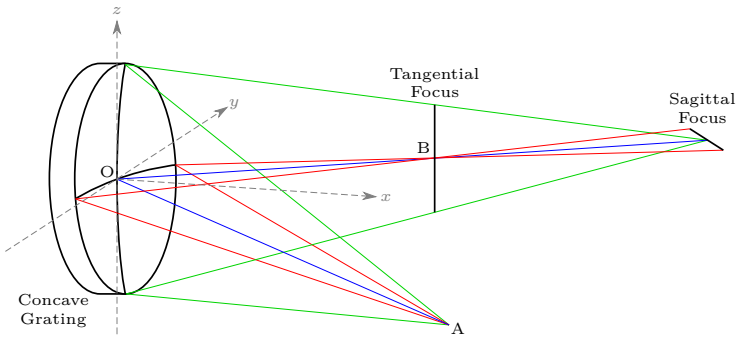

Figure 3.28.: Due to astigmatism, monochromatic light from a point A, which is located away from the optical axis of the grating, has different foci in the tangential (xy) and sagittal (xz) focal planes.

are still given by the grating equation. Thus, by plugging in the specified values for the angle of incidence α and the diffraction order m into Eq. (3.33), one obtains:

$$\beta_\lambda = \arcsin\left(\frac{\lambda}{d} - \sin 18.99°\right) \tag{3.35}$$

For the intended wavelength range from 300 to 400 nm the above equation yields the following angles β for the diffracted light:

$$\beta_{300} = +1.98°, \qquad \beta_{350} = +5.43°, \qquad \beta_{400} = +8.89°$$

The correctness of the above values was confirmed by HORIBA Jobin Yvon[2]. This can furthermore be verified, by calculating the corresponding length of spectrum l_{spec} between the diffracted light angles β_{300} and β_{400} at the location of the detector plane (see Fig. 3.29). The resulting value is 25.06 mm, which agrees very well with the specified value from the manufacturer (see Tab. 3.7). With the calculated diffraction angles and the already specified values in Tab. 3.7 it was finally possible to calculate the position of the CCD in relation to the entrance slit and the grating of the spectrograph. As can be seen in Fig. 3.29, the detector plane was chosen to be parallel to the spectrograph housing for simplicity.

Another important dimension, that could be derived from the calculated CCD position was the maximum diameter of the CCD camera housing. Because the typical reflectivity of aluminum coated mirrors is only about 90 % in the UV spectral region, additional deflection mirrors should be avoided in the design of HAIDI's spectrographs. For this purpose, CCD camera and entrance

Table 3.7.: Additional specifications of the used concave holographic grating (Type: 523 00 080) from HORIBA Jobin Yvon (Franz Josef Schäfer, Optical Components - Sales Manager HORIBA Jobin Yvon GmbH, pers. comm.).

Quantity	Value
Ruled Area Diameter D	66 mm
Radius of Curvature $R_{grating}$	207.06 mm
Substrate Thickness h	max. 12 mm
Length of Spectrum l_{spec}	25 mm
Diffraction Order m	+1
l_A	211.01 mm
l_H	206.14 mm
α	+18.99°
β_H	+0.81°

[2] Franz Josef Schäfer, Optical Components - Sales Manager HORIBA Jobin Yvon GmbH (pers. comm.)

slit have to be located on the same side of the spectrograph housing. It thus had to be ensured that the CCD camera does not intersect with the location of the fiber entrance. Taking into account the location of the CCD chip within the camera, the maximum diameter of the camera housing should not exceed 70 mm.

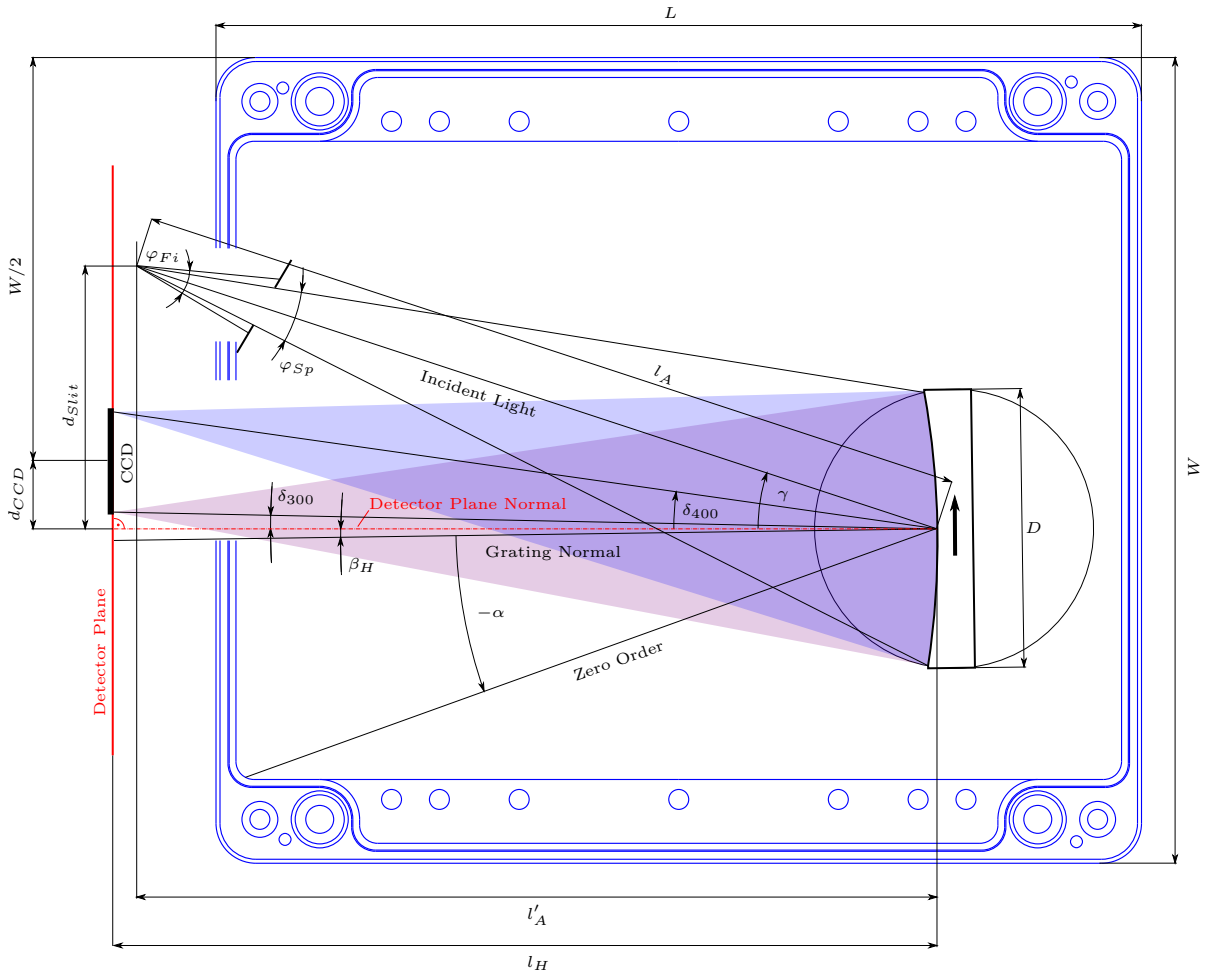

Figure 3.29.: Schematic illustration of the spectrograph showing the most important dimensions to calculate the CCD and entrance slit positions in relation to the grating. Diffraction angles δ_λ and incident angle γ were given in relation to the detector plane normal for simplicity, which is rotated about the angle β_H against the grating normal.

3.6.2. Spectrometer Characteristics

In the following, the imaging characteristics of the type 523 00 080 concave holographic grating from HORIBA Jobin Yvon and the HAIDI imaging spectrographs as a whole should be discussed in more detail. The detector used for the here presented measurements was the HAIDI CCD camera, which is described in Sec. 3.7.

3.6.2.1. Astigmatism

The most evident optical aberration in conventional concave grating spectrographs is astigmatism (Loewen and Popov, 1997). As previously mentioned, astigmatism is the property of an optical system to have different foci in the tangential and sagittal plane. The tangential plane (also called principal or dispersion plane) is defined to be perpendicular to the grooves of a conventional concave grating. Thus, when the grooves are along the z direction and the light source A is located in the xy plane, as shown in Fig. 3.28, the tangential plane also corresponds to the xy plane and contains the tangential foci B for all wavelengths. The sagittal plane instead is unique for a certain wavelength λ. It goes through the center of the grating (point O in Fig. 3.28) as well as point B and is perpendicular to the tangential plane. This means, that the spectral resolution will reach its maximum when illuminating the grating with a monochromatic light source in point A and placing the detector at the tangential focus in point B. However, as a consequence of astigmatism the image is stretched perpendicular to the dispersion direction at the same time, resulting in blurred spatial information. Shifting the image plane closer to the sagittal focus will reduce astigmatism but spectral resolution will then degrade in turn, what is called defocus.

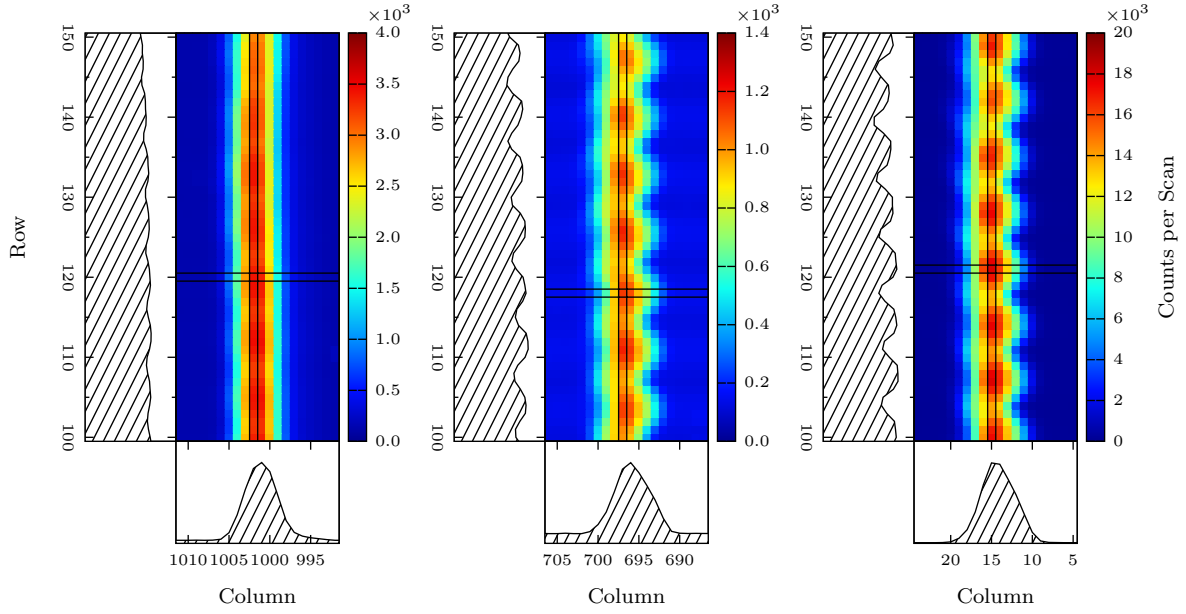

Figure 3.30.: Astigmatism in a two-dimensional image of mercury emission lines, taken with the HAIDI instrument. The whole image can be found in Fig. 3.32a. To visualize the achieved resolution along the spectral (columns) and spatial dimension (rows), cross sections of the marked rows and columns are illustrated as hatched areas. While the 302.15 nm line (left) exhibit a good spectral resolution, the image is blurred along the spatial dimension. The detector was thus located at, or close to, the tangential focus for this wavelength. The 334.15 nm (middle) and 404.66 nm (right) lines were located closer to the sagittal focus, offering a good compromise between spectral and spatial resolution.

Even though HAIDI's spectrographs use aberration corrected diffraction gratings, the existence of astigmatism is still noticeable. This can be seen, for example, in Fig. 3.30. The plots show an enlarged view of the mercury emission lines from Fig. 3.32a. As one can see, the 302.15 nm line illustrated in the left plot offers the best spectral resolution, but the individual fibers of the entrance slit can not be clearly distinguished from each other. The 334.15 nm (middle) and 404.66 nm (right) lines instead show spatial resolved fibers with slightly reduced spectral resolution in return. Astigmatism becomes especially relevant when using the CCD cameras in imaging mode (i. e. for the forward-looking telescope). Then a compromise between spectral and spatial resolution has to be found by placing the detector somewhere between tangential and sagittal focal curves. Because the used diffraction gratings are not optimized for imaging applications, it is a very challenging task to achieve an almost homogeneous spatial resolution over the whole detector surface without deteriorate the spectral resolution too much.

3.6.2.2. Dispersion and Instrument Function

Further important characteristics of a spectrograph are its dispersion and the instrument function. The dispersion of a spectrograph (more exactly: the reciprocal linear dispersion) $\mathrm{d}\lambda/\mathrm{d}x$ gives the change in wavelength corresponding to a change in location along the spectral dimension of the detector. It can be derived from the grating equation (3.33) in combination with the focal length of the spectrograph and is defined as follows (Palmer and Loewen, 2005):

$$\frac{\mathrm{d}\lambda}{\mathrm{d}x} = \frac{d \cdot \cos\beta_\lambda}{m \cdot f_{grating}}\,, \tag{3.36}$$

where x is the distance on the image plane, d the groove spacing, β_λ the diffraction angle for the considered wavelength λ, m the diffraction order and $f_{spectrograph}$ the focal length of the grating. Due to the relatively small diffraction angles, $\cos\beta_\lambda$ is assumed to be 1 in the following. Plugging in the values from Tab. 3.6 and 3.7 then yields a theoretical dispersion of:

$$\frac{\mathrm{d}\lambda}{\mathrm{d}x} = 3.97\,\mathrm{nm/mm}\,.$$

This agrees with the 4 nm/mm specified by the manufacturer (Tab. 3.6). Since HAIDI's cameras use a CCD with a pixel size of $26 \times 26\,\mu\mathrm{m}$ (see Sec. 3.7), the given value corresponds to a dispersion of 0.104 nm/pixel. In order to verify the specified value and determine the wavelength-to-pixel mapping $\lambda(j)$ of the instrument, a wavelength calibration was done using the mercury emission lines shown in Fig. 3.32a. The wavelength-to-pixel mapping was obtained in this case by fitting a polynomial of second degree to the positions (in units of pixels) of the emission lines and their well known wavelengths:

$$\lambda(j) = a_1 + a_2 \cdot j + a_3 \cdot j^2\,, \tag{3.37}$$

where j is the pixel number along the spectral dimension of the CCD (i. e. the column number in

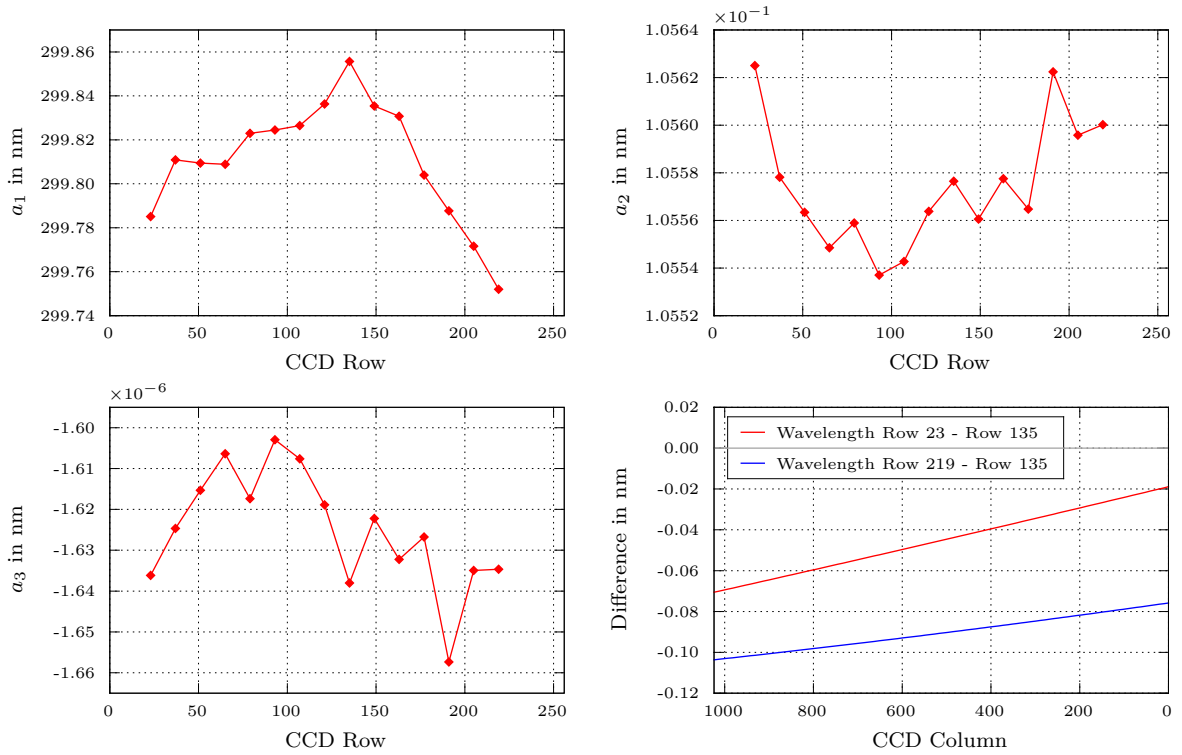

Figure 3.31.: Results from a wavelength calibration of the HAIDI system. The CCD rows of the spectrum shown in Fig. 3.32a were co-added (14 rows each ≈ 2 fibers) and the corresponding calibration coefficients plotted versus the central row number. The difference in coefficient a_1 causes a noticeable curvature of the spectral lines that is slightly compensated by coefficient a_2 for longer wavelengths (lower channel numbers). This can also be seen from the plot in the lower right corner which shows the differences in the wavelength-to-pixel mapping for different rows.

this case). The result of the calibration for different rows of the CCD is illustrated in Fig. 3.31. As can be seen from the plots, the linear dispersion coefficient a_2 approximately corresponds to the expected value. Another thing that can be seen from Fig. 3.31 is, that the coefficients of the wavelength-to-pixel mapping change as a function of the CCD row. In fact, the spectral lines are convex towards the zero order image (i. e. concave towards longer wavelengths). This effect was called "enveloping curvature" by Beutler (1945) and arises due to the finite length of the spectrograph's entrance slit. In remote sensing applications the effect is also often referred to as "spectral smile" (e. g. Ceamanos and Doute, 2010). The plot in the lower right of Fig. 3.31 shows the differences between the wavelength-to-pixel mapping of a central row (row 135) and two rows which are located close to the edge of the entrance slit (row 23 and 219). One can see, that the difference in the wavelength-to-pixel mapping and thus the curvature of the spectral lines is most evident at higher column numbers of the CCD, which means shorter wavelengths in this case.

When the linear dispersion $\mathrm{d}\lambda/\mathrm{d}x$ of a spectrograph is known, its spectral resolution can be determined by the width of the instrument function $H(\lambda)$. Since the instrument function is the

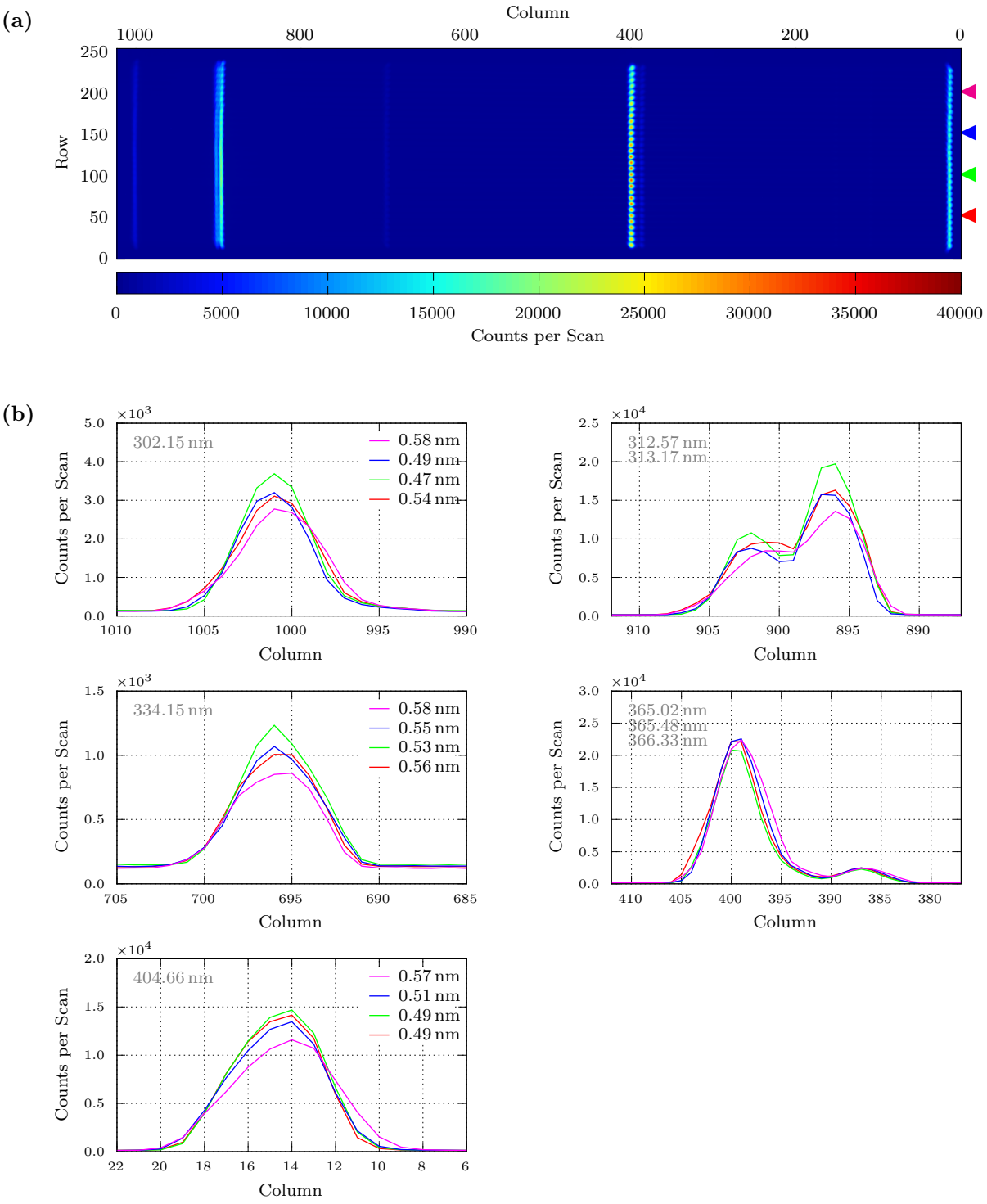

Figure 3.32.: Mercury emission lines between 300 and 407 nm taken by HAIDI's detector in full frame readout mode: (a) Intensity plot showing the image of the entrance slit for different emission lines. (b) Mercury lines plotted for different rows of the CCD (see markers in Fig. 3.32a). The full width at half maximum (FWHM) of the individual lines is given in the upper right corner of the plots. As can be seen, the peak width increases slightly towards the edges of the CCD, resulting in a lower spectral resolution. This is due to Petzval field curvature (Kidger, 2002). However, the double emission line 312.57 nm/313.17 nm can still be resolved for all CCD rows.

spectrograph's response to a delta peak of monochromatic light as input intensity distribution at the entrance slit, the spectral resolution is given by the product of the instrument function's FWHM (in units of pixel) and the linear dispersion coefficient a_2. Thereby it has to be ensured, that the width of the instrument function exceeds a certain amount of detector pixels in order to avoid undersampling ($\sim$ 5 pixels according to Platt and Stutz (2008)). In general, the width of the instrument function is dominated by the width of the spectrograph's entrance slit. Because entrance slit and CCD are both located in a distance of about twice the focal length of the grating ($f_{grating} = R_{grating}/2$, Tab. 3.7), the magnification factor of HAIDI's spectrographs should be close to 1. Hence, a fiber diameter of 150 µm and a pixel size of 26×26 µm yields a width of about 5.8 pixel for the instrument function. With an average linear dispersion of 0.106 nm/pixel (see Fig. 3.31) one obtains a spectral resolution of 0.61 nm.

The instrument function of a DOAS instrument is usually determined by measuring some mercury emission lines. Due to the low spectral width of the emission lines ($\sim$ 10 pm, Platt and Stutz (2008)) in comparison to the typical resolution of a DOAS instrument (0.1–1.0 nm), the measured intensity distribution is a good approximation for the instrument function. Figure 3.32b shows some mercury emission lines measured by the HAIDI system at different rows of the CCD. As one can see, the obtained spectral resolution is about 0.53 nm on average and thus slightly better than the value expected from theoretical considerations. Towards the upper and lower edge of the CCD, the spectral resolution usually decreases slightly. This seems to be due to a non-perfect flat-field correction of the grating and thus still existent Petzval field curvature (Kidger, 2002). However, large areas of the CCD show an almost constant instrument function. This is an important fact in the DOAS evaluation, because here the literature cross-sections are convolved with a single mercury emission peak that is preferably located within, or at least close to, the evaluation wavelength range (Sec. 2.3). If the instrument function would change significantly in the considered evaluation wavelength range, this would lead to enlarged residual structures in the DOAS fit.

3.6.2.3. Stray Light

Another potential source of residual structures in the DOAS evaluation is spectrographic stray light. Stray light is light that incidents on the detector but was not intended in the design. The effect of stray light is that it superimposes a not exactly known offset signal to the measurement. In this way, the shape of absorption spectra can be slightly changed, which manifests itself ultimately in a reduced optical density and residual structures (Platt and Stutz, 2008). Because it is difficult to correct the influence of stray light afterwards, spectrographic stray light should be reduced to a minimum from the outset.

Stray light in spectrographs may have many causes. One very common is, that the F-number of the illumination exceeds that of the spectrograph. Light is then reflected at the grating mount and the walls of the spectrograph. In order to prevent this, HAIDI's imaging spectrographs

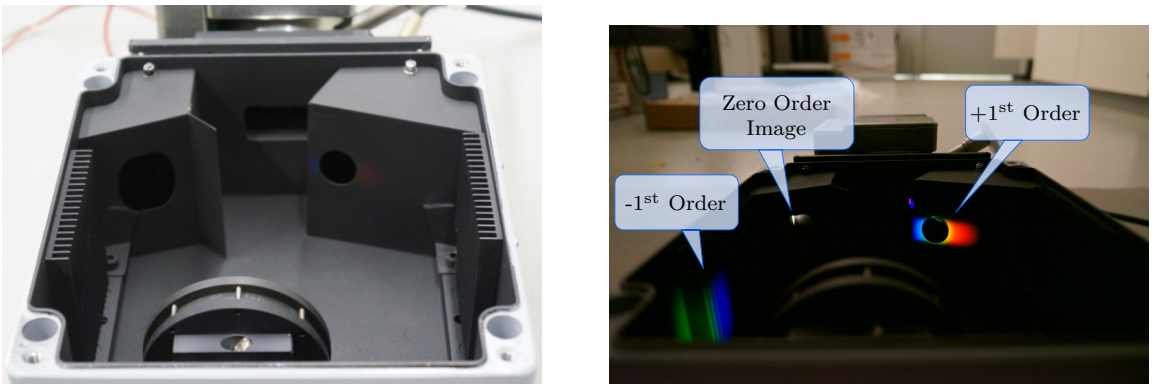

Figure 3.33.: Detailed view of HAIDI's imaging spectrographs showing the installed light traps in the inside. In order to make higher order diffracted light visible, the BG3 filter in the telescope was removed and the entrance slit then illuminated with a halogen lamp. Diffracted light from the second order of the grating is not observable.

feature an additional aperture in front of the entrance slit, which reduces the F-number of the illumination to that of the spectrograph (see also Figs. 3.23 and 3.33). Another source of stray light is the reflection of unused diffraction orders or unused portions of the spectrum at the spectrograph walls. This was reduced by two measures: First of all, the spectral range of the light entering the spectrograph was limited to the region of interest by applying an optical band-pass filter in the telescopes of the system. The filter (BG3 from Schott) has a high internal transmittance of $\geq 90\,\%$ in the spectral region between 300 and 400 nm (based on a reference thickness of 1 mm). For shorter and longer wavelength the transmittance of the filter decreases very quickly. As the BG3 filter opens up again from about 700 nm, where solar radiation is still relatively intense and the CCD detector sensitive, additional measures against stray light in the near infrared had to be taken. For this reason, the inside of the spectrograph was coated with a flat black painting (Krylon ultraflat black) which has a very low reflectivity in the infrared wavelength region (Wan et al., 1999). The second measure was to install light traps[3] for higher order diffracted light (Fig. 3.33). Also the very bright zero order image was guided to a light trap with small aperture.

The approximate percentage of stray light in a measurement spectrum can be determined by taking two different spectra from a halogen lamp. One with optical long-pass filter and the other one without (see Fig. 3.34). The applied long-pass filter (GG475 from Schott) blocked wavelengths below 475 nm (transmittance $\leq 0.001\,\%$) in this case. Because the spectrograph was set to the typical wavelength range of 300 to 407 nm, the spectrum with filter should only contain the stray light originating from wavelengths above 475 nm after the offset and dark current correction. When dividing this spectrum by the also corrected spectrum without any optical filters, one obtains the stray light ratio. As can be seen in Fig. 3.34 it is less than 0.5 % for typical intensity levels.

[3] Structures intended to absorb unwanted light (e. g. boxes with small aperture)

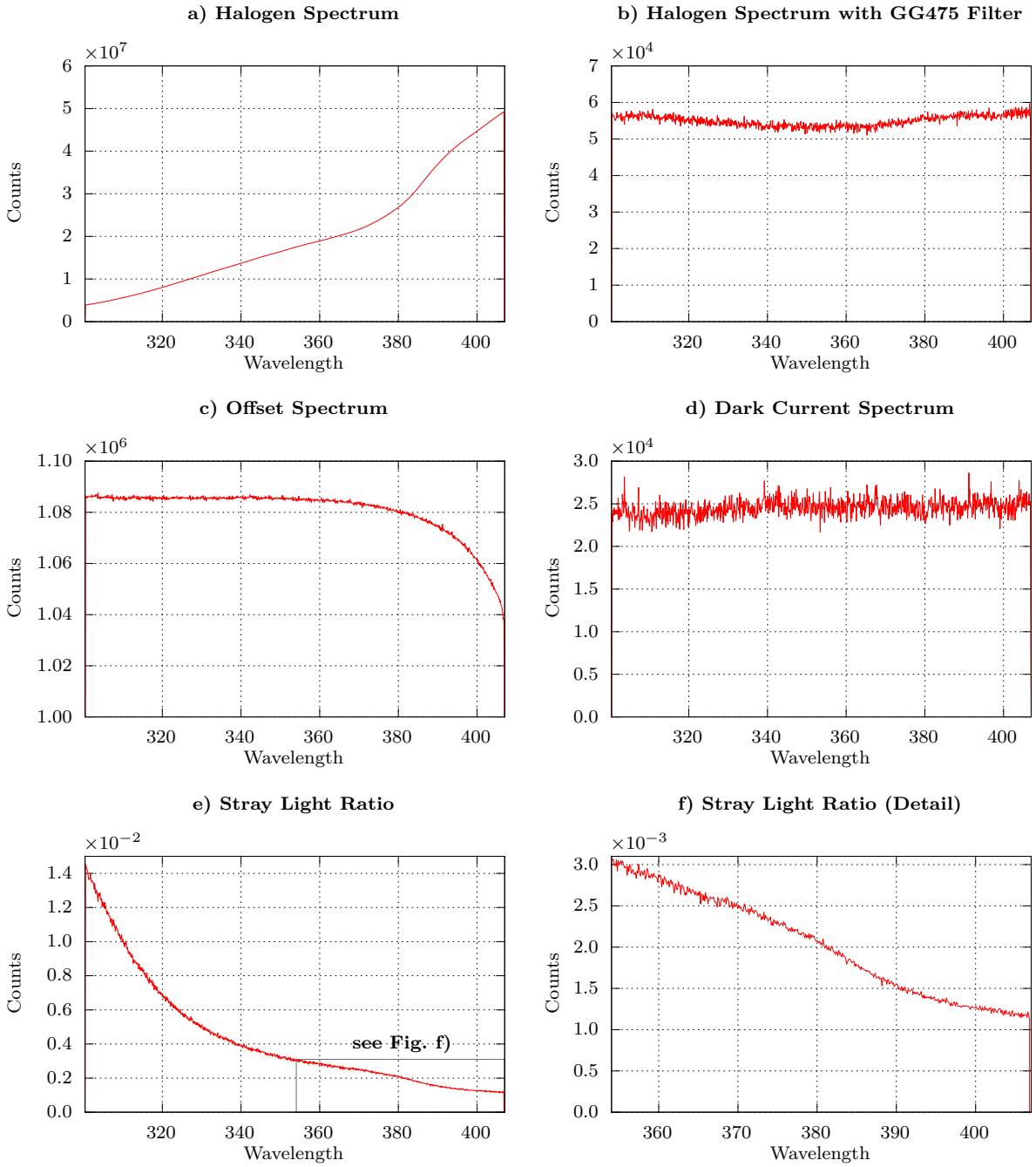

Figure 3.34.: Results from a stray light measurement of the HAIDI system. Two spectra (1000 scans each) were taken from a halogen lamp, one without any optical filters **(a)** and one with GG475 long-pass filter **(b)**. After correcting both spectra for offset and dark current (Figs. **a)**, **b)** and **d)** are shown already corrected), the stray light ratio **(e)** is obtained by dividing the spectrum with filter by the spectrum without filter. The stray light ratio thus gives the percentage of stray light in relation to the original light intensity. Figure **f)** shows an enlarged detail of the stray light ratio.

3.7. The CCD Cameras

The CCD cameras of the HAIDI system are responsible for digitizing the spectrum generated by the imaging spectrographs and are thus one of the key components of the instrument. Just like the spectrographs, readout electronics and housings of the CCD cameras are custom-made in order to adapt them to the special requirements of airborne imaging DOAS measurements. For this purpose, our workshop cooperated with the company khs-instruments from Munich, Germany, which is specialized on CCD camera readout electronics. One of the main goals was to built the cameras as small and lightweight as possible, so that the combination of imaging spectrograph and detector could later be installed also in very limited space (as e. g. in ultralight planes). Apart from the compact design, the advantage of such a custom-made camera is that its readout electronics can furthermore generate the PWM signal that controls the motion of the nadir scanner's servo motor (see Sec. 3.4.1). In this way, it can be ensured that the recording of spectra is synchronized with the scan angle β of the instrument, which is therefore known precisely for each spectrum of a swath. Also the signal for the mechanical shutter of the forward-looking telescope is generated by the readout electronics, when the camera is operated in the imaging (2D) mode.

The CCD cameras are based on CCD30-11 chips from e2v (Chelmsford, England) with an image resolution of 1024×256 pixel (pixel size: $26 \times 26\,\mu m$). The chips are back illuminated

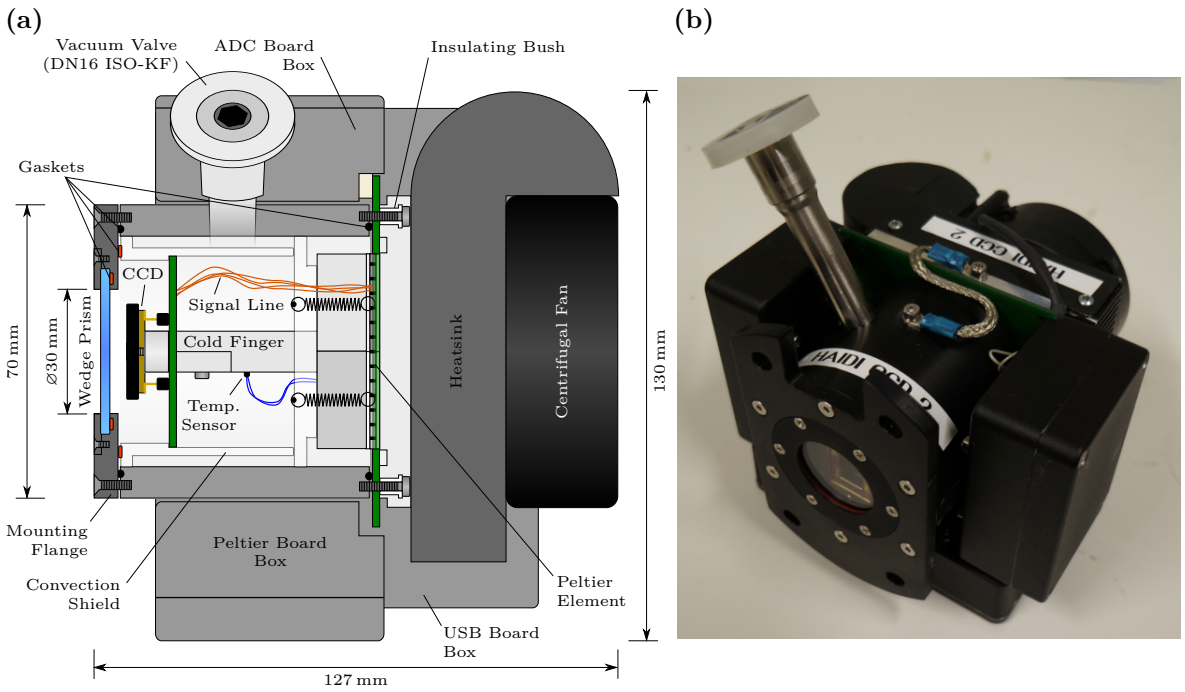

Figure 3.35.: CCD camera of the HAIDI system: (a) Cross-sectional view, showing internal components and the cooling mechanism of the camera. (b) Photo of the final version of the CCD camera.

and UV coated for enhanced sensitivity in the UV wavelength range, resulting in a quantum efficiency of 50 to 65% between 300 and 400 nm (see Fig. 3.36). Additional specifications of the CCD cameras can be found in Tab. 3.8.

In order to reduce the dark current signal of the CCD chips (see Sec. 3.7.2.1) at higher integration times and in warmer environments, HAIDI's cameras are equipped with a one-stage thermoelectric cooling (Peltier element). Figure 3.35 shows the basic construction of the cooling. The CCD chips are directly attached to an aluminum cold finger that conducts the heat from the CCD to a Peltier element (QuickCool QC-71-1.4-8.5M). An aluminum heatsink with centrifugal fan on the rear side of the camera then dissipates the heat from the warm side of the Peltier element to the ambient air. In combination with the low-profile heatsink a centrifugal fan offers a much better heat dissipation than an axial fan, because the Peltier element is located directly below the center of the heatsink, where the airflow of an axial fan is close to zero. The regulation of the cooling is realized via PID control integrated in the measurement software (Sec. 3.12). A 5 kΩ NTC temperature sensor connected to the cold finger measures the CCD temperature required for the regulation. At maximum power, the Peltier element is able to cool the CCD chip to approximately 40 K below ambient temperature. Normally, the detector is operated at a temperature of 0 °C, where the typical dark current signal is about 80 e^-/pixel/s ≈ 5 counts/pixel/s (see Sec. 3.7.2.1). Each pixel of the CCD30-11 chips has a full well capacity of 500 000 e^- and the pixel in the readout register can hold up to 1 000 000 e^-. Thus, even in full vertical binning mode, where the signal of 255 image pixels is

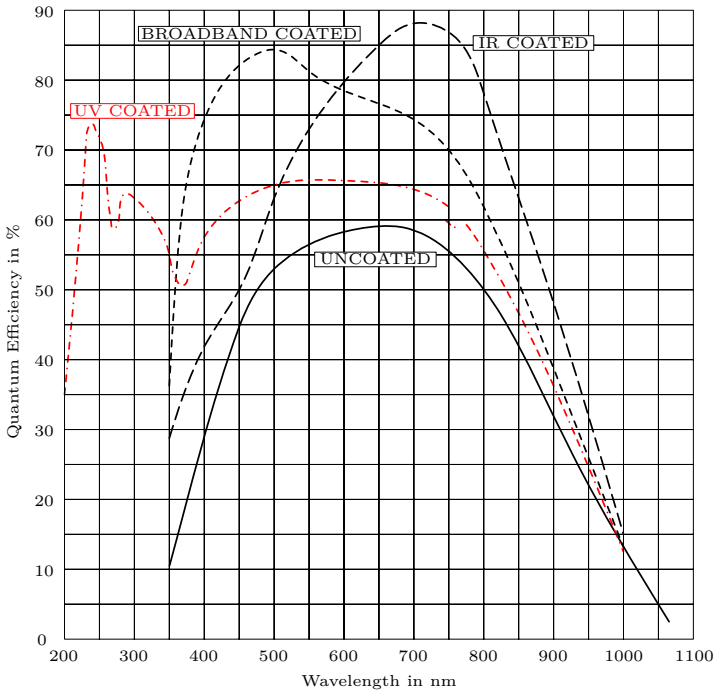

Figure 3.36.: Quantum efficiency of the CCD30-11 chip with different anti-reflection coatings. HAIDI's cameras use the version with the UV coating, which is marked in red (e2v, 2013).

transferred into one pixel of the readout register, it takes about 50 s at a temperature of 0 °C before the full well capacity of the chip is reached. Usual integration times in this mode are, however, only a few tens of milliseconds. To increase the efficiency of the cooling and reduce the heat transfer between the cooled parts within the camera (cold finger and CCD) and the camera housing, which is at ambient temperature, the camera is equipped with internal convection shields. In addition the housing is filled with argon at slight overpressure (~ 0.3 bar). Argon has a thermal conductivity lower then air and the overpressure prevents water vapor from entering the camera housing which could otherwise condensate at the cooled CCD surface and damage it. An additional protection against humidity is a small bag with molecular sieve, which is placed in the free space around the cold finger.

Further components of the CCD camera are, for example, a set of small diecast aluminum boxes, which are arranged around the main body of the camera. These boxes contain the entire electronics needed to readout and control the camera. The separation into several boxes is intended to prevent mutual interferences of the different electronic boards. Each of these boards performs a specific task. While the ADC board digitizes the incoming signals from the amplifier of the CCD, the Peltier board regulates the supply voltage of the Peltier element. Both boards are in turn connected to the USB board, which contains the FPGA[4] for controlling of the electronics and also manages the communication between computer and CCD camera via USB connection. The mounting flange, with which the camera is attached to a spectrograph, is located at the front side of the camera. Here is also the quartz window through which light enters the camera. In order to avoid Fabry-Perot etalon effects due to plane parallel reflecting surfaces, HAIDI's CCD cameras use a window with a wedge angle of 0.5°. The window is oriented in such a way that the wedge angle is perpendicular to the spectral axis of the camera, since otherwise the window will act as an additional dispersive element.

Table 3.8.: Characteristics of HAIDI's custom-built CCD detectors (e2v, 2013).

Detector characteristics	
Dimensions	$13.0 \times 13.0 \times 12.0$ cm
Weight	1.5 kg
CCD	e2v CCD30-11 (back-illuminated)
Resolution	1024×256 pixel
Image Area	26.6×6.7 mm
Pixel Size	26×26 µm
Cooling	max. 40 K below ambient temp.
Min. Int. Time	10 ms (Full Vertical Binning)
	297 ms (Full Frame Readout)
typ. Readout Frequ.	1 MHz

[4] Field Programmable Gate Array

3.7.1. Operating Principle of a CCD

The concept of the CCD was first described in 1969 by Willard Boyle and George E. Smith at the AT&T Bell Labs in Murray Hill, New Jersey, mainly intended as a new kind of semiconductor memory for computers (Boyle and Smith, 1970). However, it became clear quickly that the CCD can also be used as an imaging device. Today, the charge-coupled device (CCD) has become a widely used tool for scientific imaging applications. Willard Boyle and George E. Smith have been awarded the Nobel Prize in Physics for their invention in 2009.

A CCD essentially consists of a two-dimensional array of picture elements (pixel) that use the photoelectric effect to convert the electromagnetic energy of incident photons into a measurable electronic signal. In principle, each pixel of a CCD is made up of three layers (see Fig. 3.37). The lowermost layer consists of a semiconductor, typically p-doped silicon. This is the photosensitive part of a pixel. Directly above the p-doped Silicon layer is a very thin (∼100 nm) silicon dioxide layer that serves as an isolator. Finally, metal gate electrodes are attached on top of the silicon dioxide layer. Usually the gate electrodes are made of polycrystalline silicon or indium tin oxide (Brady, 2009). The resulting structure is called a MOS (metal oxide semiconductor) and behaves like a parallel-plate capacitor. Therefore, it is able to store electrical charge.

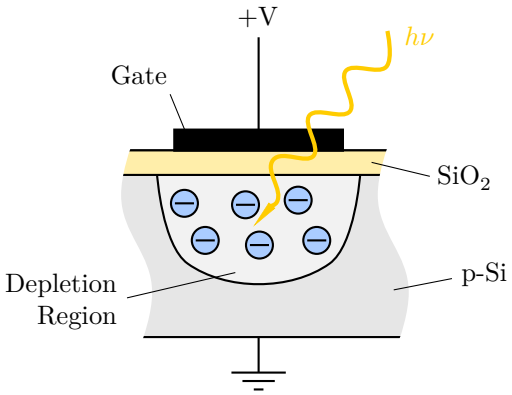

Figure 3.37.: Cross-section of a MOS structure representing a subunit of every pixel. Incoming photons generate electrons that become confined in the potential well induced by the applied voltage at the gate electrode.

Incident photons with an energy grater than the band gap of the used semiconductor material can take electrons from the valence band to the conduction band and thus generate electron-hole pairs in the semiconductor layer of a pixel. Silicon has a band gap of 1.12 eV at 300 K. Hence, incident photons need a wavelength shorter than 1100 nm to produce electron-hole pairs in a silicon based detector. Now, in order to collect the photo-induced electrons during the exposure time of the CCD and prevent them from recombination with holes, a positive voltage is applied to one of the gate electrodes of a pixel. The majority charge carriers (holes) are repelled by this potential, forming a region free of holes directly beneath the gate electrode, the so-called depletion region. The generated photo-electrons, however, are attracted by the potential and

continue to accumulate in the depletion region during the exposure time. The maximum amount of electrons that can be stored in the potential well of a single pixel is called its full well capacity and depends on the applied effective voltage at the gate electrode as well as the capacitance of the MOS capacitor. Typical values for the full well capacity range from a few tens of thousands to more than a million electrons per pixel.

However, due to various reasons only a given percentage of photons with an energy greater than the semiconductor's band gap generates photo-electrons that contribute to the output signal in the end. This is mainly due to light losses by reflection or interference on optical surfaces of the detector as well as the absorption of photons in non-sensitive areas of the CCD (Davidson et al., 2012). The ratio of measured photoelectrons to the number of incoming photons at a given energy is called the quantum efficiency of a CCD (see Fig. 3.36). Due to the aforementioned reasons, the quantum efficiency of a silicon based detector is zero for photons with a wavelength above 1100 nm. However, also for wavelengths below 400 nm the quantum efficiency of a standard CCD detector is close to zero. This is because of the transmittance

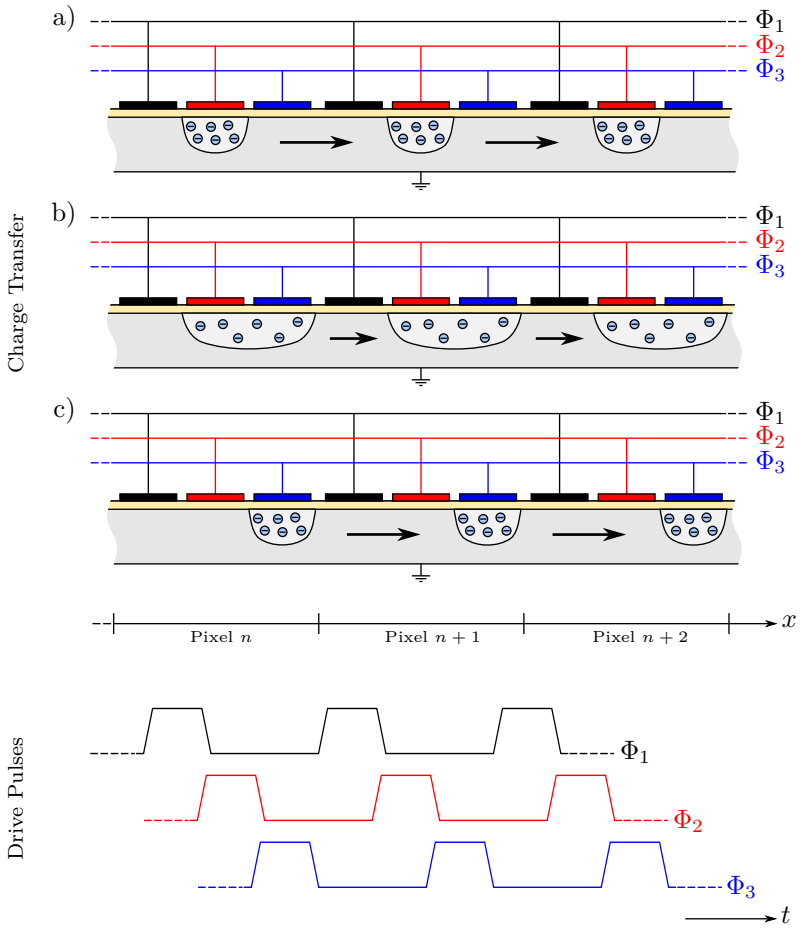

Figure 3.38.: The basic charge transfer principle in a 3-phase CCD: By clocking the electrodes with the signal shown in the lower part of the figure, the collected photo-electrons are shifted along the columns of a CCD.

of the gate material, which starts to decrease below 600 nm (Lewis and Edwards, 2001). This means that incident photons will be absorbed before they can produce an electron-hole pair. For applications in the UV wavelength region this has to be avoided. A common method to achieve this is to coat the detector surface with a fluorescent film (e. g. Lumogen). Lumogen emits light between 500 nm and 580 nm when exposed to shorter wavelength radiation (120 to 450 nm, Davidson et al. (2012)). Another way is to illuminate the CCD from its back side, so that the photons do not have to pass trough the gate electrodes and the oxide layer. This leads to a drastically enhancement of the quantum efficiency in the UV spectral region but at the same time it makes the construction of the CCD much more expensive, because the semiconductor layer has to be thinned by etching to about 10 µm (Andor Technology, 2013).

At the end of the exposure time the image information (in the form of collected electrons) has to be read out. This is done by clocking the individual gate electrodes of the pixels. Most CCDs use three electrodes per pixel (3-phase CCD) in order to transfer the collected charge. The basic principle is shown schematically in Fig. 3.38. During the exposure time a positive voltage is only applied to one of the electrodes ($\Phi_1 = 0\,\mathrm{V}$, $\Phi_2 = +\mathrm{V}$, $\Phi_3 = 0\,\mathrm{V}$), so that charge accumulates beneath. Then a neighboring electrode is also set to a positive voltage ($\Phi_1 = 0\,\mathrm{V}$, $\Phi_2 = +\mathrm{V}$, $\Phi_3 = +\mathrm{V}$), in this way the charge is distributed to both electrodes. Finally, the voltage of the central electrode is lowered ($\Phi_1 = 0\,\mathrm{V}$, $\Phi_2 = 0\,\mathrm{V}$, $\Phi_3 = +\mathrm{V}$) and the charge is shifted completely to the neighboring electrode. By continuing this procedure (next: $\Phi_1 = +\mathrm{V}$, $\Phi_2 = 0\,\mathrm{V}$, $\Phi_3 = +\mathrm{V}$), the charge is transfered stepwise along the columns of the CCD. Since all pixels of the CCD's image section are clocked identically, the lowermost row of a CCD is shifted into the readout register, while all other rows are shifted down by one. The charge in the readout register is then also shifted pixel-wise to the on-chip amplifier by clocking. From here the signal is put out to the readout electronics for digitizing. When all pixels of the readout register are read out, the charge in the image section is again shifted down by one row. This cycle is repeated until all pixels of the image section are read out.

3.7.2. Performance of the used CCD

As mentioned earlier, HAIDI's cameras use a Full-Frame-CCD from e2v with a resolution of 1024×256 pixel. A Full-Frame-CCD offers the highest light gathering capability in relation to the detector size, because all pixels are sensitive to light. A schematic illustration of the used CCD can be found in Fig. 3.39. The custom-built electronics allows to read out the CCD in two different modes. The first one is the imaging (2D) mode. As the name suggests, this mode is used when two-dimensional images are required (e. g. for the forward-looking telescope). It allows to take images with the maximum resolution of 1024×256 pixel. Since the readout register is clocked with a frequency of 1 MHz, each row of the CCD takes about 1 ms to be read out. This gives a readout time of about 266 ms for all 256 rows (including blank pixel) of the

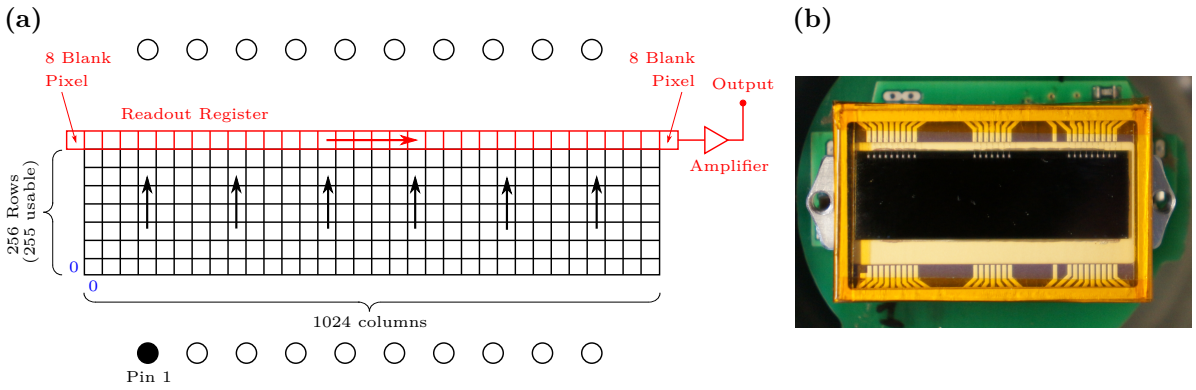

Figure 3.39.: The CCD30-11 from e2v: (a) Schematic illustration of the CCD showing its basic structure and the position of the readout register in relation to Pin 1 of the DIL package. (b) Photo of the CCD (same orientation as in Fig. 3.39a) with attached protective window. Because the window is not made of quartz glass, it was removed before closing the camera housing.

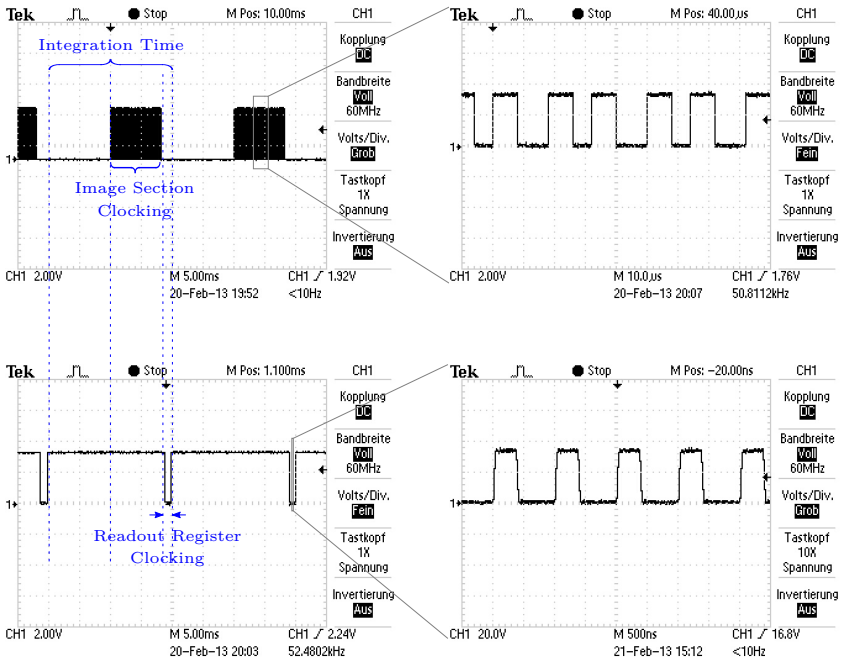

Figure 3.40.: Oscillograms of the clocking signals. The upper part of the figure shows the clocking signal of the image section for a spectrum with an integration time of 20 ms in FVB mode. In the lower part of the figure the corresponding signal for the readout register is shown. As can be seen, about half of the total integration time (~ 10 ms = minimum integration time) is needed to read out the information from the CCD. More detailed information to the clocking of the CCD can be found in the datasheet of the CCD (e2v, 2013).

CCD. Additionally the time for the vertical shifting of the rows has to be considered. A shift by one row takes about 32 µs (≈ 8.2 ms for 256 rows). Thus, together with additional delays between the shifting of rows and the readout of the register, one obtains a minimum integration

time of 297 ms for a full resolution image. Because the full vertical resolution of the CCD is unnecessary for most of the intended applications, the rows can be binned to powers of 2 (2, 4, 8, ...). This means that multiple rows will be shifted into the readout register before the pixels are transferred to the amplifier. Binning reduces the resulting file size and also the time needed for readout. The imaging mode requires the use of a mechanical shutter that protects the pixel from incident light during readout.

The second mode is the full vertical binning (FVB) mode. In this mode all 256 rows of the CCD are shifted into the readout register before it is read out. As a consequence, spatial information along the columns of the CCD is lost completely. However, the FVB mode is only used for HAIDI's nadir scanner, where spatial information is not required. The advantage is, that one obtains a readout time comparable to that of a line sensor while having at the same time a much larger area for collecting light. Since the clocking frequencies in FVB mode are the same as in 2D mode, it takes 8.2 ms to shift all rows into the readout register and about 1 ms to read out the pixels in the register. Resulting in a total minimum integration time of 10 ms in FVB mode (see also Fig. 3.40). Because the nadir scanner does not record any spatial information with the CCD that can otherwise smear during the vertical shifting of the rows, a mechanical shutter is not necessary in this case.

3.7.2.1. Dark Current and Offset

As described in Sec. 3.7.1, photons with sufficient energy can generate photo-electrons in the pixel of a CCD. The amount of collected electrons is then converted into a proportional voltage by the on-chip amplifier. An analog-to-digital converter (ADC) in the readout electronics finally digitizes the received values. However, beside the incident photons two additional components contribute to the overall measured signal $S(j)$ from the CCD. At normal temperatures and integration times the dominating one is the offset signal. This signal is added by the electronics during each readout to make sure that the ADC receives only positive values. The offset is independent of CCD temperature and integration time but varies slightly with the temperature of the readout electronics. Since the offset signal is proportional to the number of scans n_scan, it is usually determined by taking a large number of scans (i. e. several thousand) with the minimum integration time and shielded from light to avoid an electron-induced signal. The typical offset signal of HAIDI's CCD cameras can be seen in Fig. 3.41. Once the offset signal $O(j)$ is determined, recorded spectra can be corrected by the following equation:

$$I_{corr,offset}(j) = S(j) - \frac{n_{scan,meas}}{n_{scan,offset}} \cdot O(j)\,, \tag{3.38}$$

where j is the channel number of the CCD, $n_{scan,meas}$ the number of scans in the measurement spectrum and $n_{scan,offset}$ the number of scans in the offset spectrum.

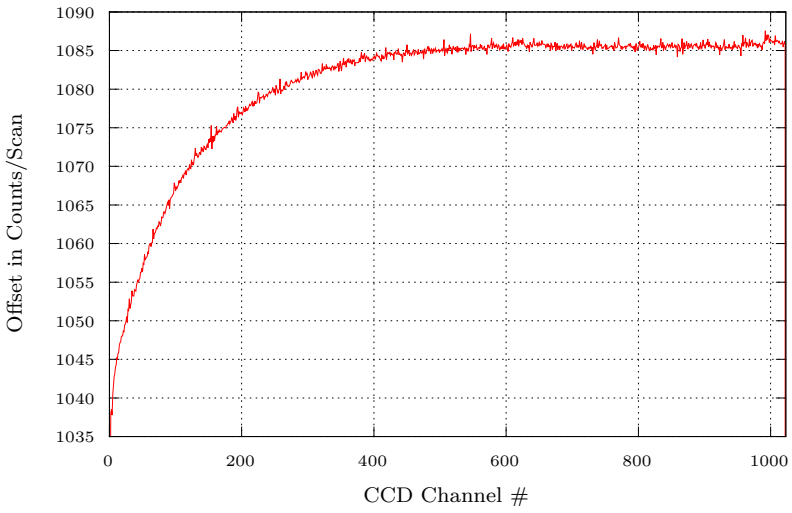

Figure 3.41.: Typical offset spectrum of HAIDI's CCD cameras, recorded with 10 000 scans at an integration time of 10 ms.

The second additional component in the measured signal $S(j)$ is the dark current. Dark current occurs due to the thermal excitation of electrons from the valence to the conduction band. It is therefore proportional to the Boltzmann-factor $e^{-\Delta E/kT}$ and also increases linearly with time. In order to correct for the dark current signal, it has thus to be determined at the same CCD temperature as the measurement spectra were taken at. This is achieved by shielding the CCD from incident light and taking a single scan with a long integration time ($\sim 50\,\%$ of the CCD's full well capacity). A typical dark current spectrum of HAIDI's cameras for a CCD temperature of 0 °C can be found in Fig. 3.42. As can be seen, the average value at this temperature is about 5 Counts/(pixel · s). The typical dark current signal $D(j)$ of the CCD30-11 in the temperature range between 230 K and 300 K is specified by the manufacturer by the following equation (e2v, 2013):

$$D(j) = D_0(j) \cdot 1.14 \cdot 10^6 \cdot T_{CCD}^3 \cdot e^{-9080/T_{CCD}}\,, \tag{3.39}$$

where $D_0(j)$ is the typical dark current signal at 293 K ($1000\,\mathrm{e^-\,pixel^{-1}\,s^{-1}}$) and T_{CCD} the temperature of the CCD. A comparison between the calculated dark current values and actually measured one can be found in Fig. 3.43. The apparent deviation from the calculated values that can be seen in the figure is possibly due to an increasing temperature gradient between the position of the temperature sensor and the position of the CCD for lower temperatures.

When a dark current spectrum $D_{meas}(j)$ is available for the appropriate temperature, the already offset-corrected measurement spectra $I_{corr,offset}(j)$ can be corrected for the dark current signal with the equation below:

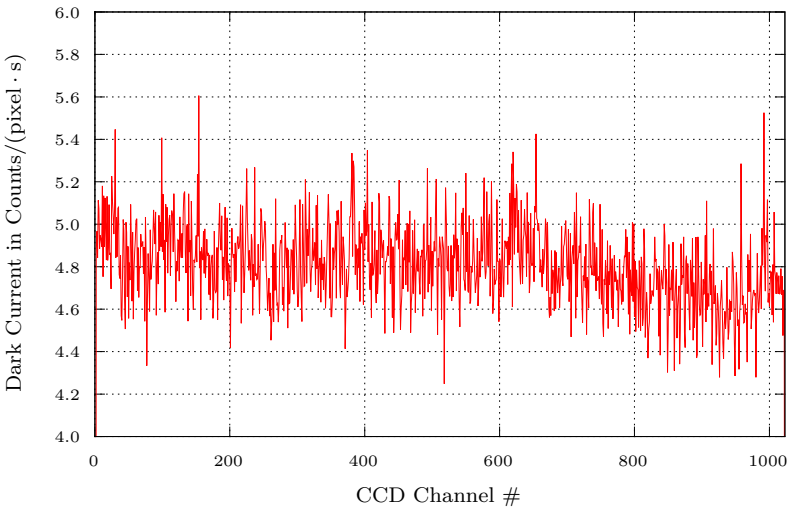

Figure 3.42.: Typical (offset corrected) dark current spectrum of HAIDI's CCD cameras, recorded with an integration time of 20 s and a CCD temperature of 0 °C.

$$I_{corr}(j) = I_{corr,offset}(j) - \frac{t_{int,meas}}{t_{int,dc}} \cdot D(j)\,, \tag{3.40}$$

where $t_{int,meas}$ is the total integration time of the measurement spectrum and $t_{int,dc}$ the integration time of the dark current spectrum. Thereby it has to be ensured, that the measured dark current spectrum first has to be corrected for the offset signal in order to obtain the true dark current spectrum $D(j)$.

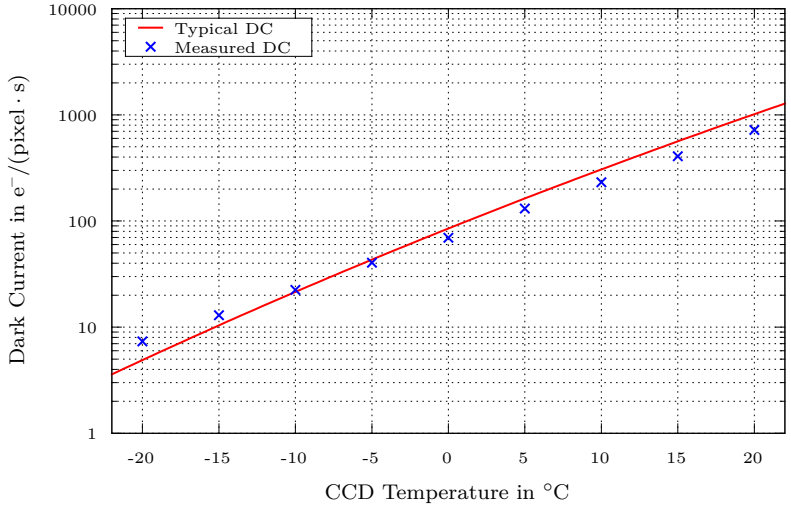

Figure 3.43.: Measured dark current as a function of the CCD temperature. The red curve shows the typical dark current signal, specified by the manufacturer, for comparison.

3.7.2.2. Linearity

An important characteristics of a CCD detector is its linearity in response to incident light. Ideally the signal gained from a pixel (Counts/ms) should be linear with respect to the amount of incident photons over the full intensity range, but normally this is not the case. Instead most detectors show a decreasing sensitivity to incident photons when approaching the full well capacity of the individual pixels. Since nonlinearities in the intensity of recorded spectra can lead to residual structures in the DOAS analysis (Chap. 4) it is mandatory to know the linear range of the used detector.

In order to test the linearity of HAIDI's CCD detectors, a large number of spectra from a temperature stabilized LED were taken with slowly increasing exposure time. In this way the intensity range of the CCD could be sampled with high accuracy. Afterwards the measured counts per millisecond were normalized to the value at 30 000 Counts for each pixel and then plotted versus the corresponding intensity level. Figs. 3.44a and 3.44b show the result of the test for the different readout modes of the detector. As can be seen the response of the detector to incident photons is almost linear in the range between 0 and 40 000 counts (ADC resolution: 16-bit $\Rightarrow$ max. 65 536 Counts). For higher intensity levels the sensitivity to incident photons decreases quickly and should therefore be avoided. Recorded spectra in the range between 0 and 40 000 counts can be corrected subsequently since the linearity in this region can be well described by a second-order polynomial. After linearization with this polynomial, the remaining nonlinearity in the measured counts per millisecond is less than 5×10^{-3} (see Figs. 3.44c to 3.44f).

3.7.2.3. Signal-to-Noise Ratio

The total noise in recorded spectra arises from photon or "shot" noise, optical noise and also instrumental noise. For a good DOAS instrument the photon noise should be the limiting factor in the achievable signal-to-noise ratio. In comparison to the other noise sources, photon noise is purely statistical and can therefore be reduced by accumulating more photons or co-adding multiple scans. The relation between the number of photons n_p and the number of co-added scans n_{scan} is thereby as follows:

$$n_p = n_{scan} \times \frac{S_{counts} \times C_{elec}}{C_{counts} \times \eta_{QE}}\,, \tag{3.41}$$

where S_{counts} is the average signal in counts of the considered spectral region, C_{elec} is the full well capacity of a readout register pixel in electrons (1 000 000 e^-), C_{counts} the corresponding ADC value to C_{elec} (2^{16} = 65 536 counts) and η_{QE} the quantum efficiency of the detector in the considered spectral region ($\sim 60\%$).

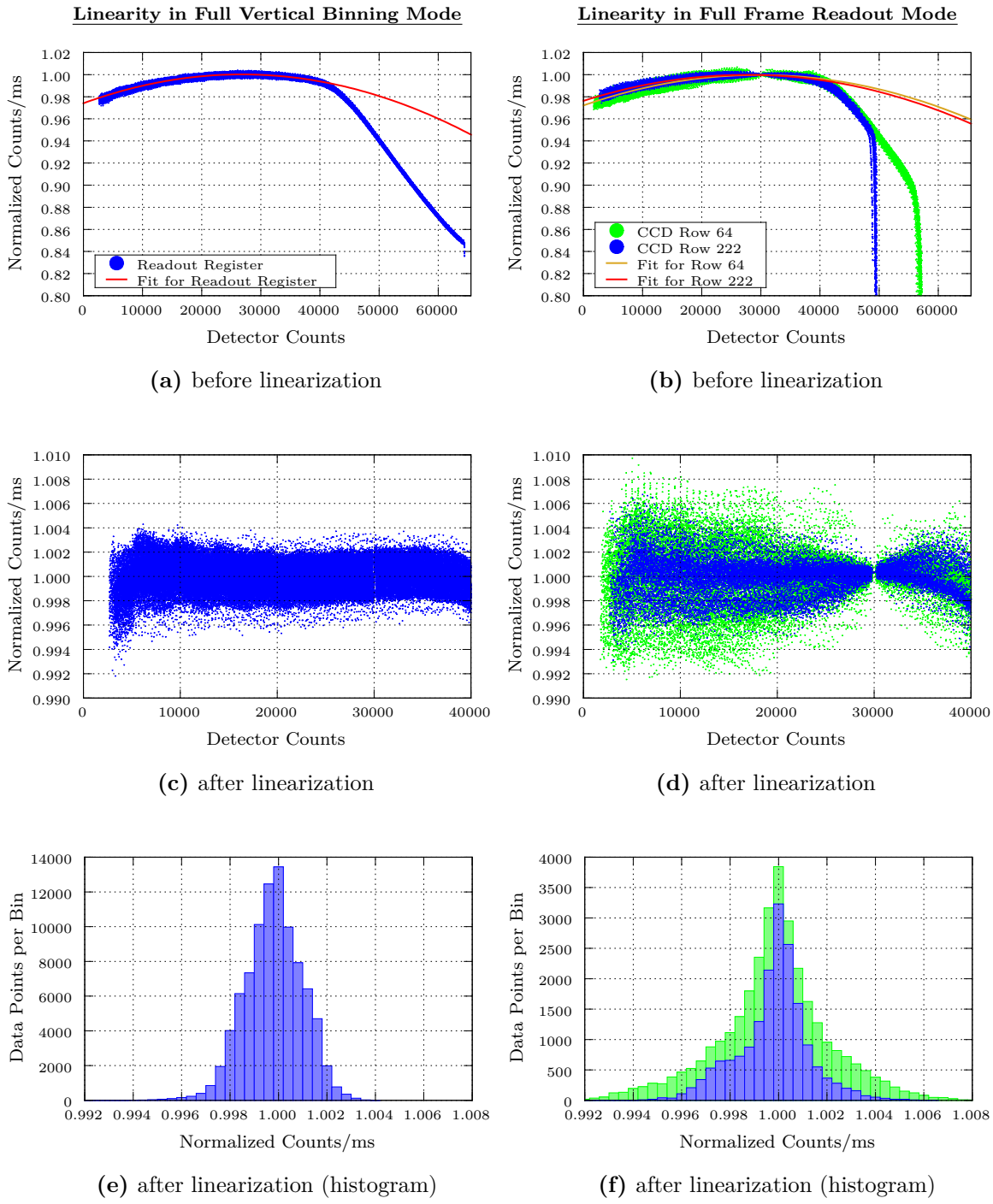

(a) before linearization

(b) before linearization

(c) after linearization

(d) after linearization

(e) after linearization (histogram)

(f) after linearization (histogram)

Figure 3.44.: Results from a linearity test of HAIDI's detectors. The displayed Counts/ms are normalized to a reference value at an intensity level of 30 000 Counts. (a), (b) Measured counts per millisecond in full vertical binning (left) and full frame readout mode (right). (c), (d) Linearity of the analyzed pixel after correction by a second-order polynomial. (e), (f) Histogram of the corrected measurements.

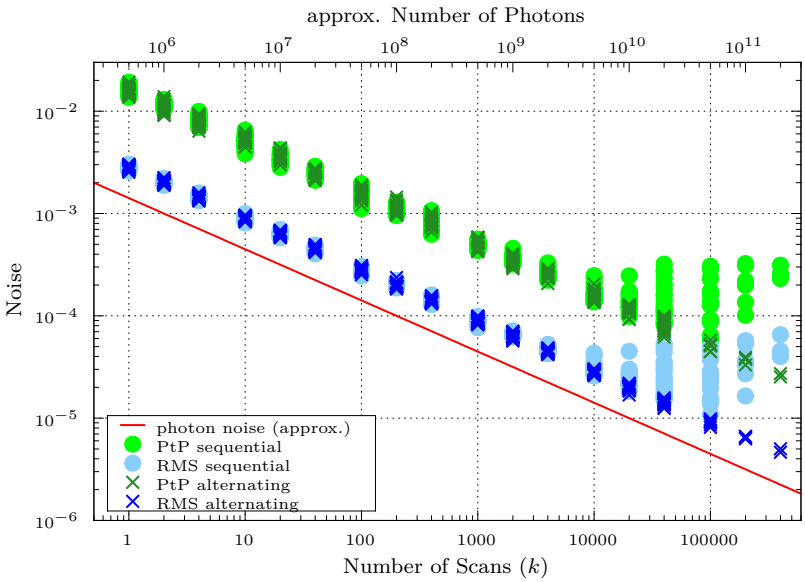

Figure 3.45.: Results from a noise test of the HAIDI system plotted on a double-logarithmic scale. Scans with an integration time of 40 ms were co-added to get a larger number of photons (approximated values). The resulting noise is given as RMS and peak-to-peak (PtP) value. For comparison also the pure photon noise (red curve) is plotted, which is given by the square root of the number of photons and represents the lowest achievable noise. The evaluation of the data was done in the wavelength region between 350 and 400 nm.

Since the detection limit of a DOAS instrument usually depends on the achievable signal-to-noise ratio (see Sec. 4), it is important to know whether and up to what degree the noise in the spectra follows photon statistics. This can be determined by recording a large number of scans of a spectrally stable light source (e. g. halogen lamp) with the instrument. The scans should have the same exposure time and a saturation level which is preferably constant in time and over the considered part of the spectrum. Here we use scans with an integration time of 40 ms each and an average signal of 20 000 counts, which approximately corresponds to 5×10^5 photons for the used detector. In order to access higher photon numbers, the recorded scans are co-added. The noise of two spectra I_1, I_2 with k co-added scans is then calculated as follows:

$$\text{Noise}\,[k] = \left[\ln \frac{I_1}{I_2}\right]_{\text{HPF=1000}}, \tag{3.42}$$

where a binomial high pass filter (HPF) with 1000 iterations is applied to the logarithm in order to remove broadband structures. For co-adding the scans, two different methods are used. In the first one (large dots, labeled “sequential” in Fig. 3.45), the number of photons in the spectra is increased by adding consecutive recorded scans S_n:

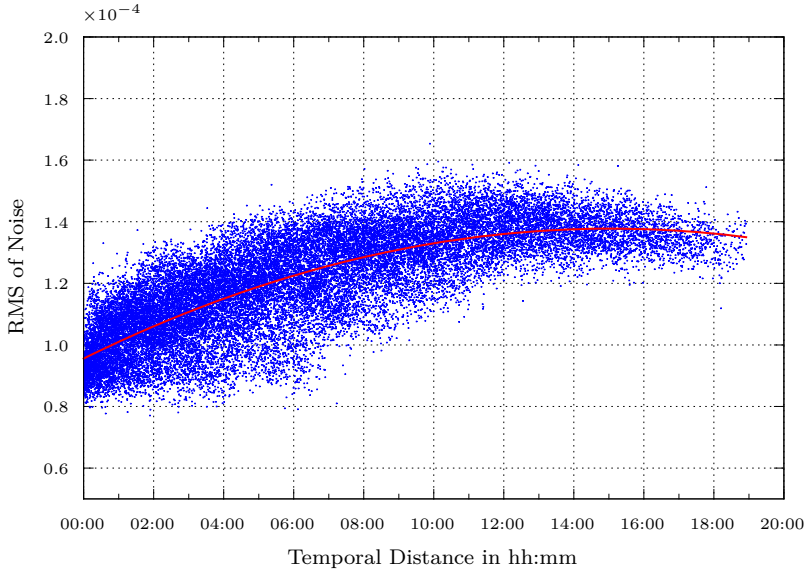

Figure 3.46.: Development of the noise for spectra with 1000 co-added scans and increasing temporal distance. Within a few hours, a slight increase in noise could be observed. Since photon noise does not change with time, the increase must have its origin in a changed instrument noise. The red line shows a polynomial fit of second order.

$$I_1 = \sum_{n=1}^{k} S_n \,, \qquad I_2 = \sum_{n=1}^{k} S_{k+n} \tag{3.43}$$

As can be seen in Fig. 3.45, the root mean square (RMS) of the noise scales with photon statistics $1/\sqrt{N}$ (red curve) first in this case, where N is the number of incident photons. Starting at about 10 000 scans or 5×10^9 photons, other noise sources (e. g. instrument noise) become dominant and the noise in the spectra can not be decreased any further. In this method, however, time-dependent effects play an important role. Since the spectra I_1 and I_2 consist of k sequentially co-added scans, the time interval between the spectra equals the time to take k scans, which is about 6.7 min (400 s) for $k = 10\,000$ and 4.4 h (16 000 s) for $k = 400\,000$. Within this time, the instrument properties can slightly change due to e. g. temperature changes. This effect can also be seen in Fig. 3.46, which shows the development of the noise with increasing temporal distance between spectra with $k = 1000$.

In the second method, the recorded scans are co-added in a different way to minimize time-dependent effects. Here, one spectrum consists of odd scans, while the other one encompasses the even scans:

$$I_1 = \sum_{n=1}^{k} S_{2n} \,, \qquad I_2 = \sum_{n=1}^{k} S_{2n-1} \,. \tag{3.44}$$

As a consequence, the average time difference between the two spectra is reduced to the time needed to record a single scan (40 ms) and temporal changes in optical or instrument noise (e. g. small changes in the halogen spectrum or a shift of superimposed odd-even structures) are almost completely canceled out. What remains is mainly the photon noise. For this reason, the noise becomes much smaller at large numbers of co-added scans with this method and still follows photon statistics up to the max. measured amount of 400 000 scans or 2×10^{11} photons (see Fig. 3.45: small crosses, labeled "alternating").

3.8. Fiber Optics

Due to the reasons discussed in Sec. 3.4 the entrance optics of the HAIDI system is separated from the rest of the instrument. Hence, the received light from the telescopes is transmitted via a system of optical fibers to the spectrographs. Optical fibers are typically made of an optically transparent core which is covered by a cladding and an additional buffer coating to protect the fiber. Core and cladding thereby have a slightly different index of refraction, where the refractive index of the cladding is always lower than the one of the core. When light is coupled into the fiber core by one of the telescopes it is first refracted at the interface between the surrounding medium and the core material (see Fig. 3.47). Afterwards it encounters the core-cladding interface. Is the light's angle of incident larger than the critical angle θ_c, total internal reflection occurs and the light propagates trough the fiber in a zig-zag-pattern[5]. Because of the interference of multiple reflected light only certain of these propagation paths are allowed in a fiber. Fibers allowing more than one propagation path or traverse mode are called multi-mode fibers (MMF). The critical angle θ_c for the core-cladding interface of optical fibers is generally given by Snell's law:

$$\frac{\sin \theta_c}{\sin 90°} = \frac{n_2}{n_1}\,, \tag{3.45}$$

where n_1 is the refractive index of the fiber core and n_2 is the refractive index of the cladding. The corresponding angle between optical axis of the fiber and incident light is called its acceptance angle α. For angles larger than α no total internal reflection arises and the light is coupled out of the fiber. The sine of the acceptance angle α is defined as the numerical aperture NA of the fiber. For $n_0 = n_{air} \approx 1$ the numerical aperture is given by the following equation (Brückner, 2003):

$$\mathrm{NA} = \sin \alpha = \sqrt{{n_1}^2 - {n_2}^2} \tag{3.46}$$

The used fibers have a NA of 0.22 according to an acceptance angle α of 12.7°. These values fit very well to the ones from the spectrograph (see Tab. 3.9) because they are only marginally

[5] Gradient-index fibers will show a rather sinusoidal pattern instead.

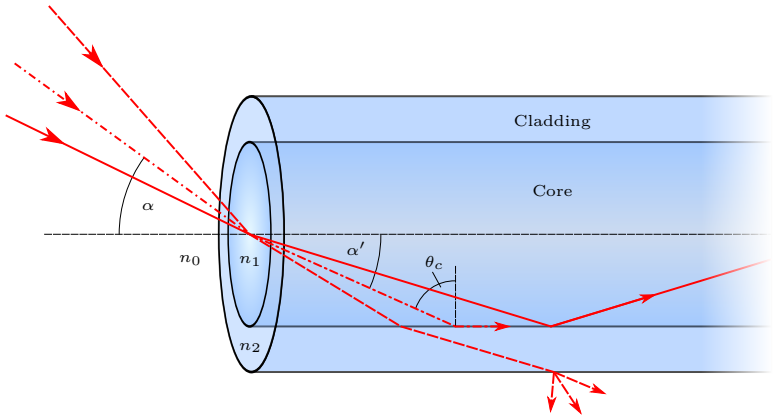

Figure 3.47.: Light propagation in optical multi-mode fibers. The entrance angle of the incident light must not exceed a certain angle α in order to fulfill the condition for total internal reflection. Only light that falls within this acceptance cone will be guided through the fiber.

higher. The next lower NA which was available for optical multi-mode fibers was 0.11 which would illuminate only a fraction of the spectrograph's grating and would also require to use much larger telescopes in order to achieve the same light gathering capability. Additionally, these fibers are very sensitive to bending and therefore not practical. Thus, to avoid stray light, the NA of the fibers is slightly reduced to match the one of the grating by an additional aperture in the inside of the spectrograph (see Sec. 3.6).

Table 3.9.: Light collecting characteristics of the individual optical elements used by the HAIDI system.

	Lenses	Fibers	Spectrograph
Angular Aperture (2α)	29.1	25.4	18.4
Numerical Aperture	0.25	0.22	0.16
F-Number	2.0	-	3.2

3.8.0.4. Fiber Setup

Due to their functional principle, whiskbroom and pushbroom scanning techniques have very different requirements regarding the setup of the individual optical fibers. For this reason each scanner type of the HAIDI system uses its own fiber optical system. The actual setup of these fiber optical systems is shown in Fig. 3.48. As can be seen here the nadir scanner uses a combination of fiber bundle and mono fiber which are connected over a F-SMA coupling. At the spectrograph side the fiber bundle has a cross-section converter where the fibers are arranged to a column, acting directly as the entrance slit of the spectrograph. An additional slit-shaped aperture in front of the fibers was omitted here to prevent misalignment and to maximize the light throughput. On the other side the bundle features a standard F-SMA (SMA 905) fiber

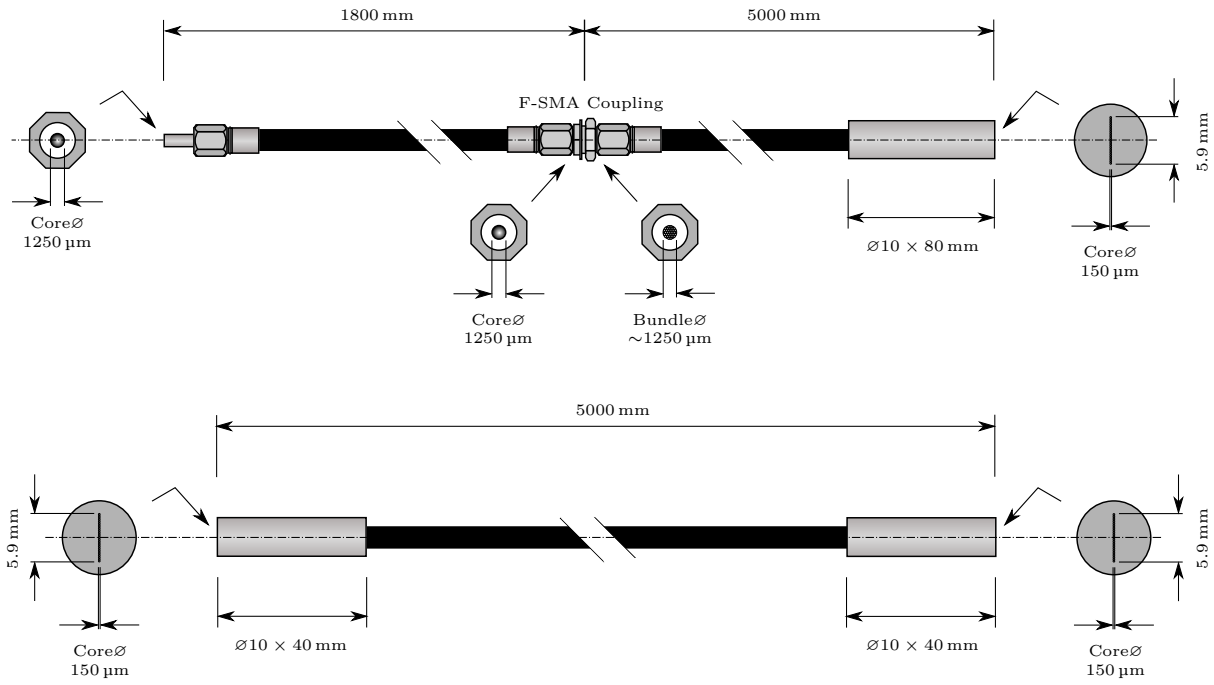

Figure 3.48.: Configuration of the different fiber optic cables with the spectrograph end on the right-hand side. The fiber optics for the nadir scanner is shown in the upper figure while the bottom one shows the bundle used for the forward-looking telescope. The metallic sheath of the nadir scanner's mono fiber is interrupted at one point, which allows to apply physical stress directly to the fiber for mode mixing.

optic connector and the fibers are arranged to a circular bundle with maximum density. In this way the attached mono fiber can have the smallest possible diameter which is beneficial for the thus resulting minimum bending radius (see Sec. 3.8.0.5).

The mono fiber is connected upstream to the bundle in order to mix the incident light from the nadir scanner, so that the fiber column at the spectrograph side is illuminated very homogeneously during measurements. This is necessary because the instruments slit function is not constant over the height of the detector and a varying weighting of individual detector parts due to a inhomogeneous illumination of the slit will therefore cause changes in the overall instrumental slit function (Stutz, 1996). This in turn will result in spectral structures in the residuum of the DOAS analysis when comparing the Fraunhofer reference spectrum to a measurement spectrum (Chap. 4). Mixing of the incident light here means the equal distribution of power to all guided modes of the fiber. This is also called mode mixing. Mode mixing can be achieved by applying physical stress to the fiber, i. e. by bending the fiber with small radii. This changes the lights angle of incident relative to the fiber-cladding interface and therefore leads to a distribution of power among neighboring modes. As a result the fiber output becomes illuminated more homogeneous (Marcuse, 1973).

The fiber bundle used by the forward-looking telescope is also shown in Fig. 3.48. Basically it is similar to the bundle of the nadir scanner. It has the same length of 5 m and uses fibers of

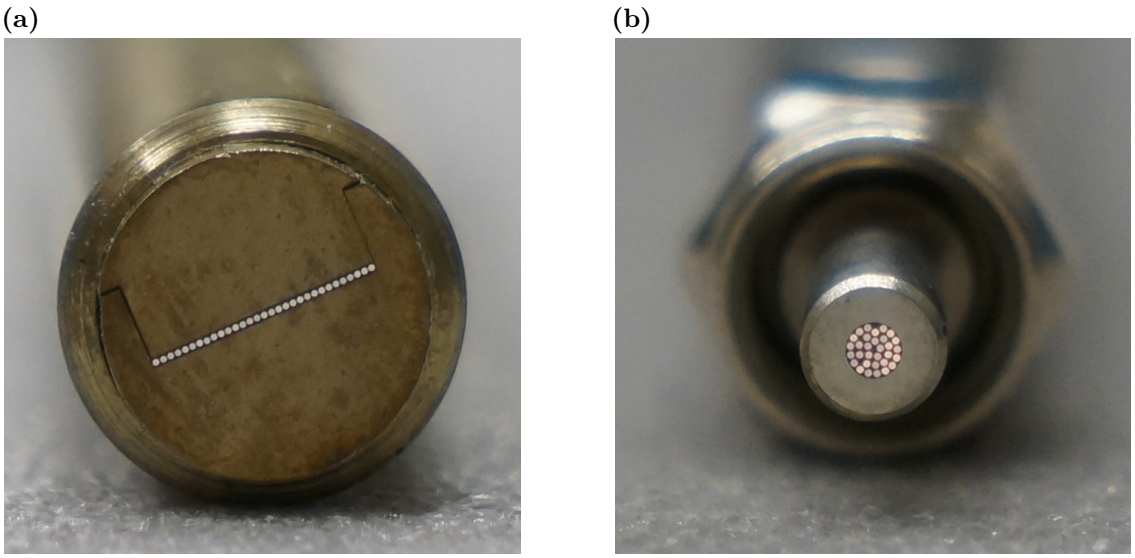

Figure 3.49.: Different fiber alignments in the HAIDI fiber optics: (a) For the nadir scanner a bundle of 31 fibers is arranged to a column at the spectrograph end, forming its entrance slit. The forward-looking telescope uses a fiber column at both ends of the fiber optics to transmit spacial information. (b) At the interface to the mono fiber of the nadir scanner the fibers of the bundle are arranged in a circle.

equal quantity and with the same NA and core diameter. However, there are two important differences between the two bundles. The bundle for the forward-looking telescope has cross-section converters on both of its ends. These cross-section converters are identical to the one of the nadir scanner bundle and feature also the same fiber column. Only the configuration of the fibers within the column plays a more important role here. Because spatial information has to be preserved for the forward-looking telescope, the fibers have an identical order at both ends. Thus, the fiber column at the spectrograph side gives an accurate image of the column at the telescope side.

All fibers used by the HAIDI system are fabricated of fused silica to minimize the extinction in the UV wavelength region. The manufacturer (FiberTech, Germany) specifies the internal transmissivity of a quartz fiber with 5 m length to 80–90 %, for wavelengths between 300 and 400 nm (LEONI, 2013). The configuration of the optical fibers was done by Loptek, Germany. For their protection all fibers are covered by a corrugated steel mantle and the fiber bundles also have an additional PE coating.

3.8.0.5. Fiber Diameter

The spectral resolution of a spectrograph depends on the spectral width of the instrument function (see Chap. 3.6.2.2). This is usually not limited by the theoretical resolving power of the diffraction grating but rather by optical aberration effects and especially by the dimensions of the used entrance slit (Palmer and Loewen, 2005). As HAIDI's spectrographs have a 1:1

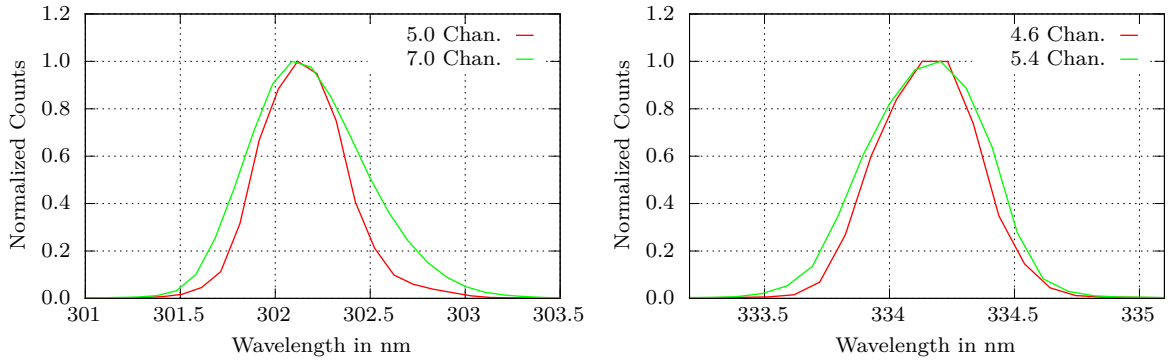

Figure 3.50.: Comparison of mercury emission lines for different fiber diameters. The spectrum of the fiber with 150 µm core diameter is shown in red while green represents the fiber with 200 µm core diameter. The dispersion of the spectrograph is about 0.10 nm/pixel and the FWHM of the peaks is given in the key of the graphs. As can be seen, the fiber with 150 µm core diameter offers a better resolution and the peaks are still resolved by an adequate number of CCD channels.

magnification from the entrance slit plane to the focal plane of the grating, the instrument function should have a width (FWHM) that approximately matches the width of the slit. Since the spectrographs of the HAIDI system do not have an additional slit in front of the fiber column it is therefore very important to choose a suitable fiber diameter. A smaller slit width or fiber diameter will basically result in a better spectral resolution of the spectrograph but the slit width cannot be reduced at will. On the one hand the light throughput of the system decreases when reducing the slit width and on the other hand the detector attached to the spectrograph must still be able to resolve the instrument function by an adequate number of pixel to avoid undersampling. According to the Nyquist-Shannon sampling theorem the FWHM of the instrument function should extend to a minimum of two detector channels (pixels). However, practical experiences and numerical modeling have shown that the spectral width of a detector pixel should be about 10–20 % of the instrument function's FWHM (Hofmann et al., 1995; Stutz and Platt, 1996; Roscoe et al., 1996; Platt et al., 1997). Thus, the instrument function should have a width of 5–10 detector channels.

In order to find the best fiber diameter for the fiber optics of the HAIDI system already in advance, a UFS 200 spectrograph from Jobin Yvon in combination with a DV420-BU detector from Andor Technology was used with fibers of different core diameter at the spectrograph's entrance. The UFS 200 spectrograph features the same grating that was later used for the imaging spectrographs of the HAIDI system and the DU420 detector has a chip with the same dimensions and pixel size like the CCD30-11 from e2v. Thus, the resulting instrument function as well as the spectral width of a detector pixel were representative for the final instrument. The result is displayed in Fig. 3.50, it shows two mercury emission lines taken with a 150 and a 200 µm fiber. As can be seen, the width of the instrument function is already at the lower end of the required number of pixel when using the 150 µm fiber. Therefore, this is the optimum

core diameter for a detector with 26 µm pixel size and a further decreasing will only be on the expense of light throughput. However also the fiber with 200 µm core diameter still yields an acceptable spectral resolution, but the core diameter is not the only aspect that has to be considered.

3.8.0.6. Number of Fibers

Another important point is the the fill factor of the fiber bundle. The fill factor is the ratio between the front surface of the bundle and the total area of the individual fiber cores in the bundle. This should be maximized to achieve a preferably high light throughput between fiber bundle and mono fiber.

The 150 µm fibers have an overall diameter of 190 µm including cladding and coating while the 200 µm fibers have an overall diameter of 245 µm. Therefore either 27 fibers with 200 µm core diameter or 35 fibers with 150 µm core diameter were needed to take advantage of the full CCD detector height (6.7 mm). By looking at the typical arrangement scheme of a fiber bundle in Fig. 3.51 one can see that 27 is a unfavorable number of fibers because three circles are required without using their full capacity. The number of used circles defines the resulting diameter of the bundle, thus 27 fibers with an outer diameter of 245 µm will result in a bundle of approximately 1700 µm diameter. Comparison of the fiber cores overall surface area with the one of the bundle leads to a fill factor of only 37 % for this setup. The usage of 150 µm fibers instead yields a bundle diameter of about 1300 µm and a fill factor of 47 %. So the setup with 150 µm fibers has a better fill factor and results in a smaller bundle diameter. The latter one is from interest because of the mono fiber that is connected to the bundle. To maximize the light throughput between both parts of the fiber optics, fiber bundle and mono fiber should have preferably the same diameter. Available mono fiber core diameters matching to this bundles were 1680 µm and 1250 µm. Also here the 150 µm fibers are advantageous because a smaller mono fiber diameter means more flexibility and higher flexibility simplifies the installation of the system. The minimum bend diameter $d_{\min}$ of a single fiber is given by the following rule of thumb:

$$d_{\min} = 600 \times d_{fiber}\,, \tag{3.47}$$

where d_{fiber} is the diameter of the fiber including cladding. The 1250 µm fiber has a diameter of 1325 µm with cladding while the 1680 µm fiber measures 1765 µm. The resulting minimum bend diameter were $d_{\min,\,1325} = 795$ mm and $d_{\min,\,1765} = 1059$ mm, respectively. For these reasons the smaller fibers with 150 µm core diameter were chosen. Since 35 fibers do not exactly fit into a diameter of 1250 µm the number of fibers was slightly reduced to 31 by omitting the 6 fibers in the corners of the outermost circle. So the final fill factor of the bundle is about 45 %.

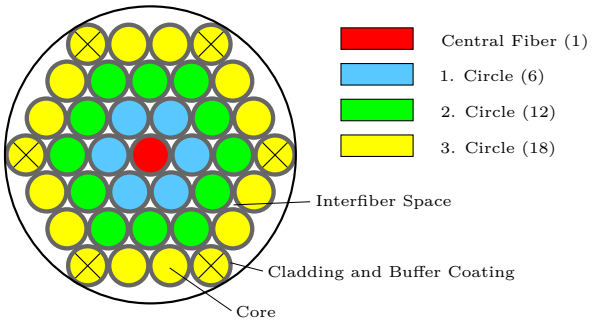

Figure 3.51.: Typical arrangement of optical fibers in a fiber bundle. Hexagonal packing minimizes the dead area between individual fibers for smaller bundles. The crossed fibers are omitted in the bundle in order to match the diameter of the mono fiber.

3.9. Instrument Rack

During measurements, the spectrographs and CCD cameras are typically stored in the instrument rack of the HAIDI system (Fig. 3.52). The instrument rack bases on a custom-built 19-inch subrack from Schroff (Karlsruhe, Germany), with a special length of 500 mm and no ventilation slots in the base for better thermal and electromagnetic insulation. It has a total height of 6 rack units (U), so the overall dimensions of the rack are $19 \times 20 \times 10.5$ in. These dimensions allow to mount up to three spectrographs with detectors lengthwise in the housing. Due to the strong forces that can act on the equipment during flight, the instrument rack was modified by our workshop with spectrograph mountings that withstands load factors of at least 9 times the acceleration due to gravity g_0. The metal struts holding the spectrographs in place can be seen in Fig. 3.52b. In addition the instrument rack features a temperature stabilized section for the spectrographs to avoid wavelength shifts due to thermal expansion.

3.9.1. Temperature Stabilization

The temperature stabilization in the instrument rack is realized by an Air-to-Air Peltier system which is intended to regulate the internal temperature to a value close to ambient temperature. In principle, the system consists of a Peltier element (PE-127-14-11-S from Supercool) with heatsinks and centrifugal fans on both sides. The inside of the temperature stabilized volume is lined with a 10 mm layer of PE-foam (MP15FR from Wulfmeyer) for thermal insulation and includes only the spectrographs and no heat producing electronics. For these reasons, the temperature stabilization can usually work with low power consumption (< 10 W). Due to the high thermal capacity of the aluminum spectrographs (≈ 2.7 kJ/K per spectrograph) it takes some time to adapt the spectrograph temperature to the air temperature inside the rack (about 1 hour for a temperature difference of 5 K) but this makes the temperature stabilization also relatively immune to short interruptions in the power supply at the same time.

The temperature stabilization for the spectrographs is controlled by an Arduino Duemilanove

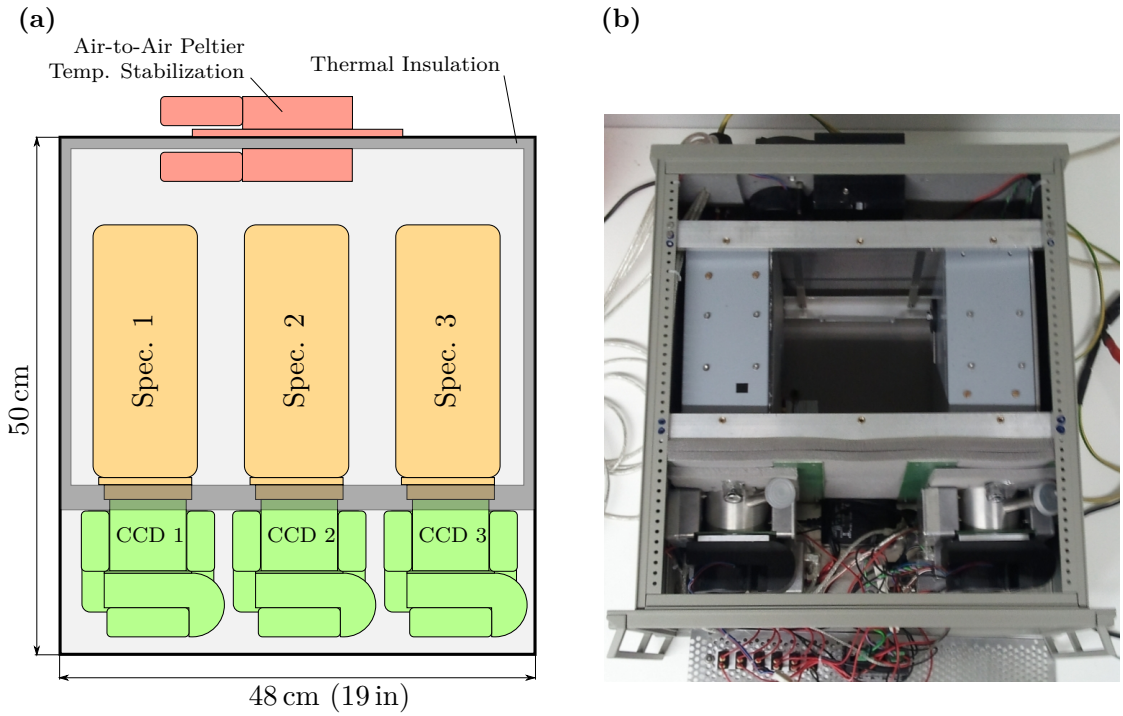

Figure 3.52.: Instrument Rack of the HAIDI system: (a) Schematic illustration of the rack showing the locations of spectrographs and CCD cameras in the inside. The Air-to-Air Peltier temperature stabilization on the rear side of the rack controls the temperature in the gray shaded section. Since the CCD cameras have a separate cooling for the detector, which produces lots of heat, they are located outside the temperature stabilized section. (b) Photo of the rack with two installed spectrographs and CCD cameras.

board plus H-bridge. Because the H-bridge can get quite warm, Arduino and H-bridge are located in a small aluminum box in the forward section of the rack where also the detectors are and is connected to four temperature sensors (ADT7410 from Analog Devices) in the stabilized section via Inter-Integrated Circuit (I^2C). Three of these sensors measure the temperature of a spectrograph housings while the fourth one measures the air temperature in the stabilized section. The air temperature is taken as input parameter for the PID control running on the Arduino. The H-bridge then regulates the power and polarity of the Peltier element according to a PWM signal from the Arduino. While the H-bridge is directly connected to the 12 VDC supply, the Arduino board itself is powered over USB.

Also located in the forward section of the rack is the controller (Eliwell IC 901) for the heating of the entrance optics (Fig. 3.53). The heating (Cirrus 40/1 60 W) features two self-regulating PTC elements with a heating capacity of 30 W each. The current version of the instrument rack has two switches on the front panel to separately turn the PTC elements on or off. In this way, the maximum heating capacity can be adapted to the current requirements. Also the temperature setpoint for the heating can be entered via control keys on the front panel

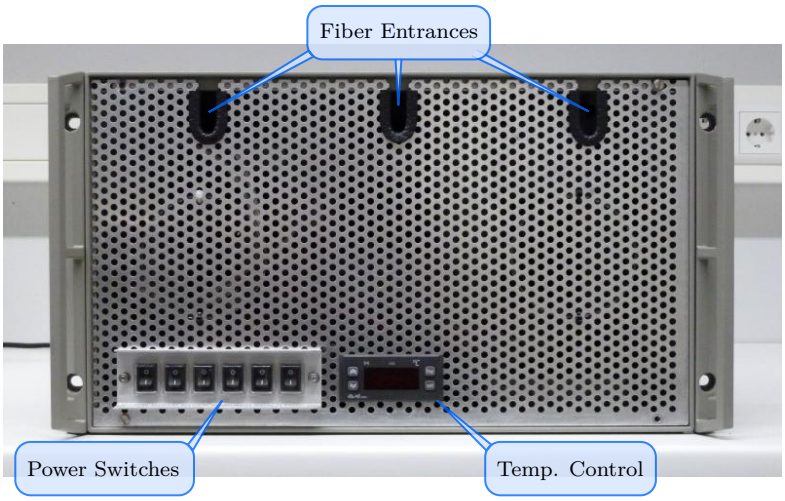

Figure 3.53.: Front view of HAIDI's instrument rack. In addition to the fibber entrances the front panel of the rack also includes some power switches to turn the different devices of the system on or off and the temperature control for the heating of the entrance optics. The air grille ensures that the heat produced by the cooling of the CCD detectors can get outside. At the same time it blocks electromagnetic fields generated by the internal electronics.

of the instrument rack. The temperature at the entrance optics is measured by a NTC-probe. When its value falls below the setpoint, the heating turns on. It then keeps heating until the temperature exceeds the setpoint by a given value (hysteresis) that can also be specified. The fan of the heating is powered independently from the PTC elements and runs continuously to ensure a uniform temperature distribution at the entrance optics.

3.9.2. Power Supply

The instrument rack provides power connections for all devices of the HAIDI system (Fig. 3.56). For this purpose, the rack itself has a power connector (Neutrik PowerCON NAC3MP-HC) on the rear side (Fig. 3.54). This socket has to be connected to a 12 VDC power supply since most of the devices work at this voltage. The 12 VDC is also looped through to three 3-pin DIN sockets at the rear side of the rack, which are used to supply the power adapters of the netbooks. Three additional 7-pin DIN sockets on the rear side of the rack supply external devices like the heating and servo motors with power and also transmit the signals used for servo motion and temperature control (Fig. 3.56). Because the servo motors are not designed to operate at a voltage of 12 VDC, there is also a box with three small DC-to-DC converters mounted in the forward section of the rack. These converters transform the 12 VDC, which is available throughout the instrument rack, to 6 VDC.

For security reasons, all electronic devices of the HAIDI system can be tuned on or off individually by switches on the front panel of the instrument rack. Furthermore, each device features a resettable fuse. The instrument rack's main fuse (20 A) is not resettable and only accessible from the rear side to avoid an accidentally restart of the system after failure.

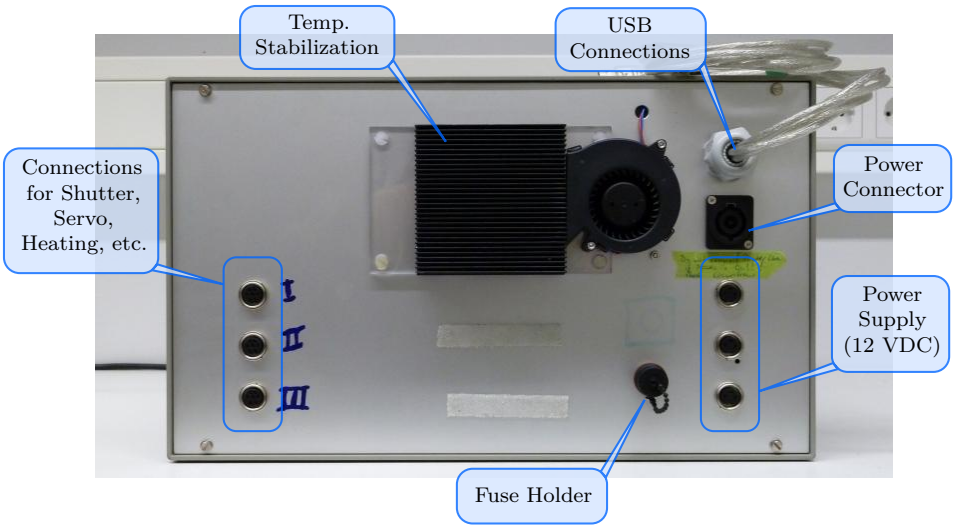

Figure 3.54.: Rear view of HAIDI's instrument rack. On the back side of the rack is the heatsink from the spectrograph temperature stabilization and a centrifugal fan for forced convection. Also several connections are located here, the USB cables for the communication with the CCD cameras and the spectrograph temperature stabilization, the DIN connectors which provide 12 VDC for the netbooks, the DIN connectors for external devices like heating or servos and the power connector of the rack. In addition the instruments main fuse is accessible from here.

3.10. Rack Drawers

Each scanner of the HAIDI system uses a separate computer for data acquisition and system control. These computers are netbooks (Asus Eee PC R051PX) with an Intel Atom N570 dual-core CPU (Pineview) and 2 GB of RAM. The netbooks have a low power consumption, what is particularly advantageous when no external power supply is available (e. g. in ultralight aircraft). To make the netbooks accessible during the flight, they can be stored in a separate subrack with a total height of 2.5U (Fig. 3.55). The subrack is equipped with two 19 in rack drawers (Adam Hall 87556), which have a height of 1U and a usable area of 412×380 mm.

Each drawer is equipped with mountings for the netbooks and also with a lock on the front side, so that the drawers can not accidentally open in flight. For operation on HALO the subrack also contains a DC-to-DC converter (Mean Well SD350B-12) that transforms the 28 VDC from HALO's Secondary Power supply (see Sec. 3.11.3.3) to 12 VDC for the instrument rack. On the input side the converter uses a MS 3459 W16-11S connector that complies with military standard MIL-DTL-5015. This plug is required in order to connect the instrument to HALO's electrical power systems. On the output side is a Neutrik PowerCON NAC3FC-HC connector that can be plugged in at the instrument racks rear side. Furthermore three power adapters for the netbooks are housed in the subrack. These power adapters are not directly connected to the main DC-to-DC converter to make the system independent from the 28 VDC power supply. In this way the 28 VDC power connection of the subrack remains optional and the whole system can still be operated by a 12 VDC power supply plugged directly to the instrument rack.

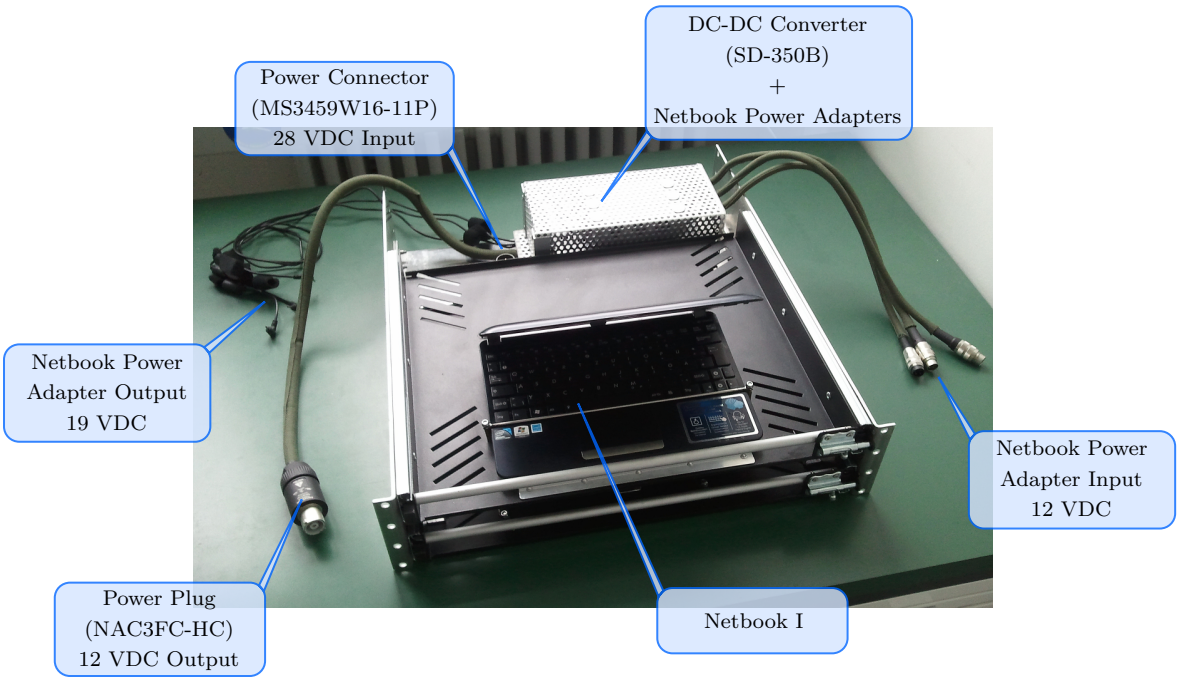

Figure 3.55.: Subrack with drawers and DC-to-DC converters for operation on HALO. The subrack is used to store up to three netbooks, which control the HAIDI system. Because there is no 12 VDC power supply available on HALO the converter is used to provide the operating voltage for the instrument rack. Netbook II and III are located on the lower drawer, rotated by 90° to fit on the tray.

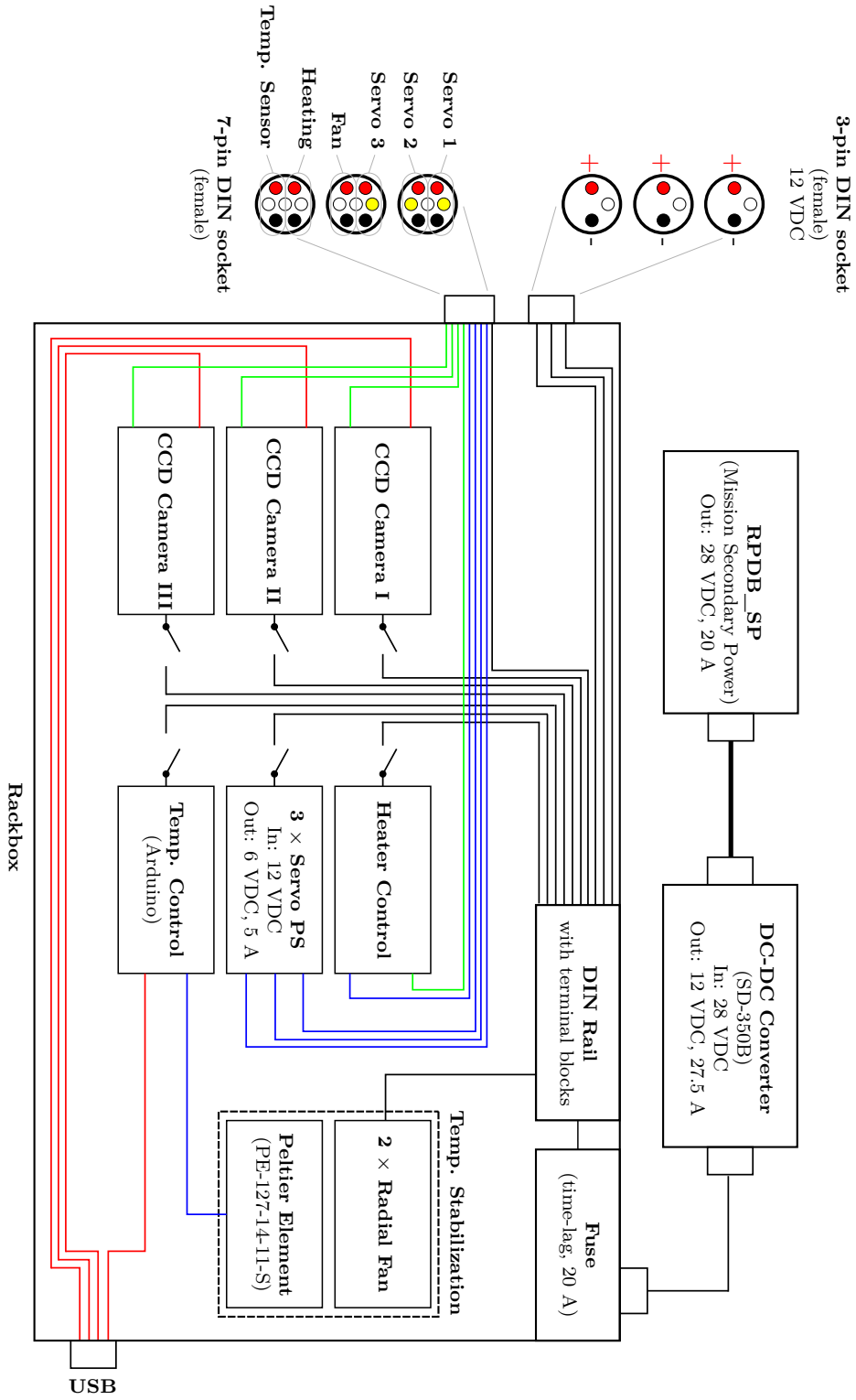

Figure 3.56.: Block wiring diagram of the equipment inside the HAIDI instrument rack. Black lines represent the power supply, red lines the USB connections and green are signal lines. The configuration of the six DIN sockets on the rear side of the instrument rack is also shown.

3.11. Installation on Aircraft

The HAIDI system was developed in the context of the DFG research project SPP-1294 (DFG PF-384 7/1 and 7/2), primarily for operation on the new German research aircraft HALO (High Altitude and Long Range Research Aircraft). For these measurements, an instrumental setup with three nadir scanners (Sec. 3.4) pointed to different directions will be used. This special viewing geometry is optimized for high altitude flights but requires an optical viewport with at least 12 cm diameter (see Sec. 3.11.3.4) in the fuselage of the aircraft. However, HAIDI is also intended to be operated on smaller aircraft. Measurement flights on such smaller aircraft were used in particular to optimize the system in preparation of the installation on HALO. These aircraft fly at lower altitude and usually do not offer sufficient space and power to operate three nadir scanners simultaneously. Furthermore a setup with three nadir scanners will not allow to retrieve accurate altitude information of absorbers when flying too low. For these reasons the instrumental setup was modified in such a way that it requires less space and power, but still provides the possibility to retrieve horizontal distributions and vertical profiles. This altered setup uses only a single nadir scanner in downward direction and in addition a forward-looking telescope, working on the basis of the pushbroom technique (Sec. 3.5). As a consequence of this approach, the necessary nadir viewport diameter could be reduced by more than a factor of 2. Since also the forward-looking telescope needs only a very small aperture in forward direction, the entrance optics of the alternative setup can be placed completely in a small external housing. In the following the particular instrumental setups used for the different aircraft are described.

3.11.1. Instrumental Setup for Flight Design CTLS ultralight

The first platform on which the HAIDI system was installed, was a small ultralight aircraft (Flight Design CTLS) operated by the FH Düsseldorf. This setup was used for a campaign on Sicily (Italy) in July 2011 (see Sec. 5.1). Because of the compactness and weight limitations of such an aircraft there was only very limited storage space available. Hence, the entire system had to be installed into the baggage compartment in the rear part of the aircraft. The baggage compartment had only a cross-section area of about 35×50 cm at the widest point and a depth of approximately 90 cm (Fig. 3.57). Therefore, neither the instrument rack of the HAIDI system nor the rack drawers could be used here and several adaptations had to be made to the original instrumental setup. As previously mentioned, one approach to this was the alternative setup with only one nadir scanner in downward direction and one forward-looking telescope. Furthermore, a kind of mini-rack was constructed that was directly screwed to the spectrographs and the temperature stabilization. The thermal insulation of the mini-rack was realized with a layer of PE-foam (MP15FR from Wulfmeyer).

Because of the forward-looking viewing direction and the lack of optical viewports on the ultralight aircraft, HAIDI's entrance optics had to be placed somewhere outside. For this purpose, a steel frame construction, which held a carbon fiber tube of 20 mm diameter (pullwinded for

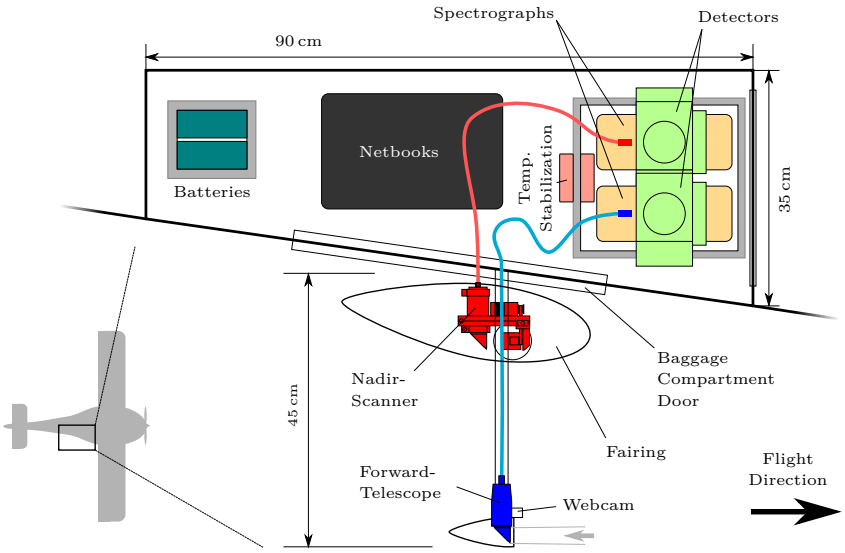

Figure 3.57.: Top view sketch of the CTLS baggage compartment with installed HAIDI system. The entrance optics of the instrument are located outside the aircraft. While the nadir scanner (red) is placed close to the aircraft fuselage, the forward-looking telescope (blue) is mounted to an extension arm in order to get a free line of sight past the propeller of the aircraft.

better flexural and torsional strength), was mounted inside the aircraft's baggage compartment. The tube went through a hole in the baggage compartment door on the starboard side (see Fig. 3.58) and protruded about 45 cm from the aircraft fuselage. The forward-looking telescope and a webcam (resolution of 640×480 pixel) were attached at the end of that tube in order to get a clear line of sight, past the propeller. The nadir scanner instead was located close to the aircraft fuselage in an aerodynamic housing, to keep the load on the carbon tube as small as possible. Due to the short distance between the spectrographs and the entrance optics of the nadir scanner, the standard mono fiber with a length of 1.8 m could not be used here because of its large minimum bending radius. Instead, a fiber with the same core diameter but a length of only 19 cm was applied. The mechanical shutter (UNIBLITZ VS25) for the forward-looking telescope was located at the entrance of one of the spectrographs, in oder to reduce the amount of components outside the aircraft to a minimum. Unfortunately, the construction proved to be unreliable, causing the forward-looking system to fail during the entire campaign.

Beside the spectrographs and detectors, also two netbooks and a Li-Po battery pack (20 A h, 14.8 V) were placed in the baggage compartment of the aircraft. While the netbooks were intended to store the data from the CCD cameras and the webcam, the battery pack had to supply the system with power, since the on-board power supply of the ultralight aircraft was insufficient to operate the whole instrument. The average power consumption of the HAIDI system in this configuration is around 100 W at an operating voltage of 12 V. Thus, the batteries could power the system for about two hours when fully charged. The netbooks did not need an additional power supply, as they can run on their own battery for approximately four hours.

Figure 3.58.: Installation of the HAIDI system on board of an ultralight aircraft (Flight Design CTLS) during the measurements on Sicily, Italy. Spectrographs, CCD cameras, netbooks and a battery pack were stored inside the baggage compartment (picture on the right) while the entrance optics is mounted outside the aircraft at a carbon fiber extension arm (left picture).

3.11.2. Instrumental Setup for Beechcraft Model 76 Duchess (ALAR)

Only a few months after the campaign in Italy the HAIDI system was successfully installed to a second platform. This was the Airborne Laboratory for Atmospheric Research (ALAR), which is a twin-engined research aircraft operated by the Purdue University. The setup was used for two measurement campaigns in October 2011 (Sec. 5.2) and March 2012 (Sec. 5.3), respectively.

ALAR is a modified Beechcraft Model 76 Duchess with a normal capacity of one pilot and three passengers. The two rear seats were removed, however, in order to create sufficient space for a 19-inch rack that can be used for the installation of scientific equipment like HAIDI's instrument rack (Sec. 3.9). All instrumentation in the rack was connected to the on-board power supply of the aircraft, which directly offers 12 VDC and a back-up battery ($\sim 10\,\mathrm{A\,h}$) for short interruptions in the alternator power supply. For longer periods of time without running engines, the aircraft was connected to an external power supply. While the spectrographs and CCD cameras could be installed into the instrument rack inside the aircraft, the entrance optics had to be placed somewhere outside also in this case. Thus, an external housing for the entrance optics was constructed, based on a Bopla diecast aluminum box (A 127 SIL) having the dimensions of $18 \times 18 \times 10\,\mathrm{cm}$. The box was mounted below the aircraft, on the left hand side of the lower shell (Fig. 3.60). This location was chosen, because it was close to the position of the instrument rack and at the same time as far away as possible from the exhaust pipes of the aircraft, whose emissions could have interfered with the measurements otherwise (Fig. 3.62). Directly above the box was a small aperture in the fuselage of the aircraft through which the fiber optics and electric cables were guided to the inside. For general protection and to reduce the aerodynamic drag, the box was surrounded by a fairing. As can be seen in Fig. 3.59, the aluminum box contains the forward-looking telescope with shutter, a nadir scanner, a webcam for each viewing direction (resolution of $640 \times 480\,\mathrm{pixel}$), PE-foam for thermal insulation and a heating. The heating (Cirrus 40/1 60 W) automatically turns on by a regulator if the temperature inside the

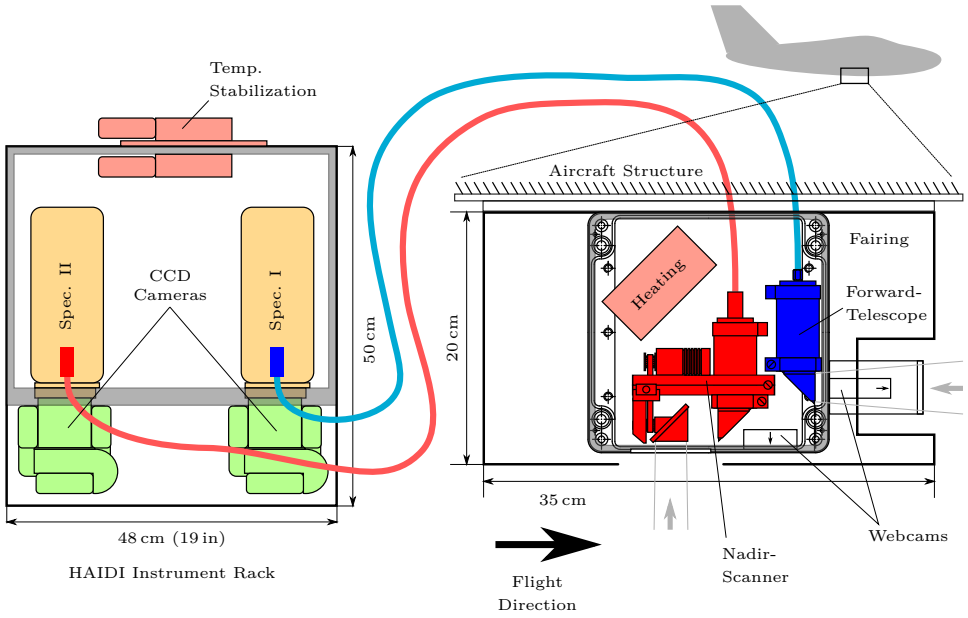

Figure 3.59.: Instrumental setup of the HAIDI system for measurement flights with the ALAR research aircraft from Purdue University. Spectrographs and CCD cameras are located in the instrument rack inside the aircraft, while the entrance optics of the system is placed in a small aluminum box below the fuselage, protected by an aerodynamic fairing. The forward-looking telescope is placed as far down as possible within the box, to ensure that its FOV does not intersect with the lower shell of the aircraft.

Figure 3.60.: Installation of the HAIDI system on the Beechcraft Model 76 Duchess from Purdue University. The picture on the right hand side shows the aircraft shortly before takeoff, the box that contains the entrance optics for nadir scanner and forward-looking telescope is marked by the red arrow. On the right hand side a closer view of the aircraft's lower shell is shown, including the aerodynamic fairing with viewports for both instruments and additional webcams. The box is connected to the spectrographs and CCD cameras inside the aircraft via a fiber optics cable going through the fuselage.

box falls below a given value (usually +10 °C), to avoid freezing or fogging of the windows. Also most of the electronics inside the box is not meant to work at temperatures below the freezing point. Because of the sufficiently sized entrance optics box, the mechanical shutter could be placed directly at the forward-looking telescope this time. Moreover, the construction with the rotary solenoid (see Sec. 3.5) was much more reliable.

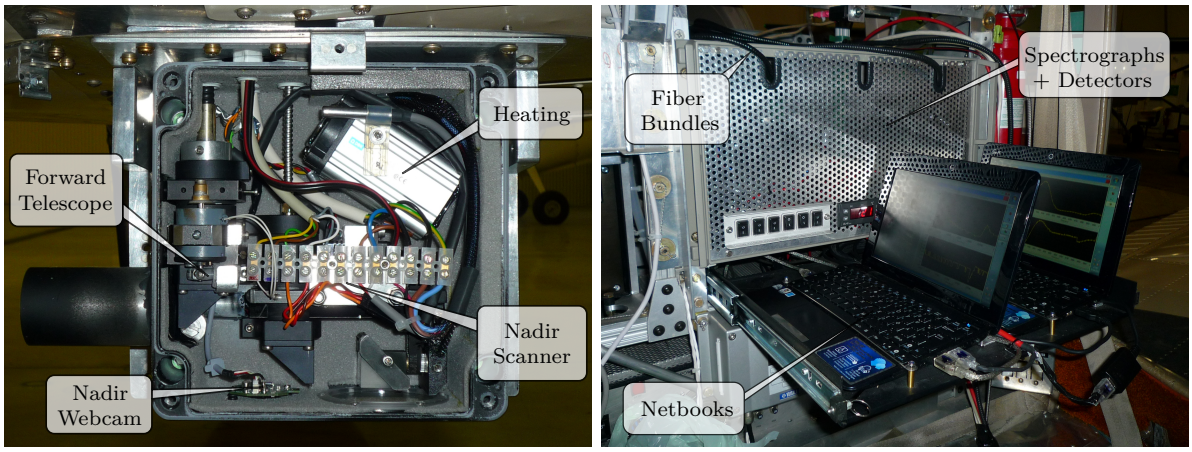

Figure 3.61.: Pictures of the HAIDI system taken during the BROMEX campaign in March 2012. The picture on the left shows the temperature stabilized inside of the aluminum box, which is located below the aircraft and contains the entrance optics of the system. In the picture on the right, HAIDI's instrument rack with spectrographs and CCD cameras can be seen. The rack drawer with the two netbooks is slided out to set up the system.

In addition to HAIDI's instrument rack, also a rack drawer with two netbooks was installed inside the aircraft's 19-inch rack. As previously mentioned, the netbooks are for system control and data storage. Each netbook was therefore connected to one of the CCD cameras via USB to store the recorded spectra. Furthermore, they were used to save the images from the two webcams and to control the CCD and spectrograph temperatures. During flight the drawer was usually slided in. By running VNC[6] software on the two netbooks, the entire HAIDI system could then be remote controlled from the co-pilot seat with a third netbook over WLAN.

3.11.3. Instrumental Setup for Gulfstream G550 (HALO)

For the near future it is planned to install HAIDI on the DLR research aircraft HALO. HALO (call sign: D-ADLR) is a modified Gulfstream G 550 ultra-long range business jet and differs from the previously used aircraft especially in terms of flight altitude and cruise speed. HALO can reach flight altitudes up to 15.5 km and a maximum speed of 1054 km/h or Mach 0.885 (DLR, 2013a). Due to the resulting high aerodynamic drag, very low temperatures and security regulations, installations outside the aircraft's fuselage are only very difficult to realize. Thus, in addition to the aforementioned reasons, the HALO setup will not use a forward-looking telescope. Because such a viewing geometry would require to mount the telescope somewhere with a clear line of sight in flight direction, which could only be implemented with an external housing. Instead a set of three nadir scanners will be applied here. The nadir scanners are thereby pointed to different directions, one in downward direction and the other two tilted by 45° in and against the flight direction. This setup allows to retrieve vertical profiles of trace

[6] Virtual Network Computing

Figure 3.62.: Single frame from a CO-sensitive infrared video camera, showing ALAR in flight. Exhaust gases and heat sources like engines are shown in white color. As can be seen, the exhaust from the two engines disperses laterally very little over the length of the aircraft and could therefore not affect the measurements. Also the exhaust from the heater (red arrow) proved to be unproblematic, since it is located on the opposite side of the aircraft's lower shell and no exhaust plume is visible. Picture courtesy of Brian Stirm.

gases also at high flight altitudes and without the need of a forward viewing direction. The nadir scanners can be installed entirely inside the pressurized cabin of the aircraft, when a sufficiently sized viewport in nadir direction is available.

3.11.3.1. Instrument Plate and Retainer

For this purpose HALO provides so-called instrument plates. Instrument plates are user customizable instrument support structures that can be mounted to apertures in the fuselage of the aircraft. In principle each kind of instrument can be attached to the inside or outside of such an instrument plate, as long as safety regulations are adhered to. They indicate, among other things, which maximum weight can be mounted to the plate and how long the moment arm can be at most. According to the HALO technical notes (DLR, 2013d), the maximum weight for internal installations, including the instrument plate itself, must not exceed 22 lbs (10 kg) and the center of gravity should not emerge more than 15 cm from the upper edge of the retainer (Fig. 3.64). The actual setup of the entrance optics complies with these specifications (see Tab. 3.10 and Fig. 3.67), it weighs about 5 kg and has a total height of 15 cm (about 9 cm from the upper edge of the retainer) measured from the surface of the instrument plate. Another important factor is the force acting on the plate and the viewport window due to pressure differences. This will be considered separately at the end of the chapter.

The retainer, which is required for the installation of an instrument plate, is provided by the DLR. As can be seen in Fig. 3.64, retainer and instrument plate are directly screwed together and then mounted to the aircraft structure (aperture support frame). Two gaskets make sure

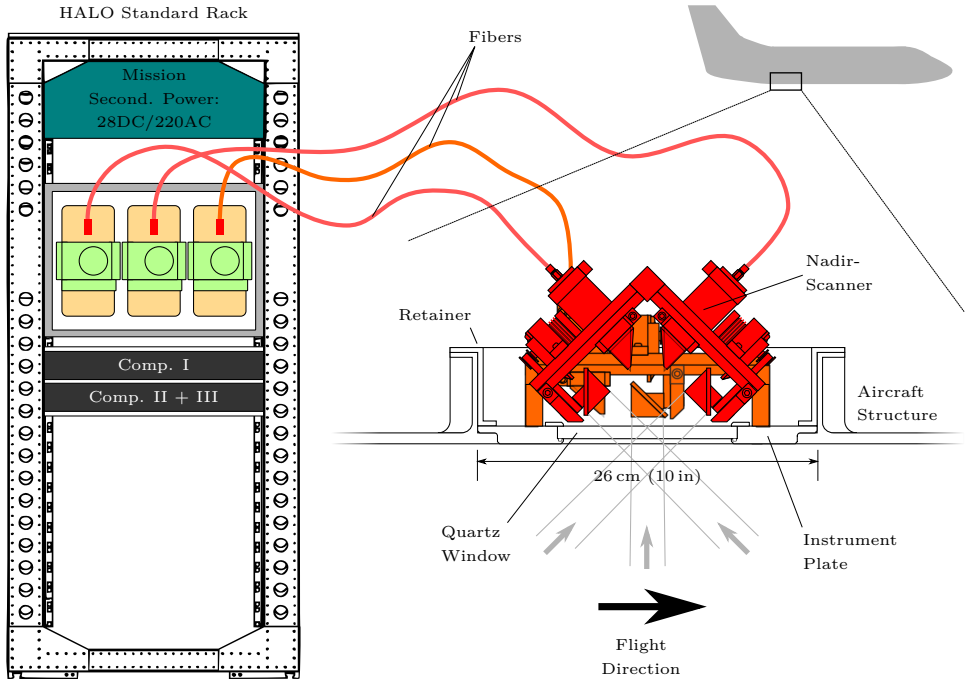

Figure 3.63.: Schematic illustration of the projected instrumental setup for operation on the HALO research aircraft. Instead of the forward-looking telescope this setup will use three nadir scanners pointed to different directions to retrieve vertical profile information about the absorbers. To get a clear line of sight, the scanners are mounted to a 10×7 inch instrument plate with a quartz window in its center. HAIDI's instrument rack and additional computers for data acquisition will be installed in a HALO standard rack. Also the 28 VDC power supply for the system is located in this rack.

that the aperture is sealed waterproof and pressure-tight. The retainer forms a flange of about 6.4 cm height around the instrument plate, which had to be considered by the design of the entrance optics. The mono fibers attached to the nadir scanners have a relatively large minimum bending radius and it had thus to be ensured that non of the fibers collide with the retainer. Therefore, all nadir scanners use a 90° quartz prism to make the fiber connectors pointing upward.

The available apertures for the installation of instrument plates in the aircraft's lower shell are shown in Fig. 3.65. In total there are 10 apertures in the lower shell where instrument plates could be mounted, 7 apertures in front of the wings (Section IV) and three behind them (Section V). The rearmost aperture ApB-11 (GVFS 837.00) and the associated rack position No. 21 in the aircraft's boiler room are not shown in the figure. Most of the instrument plates have a size (usable area) of 10×7 inch, only one position in the front section of the lower shell is available where an instrument plate with 10×14 inch can be mounted (ApB-1, GVFS 214.30 LBL 12.95). However, the preferred position for the nadir scanners is an aperture along the center line of the aircraft, so that the instrument plate is aligned as parallel as possible to earth's surface in flight and no additional tilt angle has to be compensated. This is only fulfilled by three apertures, ApB-4 (GVFS 250.00), ApB-8 (GVFS 714.20) and ApB-9 (GVFS 727.50). The apertures in the

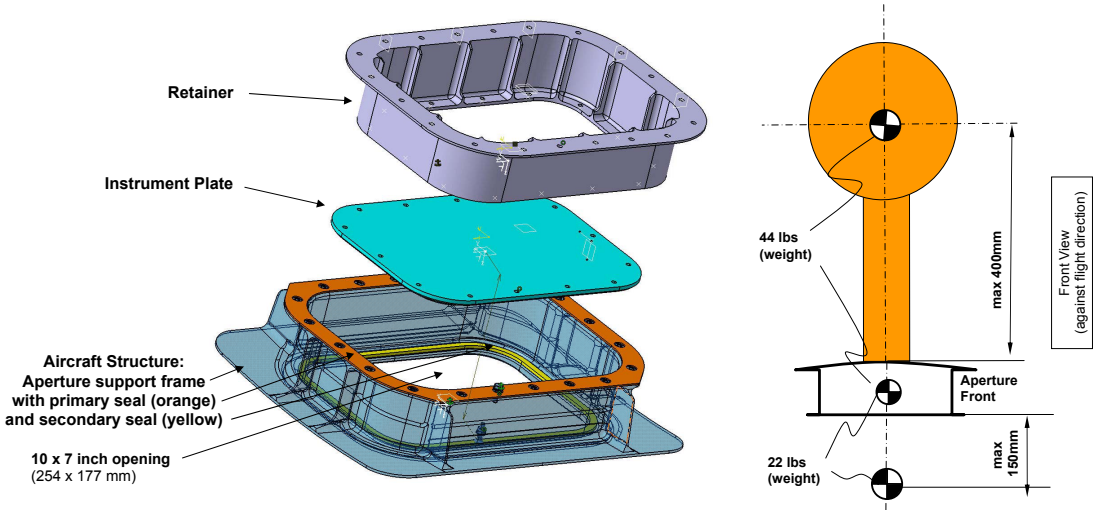

Figure 3.64.: Aperture with instrument plate (DLR, 2013d): (a) Technical drawing showing the installation principle of an instrument plate. The plate itself is not screwed to the aircraft structure. Instead it is mounted to a so-called retainer which holds the plate in place. Two gaskets ensure that the aperture is sealed waterproof and pressure-tight. (b) Schematic showing the maximum allowable weight attached to the inside and outside of the aperture with corresponding maximum length of the moment arm.

forward section of the aircraft are usually required by experiments with air inlets and outlets, because they need a preferably undistorted airflow. The HAIDI system is not affected by airflow distortions, so the apertures Apb-8 and Apb-9 in the rear of aircraft will be the best place (see also Fig. 3.66). The instrument rack with spectrographs and CCD cameras, as well as the subrack with the netbooks could then be installed in the nearby Rack No. 20 (see Fig. 3.65).

3.11.3.2. HALO Standard Rack

Most of the scientific equipment inside the cabin of HALO is installed in such standardized racks to simplify the certification process and increase the general safety. The HALO rack system is subdivided in two parts: A removable rack (shown in Fig. 3.63) and the lower supporting structure. The rack is owned by the user and can be used for the installation of instruments. Only the uppermost region of the rack is reserved for the Rack Power Distribution Box (RPDB). In total a height of 119 cm or 26.5 rack units (U) is available to the user. The equipment of the HAIDI system needs about 9 U altogether. However, the weight of the installations must also be taken into account. The overall payload mass of the rack must not exceed 150 kg, according to the HALO technical notes (DLR, 2013b). The weight of the individual HAIDI components is listed in Tab. 3.10. All components that are installed in the HALO rack (1 × rack box, 3 × spectrograph, 3 × CCD camera, 2 × rack drawer, 1 × DC-DC converter, 3 × netbook) weigh about 41 kg, in total.

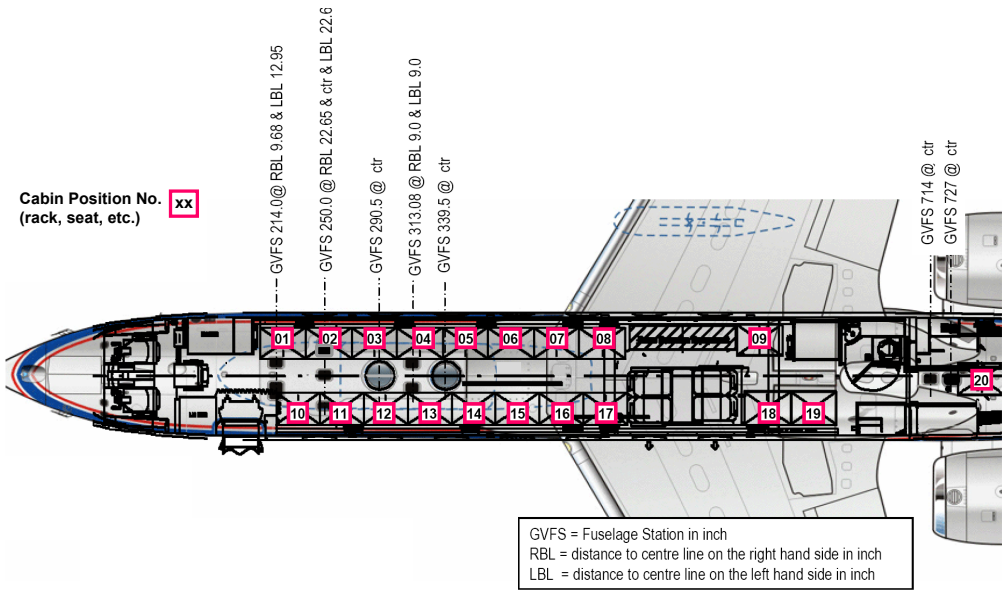

Figure 3.65.: Aperture locations on HALO's lower shell (DLR, 2013d). Each aperture can be used for the installation of instrument plates. The position is given by the distance along the center line between aircraft nose and aperture, as well as the lateral distance to the center line in inch. The preferred location for the nadir scanners of the HAIDI system are the apertures ApB-8 (GVFS 714.20) and ApB-9 (GVFS 727.50). In addition the available rack positions are marked with magenta rectangles. Hence, rack position No. 20 in the baggage compartment of the aircraft would be the ideal place for HAIDI's instrument rack.

Figure 3.66.: Picture showing HALO in flight (DLR, 2013a). The two apertures ApB-8 and ApB-9, which are the preferred position for the entrance optics of the HAIDI system, are marked by the red arrow.

Table 3.10.: Approximate weight of the individual HAIDI components and of the overall system in the configuration for the HALO research aircraft.

Component	Quantity	Weight in kg
HALO Standard Rack	1	17
Rack Box	1	15
Instrument Plate with Scanners	1	5
Rack Drawer	2	4
Spectrograph	3	3
CCD Camera	3	1.5
DC/DC-Converter	1	1
Netbook	3	1
Electric Cable	1	1
Fiber Optics	3	0.5
Total		64

3.11.3.3. Power Supply

HALO's primary power source are two generators which are integrated in the engines (Integrated Drive Generators). Each of these generators offers 3 phase AC power with 400 Hz, 115 V and up to 40 kW (DLR, 2013c). The primary power available for scientific experiments is distributed by the Mission Power Rack (MPR) to Secondary Power Distribution Boxes (SPDB) all over the aircraft. The MPR also converts the primary power to secondary power with different AC and DC voltages. An overview to the available power sources is given in Tab. 3.11.

Because there are more racks (and therefore instruments) in the aircraft than SPDBs available, each rack is also equipped with an RPDB in its upper area. The RPDBs are connected to the SPDBs and are available in three different versions: RPDB_AC (Mission AC: 115-3-AC, 115-1-AC), RPDB_SP (Mission Secondary Power: 28 DC / 220 AC) and RPDB_AI (Mission Anti-Ice: 115-3-AC). So in principle the RPDBs offer the same power sources to the user like the SPDBs do, but in addition the RPDBs provide more voltages (115 VAC) with single phase AC power, power monitoring, additional circuit breakers and an easy to access emergency shut-off. In general it is also possible to connect the instrument directly to the SPDBs, but due to the added security features the use of RPDBs is strongly recommended on HALO.

The HAIDI system will use the 28 VDC rail of a RPDB_SP with a circuit breaker rating of 20 A. However, most of the electronic of the HAIDI system operates at 12 VDC, so an additional DC-to-DC converter is required. This DC-to-DC converter (Mean Well SD350B-12) is mounted in the subrack that also contains the three netbooks. It has an input voltage range of 19 to 36 VDC and an output of 12 VDC with up to 27.5 A (330 W). The power consumption of the HAIDI system for idle and load cases can be seen in Tab. 3.12. When all components are working at full load, the power consumption could theoretical reach the limit of the DC-to-DC

converter. However, this is very unlikely for normal operation and can easily be avoided by waiting for the thermoelectric temperature controls to reach their setpoint before activating the servo motors of the nadir scanners. In addition to that, the main fuse of the instrument rack limits the maximum current to 20 A at 12 V (240 W).

All SPDBs and RPDBs on HALO are equipped with circular connectors that comply with military standard MIL-DTL-5015. The RPDB_SP uses different connectors for rails with different circuit breaker ratings or voltages to make them noninterchangeable. The rail with 28 VDC and a circuit breaker rating of 20 A uses a MS 3459 W16-11P connector from Amphenol, which is a straight female plug with self-locking coupling nut and two pins (A: Pos., B: Neg.). Thus, the DC-to-DC converter of the HAIDI system is equipped with a MS 3459 W16-11S connector, the male counterpart of the MS 3459 W16-11P plug.

Table 3.11.: Available power sources provided by SPDBs and RPDBs for scientific equipment on HALO (DLR, 2013c). †Only available per RPDB.

Identifier	Voltage	No. of Phases	Frequency	Circuit Breaker Rating
Primary Mission Power	115 VAC	3, 1†	400 Hz	20 A
Switched Mission Power	115 VAC	3, 1†	400 Hz	20 A
Secondary AC-Power	230 VAC	1	50 Hz	15 A
Secondary DC-Power	28 VDC	-	-	20 A, 50 A, 80 A

Table 3.12.: Approximate power consumption of HAIDI's individual components and of the overall system in the configuration for the HALO research aircraft.

		Power Consumption in W	
Component	Quantity	Load	Idle
Temp. Stabilization	1	75	14
Heater	1	60	0
CCD Camera	3	35	12
Netbook	3	15	5
Servo Motor	3	15	5
Webcam	1	2	2
Total		332	82

3.11.3.4. Calculation of the Window Diameter

As mentioned earlier, the nadir scanners of the HAIDI system will be installed inside the aircraft. Therefore, an optical viewport is required in the instrument plate in order to get a free line of sight. This viewport is realized by a fused quartz window made of Herasil 102. Herasil 102 is very homogeneous in the primary functional direction (along the thickness of the window) and has a high transmissivity of about 92 % between 300 and 1000 nm (sample thickness 10 mm), including Fresnel reflection losses (Heraeus Quarzglas, 2012). Another important point is that Herasil 102 has exactly defined characteristics (see Tab. 3.13), which is required by the certification process.

Since each window is a potential failure point in the integrity of the aircraft's pressurized cabin and thus has to withstand high pressure differences, it is important to keep the overall window size as small as possible. The usable size of the instrument plate does not allow to integrate a

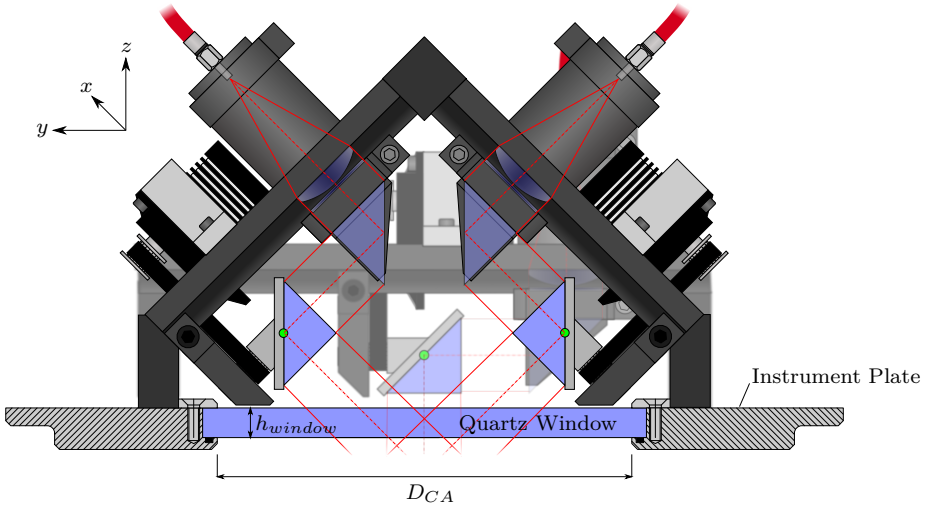

Figure 3.67.: Schematic of the entrance optics setup for HALO. Three nadir scanners are arranged on a 10 × 7 inch instrument plate over a centrical quartz window with thickness h_{window} and clear aperture D_{CA}. The red lines indicate the light path from the prisms to the optical fibers. As can bee seen, the scanners field of view overlaps in the middle of the window to keep its diameter as small as possible. The flight direction is along the y-axis in the illustration.

Table 3.13.: Selected mechanical characteristics of Herasil 102 fused quartz (Heraeus Quarzglas, 2012).

Quantity	Value
Density	2.203 g/cm^3
Modulus of Elasticity (at 20 °C)	7.0×10^4 N/mm^2
Compressive Strength	1150 N/mm^2
Tensile Strength	50 N/mm^2
Flexural Strength	67 N/mm^2

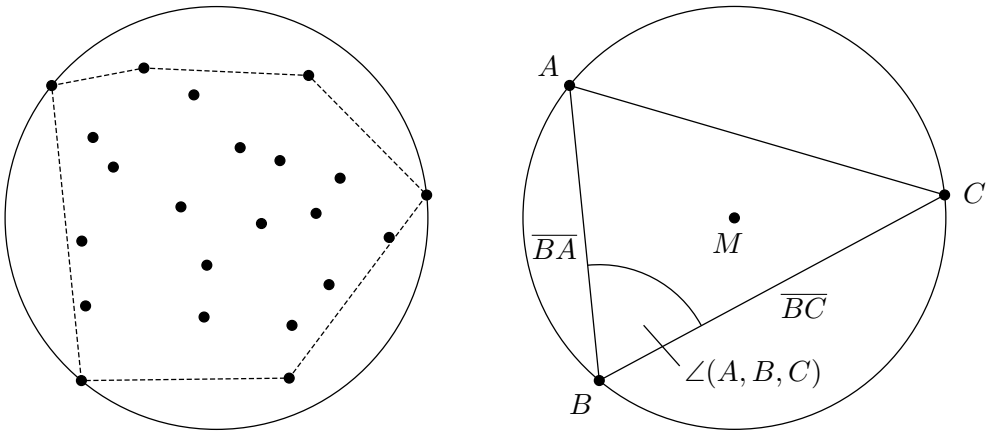

Figure 3.68.: Calculation of the smallest enclosing circle: (a) The convex hull (dashed line) of a set of points is the smallest convex set that contains all points. (b) The Skyum algorithm compares the circumcircle radii for three sequent points (A, B, C) of the convex hull at a time. When the angle spanned by these points $\angle(A, B, C)$ is smaller than 90°, the circumcircle $\bigcirc(A, B, C)$ is the smallest enclosing circle for the set of points. Else, point B is removed from the set and the circumcircle radii were calculated again.

single quartz window for each scanner, so all three scanners have to use the same window in the center of the plate. Figure 3.67 shows the actual setup of the nadir scanners on the instrument plate. All three scanners are placed as close together as possible without interfering the field of view of one of the other scanners. The calculation of the necessary window diameter for a single nadir looking scanner is a trivial task, but in combination with tiled scanners it can quickly become very complex. Hence, the required window area for the scanner setup is calculated with Maple by an algorithm similar to the one used in Chap. 3.4.3. Instead of to the ground, the field of view of the individual scanners is projected to the bottom of the quartz window in this case (where the needed window area becomes maximum). To get the smallest possible window diameter, a convex hull is laid around the calculated points for the GFOV in a first step (Fig. 3.68a). The convex hull is defined as the smallest convex set that contains all considered points. After that, center and radius of the smallest enclosing circle, i. e. the circular viewport in the instrument plate, are calculated with the Skyum algorithm (Skyum, 1991), illustrated in Fig. 3.68b. In general, the algorithm takes the points on the convex hull and calculates the radii of the circumcircles for three of theses points (A, B, C) at a time. The points A, B and C thereby cycle through all points on the convex hull either in clockwise or counter-clockwise order (in which A and C can be identical when the convex hull contains only two points). Subsequently, the circumcircles were sorted according to their radii. When the three points with the biggest circumcircle form an angle $\angle(A, B, C)$ smaller or equal than 90°, then this circumcircle is the smallest enclosing circle for all points in the convex hull. Otherwise, point B is removed from the points on the convex hull and the algorithm starts over until the condition is fulfilled.

The result of such a calculation can be seen in Fig. 3.69 and 3.70. Here, the prisms of the nadir scanners are shown as blue rectangles. The green circles (also shown in Fig. 3.67) on the midpoint of the prisms hypotenuse face were used as reference point for the position of the prism and are on the point of intersection between the scanners line of sight and the prisms axis of rotation. For each scanner the GIFOV (red ellipses) is calculated in 5° steps for a total FOV of 50°. *Ground projected* here means projected to the bottom of the window. Therefore, the minimum distance between the location of a prism (green circle) and the projection surface (bottom of the window) is given by the thickness of the window plus the necessary distance for a full rotation of the prism. Even when such a rotation is not scheduled for normal operation it can occur in case of a malfunction. Hence, due to safety reasons the minimum distance between prism and window is always chosen that way, that the prism cannot touch the window and potentially damage it. For a scanner in nadir direction (tilt angle 0°) this distance is $\sqrt{2} \times a$, where a is the edge length of the prism. Since we use 1-inch prisms, this is a distance of 18 mm. A prism with a tilt angle of 45° needs a distance of $\sqrt{3/4} \times a = 22\,\text{mm}$. The exact position of the prisms used for the calculation is shown in the figures. All calculations were done for a worst-case window thickness of 10 mm. The minimum required thickness is calculated in the next section.

As can be seen from Fig. 3.69 the minimum diameter of the windows clear aperture D_{CA} is approximately 11.7 cm for the setup that will be used on HALO. This is more than twice the diameter required by a single nadir scanner (see Fig. 3.70). Thus, for smaller aircraft where an aperture with a diameter of more than 11.7 cm is not feasible, the one scanner solution can still be an option.

3.11.3.5. Calculation of the Window Thickness

After having specified the required minimum window diameter for the three nadir scanners one can now go on with calculating the necessary window thickness. The thickness must be sufficient to withstand the pressure differences that will occur between ambient pressure and the pressurized cabin of the aircraft including some factors of safety. For the following calculations a window radius of 75 mm is assumed to have some clearance in placing or tilting the scanners.

In general two cases have to be considered:

I. Ultimate Load Case The Ultimate Load Case is composed of the maximum pressure difference $\Delta p_{max} = 723\,\text{hPa}$ that is allowed by the pressure relieve valve of the aircraft, a negative pressure $\Delta p_{Bernoulli} = 34\,\text{hPa}$ induced by fuselage flows, the Ultimate Load factor UL = 1.5 and the flight loads caused by the acceleration forces that act on the

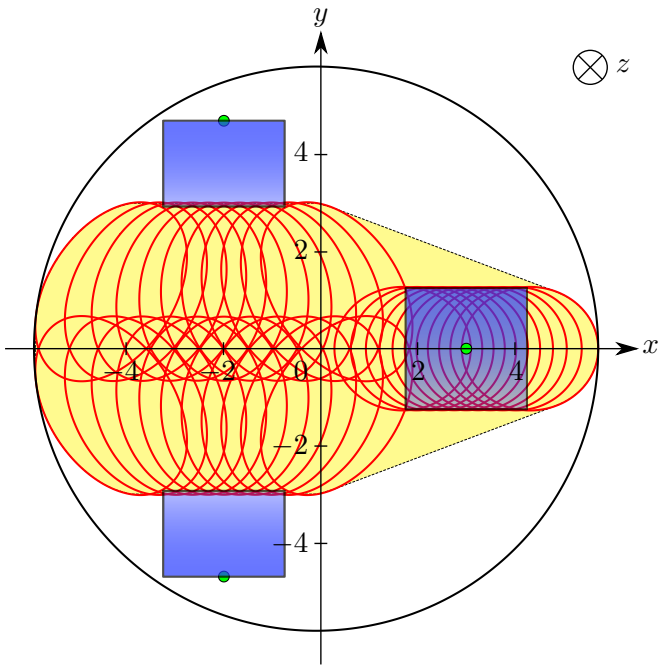

Figure 3.69.: Necessary window diameter calculated for the HALO setup with three nadir scanners. The prisms (blue rectangles) are located at $(x_{p1}, y_{p1}, z_{p1}) = (3, 0, 3)$ cm, $(x_{p2}, y_{p2}, z_{p2}) = (-2, 4.7, 3.5)$ cm and $(x_{p3}, y_{p3}, z_{p3}) = (-2, -4.7, 3.5)$ cm with tilt angles of $\beta_1 = 0°$, $\beta_2 = 45°$ and $\beta_3 = -45°$. The resulting minimum diameter for the clear aperture of the window is 11.7 cm.

quartz window due to flight maneuvers, gusts, landing conditions or emergency landings[7]:

$$\begin{aligned} p_{ult} &= \text{Ultimate Cabin Pressure} + \text{Flight Loads} \\ &= \text{UL} \times (\Delta p_{max} + \Delta p_{Bernoulli}) + \text{Flight Loads} \\ &= 1.5 \times (723\,\text{hPa} + 34\,\text{hPa}) + \text{Flight Loads} \\ &= 1136\,\text{hPa} + \text{Flight Loads} \end{aligned} \tag{3.48}$$

Table 3.14.: Applicable inertia loads for scientific equipment inside HALO (DLR, 2013d). †Only for apertures ApB-8, ApB-9 and ApB-10.

Inertia Load Case	Aircraft Axis System	Direction	ULTIMATE Inertia Load at View Ports
A-1	X	forward	$+9.0\,g_0$
A-2		backward	$-1.5\,g_0$
A-3	Y	sideward	$\pm 3.0\,g_0$
A-4	Z	downward	$+6.3\,g_0$ $(+7.1\,g_0)^\dagger$
A-5		upward	$-3.2\,g_0$ $(-4.0\,g_0)^\dagger$

[7] Dr. Andreas Fix, Institute of Atmospheric Physics - DLR (personal communication)

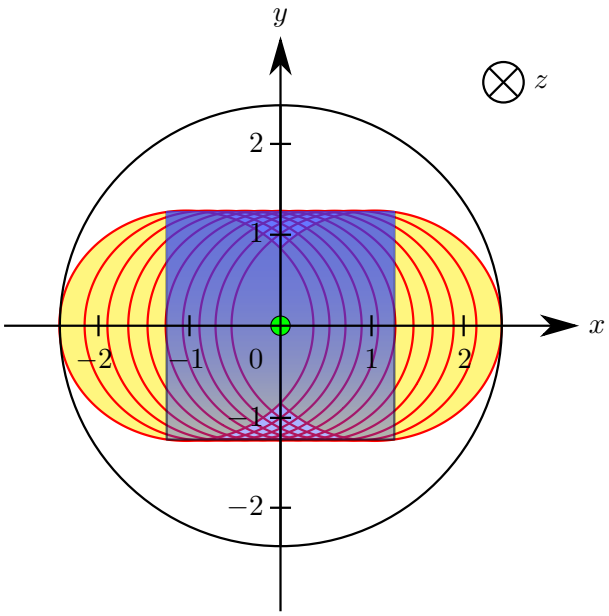

Figure 3.70.: Necessary window diameter calculated for a single nadir scanner pointed to the downward direction. The prism (blue rectangle) is located at $(x, y, z) = (0, 0, 3)\,\mathrm{cm}$ and is tilted by $\beta = 0°$. The resulting minimum diameter for the clear aperture of the window is 5.6 cm. Unpressurized aircraft like the Beechcraft Model 76 Duchess can use thinner windows, which further decreases the necessary window diameter.

The Flight Loads can be calculated with the inertia load factors given in Tab. 3.14. First of all, one needs the weight of the quartz window:

$$m_{window} = \pi \times r_{window}^2 \times h_{window} \times \rho_{quartz} \tag{3.49}$$

According to Tab. 3.13, the density ρ_{quartz} of the window material is $2.203\,\mathrm{g/cm^3}$. If one furthermore assumes a worst case thickness h_{window} of 10 mm and a radius r_{window} of 75 mm, one obtains:

$$\begin{aligned} m_{window} &= \pi \times (75\,\mathrm{mm})^2 \times 10\,\mathrm{mm} \times 2.203\,\mathrm{g/cm^3} \\ &= 389\,\mathrm{g} \end{aligned}$$

Multiplication with the standard acceleration due to gravity g_0 and the vertical inertia load factor (Load Case A-4) leads to the force that impacts on the quartz window in worst case:

$$F_{il} = m_{window} \times 9.81\,\mathrm{m/s^2} \times 7.1 \tag{3.50}$$
$$= 27.09\,\mathrm{N}$$

This force affects the whole surface of the quartz window and is therefore expressible as a pressure:

$$p_{il} = F_{il}/A_{window} \tag{3.51}$$
$$= \frac{27.09\,\mathrm{N}}{\pi \times (0.075\,\mathrm{m})^2}$$
$$= 1532.98\,\mathrm{kg/(s^2\,m)}$$
$$= 15.33\,\mathrm{hPa}$$

According to equation (3.48) the Ultimate Load Case then equals a total pressure p_{ult} of:

$$p_{ult} = 1136\,\mathrm{hPa} + 15.33\,\mathrm{hPa}$$
$$= 1151.3\,\mathrm{hPa}$$

II. Burst Pressure Case The Burst Pressure p_{burst} stands for a worst case scenario pressure, which is denoting to either a single failure condition or a maximum normal operating condition. It is defined as the minimum pressure level at which rupture of the pressurized vessel occurs and is composed in the following way[8]:

$$p_{burst} = \mathrm{UL} \times \mathrm{BF} \times \Delta p_{max} \tag{3.52}$$

In this case BF is the Burst Factor which increases with height and has a value of 1.67 for altitudes above 45 000 ft.

$$\Rightarrow p_{burst} = 1811\,\mathrm{hPa}$$

As one can clearly see, the Burst Pressure Case exceeds the Ultimate Load Case ($p_{burst} > p_{ult}$) and therefore marks the worst case pressure that may impact on the window during operation. Thus, the Burst Pressure p_{burst} is applied to calculate the necessary window thickness. Assuming

[8] Dr. Andreas Fix, Institute of Atmospheric Physics - DLR (personal communication)

the following criteria, the necessary thickness can then be calculated via the Kirchhoff plate theory for thin plates (Center for Aerospace Structures - University of Colorado Boulder, 2013):

- The thickness h of the plate is much smaller than its diameter.
- The lateral defection f is negligible compared to the thickness h.
- The extension of the midsurface does not change in a significant way during deformation.
- The plate thickness h is approximately homogeneous and does not change during deformation.

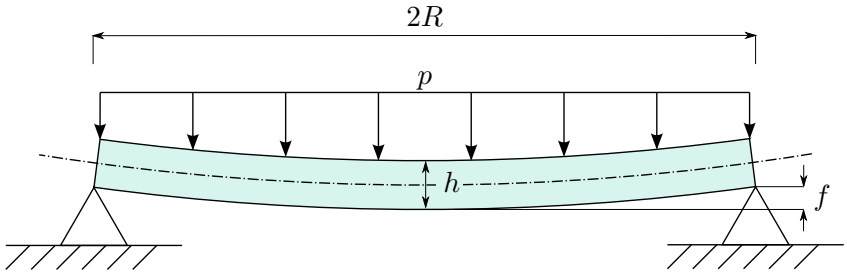

Figure 3.71.: Lateral deflection f of a thin plate, which is supported at its outermost edge, as a result of pressure difference p acting on the upper side.

The Kirchhoff plate theory leads to the following equations for a free circular plate under uniformly distributed load that is supported at its outer radius (Grote and Feldhusen, 2011):

$$f = 0.696 \cdot \frac{pR^4}{Eh^3}\,, \tag{3.53}$$

$$\sigma_r = 1.24 \cdot \frac{pR^2}{h^2}\,, \tag{3.54}$$

where f is the lateral deflection and σ_r the flexural stress that is applied to the quartz window. When the applied flexural stress reaches the flexural strength of a material, fracture occurs. As can be seen from equation (3.54), the flexural stress acting on a thin circular plate is inversely proportional to h^2 when pressure and radius are held constant. Due to this fact, a window with twice the thickness could withstand four times the pressure. The flexural strength of Herasil 102 is specified with $67\,\mathrm{N/mm^2}$ (Tab. 3.13). Figure 3.71 shows a computation of flexural stress σ_r and lateral deflection f in dependency of the thickness of a thin plate with radius $R = 75\,\mathrm{mm}$ and an applied pressure of $p_{burst} = 1811\,\mathrm{hPa}$. The gray shaded area in the upper part of the plot represents the region where the flexural stress becomes larger than the flexural strength of the quartz window. According to this, the quartz window will burst when its thickness is less than 4.3 mm. The corresponding maximum lateral deflection of the window is about 0.7 mm.

For this reason, a suitable window for operation on HALO should have a thickness of at least 4.3 mm to meet the requirements.

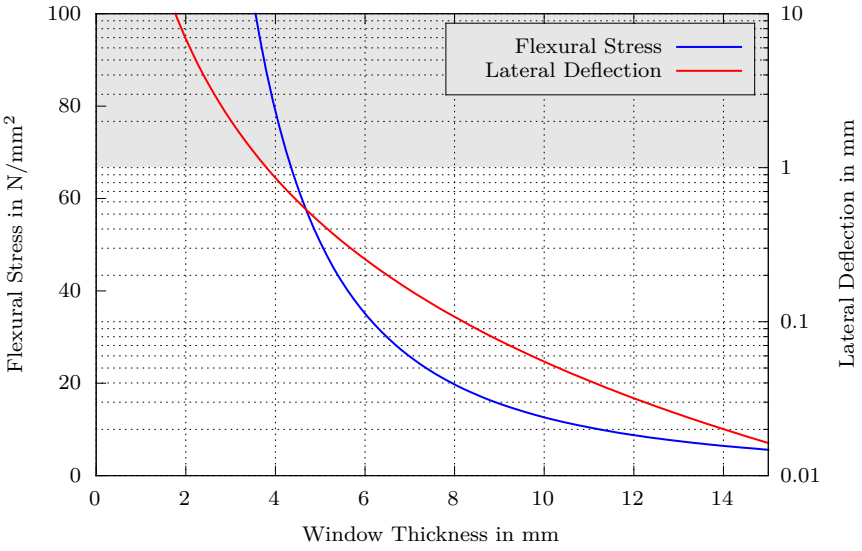

Figure 3.72.: Lateral deflection and flexural stress of a quartz windows with a diameter of 150 mm. The applied pressure difference is $p_{burst} = 1811$ hPa. For thicknesses smaller than 4.3 mm the flexural stress becomes larger than the flexural strength of quartz glass (lower border of the gray box), resulting in failure of the window.

The window that will actually be used for HALO has a diameter of 15 cm ($D_{CA} = 14$ cm) and a thickness of 10 mm. In this way the window can not only easily withstand the required Burst Pressure but will also show a much smaller lateral deflection. A window with a thickness of 10 mm will have a lateral deflection of merely 0.05 mm at the Burst Pressure Case, whereby the optical properties of the window should not be affected. According to equation (3.54), this window can withstand pressures up to 9606 hPa, which equals a force of 5403 N distributed over the surface of the window. This exceed the required values by more than a factor of 5.

3.12. Computer and Measurement Software

Due to the readout electronics of the CCD cameras, there was no already available software for data acquisition and controlling of the detector features that could have been used. Therefore, a measurement software has been written that is able to store the spectra from the CCD camera in a specific directory structure and furthermore controls the thermoelectric cooling of the detector, the movement of the nadir scanner's servo motor and other parameters of the camera like exposure time or co-adding of multiple spectra. The current version of this software is written in LabVIEW 2013 and can be used with Windows XP or later. To communicate with the CCD camera hardware, the LabVIEW program uses a dynamic-link library (dll) file provided by khs-instruments. The dll offers three main functions, *khsdll_set_comm*, *khsdll_var_get_float*

and *khsdll_scan_get*, to which the program can send commands. For example, the integration time of a spectrum can be set by using the function *khsdll_set_comm* (see Tab. 3.15). This function has three input parameters: *cmd*, *dat* and *func*. Setting *cmd* to 10 and *dat* to −3 allows to input the exposure time in milliseconds with the parameter *func*. Lists with the most important commands can be found in Tab. 3.15 and 3.16. For a complete list of available commands please refer to the header file *khsdll.h* which can be obtained from khs-instruments.

As the prototypes of the CCD cameras were not able to switch between imaging mode (full frame readout for pushbroom scanning) and FVB mode (full vertical binning for whiskbroom scanning), two different versions of the measurement software were originally written. One for the CCD camera that was used with the nadir scanner and one for the CCD camera that was used with the forward-looking telescope. However, the differences are only minor and should not be discussed here. Since the current version of the CCD camera hardware provides both operation modes and most of the commands are also identical in the different modes, the two programs can be easily unified in the future.

The measurement software is intended to run on netbooks (Asus Eee PC R051PX), therefore the graphical user interface (GUI) is optimized for a screen resolution of 1024 × 600 pixel. To create sufficient space for the individual features of the software, the GUI is subdivided to several tabs which are described in detail below.

3.12.0.6. The “Taking Spectra” Tab

When the software starts up, the “Taking Spectra” tab is displayed. On this tab all necessary settings can be done to record spectra and store them in a customizable directory structure. It also features a display for visualization of the taken spectra. In the following the possible settings for this tab are explained:

- **Start Readout** By pressing this button, the program submits the entered exposure time to the CCD camera and starts to read out spectra.
- **Stop Readout** This button interrupts the readout procedure after finishing the current spectrum.
- **Display Spectrum** Toggles the visualization of the taken spectra on or off (can save some computing power, if necessary).
- **Autoscale** Automatically scales the display axes to fit the taken spectra (should be deactivated before using the zoom function).
- **Continuous Readout** Reads out spectra until the “Stop Readout” button is pressed.
- **Auto Exposure Time** This function automatically changes the exposure time when the taken spectra are over- or under-exposed. Additional settings to this feature can be made in the “Settings” tab.

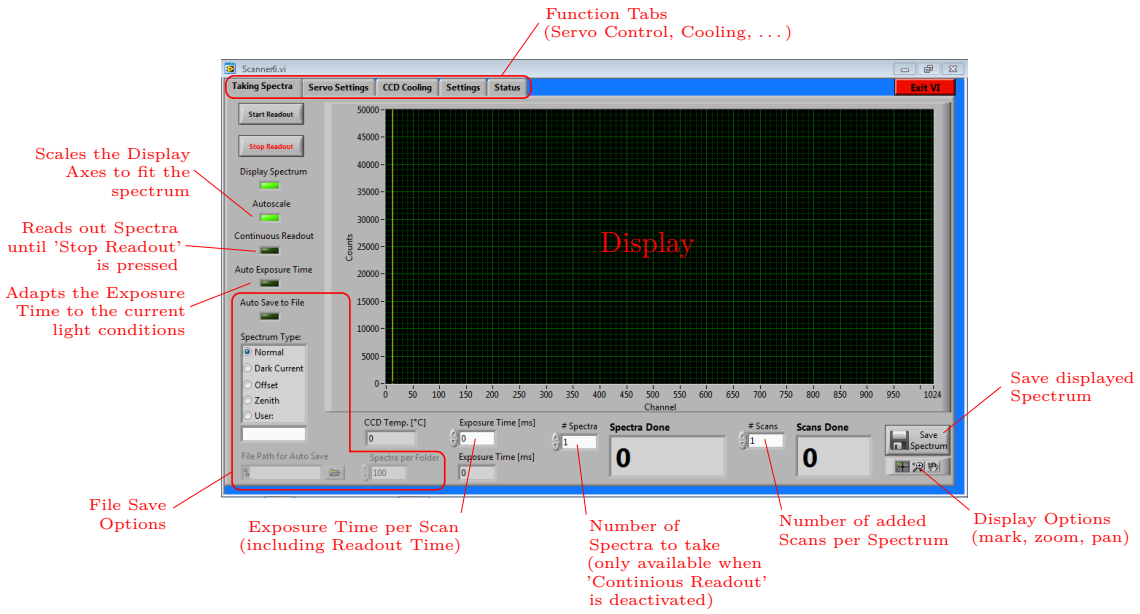

Figure 3.73.: The "Taking Spectra" tab is the main window of the measurement software and shows all important information regarding the taken spectra. From here not only single spectra can be taken but also the automatic measurement routine can be started. In addition it allows to set up the directory structure for storage.

- **Auto Save to File** Saves the taken spectra to a file according to the settings below, when activated. The directory tree will look as follows:

```
/ ..... Storage Root Directory
└─ raw
   └─ measurement_spectra ..... Depends on "Spectrum Type"
      ├─ spec0000000
      │  ├─ spec0000000.std
      │  ├─ ...
      │  └─ spec0000099.std
      ├─ spec0000100 ..... Depends on "Spectra per Folder"
      │  ├─ spec0000100.std
      │  ├─ ...
      │  └─ spec0000199.std
      └─ ...
```

  The storage root directory can be entered into an input box at the bottom left corner of the screen (see Fig. 3.73). Located next to this input box is also a control panel to set the maximum number of stored spectra per folder. Every time the maximum is reached, a new folder with the name of the following spectrum file is created. All spectra are saved in Extended Standard Format (.std), which is a human-readable ASCII-based file format. This makes it easier to process the contained data also with other programs like MATLAB or Gnuplot. In addition to the required information for the default header of the std-files (see Kraus (2006)), the program also stores some extra information in the

extended spectrum properties: property *UserParam5* contains the current temperature of the CCD and property *LightSource* shows the corresponding PWM value of the CCD camera's integrated Peltier cooling.

- **Spectrum Type** Allows to quickly change the folder name one level below the "raw" folder to some presets. The bottommost entry "User" also allows to enter a custom folder name (invalid characters such as umlauts or spaces will be ignored).
- **Exposure Time** Sets the exposure time of the spectra in milliseconds. The field below shows the actually set exposure time. There can be a discrepancy between the two times because the readout electronics can not accept all values for the exposure time.
- **# Spectra** Sets the number of spectra the program should take before the readout process is stopped automatically ("Continuous Readout" has to be deactivated prior to this).
- **# Scans** Sets the number of co-added scans per spectrum.
- **Save Spectrum** Saves the currently displayed spectrum to a file.

3.12.0.7. The "Servo Settings" Tab

The "Servo Settings" tab is used to control the motion of the nadir scanner and is therefore only available in the imaging mode version of the measurement software. In addition to the manual adjustment of the scanners viewing direction it also allows to modify the automatic scanning routine. The individual controls are explained below:

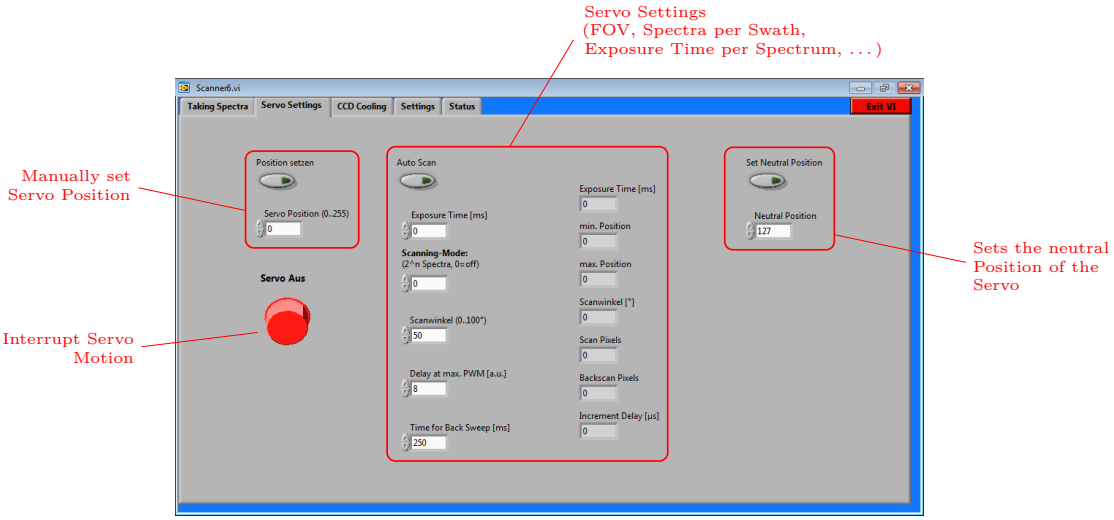

Figure 3.74.: The "Scanner Settings" tab of the measurement software allows to set all required settings for the nadir scanner. Here, the scanners FOV can be set to values between 0 and 100° as well as the number of recorded spectra per swath and their integration time. The number of spectra and their integration time determine the total duration of one swath and therefore the rotational speed of the prism.

- **Set Position** When this button is pressed, the scanner moves to the position specified by the numeric control below. The position can be entered as a value between 0 and 255, corresponding to a deflection angle of −50° to +50°.

- **Auto Scan** Starts the automatic scan routine for the nadir scanner with the settings made below.

- **Exposure Time** Sets the exposure time of the spectra (setting will be transferred to the equivalent numeric control on the "Taking Spectra" tab).

- **Scanning Mode** Controls the number of taken spectra per swath. The numbers are entered as powers of 2, so 0 means 1 spectrum per swath and 8 is 128 spectra per swath. Due to the high rate of spectra generated by the whiskbroom system (up to 100 spectra per second), all spectra taken during one swath are buffered inside the camera electronics first. After the last spectrum of a swath is taken, the measurement software starts to read out the data and stores it into a single file. During this time the nadir scanner can already start to record the next swath. The resulting files therefore contain all spectra of a swath stringed together ($1024 \times$ *number of spectra per swath* = *number of channels per file*) and are only separated during the data analysis. The start and stop time of the taken spectra is generally saved with millisecond precision by the software, so that the recording position can later be exactly determined by comparison with the GPS log. Due to a linear movement of the prism during scan, the recording times for every single spectrum of a swath can be calculated afterwards.

- **Scan Angle** Sets the total scan angle of the nadir scanner to values from 0 to 100°. Since the servo's range of motion is only subdivided to 512 positions, the entered value will be adapted to the closest possible and displayed in the numeric indicator on the right. The corresponding minimum and maximum values of the PWM signal are also shown here.

- **Delay at max. PWM** Adds a short delay when the PWM ramp has reached its maximum position. This can compensate a lag between the PWM value and the actual position of the scanner. Allowed are values between 0 and 255.

- **Time for Back Sweep** Time needed by the scanner to sweep back to its initial position. For a scanning angle of 50° this is approximately 250 ms. The value is required to calculate the increment delay between two PWM values. In addition the software shows the number of spectra that will be taken during the forward and back scan.

- **Set Neutral Position** Sets the neutral (downward) position of the scanner to the value specified by the numeric control. The scan range will always be symmetrically to this value if possible. Accepted are integers between 0 and 255.

3.12.0.8. The "CCD Cooling" Tab

On the "CCD Cooling" tab the settings for the thermoelectric colling of the CCD can be made. When the cooling is switched on, the cooling capacity is linearly increased on a slow rate first (linear phase) until the temperature comes close to the setpoint. Not until then the PID control loop is activated (PID phase). This ensures that the cooling capacity of the Peltier element is not switched to 100 % immediately and the CCD is thus not cooled down by more than 5 K/min. A faster temperature change can damage the CCD due to thermal stress (e2v, 2013). When the cooling is deactivated, the cooling capacity is decreased in a similar way before the Peltier current is turned off. For this reason, the measurement software should not be closed before the cooling capacity is ramped down. The tab provides two displays, one shows the temperature trend and the other one the time curve of the Peltier current.

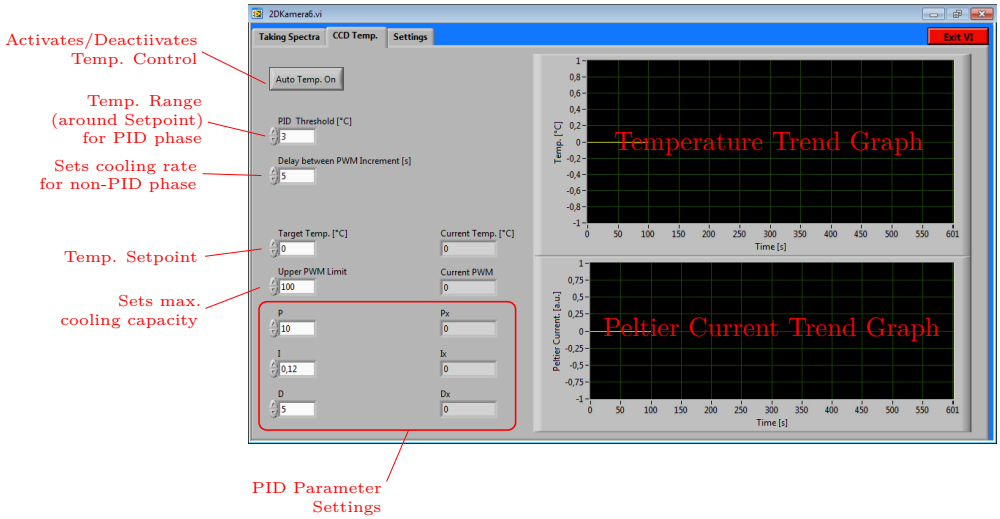

Figure 3.75.: With the "CCD Cooling" tab of the measurement software the temperature of the CCD detector can be controlled. When the given temperature setpoint differs more than a certain value from the actual temperature of the CCD the cooling capacity is linear increased by an adjustable rate first, before a PID control loop stabilizes the temperature. This is because the CCD should not be cooled down or heated up by more than 5 K/min (e2v, 2013). The Peltier element can only be used to cool the CCD, so the temperature setpoint should be below ambient temperature.

- **Auto Temp. On/Off** Activates or Deactivates the temperature control.
- **PID Threshold** Sets the temperature range around the setpoint within which the PID control works. Outside this range the cooling capacity is raised or lowered by a ramp with customizable slope. Hence, when the threshold is set to 3 °C (default) and the setpoint is −10 °C than the PID control starts working below −7 °C.
- **Delay between PWM Increment** Sets the time interval between two consecutive PWM values during the linear phase of the cooling. This influences the rate with which the CCD temperature is changed.

- **Target Temp.** Sets the temperature setpoint.
- **Upper PWM Limit** Sets the maximum PWM value for the cooling. A higher value means a higher maximum cooling capacity. Values above 100 should be avoided because the Peltier current is interrupted by the electronics if it exceeds a certain value.
- **P** Sets the proportional (P) gain of the PID control.
- **I** Sets the integral (I) gain of the PID control.
- **D** Sets the derivative (D) gain of the PID control.

3.12.0.9. The "Settings" Tab

The "Settings" tab of the measurement software mainly contains settings needed for the automatic exposure time calculation. Because the nadir scanner can only toggle between a limited set of predefined exposure times in order to preserve a constant scan pattern, some of these settings are only available in the software for the forward-looking telescope. A list of the different settings is given below:

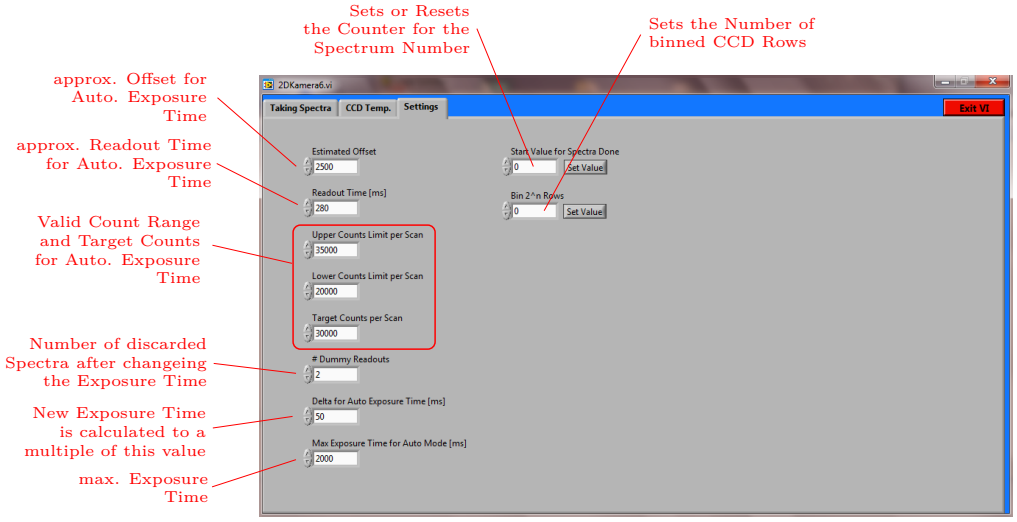

Figure 3.76.: The "Settings" tab provides some additional settings for the filenames of the spectra (start number of next spectrum), row binning (only in imaging mode software) and the automatic exposure time routine.

- **Estimated Offset** Sets the estimated value for the offset signal in counts (value can change due to ambient temperature).
- **Readout Time** Sets the readout time for a spectrum.
- **Upper Counts Limit per Scan** Sets the maximum allowed counts per pixel of a single spectrum. When one channel of the CCD exceeds this value, the exposure time is automatically recalculated to match the target counts per scan. The entered value is without offset.

- **Lower Counts Limit per Scan** Sets the minimum allowed counts per pixel of a single spectrum. Only when all channels of the CCD fall below this value, the exposure time is increased. The entered value is without offset.
- **Target Counts per Scan** Sets the desired maximum counts per pixel for the automatic exposure time calculation.
- **# Dummy Readouts** Sets the number of dummy readouts that will be taken after the exposure time was changed.
- **Delta for Auto Exposure Time** The recalculated exposure time is rounded to the closest multiple of this value.
- **Max Exposure Time for Auto Mode** Limits the maximum exposure time to the set value.
- **Start Value for Spectra Done** Sets the counter value for the next taken spectrum.
- **Bin 2^n Rows** Sets the number of binned CCD rows in imaging mode. Values are entered as powers of 2.

Table 3.15.: List of the most important commands for the dll function khsdll_set_comm.

khsdll_set_comm			
Function	cmd	dat	func
Set PWM value for CCD Cooling	13	0..100	1
Set Servo Position	162	0..255	2
Set max. PWM value for Servo	162	0..255	3
Set min. PWM value for Servo	162	0..255	4
Set PWM Increment Delay for Servo	162	0..65535 (µs)	5
Servo Off	162	0	6
Servo Manual Pos. Mode	162	1	6
Servo Auto. Pos. Mode (Scanning)	162	2	6
Set Number of binned Rows in 2D Mode	72	0..8 (n for 2^n Spec.)	16
Set Number of Spectra per Swath in Scanner Mode	64	0..8 (n for 2^{8-n} Spec.)	81
Set Camera to Scanner Mode	64	2	82
Set Camera to 2D Mode	64	3	82
Set Exposure Time	10	-3	0..65535 (ms)

Table 3.16.: List of the most important commands for the dll function khsdll_var_get_float.

khsdll_var_get_float	
function return	dat
Peltier Current	128
CCD Temperature	54
Exposure Time	34

4. Data Evaluation

The following chapter is intended to give a general overview to the evaluation procedure used for the measurement data presented in Chaps. 6, 7 and 8. Beside details on the retrieval of trace gas slant column densities with the DOAS method, an approach is shown to convert measurement results from HAIDI's nadir scanner to tropospheric vertical column densities on the basis of a simple geometrical approximation of the light path.

4.1. Spectral Retrieval

In order to retrieve slant column densities (SCDs) of the investigated trace gases from the recorded spectra, the data was analyzed with the DOAS method (Chap. 2), which is implemented in the here applied DOASIS (v3.2.4422.31514) software (Kraus, 2006). Due to the large amount of data (about half a million spectra per measurement flight) the evaluation process was automated using the software's integrated JScript support. In the process of the DOAS evaluation basically a Fraunhofer reference spectrum (FRS, $I_0(\lambda)$) and absorption cross-sections of several trace gases are fitted simultaneously to the measurement spectra in a given wavelength region by a least-squares fitting algorithm (Sec. 2.4). For each measurement campaign different amounts and types of fitted absorbers were used, because the focus was on different target trace gases and there were also large differences in the ambient temperature. An overview of the used wavelength intervals and fitted absorbers can be found in Tabs. 4.1 and 4.2. Apart from the listed absorbers also a polynomial for the broadband absorption part, an inverse FRS to account for stray light, a Ring spectrum calculated from the FRS by the DOASIS software, an additional Ring spectrum that is multiplied by λ^4 (Sec. 2.5) and some odd-even structures (Sec. 4.1.6) were fitted to the measured spectra.

4.1.1. Preparation of the Spectra

Prior to the actual DOAS analysis all required spectra are prepared by the evaluation script for further usage. This includes co-adding of measurement spectra as well as the subsequent correction for offset and dark current. Moreover, the literature absorption cross-sections are adapted to match HAIDI's spectral resolution. This is achieved by the convolution with an instrument function (Sec. 2.3), which is derived from measurements of a mercury emission line located within or close to the chosen retrieval wavelength range. For the O_3 absorption

Table 4.1.: List of literature absorption cross-sections used for the DOAS analysis.

No.	Molecule	Reference
1	SO_2 (298 K)	Vandaele et al. (2009)
2	BrO (298 K)	Fleischmann (2004)
3	BrO (243 K)	Fleischmann (2004)
4	NO_2 (246 K)	Voigt (2002)
5	NO_2 (293 K)	Voigt (2002)
6	O_3 (223 K)	Voigt (2001)
7	O_3 (246 K)	Voigt (2001)
8	O_3 (293 K)	Voigt (2001)
9	O_4 (293 K)	Hermans et al. (1999)
10	HCHO (298 K)	Meller & Moortgat (2000)
11	OClO (293 K)	Kromminga et al. (1999)

cross-section furthermore an I_0-correction is performed (Sec. 2.6), when applying the wavelength ranges of SO_2 or BrO fit scenarios. Finally, the wavelength-to-pixel mapping of the instrument is determined (Sec. 2.3). A rough initial calibration is done with the recorded mercury spectra. However, since the calibration parameters can change due to e. g. air pressure differences (see Sec. 4.1.4) the FRS is then re-calibrated by fitting it to a high resolution solar spectrum (Chance and Kurucz, 2010), which was previously convolved with the instrument function. Beside these things, the script also reads out information from the flight log (e. g. position, orientation, air pressure, wind speed, wind direction) and adds the data to the result file. This information is used to calculate the solar zenith and azimuth angles, for example, and they are also important input parameters for later plotting of the results.

4.1.2. Recording of the FRS

In order to minimize systematic noise during the DOAS analysis (see Sec. 2.4), the temporal distance between the reference and the actual measurement spectra was kept as small as possible. For this purpose, the FRS was normally taken for each individual flight, if possible. The recording procedure thereby differs for the two scanner types of the HAIDI system. While the nadir scanner uses a normal in-flight measurement taken in a presumably clear area as reference, the forward-looking telescope uses a spectrum taken at the ground where sunlight is guided to the telescope with a sand blasted teflon plate. Special care was taken, that the reference spectra were recorded in a region where the remaining absorption by the investigated trace gases was as close to zero as possible. For cases where the primary emission source of the considered species was known (e. g. volcanic emissions of SO_2, BrO, OClO), this was typically achieved by taking the FRS on the windward side of the emission source. Else an iterative approach was used, where spectra with the lowest retrieved dSCD were set as the new reference.

Table 4.2.: List of fitted absorbers and selected wavelength intervals. In Italy two different fit ranges for SO_2 were applied, due to non-linearity at high optical densities (Kern et al., 2010; Bobrowski et al., 2010).

Target Trace Gas	Wavelength Range in nm	Fitted Absorber	Polynomial Order	Campaign
SO_2 (Fit 1)	310.0...322.0	1, 2, 5, 6, 8, 10	3	Italy 2011
SO_2 (Fit 2)	314.8...326.8	1, 2, 5, 6, 8, 10	3	
BrO	332.8...364.0	1, 2, 5, 6, 8, 9, 10, 11	3	
NO_2	358.0...387.0	1, 5, 9, 11	3	
NO_2	358.0...387.0	5, 9	3	USA 2011 (Indiana)
BrO	336.0...365.0	3, 4, 6, 7, 9, 10	3	USA 2012 (Alaska)
NO_2	358.0...387.0	4, 9	3	

Because each viewing direction of a pushbroom scanner has a slightly different slit function, the forward-looking telescope uses a separate FRS for each elevation angle. The nadir scanner instead has the same slit function for all viewing directions and therefore uses only a single FRS for the analysis of the spectral data.

4.1.3. Retrieval Wavelength Ranges

The optimal fit range for the evaluation of the different absorbers was determined with the help of so-called "Vogel-Sihler-Plots" (Vogel et al., 2013). These are contour plots which show DOAS retrieval results (e. g. fit error, column density, etc.) color coded as a function of the lower and upper wavelength interval limits. In this way the influence of non-perfect absorption cross sections, cross correlations or instrumental features can be investigated for a large set of evaluation wavelength ranges at once. Some sample plots for the fit scenarios shown in Tab. 4.2 can be found in Appendix A.1.1, A.2.1 and A.3.1. Thereby, no significant differences in the optimal retrieval wavelength ranges were seen between data from the nadir scanner and from the forward-looking telescope.

As can be seen from Tab. 4.2, two different fit ranges were chosen for the evaluation of SO_2 in the emission plume of Mt. Etna: Fit 1 extends from 310.0 to 322.0 nm and was used for SO_2 column densities below 5×10^{17} molec/cm^2. The second fit scenario (Fit 2) uses a wavelength range from 314.8 to 326.8 nm instead and was applied for the evaluation of higher SO_2 dSCDs, in accordance with the investigations by Vogel (2011). This procedure was necessary due to non-linearity at high optical densities of SO_2 (Kern et al., 2010; Bobrowski et al., 2010). Figure 4.1 shows the effect by comparing results from the two fit scenarios. The other investigated trace gases had considerably lower optical densities and their evaluation was thus not affected by similar effects. A retrieval wavelength range from 358.0 to 387.0 nm showed good results for the

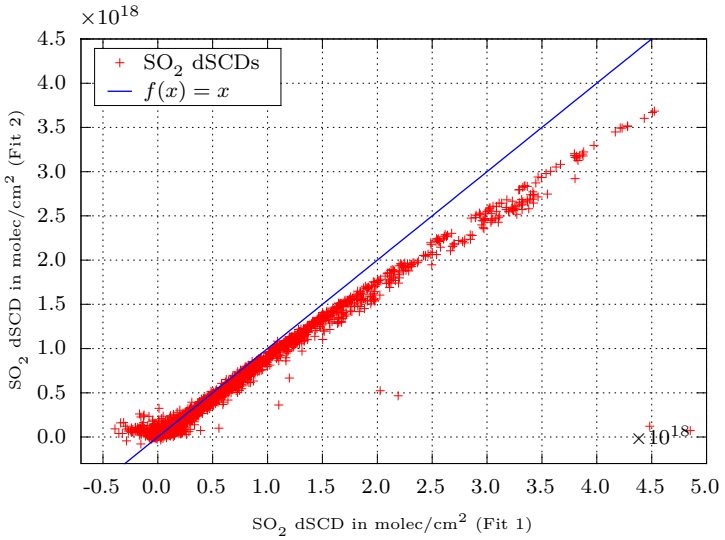

Figure 4.1.: Comparison of SO_2 column densities retrieved from two different wavelength ranges. Starting at about 0.5×10^{18} molec/cm^2 the SO_2 dSCDs are underestimated by fit scenario 1 (310.0 to 322.0 nm) due to non-linearity at high optical densities.

evaluation of NO_2 throughout all measurement campaigns. However, for the evaluation of BrO different wavelength ranges were found to be optimal. For the measurements on Sicily (Italy) a wavelength range from 332.8 to 364.0 nm was used to retrieve BrO and OClO column densities, while the best results for the flights at Barrow (AK, USA) were achieved with a wavelength range from 336.0 to 365.0 nm. Exemplary fit results for the evaluation of SO_2, BrO, OClO and NO_2 from the different campaigns can be found in Figs. 4.3 to 4.6.

4.1.4. Air pressure-induced Wavelength Shift

During the DOAS analysis it could be observed, that the fit routine applied a wavelength shift to the used reference spectra in dependency of the flight altitude. The observed values for the shift were linear with respect to the measured change in ambient pressure and of the order of 1×10^{-4} nm/mbar. This is in very good agreement with the theoretical wavelength shift caused by pressure-induced changes in the refractive index of air (0.988×10^{-4} nm/mbar at 350 nm). The shift is therefore due to the fact that all measurement flights up to now were performed in smaller, unpressurized aircraft and that HAIDI's spectrographs are also not pressure stabilized. During the BROMEX campaign (Alaska, 2012), flight altitudes of up to 3300 m were reached with a pressure difference of about 380 mbar in total. This means a shift of approximately 0.04 nm compared to spectra taken close to the ground. Figure 4.2 shows measurement data from a flight conducted during the campaign in Alaska to illustrate the effect. Here the wavelength shift applied to the reference spectrum by the DOAS fit routine is plotted versus the measured ambient pressure. The linear fit of the data yields a slope of 0.855×10^{-4} nm/mbar. In order to obtain better initial conditions for the DOAS fit, the values obtained from such plots were used

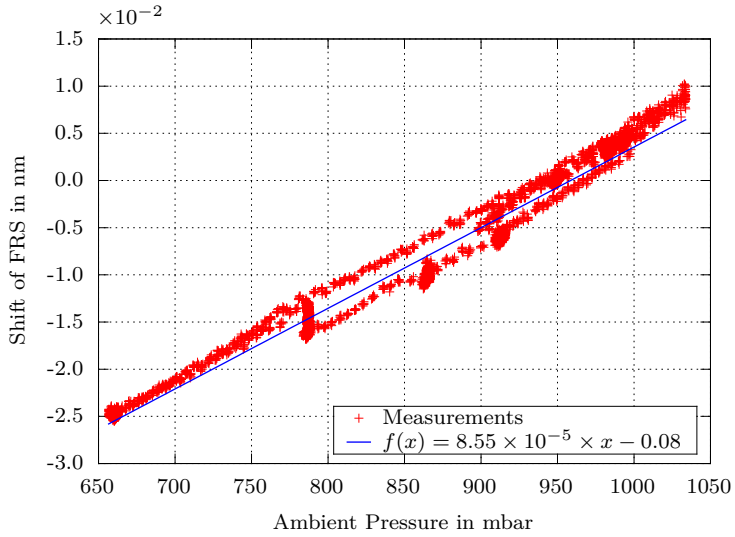

Figure 4.2.: Flight on 13$^{\text{th}}$ March 2012. The shift of the FRS shows a linear dependence on the pressure difference between reference and measurement spectrum. In this case the FRS was taken at an altitude of 630 m, which corresponds to an ambient pressure of 950 mbar.

to shift the measurement spectra according to their pressure difference from the FRS prior to the DOAS analysis. Since the initial wavelength calibration of HAIDI's instruments was done with the help of mercury emission lines on the ground but the reference spectra were taken somewhere in flight, the Fraunhofer references were re-calibrated using a high resolution solar spectrum (Chance and Kurucz, 2010) at the beginning of the evaluation procedure.

While ambient pressure informations is available for the flights performed in Indiana and Alaska, unfortunately no data exists for the flights at Mt. Etna. However, since the GPS device used to record the flight track also logs the actual altitude when receiving a sufficient number of satellites, the barometric formula was applied to calculate the corresponding pressure (Kuchling, 2001):

$$p(h_1) = p(h_0) \times \left(1 - \frac{0.0065 \times \Delta h}{T(h_0)}\right)^{5.255} \tag{4.1}$$

where $p(h_1)$ is the pressure at flight altitude (above mean sea level), $p(h_0)$ the pressure at the reference height, Δh the altitude difference between flight altitude and reference height and $T(h_0)$ the temperature at the reference height. As reference height one can take the mean sea level for instance. The pressure at mean sea level can be obtained from the data of a sounding balloon which is launched twice a day from Trapani Airport (LICT) in western Sicily (UWYO, 2011). For an estimated ambient temperature of 35 °C (308.15 K) at mean sea level, the calculated pressure curve shows a very good agreement with the data from the soundings balloon.

4.1.5. Typical Fit Results and Residuals

The residual spectrum of a DOAS analysis contains all structures that could not be assigned to one of the fitted absorbers. This could be, for example, noise, instrumental structures or unknown absorbers. The size of the residual is thus a good indicator for the quality of the measured spectra and the spectral analysis (Stutz, 1996). Some exemplary fit results with corresponding residual spectra are shown in Figs. 4.3 to 4.6. For a DOAS analysis free of systematic effects the size of the residual structures should mainly depend on the number of incident photons or on the number of co-added spectra, respectively. The calculated photon noise in Fig. 3.45 is therefore the best achievable value for the RMS of the residual. However, for atmospheric measurements the size of the residual structures will usually deviate earlier from the values predicted by photon noise. This can be due to varying reasons, a not perfectly uniform illuminated entrance slit, spectral structures caused by different ground features or viewing directions, a suboptimal fit scenario or imperfect reference spectra. In Tab. 4.3 the size of the residual structure as well as the achieved detection limit (4× fit error) is listed for different numbers of co-added scans. The co-added scans are thereby taken from a flight on 31st March 2012, from the same time interval as the exemplary fit results shown in Fig. 4.5 and 4.6. Since increasing the number of co-added scans will degrade the spatial resolution of the HAIDI system, a compromise between detection limit and spatial resolution has to be made depending on the optical density of the trace gas of interest.

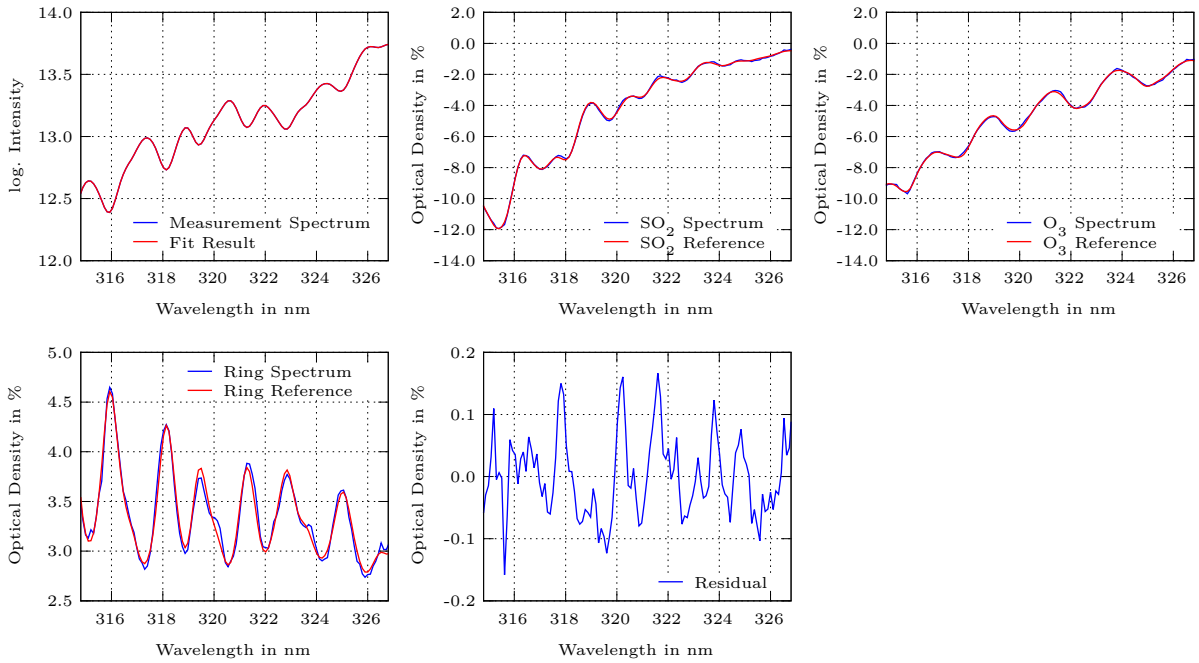

Figure 4.3.: Exemplary SO_2 fit from the flight on 9th July 2011. The SO_2 dSCD in this spectrum is 1.01×10^{18} molec/cm^2, thus the fit scenario for high optical densities (Fit 2, see Tab. 4.2) was applied here.

Table 4.3.: Influence of scan binning on spatial resolution and detection limit of the nadir scanner. The first value of the binning is the amount of included swaths, while the second value gives the number of co-added scans within each of these swaths. The spatial resolution ($P_{\parallel} \times P_{\perp}$) is calculated by equations (3.13) and (3.14) for average flight conditions ($h_{agl} = 1500\,\mathrm{m}$, $v_{air} = 55\,\mathrm{m/s}$).

Trace gas	Scan Binning	Spatial Res. in m	Tot. Integration Time in s	RMS of Residual	Detection Limit in molec/cm^2
BrO	1×8	39×137	0.2	5.41×10^{-4}	7.04×10^{13}
BrO	2×16	181×234	0.6	2.78×10^{-4}	3.63×10^{13}
BrO	4×16	465×234	1.3	2.24×10^{-4}	2.93×10^{13}
BrO	4×32	465×429	2.6	1.89×10^{-4}	2.47×10^{13}
NO_2	1×8	39×137	0.2	6.08×10^{-4}	5.60×10^{15}
NO_2	2×16	181×234	0.6	3.77×10^{-4}	3.47×10^{15}
NO_2	4×16	465×234	1.3	3.34×10^{-4}	3.07×10^{15}
NO_2	4×32	465×429	2.6	3.06×10^{-4}	2.81×10^{15}

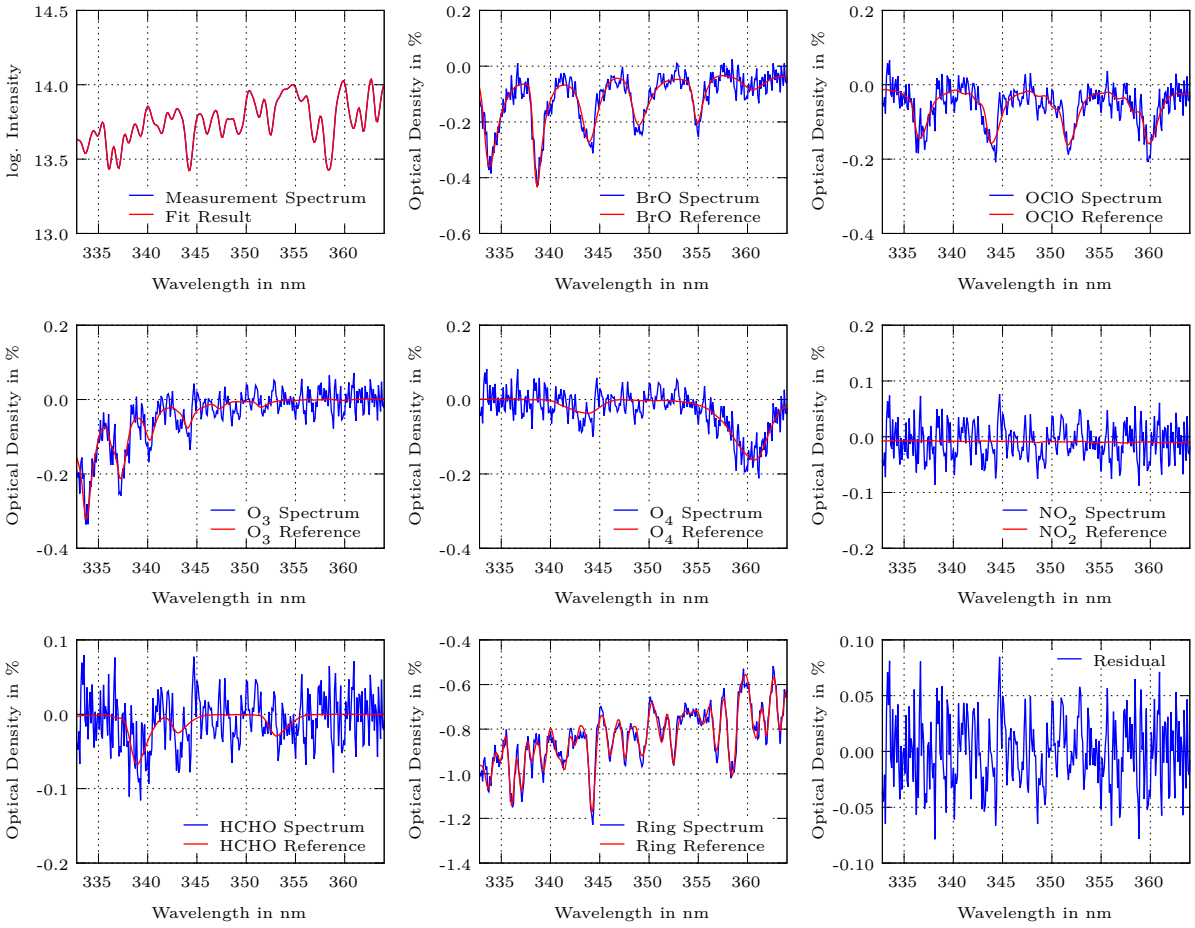

Figure 4.4.: Exemplary BrO fit from the flight on 9$^{\mathrm{th}}$ July 2011 showing a BrO dSCD of 3.01×10^{14} molec/cm^2 and a OClO dSCD of 1.53×10^{14} molec/cm^2.

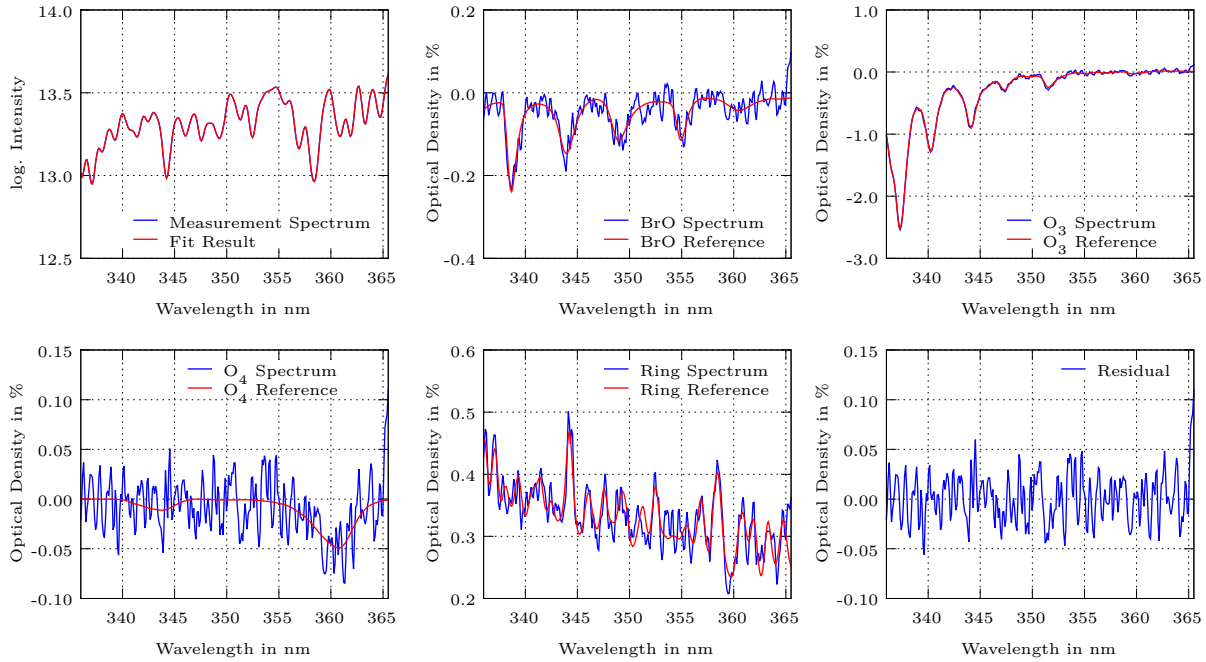

Figure 4.5.: Sample BrO fit (dSCD $\approx 1.6 \times 10^{14}$ molec/cm^2) of a nadir measurement taken from the flight to Prudhoe Bay on 31/03/2012 at 02:05 UTC. The red line shows the fitted absorption structure whereas the blue line shows the fit result plus the residual.

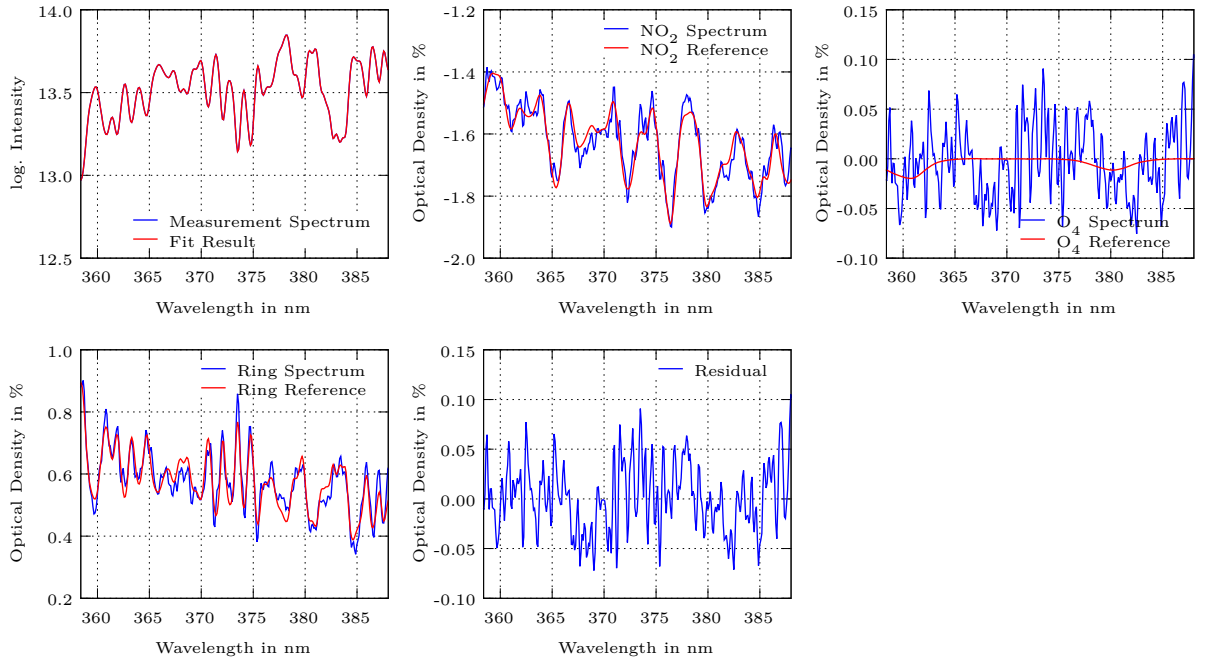

Figure 4.6.: Sample NO_2 fit (dSCD $\approx 3.1 \times 10^{16}$ molec/cm^2) of a nadir measurement taken from the flight to Prudhoe Bay on 31/03/2012 at 01:58 UTC. The red line shows the fitted absorption structure whereas the blue line shows the fit result plus the residual.

4.1.6. Fitting of odd-even Structures

Especially during the first two measurement campaigns (Italy 2011 and USA 2011) the CCD cameras of the HAIDI system were still affected by some technical problems. The most striking one was an increased electronic noise, which shows up as odd-even structure in the recorded spectra. Similar observations were already made by Lampel (2010), who used a readout electronic from the same manufacturer. In case of the HAIDI system, it turned out that the structures were somehow connected to the PWM signal of the CCD cooling and that their position in the spectrum changes with the value of this signal. Because the electronic noise results in larger residual structures during the DOAS analysis, it was necessary to reduce the odd-even structures to a minimum. However, since the structures had no fixed position in the spectrum, they could not be simply removed by subtracting the offset. Instead, synthetic odd-even structures were added as pseudo-absorbers to the fit scenarios.

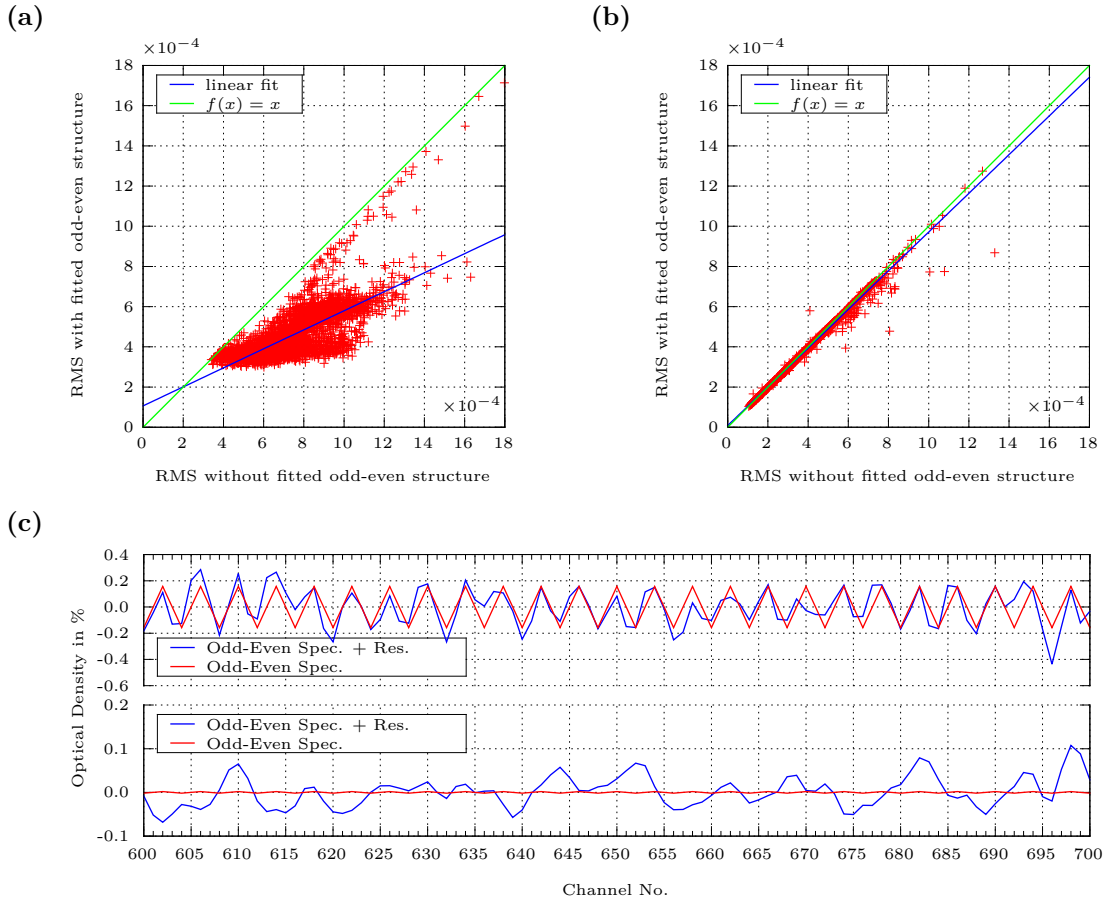

Figure 4.7.: Comparison of fit scenarios with and without fitted odd-even spectrum: (a) Resulting RMS of the residual for a measurement flight on 24$^{\text{th}}$ October 2011 (Binning: 1×128) (b) Resulting RMS of the residual for a measurement flight on 13$^{\text{th}}$ March 2012 (Binning: 1×128) (c) Fit of the odd-even spectrum with exemplary spectrum from 24$^{\text{th}}$ October 2011 in the upper half and from 13$^{\text{th}}$ March 2012 in the lower half.

The result of this effort can be seen in Fig. 4.7. Figure 4.7a shows data from a measurement flight, which was conducted during the campaign in Indiana (24$^{\text{th}}$ October 2011). Here the RMS of the residual is plotted for NO_2 fit scenarios with and without included odd-even spectrum. As one can see, the RMS decreases by about 50 % when the odd-even spectrum is included in the fit. A corresponding fit of the odd-even spectrum can be found in the upper part of Fig. 4.7c. Figure 4.7b instead shows data from a flight performed in the context of the BROMEX campaign (13$^{\text{th}}$ March 2012). At this time, the electronic noise has already been significantly reduced. For the evaluation of the data the same fit scenarios as for the flight in Indiana were applied, only the NO_2 absorption cross-section has been replaced to account for the different ambient temperatures (see Tab. 4.2). As can be seen, the fitting of the odd-even spectrum has virtually no effect anymore and the RMS of the residual is also generally lower compared to the data from Indiana. Thus, only very low optical densities can be seen from the fit of the odd-even spectrum in the lower part of Fig. 4.7c.

4.2. Geometrical Approximation of the Light Path

Because the DOAS analysis compares measured spectra against a reference spectrum, the retrieved results are so-called differential slant column densities (dSCDs), S'. The dSCDs give the concentration of the observed trace gases integrated along a particular light path through the atmosphere minus the integrated concentration already existing in the Fraunhofer reference spectrum. Since the light path through the absorber depends on several factors, like e. g. measurement geometry, solar zenith angle (SZA), θ, or weather conditions, measured dSCDs cannot be directly compared with measurements from other DOAS instruments (e. g. satellite measurements) or even in-situ measurements. Thus, to make the results more comparable, slant column densities are usually converted to vertical column densities (VCDs), which give the concentration along a vertical path through the atmosphere instead and are therefore independent of the used viewing direction. For this, the actual path taken by the photons through the absorber must be known. This is commonly achieved by applying radiative transfer models (RTM). However, for particular circumstances the light path of a measurement can also be estimated by a more simple geometric approximation. This is especially true for the whiskbroom scanner used in nadir direction, when flying at relatively low altitudes (≤ 3000 m) over areas with high surface albedo (e. g. ice, snow). In the following the light paths seen by the different viewing directions of the HAIDI system are described by geometrical considerations. In addition an approach is given to convert dSCDs, measured by HAIDI's nadir scanner, to tropospheric vertical column densities (VCD_{trop}), V_{trop}, on the basis of these considerations. Even if the geometric approximation is a strong simplification and RTM could give more precise results, it still has some advantages. It is very fast and relative simple to calculate, it does not depend on a priori values and gives a robust output.

4.2.1. Nadir Observations

Under the assumption that the majority of the detected photons are only once scattered on the ground (or very close to it) before entering the instrument and that the tropospheric absorber layer is horizontally homogeneously distributed on scales of a few hundred meters, there are three possible measurement scenarios for the nadir scanner. Either the aircraft is located above the absorber layer (Fig. 4.8a), within the absorber layer (Fig. 4.8b) or below the absorber layer (Fig. 4.8c). In each of these cases the length of the light path changes as a function of solar zenith angle θ, scan angle β and aircraft roll angle φ (see Fig. 4.8). The factors A_1 and A_2 thereby express the extension of the actual light path relative to to a vertical one and thus represent a proportionality factor between observed slant column densities and VCDs, the so-called air mass factor (AMF), $A = {}^{S}/_{V}$.

A_1 and A_2 are given by the following equations:

$$A_1 \approx \frac{1}{\cos\theta} \tag{4.2}$$

$$A_2 \approx \frac{0..1}{\cos(\beta - \varphi)} \tag{4.3}$$

The numerator of A_2 depends on the position of the aircraft in relation to the absorber layer and ranges from 1 (above the absorber) to 0 (below the absorber). The total extension of the light path in the troposphere is then given by the following equation:

$$A_{trop} = A_1 + A_2 \tag{4.4}$$

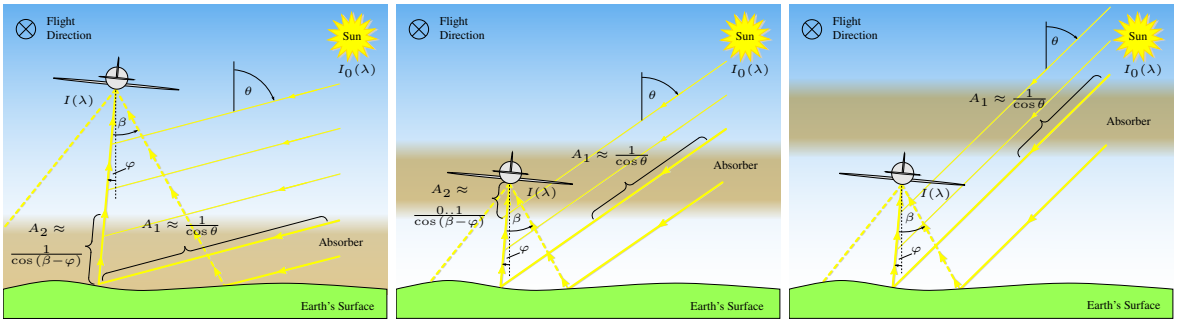

(a) aircraft above absorber **(b)** aircraft within absorber **(c)** aircraft below absorber

Figure 4.8.: Simple geometric approximation of the optical light path for the nadir looking whiskbroom scanner. Due to clear sky conditions and low flight altitudes ($\sim 1500\,\mathrm{m}$) most of the collected light is scattered on the ground. The length of the optical light path inside the absorber is determined by the factors A_1 and A_2.

The scenario where the aircraft is located above the absorber (Fig. 4.8a) can be applied in good approximation to the measurement campaigns II and III (see Tab. 5.1). Here, the trace gas layers were expected to be within the planetary boundary layer and thus below the typical flight altitude of the aircraft equipped with HAIDI. This could also be confirmed by the data from the forward-looking DOAS system. Hence, the tropospheric AMFs assumed for the measurements presented in Chaps. 7 and 8 were calculated as follows:

$$A_{trop} = \frac{1}{\cos\theta} + \frac{1}{\cos(\beta - \varphi)} \tag{4.5}$$

For the flights at Mt. Etna instead, where the absorber layer was not located close to the ground, one has to distinguish between measurements taken above the emission plume and those taken below. Measurements from below the plume are expected to show generally lower dSCDs, due to the smaller AMFs (see Eq. (4.3)). In addition there can be a spatial offset in dependency on the solar zenith and azimuth angles. Thus, for a better comparability, maps presented from Mt. Etna in Chap. 6 show only data for flight altitudes greater than the expected height of the emission plume.

4.2.2. Conversion of dSCDs to tropospheric VCDs

In order to convert dSCDs to tropospheric VCDs, one has to consider that the observed signal does not only arise from tropospheric absorbers. Many of the fitted trace gases are also present in the stratosphere. Since the flight altitude of an unpressurized aircraft will not reach the height of stratospheric absorbers, the stratospheric AMF remains unchanged for all three measurement scenarios described in the previous section. The stratospheric AMF, A_{strat}, therefore only depends on the SZA and can be approximated similar to A_1 in the troposphere:

$$A_{strat} = \frac{1}{\cos\theta} \tag{4.6}$$

Before A_{trop} and A_{strat} can be used to convert the measured dSCDs, S', to tropospheric VCDs, one first has to make clear that the column density in the measurement spectra is composed as follows:

$$\begin{aligned} S' &= S'_{trop} + S'_{strat} \\ &= \underbrace{S_{trop} - S_{Ref,trop}}_{S'_{trop}} + \underbrace{S_{strat} - S_{Ref,strat}}_{S'_{strat}} \end{aligned} \tag{4.7}$$

where S_{trop} is the tropospheric SCD in the measurement, $S_{Ref,trop}$ the tropospheric SCD in the Fraunhofer reference, S_{strat} the stratospheric SCD and $S_{Ref,strat}$ the stratospheric part of the

SCD in the Fraunhofer reference. The relative change in stratospheric SCD, S'_{strat}, can then be expressed by the stratospheric AMF:

$$\begin{aligned} S'_{strat} &= S_{strat} - S_{Ref,strat} \\ &= V_{strat} \times A_{strat} - V_{Ref,strat} \times A_{Ref,strat} \end{aligned} \tag{4.8}$$

By assuming that the stratospheric VCD remains relatively constant during the flight (be aware that this assumption is not valid for all trace gases) and thus V_{strat} and $V_{Ref,strat}$ are identical, one obtains:

$$S'_{strat} = V_{strat} \times (A_{strat} - A_{Ref,strat}) \tag{4.9}$$

and thus:

$$\begin{aligned} S' = V_{trop} \times A_{trop} - \underbrace{V_{Ref,trop} \times A_{Ref,trop}}_{\approx 0} \\ + V_{strat} \times (A_{strat} - A_{Ref,strat}) \end{aligned} \tag{4.10}$$

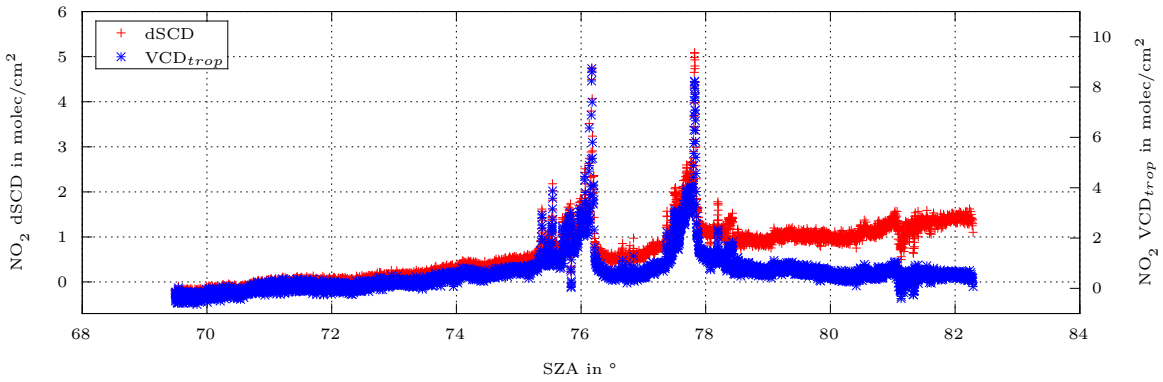

Figure 4.9.: Comparison of measured NO_2 dSCDs and resulting tropospheric VCDs from a flight on 31st March 2012. While the dSCDs show a continuous increase due to an increasing stratospheric AMF (Eq. (4.9)), this is almost compensated in the calculated tropospheric VCDs (Eq. (4.11)) by assuming a stratospheric NO_2 VCD of 2.5×10^{15} molec/cm^2 (Wenig et al., 2004).

With a careful selection of the Fraunhofer reference spectrum, $V_{Ref,trop}$ can be assumed to be zero. This selection can be e. g. if the reference spectrum was taken upwind of an emission source or if additional measurements like from the forward-telescope approve a zero VCD. The above equation can finally be rearranged to V_{trop}:

$$\Rightarrow V_{trop} = \frac{S' - V_{strat} \times (A_{strat} - A_{Ref,strat})}{A_{trop}} \tag{4.11}$$

The required stratospheric VCD of the absorber can then be obtained from model calculations or reference data, if available. An example for the conversion of measured dSCDs to tropospheric VCDs can be seen in Fig. 4.9.

4.2.3. Limb Observations

The following section is adapted from (General et al., 2014).

For a telescope looking towards the horizon (limb geometry) the geometrical AMF would lead to significant deviations, because in contrast to the nadir observations it cannot be assumed here that the majority of the collected light is scattered at a given location. Instead light is scattered into the telescope from somewhere along its line of sight (LOS). Under clear sky conditions most direction changes of light are induced by Rayleigh scattering on air molecules. Thus, due to typical Rayleigh extinction lengths of about 14 km at 350 nm, very long light paths can be obtained within horizontally extended absorbers.

Limb observations performed at different flight altitudes are particularly well suited for a reconstruction of trace gas and aerosol profiles at high vertical resolution (e. g. Heue et al., 2011; Prados-Roman et al., 2011; Merlaud et al., 2012; Baidar et al., 2013; Dix et al., 2013). This is usually done in a two-stage process using inverse modeling of the atmospheric radiative transfer (e. g. Sinreich et al., 2005; Wagner et al., 2004; Frieß et al., 2006; Irie et al., 2008; Clémer et al., 2010; Wagner et al., 2011). First, the aerosol extinction profile is retrieved from the absorption of the oxygen collision complex O_4, which has a horizontally constant atmospheric concentration (apart from pressure variations) and therefore serves as a proxy of the light path which is affected by aerosols. Second, the trace gas vertical profile is retrieved using the measured trace gas dSCDs together with the aerosol profile retrieved in the first step. Resting upon the Bayesian approach, our retrieval algorithms determine the maximum a posteriori solutions of the given inverse problems on the basis of the well-known optimal estimation method (Rodgers, 2000) and use the SCIATRAN (Rozanov et al., 2001) and McArtim (Deutschmann et al., 2011) radiative transfer code as forward models for the aerosol and trace gas retrievals, respectively. This method has been applied e. g. to ground-based MAX-DOAS measurements of BrO and aerosols in the scope of the OASIS Barrow 2009 campaign (Frieß et al., 2011).

A key quantity that describes the performance of the profile retrieval is the weighting function $\mathbf{K} = \partial\mathbf{y}/\partial\mathbf{x}$, which represents the sensitivity of the measurement $\mathbf{y}$ to variations of the state vector (i. e., aerosol or trace gas vertical profile) $\mathbf{x}$. In case of trace gas profiles, the weighting function is equal to the box airmass factor, i. e. the derivative of the measured slant column density with respect to the partial vertical column in an altitude layer $[z, z + \Delta z]$. Figure 4.10

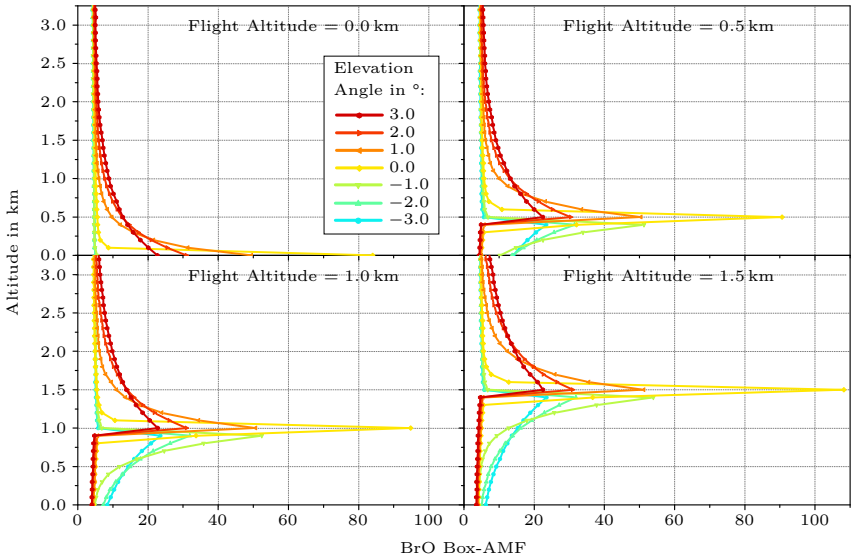

Figure 4.10.: BrO box AMFs calculated for the different viewing directions of HAIDI's forward-looking telescope.

shows BrO box AMFs calculated at a wavelength of 350 nm for a small aerosol extinction of 0.01 km^{-1} between surface and 1 km altitude and zero above for the viewing geometry of the HAIDI limb telescope. The calculations were performed for flight altitudes of 0 km, 0.5 km, 1 km and 1.5 km. As expected, the highest sensitivity for trace gases is achieved directly at the flight altitude when looking towards the horizon (elevation angle of 0°), here the box-AMF reaches values of more than 100. However, with viewing directions covering ±3°, the range where measurements are sensitive is restricted to about 1 km around the flight altitude. Thus, measurements with the forward-telescope (pushbroom) are especially suited for the observation of volcanic plumes close to the flight altitude (Vogel et al., 2011), or to investigate boundary layer absorbers when flying low. A reconstruction of the whole tropospheric profile (surface to 10 km) is only possible when measurements during a whole ascent or descent of the airplane are used as input for the retrieval.

5. Measurement Campaigns

In this chapter, the measurement campaigns conducted with the first setups of the HAIDI system are presented. Beside the scientific goals these measurements were likewise intended as a test of the overall system. Thus, not only the hardware components like whiskbroom scanner, CCD camera and spectrographs could be checked for their functionality under various conditions, but also the software written for instrument control, temperature stabilization as well as data evaluation and visualization could be tested and improved. In total three measurement campaigns to different regions of the world were accomplished between July 2011 and March 2012. The first one already started in summer 2011, where the HAIDI system was used for several flights aboard an ultralight aircraft in order to map volcanic emission plumes at Mt. Etna and Mt. Stromboli on Sicily, Italy. Afterwards, in fall of the same year, some flights over Indianapolis, Indiana, were performed to investigate the air pollution in urban regions. Finally the system was used to map BrO and NO_2 distributions in the polar boundary layer around Barrow, Alaska in context of the BROMEX campaign in spring 2012. Up to now a total of 18 measurement flights were performed with the HAIDI system. An overview of the conducted measurement campaigns can be found in Tab. 5.1.

Table 5.1.: List of conducted measurement campaigns to date, with corresponding time period and number of flights.

Campaign	Base Airport	Date of first flight	Date of last flight	total number of flights
I	Calatabiano, Sicily (Italy)	07/07/2011	09/07/2011	4
II	West Lafayette, Indiana (USA)	23/10/2011	25/10/2011	3
III	Barrow, Alaska (USA)	13/03/2012	31/03/2012	11

5.1. Etna Campaign (2011)

The first measurement flights with the HAIDI system were performed in July 2011 on Sicily, Italy. For these flights the system was installed on a Flight Design CTLS ultralight aircraft

Table 5.2.: List of conducted flights during the measurement campaign in Italy. Shown are the particular flight times and the availability of important flight parameters like GPS or INS. Also the existence of images from forward (F) and nadir (N) webcam is indicated. ✓: data available ✗: no data available.

Date	Takeoff (UTC)	Landing (UTC)	Flight Duration	SZA Range	Webcam (N/F)	GPS	INS	Comments
07/07/2011	11:30	-	-	-	✗ ✗	✗	✗	no GPS
07/07/2011	17:50	19:57	127 min	85...105°	✗ ✓	✓	✗	low light
07/08/2011	07:50	09:51	121 min	44...22°	✓ ✗	✓	✗	-
07/09/2011	08:00	10:46	166 min	42...16°	✓ ✗	✓	✗	-

with the setup described in Chap. 3.11.1. The aircraft was operated by the FH Düsseldorf under the leadership of Prof. Konradin Weber and piloted by Uwe Post. Between the 7th and 9th of July four flights to Mt. Etna and Mt. Stromboli were conducted in total. However, due to several technical problems sufficient data for analysis is only available from the last two flights to Mt. Etna (see Tab. 5.2). There were, for example, repeatedly blackouts in the hangar so that the main battery of the system could hardly be charged completely and the power supply for the instruments already failed shortly after take off in some cases. Other difficulties occurred with the CTLS's inertial navigation system (INS) and GPS. The log file of these systems could unfortunately not be exported to a readable file format, because it was only intended for service. Therefore, pitch and roll angles are not available and GPS data only exists for a part of the flights, where an additional GPS handheld was aboard the aircraft. Also some technical problems with the instrument itself appeared. The CCD camera still suffered from an increased electronic noise, which resulted in larger residual structures during the data analysis and thus lower measurement accuracy than usually achievable with the system (Sec. 4.1.6). Moreover, the forward-looking telescope could not be used throughout the whole campaign due to a shutter malfunction. The reliability of the shutter mechanism could be improved afterwards the campaign but the elimination of the electronic noise required revised readout electronics for the CCD cameras, which were not available until the campaign in Alaska.

Mount Etna is Europe's highest[1] and most active volcano. It is located on the east coast of Sicily in southern Italy (37.755° N, 14.995° E), close to Catania. Since Mt. Etna is located directly above a convergent plate boundary, it is assumed that the volcano was formed about 600 000 years ago by processes involved in the subduction of the African Plate beneath the Eurasian one (Gvirtzman and Nur, 1999). The summit area of the volcano actually reaches an altitude of approximately 3323 m and consists of four craters: Bocca Nuova (with two vents,

[1] Considering only European mainland. The highest volcano of the entire European territory is Mount Teide on Tenerife with 3718 m.

one in the northwest and one in the southeast), Voragine, the North-East crater (NEC) and the South-East crater (SEC). Since its formation in 1971 the SEC is the most active summit crater of Mt. Etna (Neri and Acocella, 2007). However, during the last few years the volcanic activity increasingly shifted towards a new crater, which formed on the eastern flank of the old SEC cone in the beginning of 2011 (Scollo et al., 2012; Rizzo et al., 2013). The new crater is therefore informally called the New South-East Crater (NSEC). Typical volcanic activity at Mt. Etna is characterized by persistent degassing from one or more of the summit craters and frequent strombolian activity as well as lava flows, which mostly originate from flank eruptions (Coltelli et al., 1998). Since almost a million people live in the area potentially threatened by these eruptions, Mt. Etna's activity is regularly monitored by the Istituto Nazionale di Geofisica e Vulcanologia (INGV) in Catania (Bonaccorso et al., 2011).

5.1.1. Volcanic Activity

July 2011 was generally marked by a notable intensification of eruptive activities at Mt. Etna (INGV, 2011). Already in the beginning of July ash emission from the Bocca Nuova crater and moderate strombolian activity at the NSEC could be observed (Fig. 5.1a). The night between the 7^{th} and 8^{th} of July furthermore showed a progressive increase in tremor amplitude and strombolian explosions from the active vent at the south-eastern flank of the old SEC. Although various signs indicated the imminence of the fifth paroxysm of the year, volcanic activity decreased towards morning of the 8^{th} July and only weak gas emissions from the NSEC and occasional ash releases at Bocca Nuova were observed after daybreak (INGV, 2011). Towards morning of the 9^{th} July volcanic activity at Mt. Etna increased again. This increase was initially rather weak with only little strombolian activity at the NSEC. Then, shortly after 11:00 UTC (13:00 local time) the tremor amplitude started to increase rapidly and at around 13:45 UTC lava fountaining occurred at the NSEC, accompanied contemporaneously by strong explosive ash emission from the Bocca Nuova crater and a lava flow into the Valle del Bove (INGV, 2011). The volcanic activity finally reached its maximum between 14:00 and 15:00 UTC. In total, the paroxysmal activity lasted for about one hour and quickly attenuates after 15:00 UTC (INGV, 2011). The emitted ash column extended several kilometers in height and propagated with the wind in south-eastern direction. This leads to ash and lapilli rain over inhabited area in the vicinity of Mt. Etna (INGV, 2011). Also the nearby Catania airport was temporary closed due to the ash emissions. Photos from the two measurement days, showing meteorological conditions and volcanic activity can be found in Fig. 5.1.

5.1.2. Scientific Objectives

Beside the fact that the first flights with the HAIDI system were used as a general test for the instrument under real measurement conditions, also a number of scientific objectives were pursued during the campaign. One goal was the spatially high-resolved imaging of trace gases

(a) 7th July, 5:58 UTC

(b) 8th July, 4:38 UTC

(c) 9th July, 09:39 UTC

(d) 9th July, 14:09 UTC

Figure 5.1.: Pictures of Mt. Etna, showing the volcanic activity and meteorological conditions: (a) Explosions at Etna's Bocca Nuova crater with ash emission forming a plume of several hundred meters height. (b) View at Mt. Etna from the location of the airport. Since the airport is located to the east of the volcano, one can see the emission plume propagating to the south. The altitude of the plume is thereby approx. equal to the height of the summit (3300 m). (c) Mt. Etna during the measurement flight at about noon local time. (d) Photo taken from the aircraft shorty after the beginning of the paroxysm. A large ash plume from Bocca Nuova can be seen propagating to the south.

like BrO, OClO and SO_2 in volcanic plumes with the nadir scanner of the system. Reactive halogen compounds like BrO are of special interest due to their impact on tropospheric chemistry (see Sec. 1.1). SO_2 instead is a relatively inert gas and its concentration is therefore expected to be quite constant in time (depletion rate of $\sim 4\,\%$ per hour, McGonigle et al. (2004)). For this reason SO_2 can be used as a tracer for the dilution of volcanic gases, which allows to study ongoing bromine chemistry in volcanic plumes by observing the spatial and temporal evolution of the BrO/SO_2 ratio. Since BrO itself is no initial constituent of the emitted gases, it is believed to be produced by an autocatalytic reaction in the plume from emitted HBr (Sec. 1.1.2.1). Because the required O_3 and HO_2 have to be mixed into the plume from the ambient air, the oxidation of halogenides should be more effective at the edges of the plume, resulting in enhanced BrO towards the edges. This has already been shown by Bobrowski et al. (2007) and Louban et al. (2009), and is again observed in the here presented measurements. Furthermore, the BrO/SO_2 ratio in plumes generally increases with distance from the emission source

(e. g. Oppenheimer et al., 2006a; Bobrowski et al., 2007; von Glasow, 2010) indicating a chemical production of BrO in the volcanic plume. New enhanced data sets (e. g. Vogel, 2011; Bobrowski and Giuffrida, 2012; Platt and Bobrowski, 2014) show that after an initial increase the BrO/SO_2 ratio reaches a quasi-equilibrium state for a certain - still to be determined - period of time. The investigation of reactive species like BrO and OClO in volcanic emissions is hence still an active field of research. However, do date there is only a very limited number of investigations showing the spatial distribution of these trace gases in volcanic plumes.

5.1.3. Instrumental Settings

Due to high ambient temperatures of more than 30 °C on the ground, the spectrographs were stabilized to 25 °C during all flights. This temperature was within the cooling capabilities of the temperature stabilization and could also be kept on high flight altitudes thanks to a heated cockpit. Additional instrumental settings can be found in Tab. 5.3. The table also shows the scan binning used for the maps and time series presented in this chapter, unless otherwise specified in the figures. Thereby, the first value of the binning is the amount of included swaths, while the second value gives the number of co-added scans within each of these swaths.

Table 5.3.: Instrumental settings used for the measurement campaign in Italy. The forward-looking telescope was not operational due to a shutter malfunction.

	Nadir Scanner	Forward-looking Telescope
CCD Temperature	−10 °C	n/a
Wavelength Interval	288.1...394.8 nm	n/a
Integration Time	51.1 ms (8^{th}) / 100.8 ms (9^{th})	n/a
Binned Scans	32 (2×16)	n/a
Webcam Interval	5 s (8^{th}) / 10 s (9^{th})	n/a
Spectrograph Temp.	25 °C	

5.1.4. Flight Tracks

All measurement flights during this campaign were performed from a small airport (37.800° N, 15.228° E) close to Calatabiano in the northeast of Mt. Etna. In order to investigate the emission plume of Mt. Etna, several traverses were flown along the centerline of the plume and perpendicular to its propagation direction. Thereby, distances of 1–19 km to the summit crater region (according to plume ages of 2–34 min) and altitudes up to 3800 m were covered. Since

the meteorological conditions were relatively constant during the campaign, the flight tracks of 8th and 9th are very similar. A map with the flight tracks can be found in Fig. 5.2.

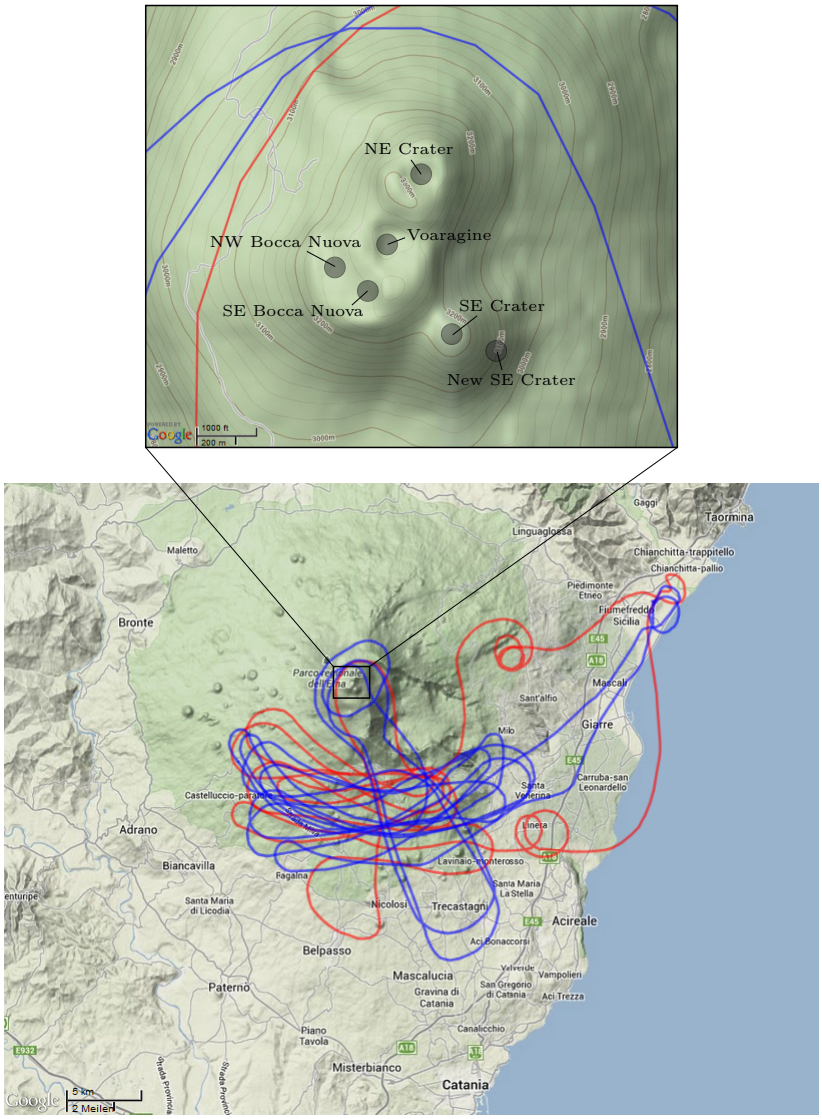

Figure 5.2.: Topographical map of the region around Mt. Etna (Sicily, Italy), showing the full flight tracks from 8th (red) and 9th (blue) July 2011. All flights were performed from the airport in Fiumefreddo, in the northeast of the map. In the upper part of the figure a detail from the map with the summit craters of Mt. Etna is shown (Google, 2013).

5.1.5. Meteorological Conditions

In the following, meteorological data is shown for the flights presented in Sec. 6. Since the ultralight aircraft was not equipped with additional instruments for the recording of atmospheric conditions such as wind speed, wind direction and air temperature, the required information was obtained from sounding balloon data (UWYO, 2011). Plots of the respective data can

be found in Fig. 5.3. The balloon measurements started every day at about 12:00 UTC from Trapani Airport (37.91° N, 12.50° E), approximately 200 km western of Mt. Etna. Furthermore, Fig. 5.4 shows some true color images from the Moderate Resolution Imaging Spectroradiometer (MODIS) instruments aboard the NASA satellites Terra and Aqua, which reveal the cloud cover for the period of the flights (NASA, 2011).

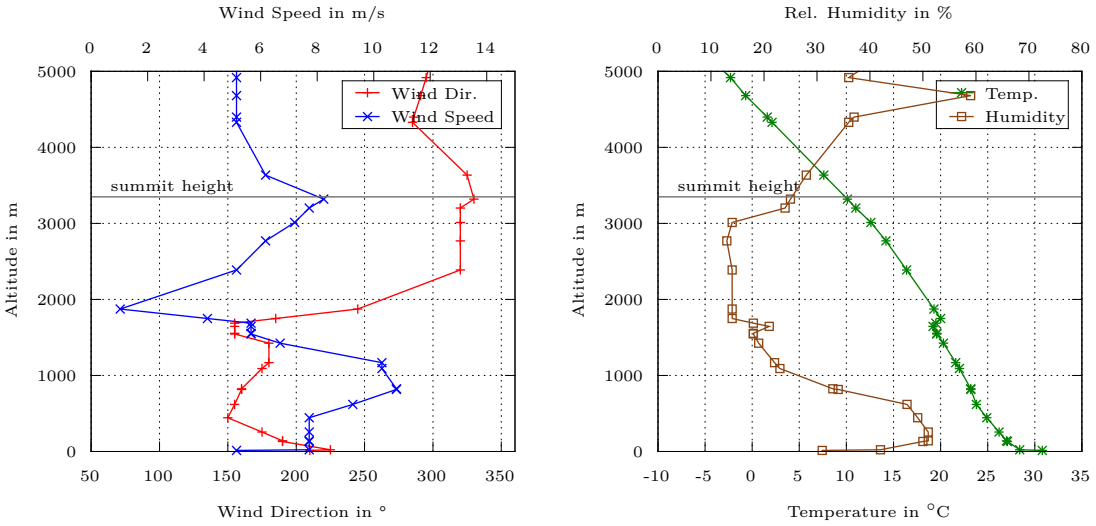

(a) Data from 8th July

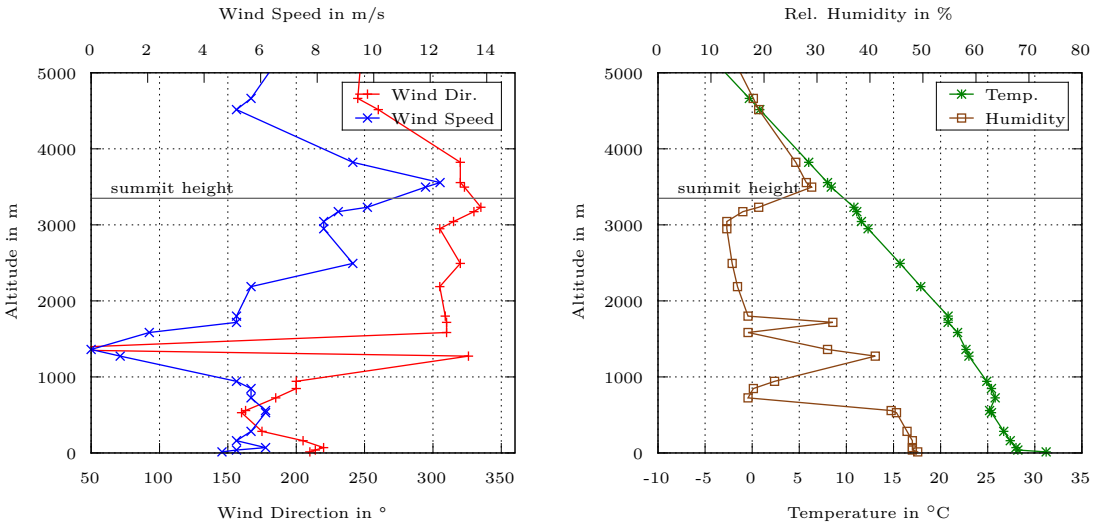

(b) Data from 9th July

Figure 5.3.: Sounding balloon data showing the meteorological conditions on 8th and 9th July 2011 (UWYO, 2011). Measurements at the summit height of Mt. Etna are indicated by the gray horizontal line.

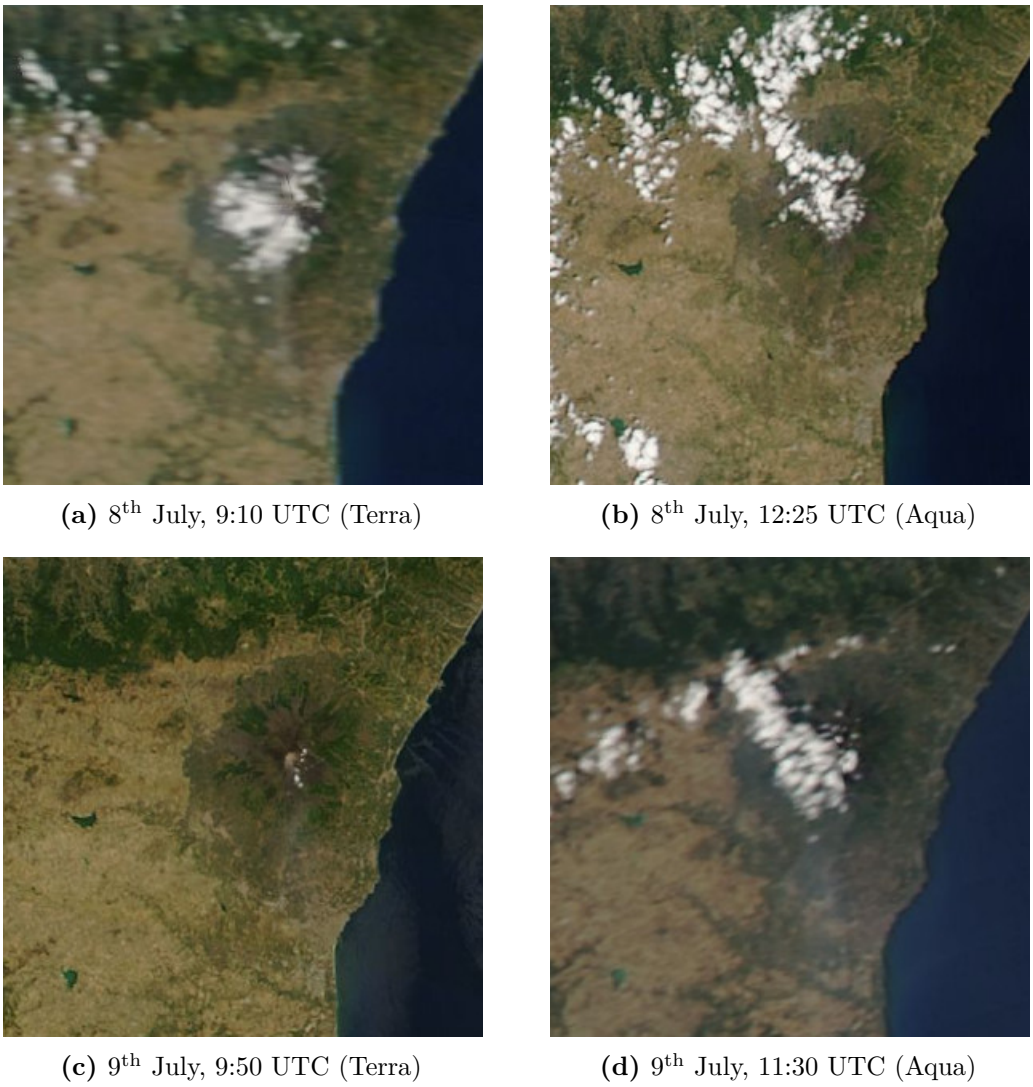

(a) 8th July, 9:10 UTC (Terra)

(b) 8th July, 12:25 UTC (Aqua)

(c) 9th July, 9:50 UTC (Terra)

(d) 9th July, 11:30 UTC (Aqua)

Figure 5.4.: True color satellite images from 8th and 9th July 2011 showing the region around Mt. Etna. The images were taken at different times by the MODIS instruments on Terra and Aqua (NASA, 2011).

5.2. Indiana Campaign (2011)

The second campaign took place at Purdue University in fall of 2011. Purdue University is located in West Lafayette, Indiana (USA). Following an invitation from Professor Paul Shepson, HAIDI was installed on the Airborne Laboratory for Atmospheric Research (ALAR), which is a twin-engined research aircraft (modified Beechcraft Duchess) operated by the Purdue University Department of Chemistry and usually piloted by Professor Shepson himself. The aircraft is equipped with several instruments for atmospheric research, including an air flow measurement probe (**B**est **A**ir **T**urbulence probe) and an ozone monitor (2B Technologies, Model 205). A detailed description of the instrumental setup for the campaign can be found in Sec. 3.11.2.

In total three measurement flights to the greater area of Indianapolis were performed in the

context of the campaign between 23rd and 25th of October. Tab. 5.4 shows an overview of the performed flights. As can be seen in the table, there were some problems with the control of HAIDI's nadir scanner. During two of the three flights the prism of the nadir scanner did not move as intended, resulting in a loss of spatial information.

Table 5.4.: List of conducted flights during the measurement campaign in Indiana, USA. Denoted are the particular flight times and the availability of important flight parameters like GPS or INS. ✓: data available ✗: no data available.

Date	Takeoff (UTC)	Landing (UTC)	Flight Duration	SZA Range	Webcam (N/F)	GPS	INS	Comments
10/23/2011	18:26	21:06	160 min	53...72°	✗ ✓	✓	✓	partly no GPS
10/24/2011	16:31	19:01	150 min	53...56°	✓ ✗	✓	✓	scanner problems
10/25/2011	16:42	18:54	132 min	53...56°	✓ ✓	✓	✓	scanner problems

5.2.1. Scientific Objectives

The flights at Purdue University were primary intended to check HAIDI's overall instrumental setup in preparation for the BROMEX campaign (Chap. 8) at the beginning of 2012. However, since Purdue University is located about mid-way between the metropolitan areas of Indianapolis and Chicago, the flights also offered the opportunity to investigate the air pollution over larger urban areas. In particular, the spatial distribution of tropospheric NO_2 was investigated by the measurements. NO_2 mainly enters the atmosphere in the form of NO from anthropogenic sources such as the burning of fossil fuels and can cause enhanced ground level ozone, the so-called photosmog, during sunny days. Both, ozone as well as nitrogen dioxides are toxic to humans when inhaled at higher concentrations for a prolonged period of time. Tropospheric NO_2 also contributes to acid rain, resulting from its oxidation to HNO_3. Moreover, the emission strength of air pollutants like NO_2 from individual sources, or from a given area, is an important input factor for atmospheric chemistry and transport models. Therefore, data from the measurements was also used to determine the total NO_2 flux of the Indianapolis metropolitan area by flying traverses downwind of the city.

5.2.2. Flight Preparations

In preparation for the measurement flights several attempts were made to calibrate the viewing direction of the forward-looking telescope by the method described in Sec. 3.5.1. Unfortunately

the necessary INS data could not be recorded during any of these attempts, because of technical problems with the data storage system of the aircraft. Therefore, the exact viewing direction of the telescope remains unknown. However, since the used mount for the entrance optics box was the same as during the later BROMEX campaign, the viewing direction of the forward-looking telescope, relative to the orientation of the aircraft, was assumed to be identical for both campaigns in the following. Thus, an offset of $-0.8°$ was added to the pitch angle of the aircraft to get the center viewing direction of the telescope. The viewing angles displayed in the time series data of the forward-looking telescope (Figs. 7.1, A.5 and A.8) were already corrected by this angle. Furthermore the pitch angle of the aircraft has been added, so that the displayed values directly give the viewing directions of the telescope in relation to the horizon.

5.2.3. Instrumental Settings

For the campaign in Indiana the spectrographs were set to a temperature of 23 °C, which was approximately the ambient temperature on the ground. Additional parameters are listed in Tab. 5.5.

Table 5.5.: Instrumental settings used for the measurement campaign in Indiana.

	Nadir Scanner	Forward-looking Telescope
CCD Temperature	−5 °C	0 °C
Wavelength Interval	300.7...407.3 nm	300.0...406.5 nm
Integration Time	20.2 ms (10.8 ms on 23rd)	dynamic (∼ 1000 ms)
Binned Scans	1 × 128 (4 × 16 on 23rd)	10
Webcam Interval	5 s (2 s on 25th)	5 s
Spectrograph Temp.	23 °C	

5.2.4. Flight Tracks

The measurement flights in Indiana were performed from a small airfield (40.412° N, 86.937° W), which is operated by the Purdue University close to the urban area of West Lafayette. A map with the flight tracks can be found in Fig. 5.2. In order to investigate the emissions originating from Indianapolis, traverses were flown according to the particular wind direction on that day.

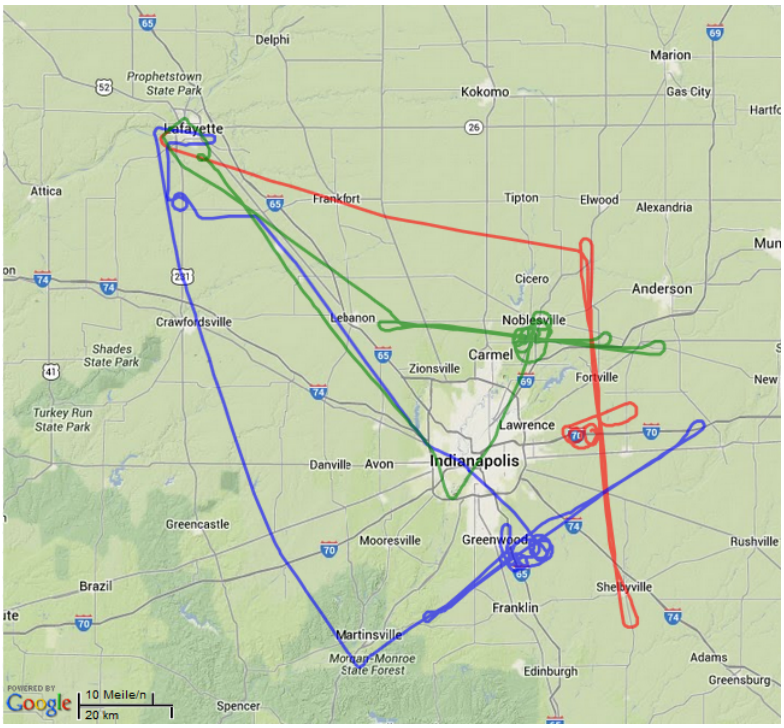

Figure 5.5.: Topographical map of the region around Indianapolis (Indiana, USA), showing the full flight tracks from 23rd (red), 24th (blue) and 25th (green) October 2011. All flights were performed from the airport in West Lafayette, in the northwest of the map (Google, 2013).

5.2.5. Meteorological Conditions

In the following, meteorological data is shown for the measurement flights performed in Indiana. Atmospheric conditions like wind speed and wind direction were recorded by the BAT probe of the aircraft during all flights with a sampling rate of 100 Hz. An overview of average wind speeds and directions can be found in Tab. 5.6. Additional time series with the BAT probe data can furthermore be found in the result section (Sec. 7). For the flight on 24th October, which is discussed in Sec. 7, the cloud cover was documented by some in-flight photos (Fig. 5.6). On a larger scale, the cloud cover can be seen on true color satellite images from the two MODIS instruments (Fig. 5.7).

Table 5.6.: Average wind directions and speeds for flight altitudes below 1000 m measured by ALAR's BAT probe during the campaign in Indiana.

Date	Wind Direction in °	Wind Speed in m/s
10/23/2011	239 ± 18	6.1 ± 1.3
10/24/2011	309 ± 15	7.7 ± 1.9
10/25/2011	205 ± 12	12.2 ± 4.8

(a) 17:17 UTC, ①

(b) 18:04 UTC, ②

(c) 18:25 UTC, ③

(d) 18:47 UTC, ④

Figure 5.6.: Photos taken during the flight to Indianapolis on 24$^{\text{th}}$ October 2011. The corresponding recording locations can be found in Fig. 7.2, indicated by the encircled numbers: (a) At the beginning of the flight a dense cloud layer could be observed eastern of Indianapolis. (b) Some smaller clouds were also seen in the south. (c) View from the town center to the east with clouds in the background. (d) Clear sky close to Purdue University airport at the end of the flight.

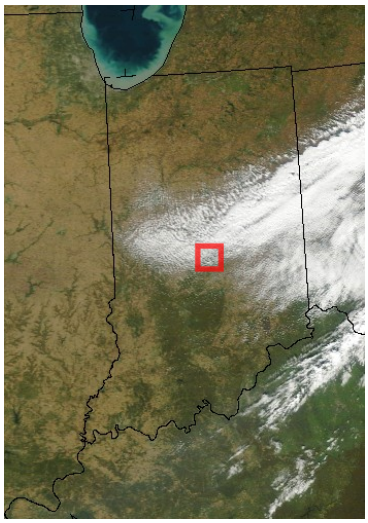

(a) 16:03 UTC (Terra)

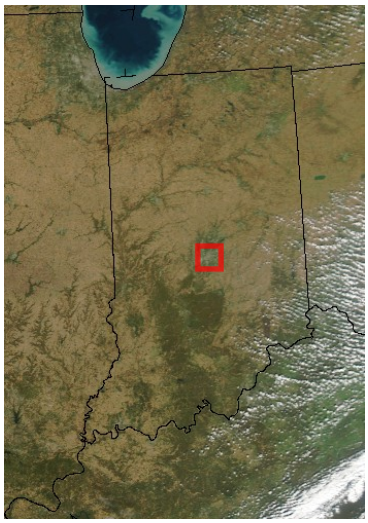

(b) 19:22 UTC (Aqua)

Figure 5.7.: True color satellite images taken by the MODIS instruments on 24$^{\text{th}}$ October showing the cloud cover during the second measurement flight of the campaign (SSEC, 2011). The location of Indianapolis is marked by the red quadrangle.

5.3. BROMEX Campaign (2012)

The most recent measurement flights with the HAIDI system were conducted between 11th March and 1st April of 2012, in context of the BRomine, Ozone, and Mercury EXperiment (BROMEX) campaign. For these flights HAIDI was again installed on the Beechcraft Duchess from Purdue University. The used instrumental setup was therefore very similar to the one used in Indiana in October of the year before and contains only minor improvements. Since the measurement flights were performed around Barrow (Alaska, USA), northern of the Arctic Circle, especially the downward looking optics of the system had to be prepared for surface albedos above 80 % in the ultraviolet (Tanskanen and Manninen, 2007). So, for example, the webcams for nadir and forward direction were equipped with additional UV and neutral density filters in consequence of the bright light conditions. For the same reason the entrance slit of the nadir scanner's spectrograph was reduced in height by about 50 % with an additional aperture. Further modifications were done on the instrument rack. Every component of the HAIDI system could now be switched on or off from the front panel of the instrument rack in order to be able to reboot the system during flight or to power it off in case of emergency. More details of the instrumental setup can be found in Sec. 3.11.2.

Table 5.7.: List of conducted flights during the measurement campaign in Barrow, Alaska. Denoted are the particular flight times and the availability of important flight parameters like GPS or INS. ✓: data available ✗: no data available.

Date	Takeoff (UTC)	Landing (UTC)	Flight Duration	SZA Range	Webcam (N/F)	GPS	INS	Comments
03/13/2011	19:50	22:45	175 min	79...74°	✓ ✓	✓	✓	-
03/15/2011	20:40	23:59	199 min	75...74°	✓ ✓	✓	✓	-
03/18/2011	20:53	21:29	36 min	74...73°	✓ ✓	✓	✗	cockpit heating failed
03/19/2011	00:45	03:30	165 min	75...85°	✓ ✓	✓	✗	-
03/20/2011	20:20	21:10	50 min	74...72°	✓ ✓	✓	✓	cockpit heating failed
03/22/2011	19:05	22:05	180 min	78...70°	✓ ✓	✓	✓	-
03/24/2011	19:55	23:05	190 min	74...70°	✓ ✓	✓	✓	-
03/26/2011	18:35	22:05	210 min	78...69°	✓ ✓	✓	✓	-
03/28/2011	21:45	01:10	205 min	68...72°	✓ ✗	✓	✓	-
03/30/2011	18:12	20:05	113 min	78...71°	✗ ✓	✗	✗	no GPS
03/31/2011	00:25	03:45	200 min	69...82°	✓ ✓	✓	✓	-

Both scanners (nadir and forward-looking) of the HAIDI system worked without significant problems throughout the campaign, so that most of the performed flights were successful (Tab. 5.7). However, during some flights the heating of the aircraft cockpit failed. As a result, the flights had to be aborted, because water vapor condensed on the windshield, froze and limited the view to the outside.

5.3.1. Scientific Objectives

The BROMEX field study in 2012 was funded by NASA and carried out as an interdisciplinary research project with the collaboration of teams from several institutes, e. g. NASA/JPL, Cold Regions Research and Engineering Laboratory, University of Alaska, Purdue University, Environment Canada and University of Washington (UW, 2012). Scientific objectives of the BROMEX campaign focused on the understanding of the chemical mechanisms that are responsible for an almost complete destruction of lower tropospheric ozone during Arctic springtime and the associated contamination of the tundra region by the deposition of atmospheric mercury (Sec. 1.3). Also the impact of Arctic sea ice reduction on these mechanisms was subject of investigation. For this purpose, a broad spectrum of ground-, sea ice/buoy-, aircraft-, helicopter-, and satellite-based measurements were accomplished.

5.3.2. Flight Preparations

Prior to the measurement flights, all instruments of ALAR and HAIDI were synchronized in time via GPS signal. In this way, the recording time of individual spectra or webcam images could later be assigned to a specific aircraft location and orientation. Moreover, the viewing direction of the forward-looking telescope had to be calibrated again by the procedure described in Sec. 3.5.1. The measurements showed that the center fibers of the telescope had a viewing angle of about $+0.94°$ relative to the horizontal, while the INS of the aircraft reported a pitch angle of $+1.73°$ at the same time. Therefore, the individual viewing angles of the forward-looking telescope had an offset of approximately $-0.8°$ regarding the given pitch angle of the aircraft. The viewing angles displayed in the time series of the forward-looking telescope in Figs. 8.1, 8.5, 8.9 and 8.12 (Sec. 8) were already corrected for offset and pitch angle to directly show the viewing angles of the telescope relative to the horizon.

5.3.3. Instrumental Settings

Due to the high temperature difference between the inside of the hangar (10 to 20 °C, when the hangar door was closed) and the outer ambient temperature in Barrow (up to −30 °C), it was very difficult to stabilize the spectrographs to a constant temperature. Especially, since the heating of the aircraft failed during some flights and the temperature in the cockpit fell below the freezing point. Finally, a setpoint of 15 °C turned out to be a good compromise for

the spectrograph temperature, because it could be reached while standing inside the hangar and it could also be maintained for a few minutes while the aircraft was moved outside and the cockpit heating was not already running. Additional settings for the instrument can be found in Tab. 5.8.

Table 5.8.: Instrumental settings used for the measurement campaign in Barrow, Alaska.

	Nadir Scanner	Forward-looking Telescope
CCD Temperature	0 °C	0 °C
Wavelength Interval	300.3...406.9 nm	299.8...405.9 nm
Integration Time	20.2 ms	dynamic ($\sim$ 1000 ms)
Binned Scans	4×16	10
Webcam Interval	5 s (10 s from 13^{th}–22^{nd})	5 s
Spectrograph Temp.	15 °C (20 °C from 13^{th}–20^{th})	

5.3.4. Flight Tracks

In the framework of the BROMEX campaign a total of 11 measurement flights were conducted from the Wiley Post-Will Rogers Memorial Airport (71.291° N, 156.789° W) in Barrow (Alaska, USA). As can be seen in Fig. 5.8, most flights went near the coast or to the south of Barrow in order to investigate the snow-covered surface of first-year sea ice and tundra. An exception was the flight to Prudhoe Bay on 31^{st} March, which went more than 350 km to the east.

5.3.5. Meteorological Conditions

In this section, meteorological data is shown for the measurement flights performed during the BROMEX campaign in March 2012. Atmospheric conditions like wind speed and wind direction were again recorded by the BAT probe of the aircraft. Average values of these parameters for the individual flights can be found in Tab. 5.9. Time-resolved data from the BAT probe can additionally be found in the result section (Sec. 8). Furthermore, some satellite images from MODIS (Terra) are shown below (Fig. 5.9) for the flights discussed in Sec. 8. In these images a special band combination is used in order to distinguish between clouds and ice/snow. The Terra satellite passed over the area at around 22:00 UTC on the respective days, which is within or close to the measurement time in most cases. Further meteorological information for March 2012, including ozone mixing ratios and air temperature, can be found in Fig. 5.10. The data is taken from the Barrow Observatory, which is located in the north of Barrow (71.323° N, 156.611° W), and shows hourly measurements close to the surface ($\sim$ 10 m).

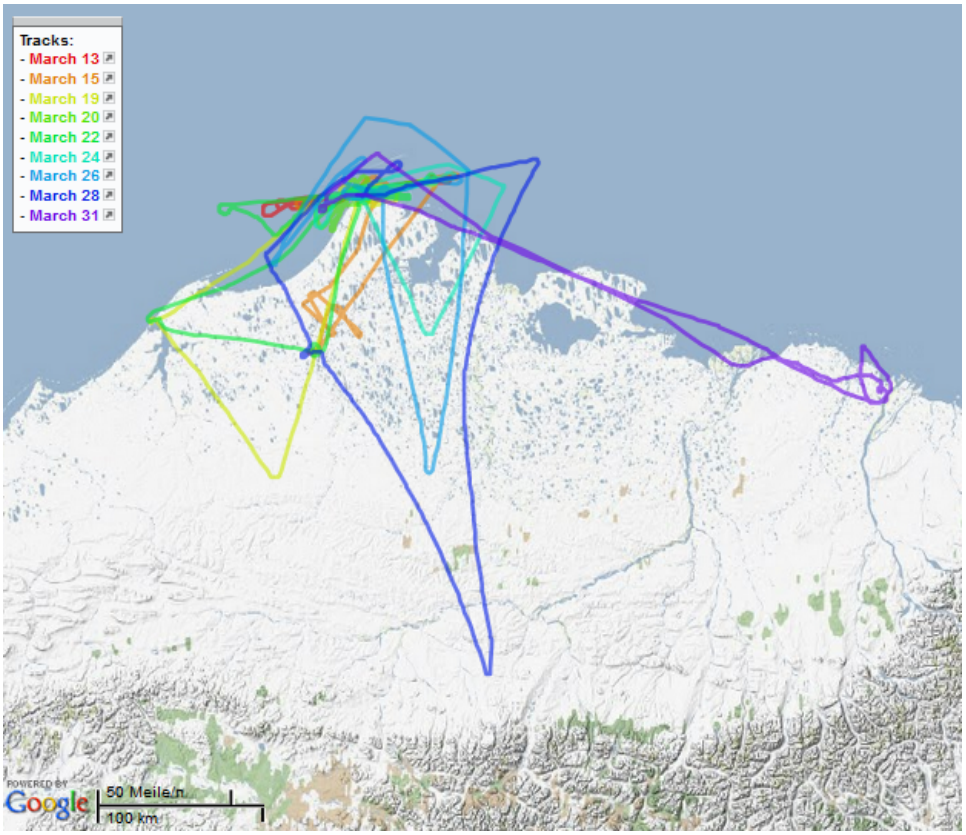

Figure 5.8.: Topographical map of the region around Barrow (Alaska, USA), giving an overview of the performed flights during March 2012 (Google, 2013). A legend indicating the individual flight tracks can be found in the upper left corner of the map.

Table 5.9.: Average wind directions and speeds for flight altitudes below 1000 m measured by ALAR's BAT probe during the BROMEX campaign.

Date	Wind Direction in °	Wind Speed in m/s
03/13/2012	70 ± 10	11.6 ± 2.4
03/15/2012	70 ± 7	13.1 ± 2.1
03/18/2012	n/a	n/a
03/19/2012	n/a	n/a
03/20/2012	57 ± 9	7.2 ± 1.2
03/22/2012	84 ± 7	11.6 ± 1.8
03/24/2012	82 ± 6	17.3 ± 1.5
03/26/2012	68 ± 9	9.2 ± 1.5
03/28/2012	72 ± 14	10.5 ± 5.2
03/30/2012	n/a	n/a
03/31/2012	62 ± 16	6.4 ± 1.3

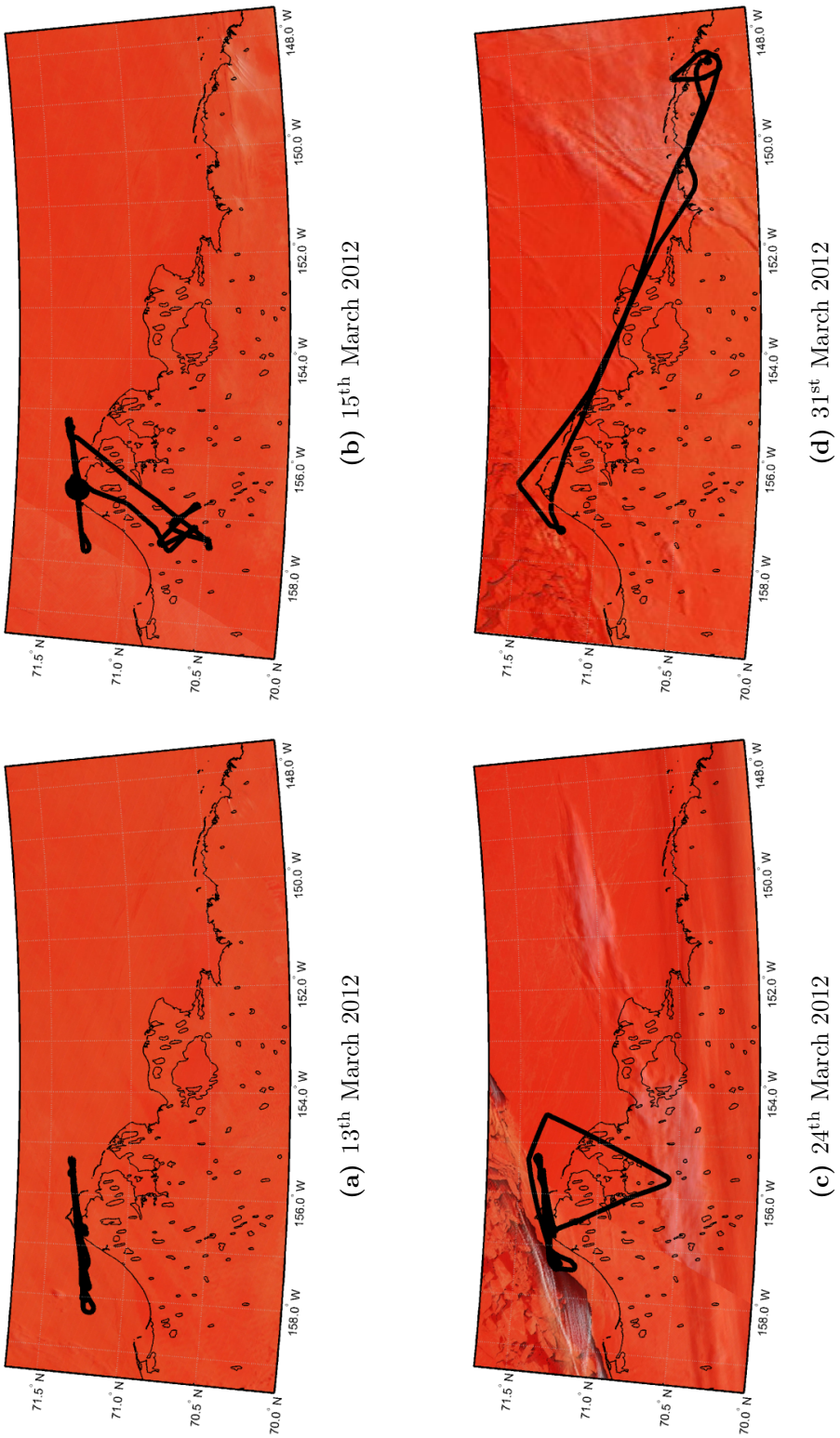

Figure 5.9.: MODIS (Terra) satellite images from selected measurement flights during the BROMEX campaign (NASA, 2012). The combined information from MODIS Bands 3-6-7 allows to differentiate sea ice from clouds. While red shades indicate ice, tan and white shades indicate clouds. The thick black line shows the flight track of the corresponding day.

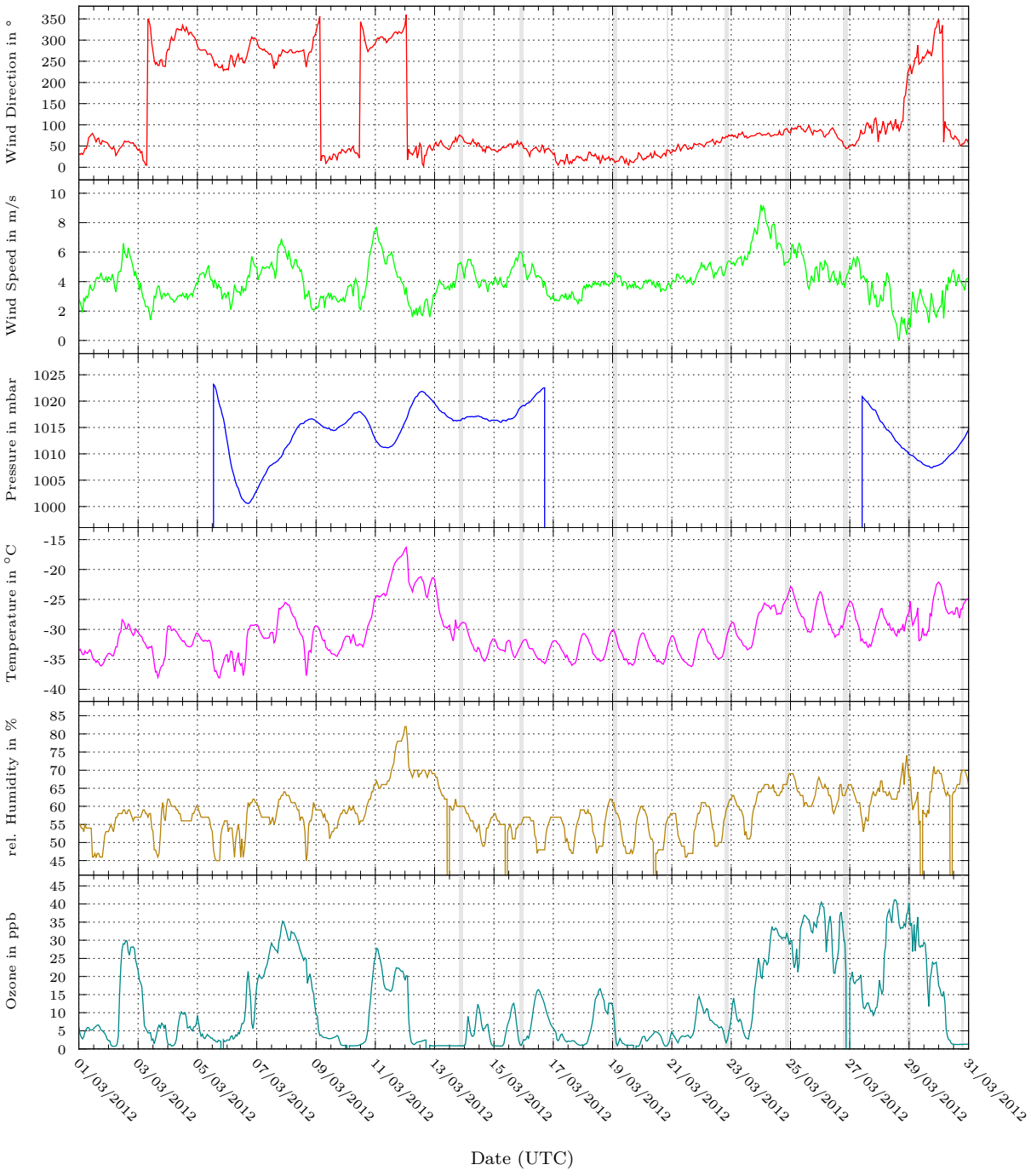

Figure 5.10.: Meteorological data and ozone mixing ratios measured at the Barrow Observatory (71.323° N, 156.611° W) in March 2012 (NOAA, 2013). The surface ozone data reveals the occurrence of numerous ODEs at the location of the observatory. Gray shaded sections indicate periods of time where measurement flights were performed.

6. Results of the Etna Campaign (2011)

In this chapter data from the flights to Mt. Etna is presented and analyzed for the BrO/SO_2 and $OClO/SO_2$ ratios in terms of plume age, measurement location and time. Beside time series, the results from the DOAS analysis are also plotted into topographical maps of the area around Mt. Etna to reveal the spatial distribution of the trace gases named above. Each plotted pixel thereby corresponds to the signal of 32 co-added spectra with an integration time of 50–100 ms (Tab. 5.3). Because of the different AMFs expected for measurements above and below the emission plume, the data for the maps was split into two parts. While maps shown in the left column of each figure contain only data which was taken above the expected height of the emission plume, maps in the right column show measurements taken below the plume. Due to visual observations (see Fig. 5.1), the height of the plume can be put in good approximation on a level with the height of the summit (~ 3300 m). Thus, in case of measurements above the plume, the nadir scanner's FOV is projected to a plane at 3300 m altitude (see Fig. 3.3). For measurements below the plume, the nadir scanner's FOV is projected to the ground instead, where the corresponding topographic height is derived from Shuttle Radar Topography Mission (SRTM) data (USGS, 2012). To simplify the discussion on the chemical evolution of the volcanic plume, regarding age and time, only measurements from above the plume are taken into account. Furthermore only measurements which are above the detection limit (4× fit error) are shown in the following. The approximate centerline and expansion of the emission plume, displayed in the maps, were derived from meteorological data , satellite images as well as from our measurements and visual observations (see Secs. 5.1.1 and 5.1.5).

6.1. Flight on 8th July

After some tests, the first successful measurement flight to Mt. Etna was conducted on 8th July 2011, between 07:50 and 09:51 UTC (09:50–11:51 LT). The prevailing conditions showed generally clear-sky and quiescent degassing from the summit craters. Only towards the end of the flight some small clouds could be seen close to the summit of Mt. Etna (Fig. 5.4b). Sounding balloon data from that day states a wind direction of about 330° (NNW) and a wind speed of 8 m/s for the height of the summit (see Sec. 5.1.5), which agrees with visual observations (Fig. 5.1b). Also the spatial distributions of SO_2 and BrO from measurements above 3300 m flight altitude (Figs. 6.2a and 6.2c) clearly indicate the propagation direction and expansion of the plume. As can be seen in Fig. 6.1 SO_2 dSCDs of up to 1.8×10^{18} molec/cm^2 and BrO dSCDs

of about 2.3×10^{14} molec/cm^2 could be observed while flying over the centerline of the plume. Measurements from below 3300 m (Figs. 6.2b and 6.2d) show overall lower column densities. This is most likely due to a different measurement geometry, where light received by the nadir scanner has passed the absorber only once (lower AMF).

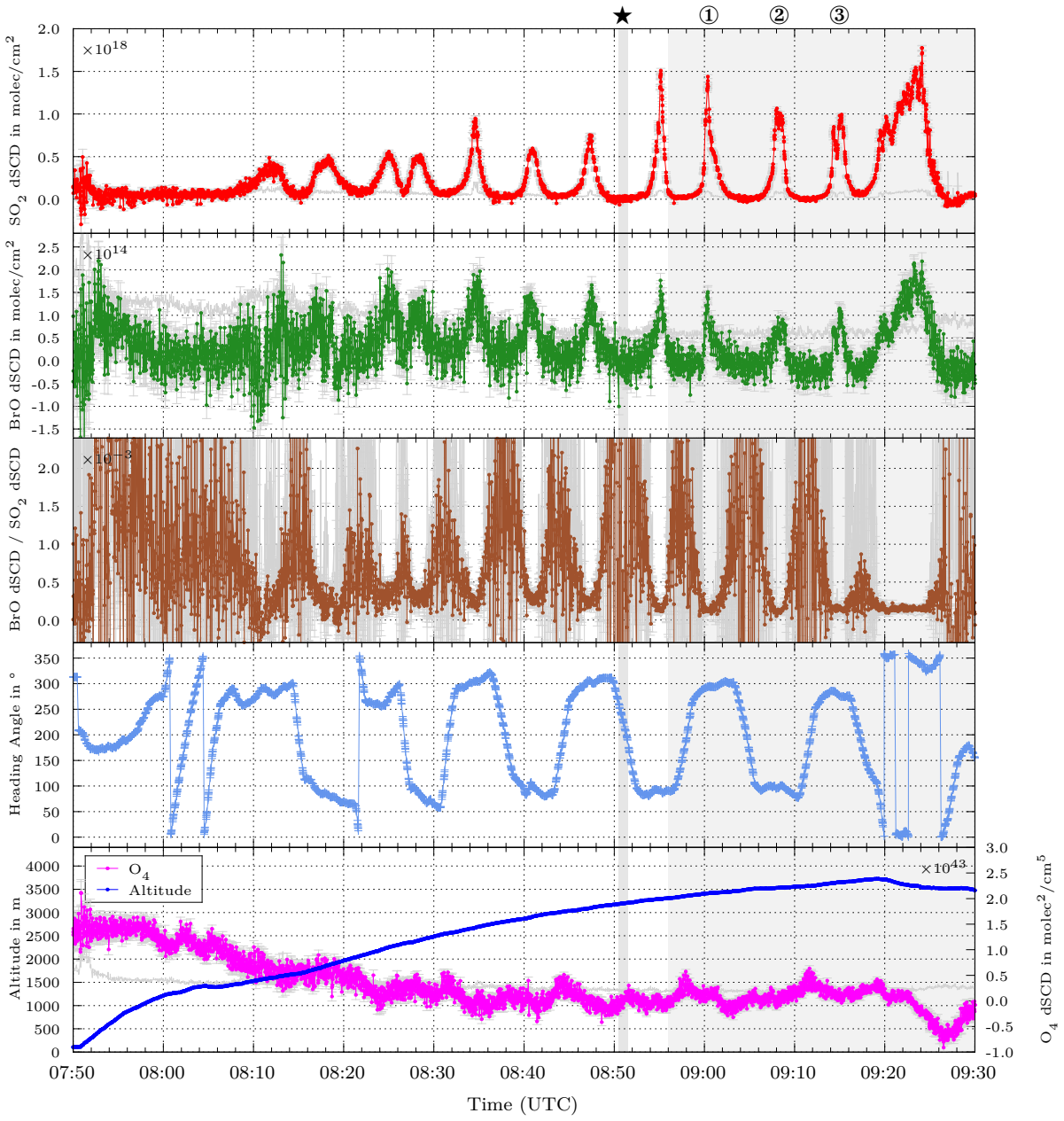

Figure 6.1.: Time series of measurement data from 8$^{\text{th}}$ July 2011. Due to an empty main battery, there is no data from the last 20 min of the flight. The period shaded in gray indicates flight altitudes above 3300 m. Traverses of the plume are marked by encircled numbers on the upper time axis of the plot (see also Fig. 6.2). Errors and detection limits are plotted in gray. ★: Recording period of nadir scanner in-flight FRS.

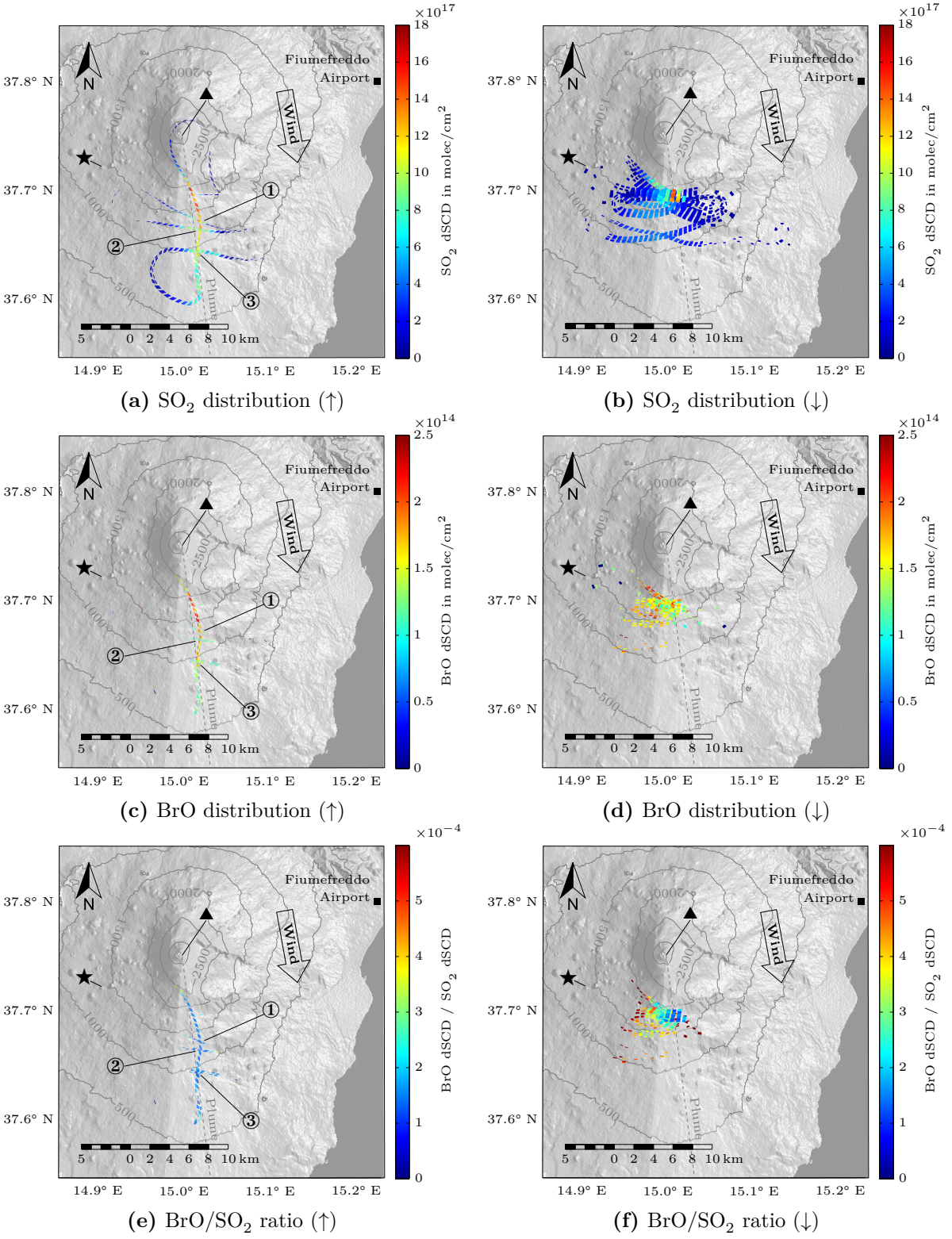

(a) SO_2 distribution (↑)

(b) SO_2 distribution (↓)

(c) BrO distribution (↑)

(d) BrO distribution (↓)

(e) BrO/SO_2 ratio (↑)

(f) BrO/SO_2 ratio (↓)

Figure 6.2.: Maps showing the spatial distribution of SO_2, BrO and the BrO/SO_2 ratio measured by HAIDI's nadir scanner during the flight on 8th July 2011. The left column shows measurements taken above 3300 m (↑) while the right column shows measurements between 1300 and 3300 m (↓). Traverses of the emission plume are labeled by encircled numbers in chronological order. ★: Recording position of nadir scanner in-flight FRS, ▲: Location of the NSEC.

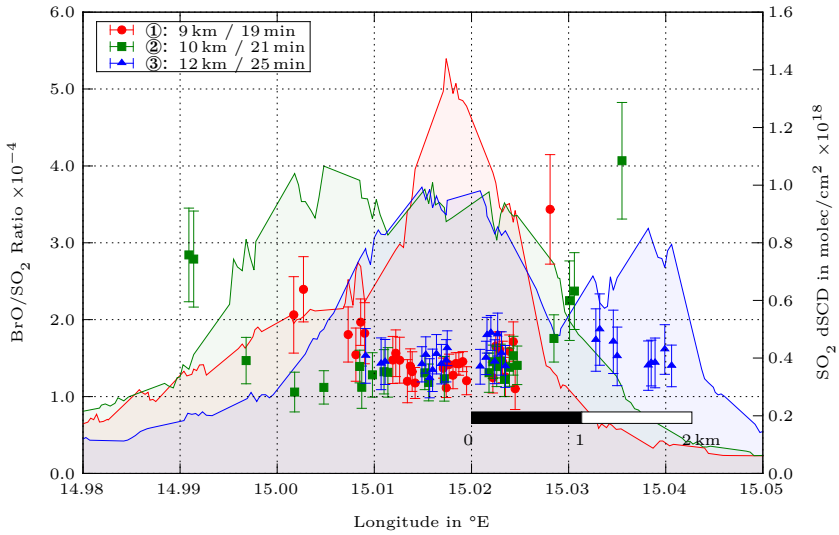

Figure 6.3.: BrO/SO_2 ratios from 8th July 2011, measured during plume traverses along the east-west direction in three different distances to the summit (see also labels in Fig. 6.2e). The respective SO_2 dSCDs are shown as colored surfaces, to get an idea of the plume width and location. Plume ages at the three traverses and corresponding average distances to the NSEC are given in the legend.

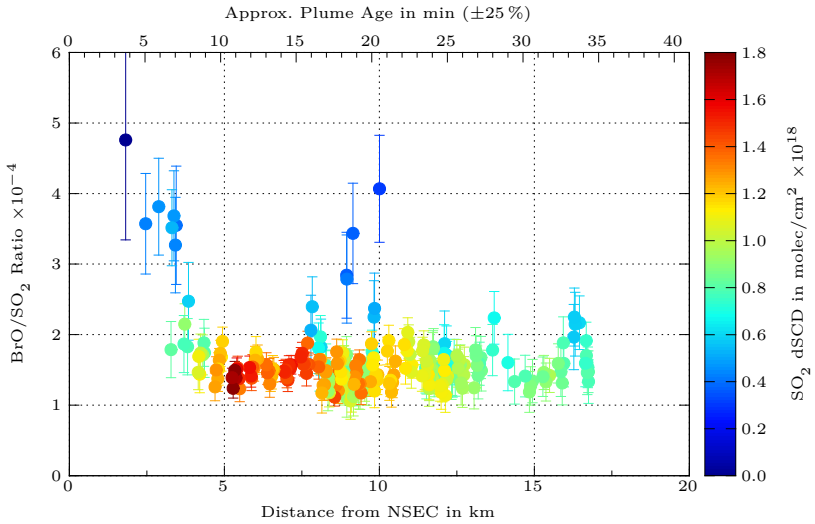

Figure 6.4.: Retrieved BrO/SO_2 ratios from 8th July 2011, plotted versus the distance to the NSEC and the approx. plume age. For the calculation of the plume age a constant wind speed of 8 m/s with an error of 25 % was assumed (UWYO, 2011). Measurements close to the centerline of the plume are identified by high SO_2 dSCDs.

6.1.1. Retrieved BrO/SO_2 Ratios

The spatial distribution of the BrO/SO_2 ratio is also illustrated in the maps (Figs. 6.2e and 6.2f). BrO/SO_2 ratios from flight segments along the east-west direction (perpendicular to the direction of the plume) are furthermore shown in Fig. 6.3. Here the BrO/SO_2 ratio is plotted

versus the longitude of the measurement location to show cross sections of the plume for different distances to the summit. As one can see, the BrO/SO_2 ratio clearly increases towards the edges of the plume, by about a factor of two to three. However, the BrO/SO_2 ratio measured at the center of the plume was about 1.4×10^{-4} during all traverses. The same can be seen in Fig. 6.4, where the BrO/SO_2 ratio is plotted versus the distance from the NSEC and the respective plume age for the whole data set. BrO/SO_2 ratios are only significantly enhanced for low SO_2 dSCDs, which indicate measurements at the edge of the volcanic plume. Thus, no change in the BrO/SO_2 ratio could be measured within the here observed plume ages (10–34 min).

6.2. Flight on 9th July

The second flight to Mt. Etna was performed on 9th July between 08:00 and 10:46 UTC. This was only a few hours before the paroxysm when already increasing numbers of strombolian explosions occurred. Meteorological conditions were similar to the day before, with virtually cloud-free sky (Fig. 5.4c). Also the wind came roughly again from NNW direction (330°) with a speed of about 10 m/s at the height of the summit (Sec. 5.1.5). As can be seen in the time series (Fig. 6.6) and the maps from that day (Figs. 6.7 and 6.8), the observed SO_2 and BrO dSCDs are about twice as high as those of 8th July. During overflights of the volcanic plume maximum values of 4.6×10^{18} molec/cm^2 for SO_2 and 4.2×10^{14} molec/cm^2 for BrO were detected.

6.2.1. Retrieved BrO/SO_2 Ratios

Since more measurements exceeded the detection limit, an improved spatial coverage also allows a more detailed observation of increased BrO/SO_2 ratios at the edges of the plume (Fig. 6.5a). Similar to the day before, a significant increase up to 5.0×10^{-4} could be observed towards the outermost regions of the plume, approx. 4 km away from the centerline. This is again about 2–3 times the value of the plume center. Already Louban et al. (2009) observed increases by a factor of two in the BrO/SO_2 ratio by comparing center and edge measurements of Mt. Etna's emission plume applying a ground based I-DOAS instrument. In contrast to measurements from 8th July, also a slight increase of the BrO/SO_2 ratio along the centerline of the plume can be seen in Fig. 6.5a. While the ratio was about 1.3×10^{-4} in a distance of 2 km (plume age: 3 min) from the summit, more distant measurements show higher ratios, which finally reach a value of 2.2×10^{-4} at 10 km (plume age: 17 min). Looking at the data set as a whole (Fig. 6.9), it seems like the ratio along the plume increases even further, beyond a distance of 10 km. On the first glance this increase up to 19 km (plume age: 31 min) might be surprising, as it stays in contrast with several measurements reported in the past (e. g. Bobrowski and Giuffrida, 2012; Vogel, 2011) and also with the results from the previous day. However, since the data does not provide a complete or even partly plume cross section for distances greater than 10 km to the summit, it cannot be excluded that the measured ratios were taken on the outer edge of

the plume rather than along its centerline. In fact, SO_2 dSCDs and the general distribution of the plume seem to confirm that the flight track on 9th July departed from the centerline of the plume with increasing distance to the summit (see Figs. 6.9, 6.7a). The very low SO_2 column densities which can be seen in Fig. 6.9 for measurements beyond 10 km distance suggest that these measurements were predominantly taken at the eastern edge of the volcanic plume. Moreover, the observed total increase in the BrO/SO_2 ratio is about a factor of 2–3, which agrees with the increase measured between the center and the edge of the plume.

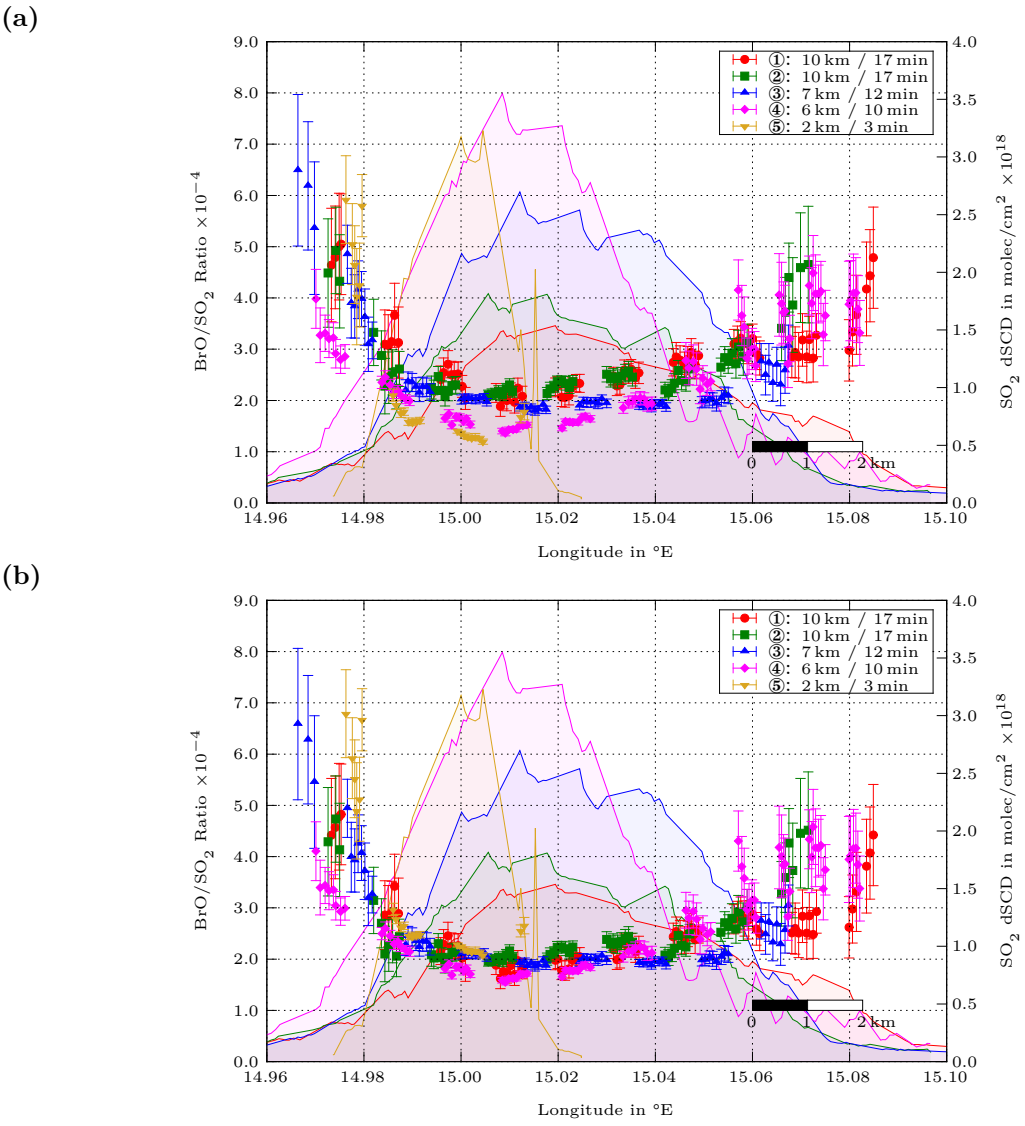

Figure 6.5.: BrO/SO_2 ratios from 9th July 2011, measured during five plume traverses along the east-west direction (see also Fig. 6.7e). The respective SO_2 dSCDs are shown as colored surfaces, to get an idea of the plume width and location. Plume ages at the traverses and corresponding average distances to the NSEC are given in the legend: (a) Original data (b) Data after compensation of the observed time dependent change.

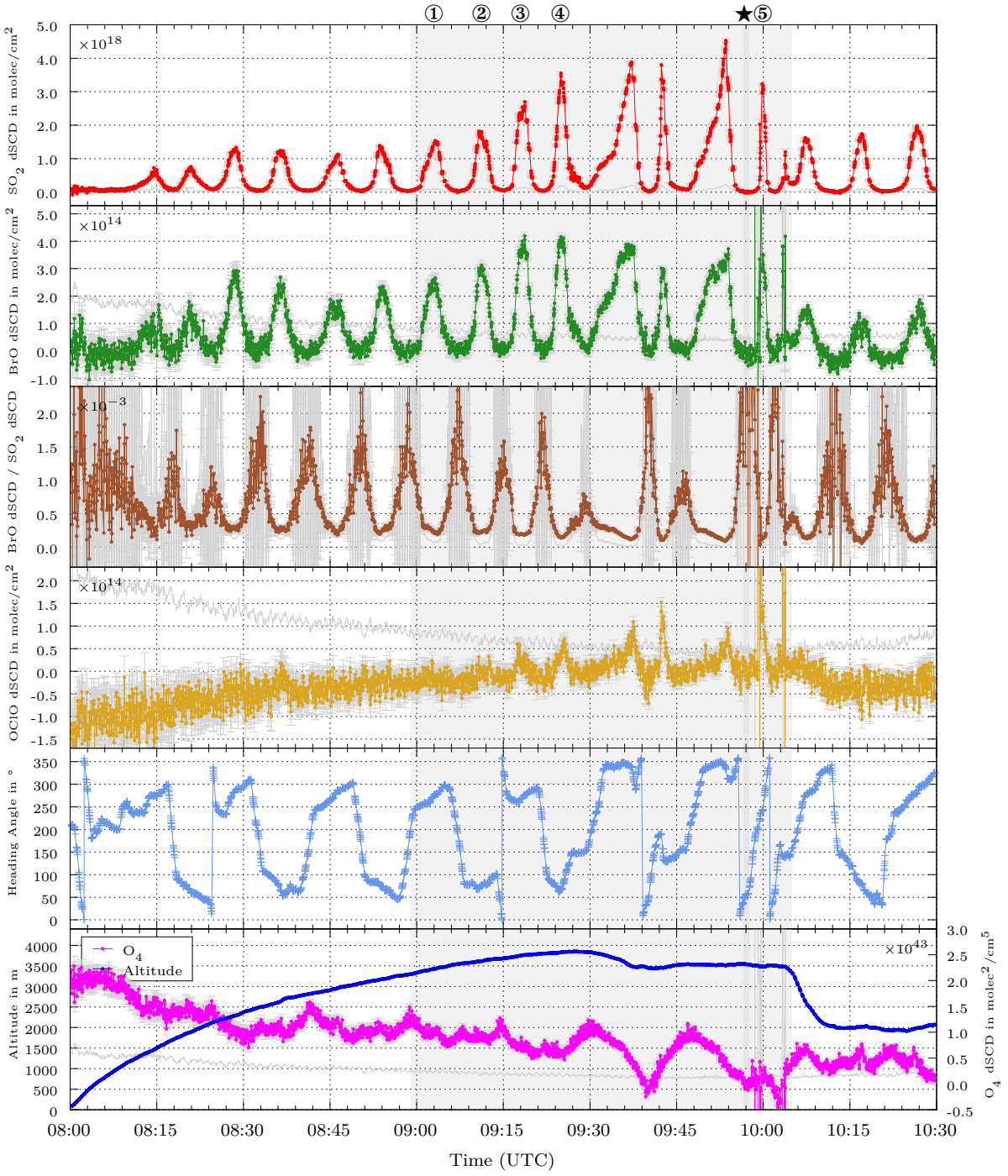

Figure 6.6.: Time series of measurement data from 9th July 2011. Due to an empty main battery, there is no data from the last 16 min of the flight. The period shaded in gray indicates flight altitudes above 3300 m. Traverses of the plume are marked by encircled numbers on the upper time axis of the plot (see also Figs. 6.7 and 6.8). Errors and detection limits are plotted in gray. ★: Recording period of nadir scanner in-flight FRS.

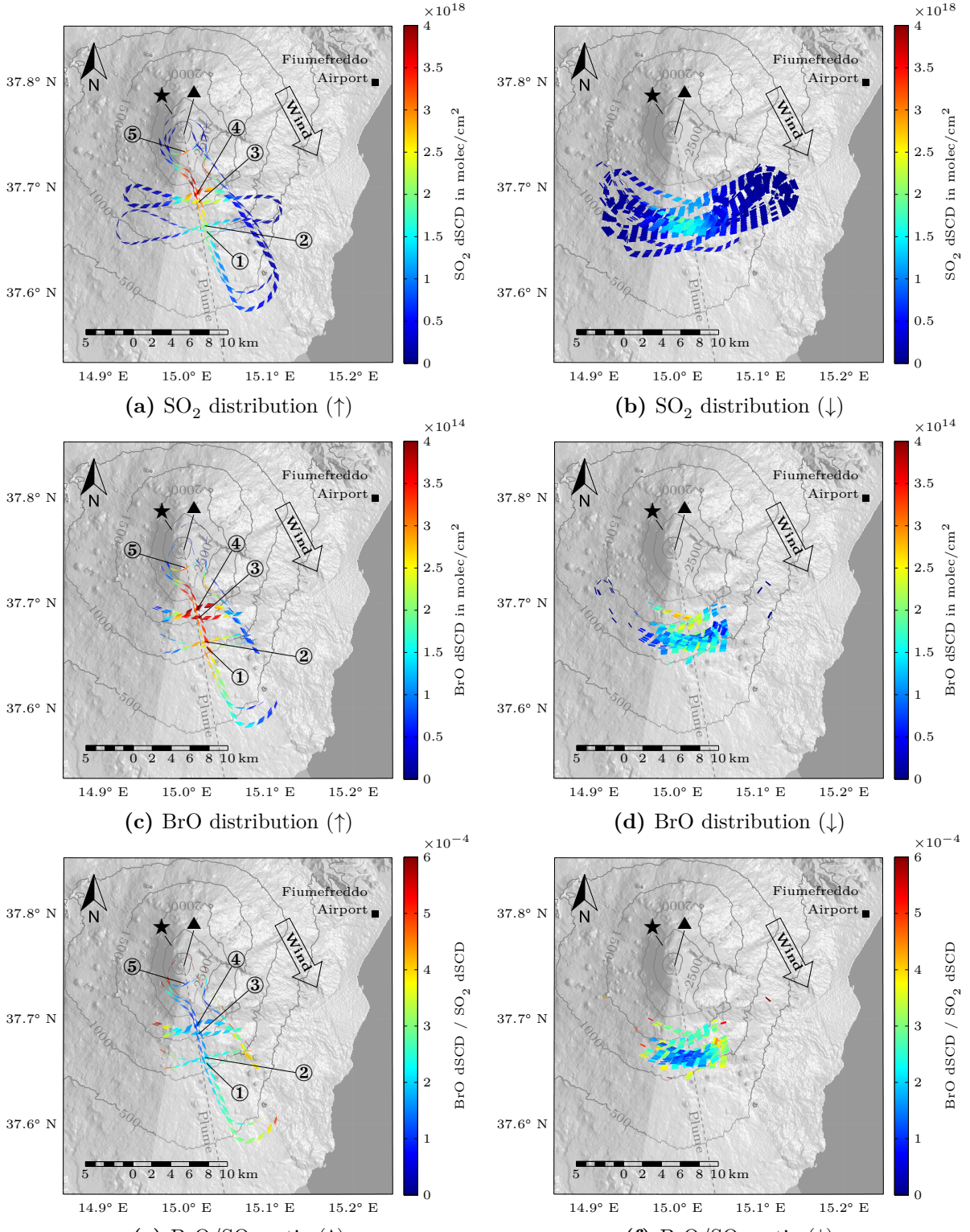

(a) SO_2 distribution (↑)

(b) SO_2 distribution (↓)

(c) BrO distribution (↑)

(d) BrO distribution (↓)

(e) BrO/SO_2 ratio (↑)

(f) BrO/SO_2 ratio (↓)

Figure 6.7.: Maps showing the spatial distribution of SO_2, BrO and the BrO/SO_2 ratio measured by HAIDI's nadir scanner during the flight on 9th July 2011. The left column shows measurements taken above 3300 m (↑) while the right column shows measurements between 1300 and 3300 m (↓). Traverses of the emission plume are labeled with encircled numbers in chronological order. ★: Recording position of nadir scanner in-flight FRS, ▲: Location of the NSEC.

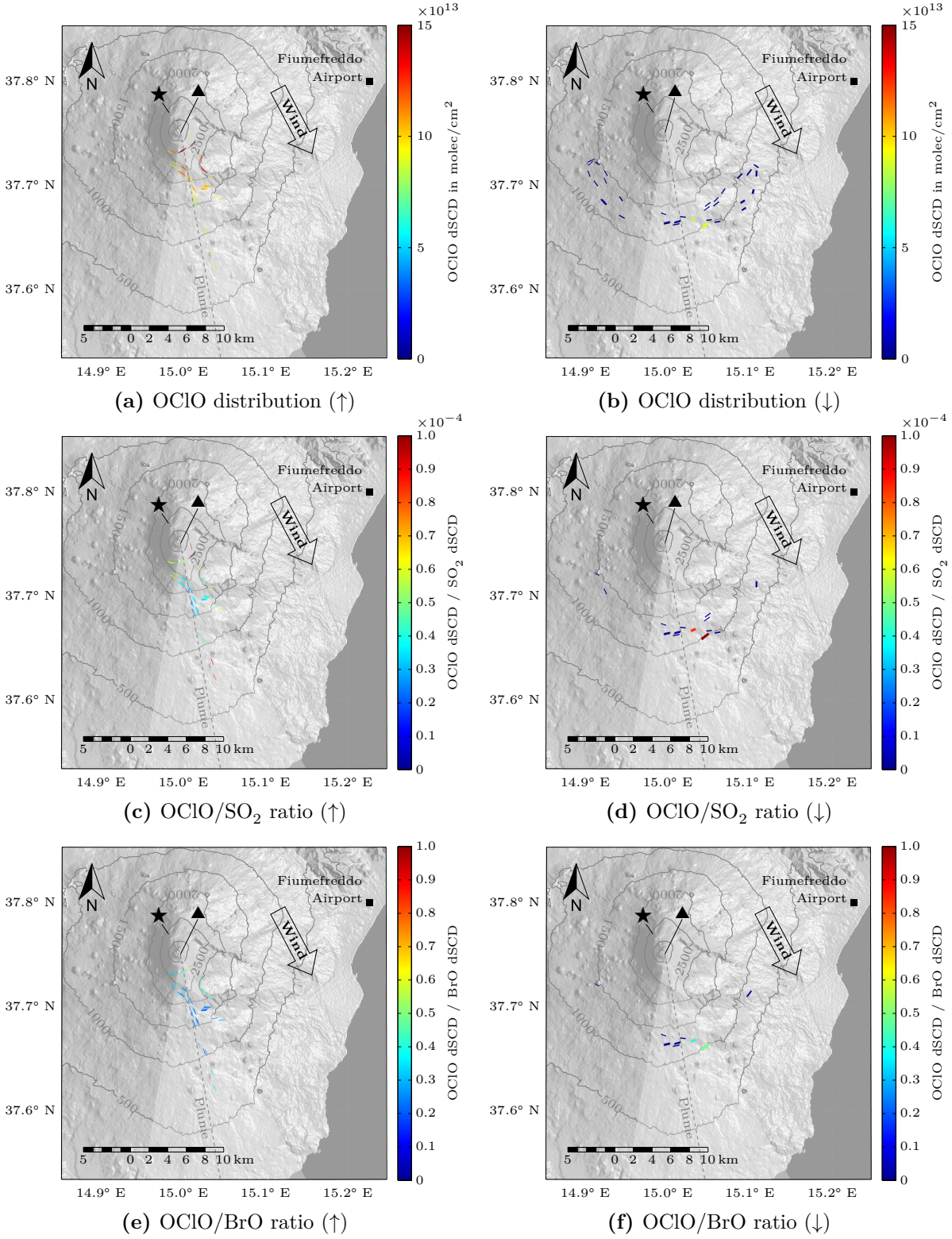

(a) OClO distribution (↑)

(b) OClO distribution (↓)

(c) $OClO/SO_2$ ratio (↑)

(d) $OClO/SO_2$ ratio (↓)

(e) OClO/BrO ratio (↑)

(f) OClO/BrO ratio (↓)

Figure 6.8.: Maps showing the spatial distribution of OClO as well as the $OClO/SO_2$ and OClO/BrO ratios measured by HAIDI's nadir scanner on 9th July 2011. The left column shows measurements taken above 3300 m (↑) while the right column shows measurements between 1300 and 3300 m (↓). ★: Recording position of nadir scanner in-flight FRS, ▲: Location of the NSEC.

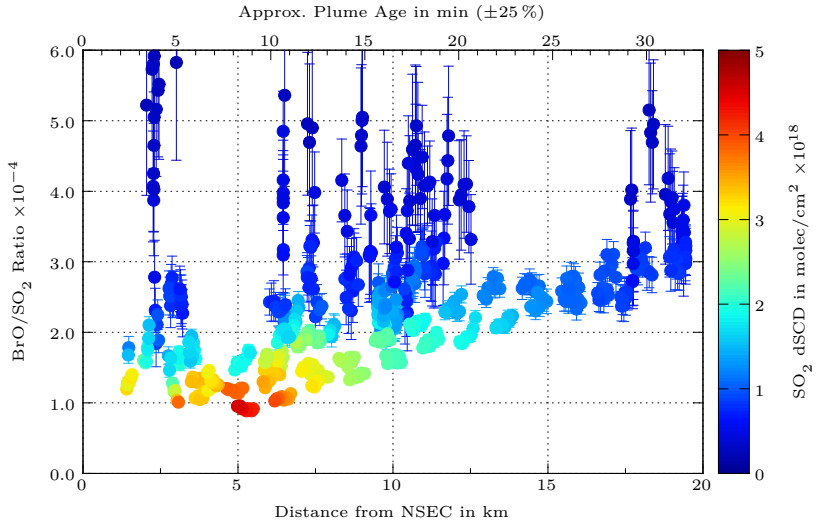

Figure 6.9.: Retrieved BrO/SO_2 ratios from 9th July 2011, plotted versus the distance to the NSEC and the approx. plume age. For the calculation of the plume age a constant wind speed of 10 m/s with an error of 25 % was assumed (UWYO, 2011). Measurements close to the centerline of the plume are identified by high SO_2 dSCDs.

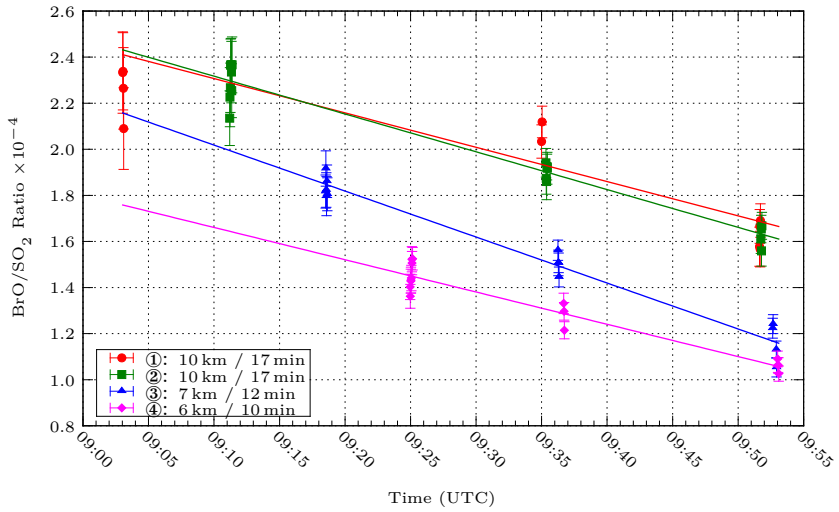

Figure 6.10.: BrO/SO_2 ratios from 9th July 2011, plotted versus the time of measurement. Each color corresponds to a specific location on the map (see numbers in Fig. 6.7) which was overpassed several times. As can be seen, the BrO/SO_2 ratios decrease in all locations with an almost identical rate. Since the measurements originate from different locations within the plume (center, edge) they cannot be directly compared with each other.

Investigating the BrO/SO_2 ratio over time reveals another interesting feature. It can be seen that later measurements taken at the same coordinates, thus similar plume age, show a lower BrO/SO_2 ratio (Fig. 6.10). The observed rate of decrease was about -1.63×10^{-6}/min (over an observed time frame of approx. one hour) and seems to be independent from the plume age,

as measurements from different locations (plume ages of 10, 12 and 17 min) show an almost identical result. When correcting the data in Fig. 6.5a with the observed rate of decrease in terms of different measurement times and plume ages, one obtains Fig. 6.5b. The corrected data does not longer show a significant increase of the BrO/SO_2 ratio along the plume's center within the measurement error. It is therefore assumed that there is also no change in the BrO/SO_2 ratio for distances greater than 10 km and the observed enhancement is only caused by the center to edge enhancement of the BrO/SO_2 ratio.

6.2.2. Retrieved $OClO/SO_2$ Ratios

Due to a higher signal and thus higher signal-to-noise ratio compared with the measurements on the day before, also OClO could successfully be detected in the volcanic plume on 9th July 2011. Peak column densities of approximately 1.5×10^{14} molec/cm^2 were found 5 km downwind of the summit craters. The average $OClO/SO_2$ ratio was about 0.3×10^{-4} for measurements close to the center of the plume, while it increased up to 0.9×10^{-4} at low SO_2 SCDs, which indicate plume edge measurements (see Fig. 6.11). However, unfortunately the amount of data above the detection limit is insufficient for a more detailed discussion and does not show a full $OClO/SO_2$ cross section of the plume for any distance to the source. Therefore, it cannot be assured that the $OClO/SO_2$ ratio generally increases towards the edges of the plume, as observed for the BrO/SO_2 ratio. Moreover, only data with low SO_2 SCDs is available for larger distances to the summit craters and thus the same argumentation regarding the measurement location applies here as for BrO. Most likely there was a mixed observation of an aged plume and an increased ratio due to the variation from plume centered measurements to plume edge measurements. For this reason, no statement can be made about the evolution of the $OClO/SO_2$ ratio for plume ages > 13 min.

6.2.3. Calculation of ClO Mixing Ratios

Because OClO and BrO were evaluated in the same wavelength range (see Chap. 4), differences in the radiation transport for the two species are negligible and it can be assumed that the ratio of the measured OClO and BrO slant column densities (S_{OClO}/S_{BrO}) is the same as the ratio of the respective concentrations:

$$\frac{S_{OClO}}{S_{BrO}} \approx \frac{[OClO]}{[BrO]} . \tag{6.1}$$

Thus, we can use Eq. (1.10) (Sec. 1.1.2.2) to calculate the ClO-concentration in the plume. Figure 6.12 shows the resulting concentrations converted to mixing ratios in units of parts per trillion (ppt, 1×10^{-12}). Since the emission plume is at an altitude of about 3300 m, a temperature of 283 K and a pressure of 700 mbar were assumed for the conversion, according to

the sounding balloon data (UWYO, 2011). As can be seen, the calculation yields ClO mixing ratios of 80 to 300 ppt in the plume for the first 13 min after emission.

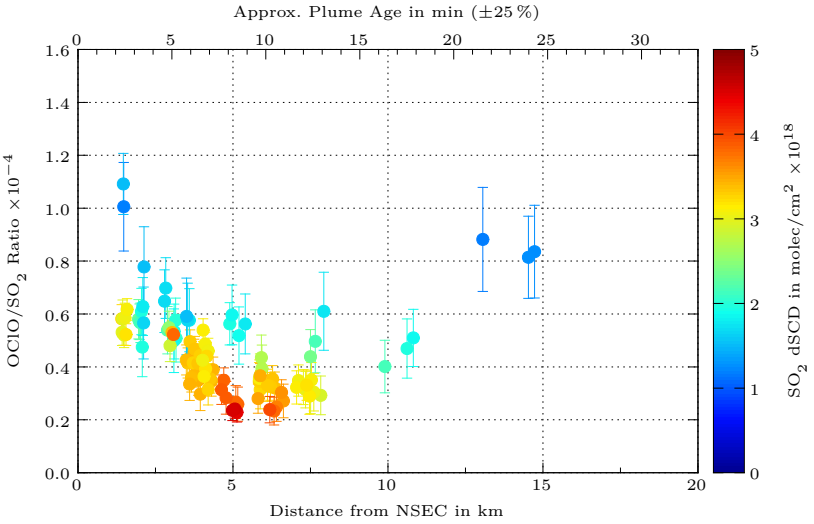

Figure 6.11.: Retrieved $OClO/SO_2$ ratios from 9th July 2011, plotted versus the distance to the NSEC and the approx. plume age. For the calculation of the plume age a constant wind speed of 10 m/s with an error of 25 % was assumed (UWYO, 2011). Measurements close to the centerline of the plume are identified by high SO_2 dSCDs.

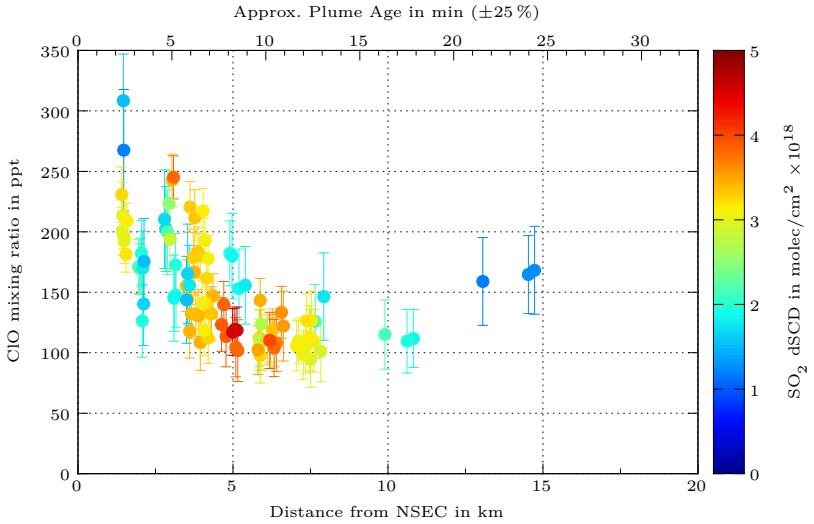

Figure 6.12.: ClO mixing ratios calculated from the retrieved OClO and Br_2O slant column densities as a function of plume age. For the calculation of the plume age a constant wind speed of 10 m/s with an error of 25 % was assumed (UWYO, 2011). Measurements close to the centerline of the plume are identified by high SO_2 dSCDs.

7. Results of the Indiana Campaign (2011)

In the following, especially the results from the flight on 24$^{\text{th}}$ October will be addressed in more detail, because the emission plume of Indianapolis was most clearly observable on that day. Maps and time series with the data of the remaining flights can be found in Appendix A.2. Since there was a problem with the control of the nadir scanner's servo motor on 24$^{\text{th}}$ October (Tab. 5.4), all spectra recorded during a swath were binned together, resulting in a binning of 1×128 per plotted pixel in the presented maps. Another problem occurred with the recording of the Fraunhofer reference spectrum for the forward-looking telescope. In contrast to the method described in Sec. 3.5.1, a mirror was used here to take the reference spectra on the ground. This approach resulted in large residual structures, probably due to the coating of the mirror. Also with in-flight reference spectra the data from the forward-looking telescope is unfortunately very noisy, in particular for positive viewing directions.

7.1. Flight on 23$^{\text{rd}}$ October

The measurement flight from 23$^{\text{rd}}$ of October can be found in Appendix A.2.

7.2. Flight on 24$^{\text{th}}$ October

The second flight performed during the campaign started on 24$^{\text{th}}$ October at 16:31 UTC (12:31 LT) from Purdue University airport. As on the other days the destination of the flight was the metropolitan area of Indianapolis, which is located around 100 km southeasterly of the airport. To investigate the emissions originating from Indianapolis, several traverses were flown downwind of the city. As can be seen from Figs. 5.6 and 5.7 a dense cloud cover could be observed to the northeast of Indianapolis during the first half of the flight. However, since the measured average wind direction within the boundary layer was $(309 \pm 15)°$ with a wind speed of (7.7 ± 1.9) m/s (Tab. 5.6), the traverses were made in the southeast of the city and should therefore not be affected by changing cloud conditions.

A time series with the measurement results from 24$^{\text{th}}$ October 2011 can be found in Fig. 7.1. As one can see here, NO_2 dSCDs of up to 2.4×10^{16} molec/cm^2 could be observed by HAIDI's nadir scanner during the flight. A part of the data from that day is also plotted into a topographic map of the area around Indianapolis (Fig. 7.2). Here, the measured NO_2 dSCDs are illustrated as color-coded patches, corresponding to the nadir scanner's GIFOV. The spatial

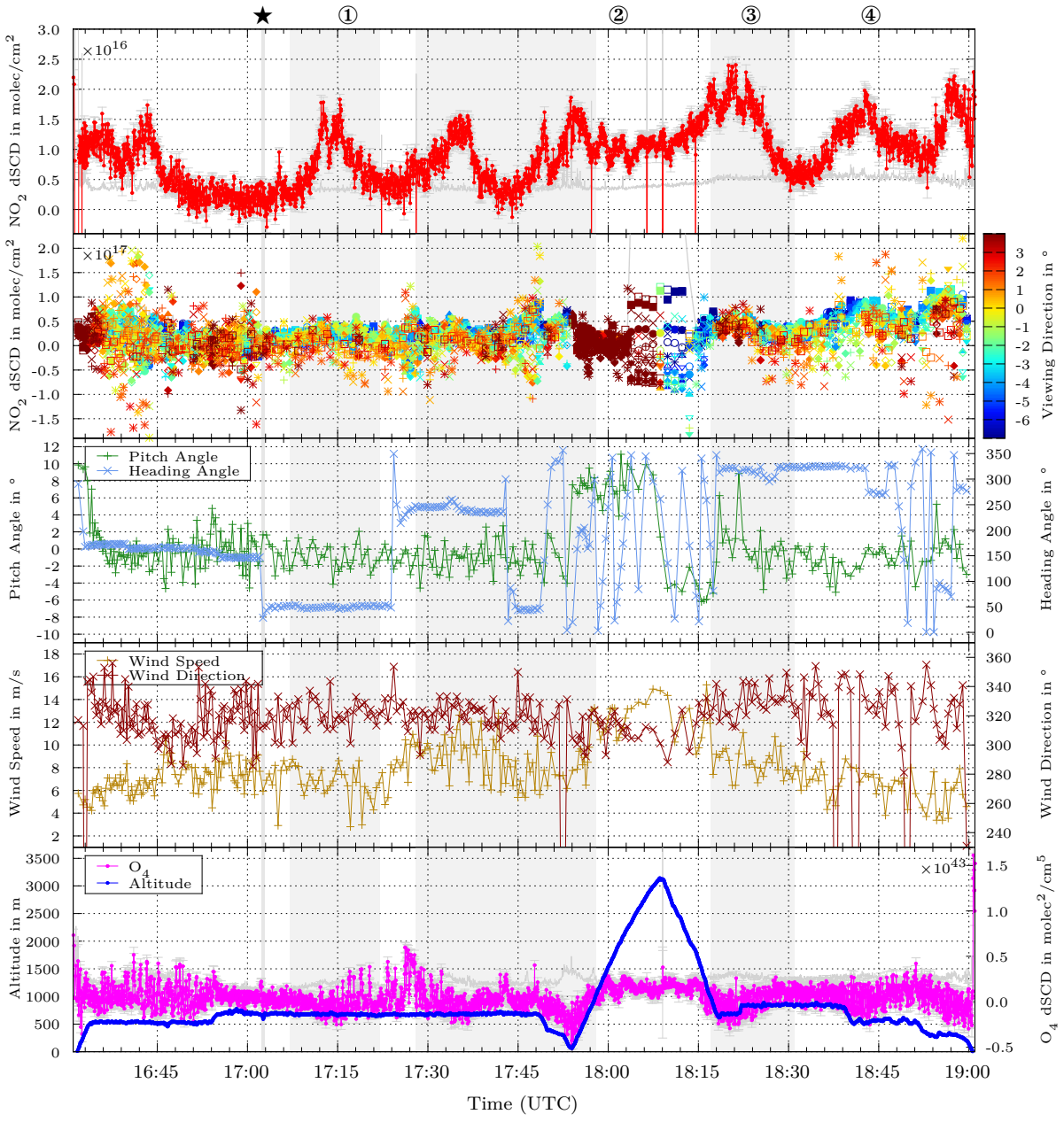

Figure 7.1.: Time series of measurement data from 24th October 2011. The gray shaded sections correspond to periods from which data is presented in the map (Fig. 7.2). Errors and detection limits are also plotted in gray. ★: Recording period of nadir scanner in-flight FRS. ①–④: Recording time of the images shown in Fig. 5.6.

distribution of the NO_2 reveals that the highest dSCDs were found southeasterly of the city core, following the wind direction. These emissions were partly caused by the coal-burning power plants of Indianapolis. The two largest of them, Harding Street Generating Station (nameplate capacity: 1170 MW) and Perry K Plant (nameplate capacity: 20 MW) are located close to the

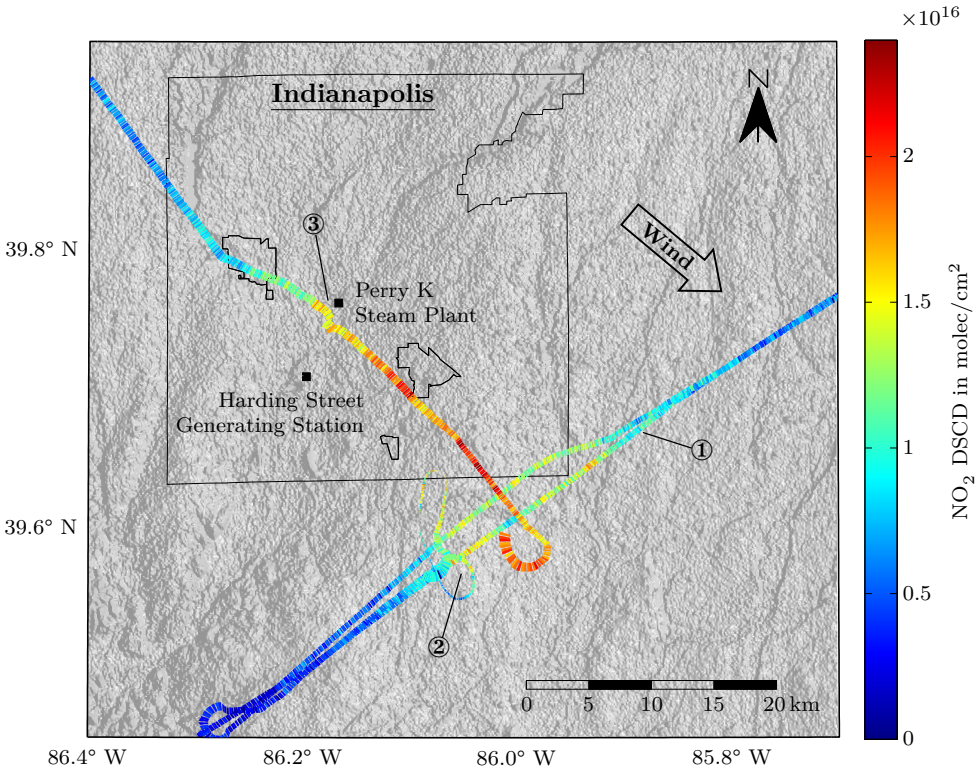

Figure 7.2.: Detail of the flight on 24$^{\text{th}}$ October 2011 showing measured NO_2 column densities plotted into a topographic map of the area around Indianapolis (SRTM data taken from USGS (2012)). Because of the scanner malfunction a binning of 1×128 is used here. The spatial distribution of NO_2 clearly shows the emission plume, originating from Indianapolis with its coal-burning power plants, blowing downwind. For a better overview only data for flight altitudes below 1000 m is shown.

center of the city (see also Fig. 7.2). Thus, the transect flown to the southeast follows the power plant plume, while one can see the more diffuse mobile source NO_2 emission in the transects that go perpendicular to the wind direction. A map showing all measurement data from this flight can be found in Fig. A.7 (Appendix A.2).

7.2.1. Calculation of the NO_2 Flux

The total flux F of trace gas molecules from an area encircled by path S is generally given by the following equation (Ibrahim et al., 2010):

$$F = \oint_S V(s) \cdot \vec{W} \cdot \vec{n}(s) \cdot \mathrm{d}s\,. \tag{7.1}$$

Here $V(s)$ is the vertical column density of the target trace gas at position s, $\vec{W}$ the average wind vector within the trace gas layer and $\vec{n}(s)$ the normal vector parallel to Earth's surface and orthogonal to the actual heading angle of the instrument. Because $V(s)$ is only measured

piecewise by individual measurement spectra, Eq. (7.1) is expressed as a sum in the following. This yields the equations below for the total emission of NO_2:

$$F_{NO_2} = \sum_i V_{trop,NO_2}(s_i) \cdot \vec{W} \cdot \vec{n} \cdot \Delta s_i \tag{7.2}$$

$$= \sum_i V_{trop,NO_2}(s_i) \cdot W \cdot \sin(\beta)(s_i) \cdot \vec{n} \cdot \Delta s_i \,, \tag{7.3}$$

were Δs_i is the distance traveled during the i-th measurement and β the angle between the wind direction and the heading angle of the aircraft. Since the observed slant column densities of NO_2 were rather low ($< 7.0 \times 10^{15}$ molec/cm^2) upwind of Indianapolis (Fig. 7.2), the influx into the probed area can be neglected in good approximation. This allows to determine the approximate NO_2 emission of Indianapolis by using the data from the traverses flown downwind of the city. For this purpose the measured NO_2 dSCDs were converted to tropospheric VCDs with the help of Eq. (4.11), assuming a stratospheric NO_2 VCD of 2.0×10^{15} molec/cm^2 (Wenig et al., 2004). The mean wind speed ((7.7 ± 1.9) m/s) and direction ($(309 \pm 15)°$) within the assumed boundary layer height of 1000 m were taken from the BAT probe data (Tab. 5.6). Hence, a total NO_2 emission of $(1.4 \pm 0.2) \times 10^{25}$ molec/s or (3.95 ± 0.62) t/h, respectively, could be computed on the basis of the data from 24$^{\text{th}}$ October 2011. For comparison, the total NO_x emission of the Mannheim/Ludwigshafen area was determined to be $(7.4 \pm 1.8) \times 10^{24}$ molec/s or (2.04 ± 0.50) t/h, respectively, by Ibrahim et al. (2010) in August 2006 using car-based MAX-DOAS measurements.

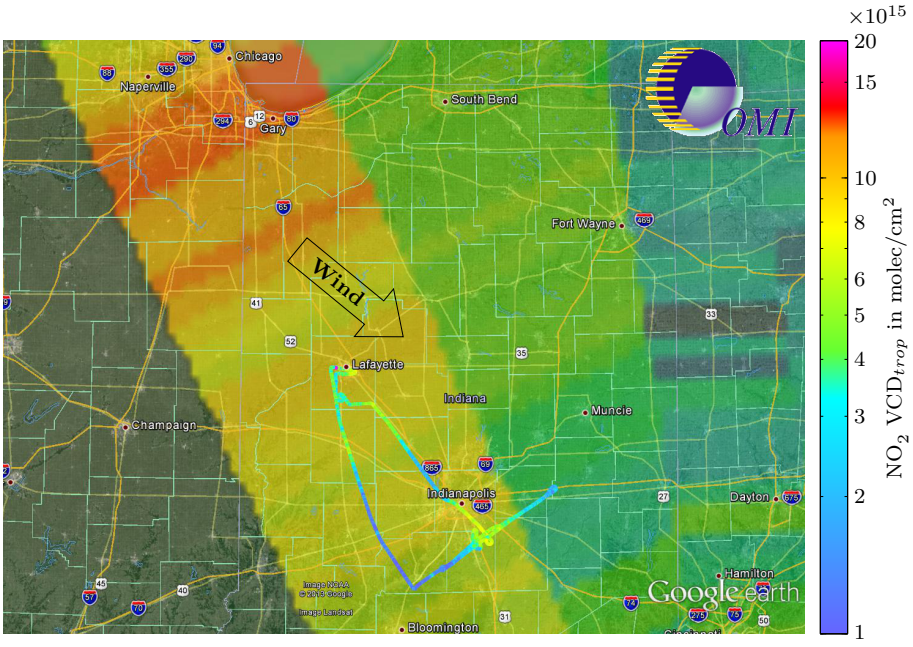

Figure 7.3.: Comparison of NO_2 measurements between OMI (Aura) and HAIDI's nadir scanner on 24$^{\text{th}}$ October 2011, visualized as overlay in Google Earth (TEMIS, 2013).

7.2.2. Comparison with Satellite Data

A map showing the calculated NO_2 VCDs for 24th October can be found in Fig. 7.3, together with measurements from the Ozone Monitoring Instrument (OMI) for comparison. OMI is a UV–Vis DOAS instrument aboard the NASA satellite Aura and intended to monitor the global ozone distribution as well as other key air quality components such as NO_2 and SO_2. It works on the basis of the pushbroom technique and has a spatial resolution of 13×24 km by default, which can be zoomed to 13×13 km (NASA, 2011). By looking at Fig. 7.3 one can see, that the OMI data clearly shows enhanced NO_2 downwind of Chicago. However, due to the high flight altitude of the satellite (~ 710 km) and the thus resulting low spatial resolution, measurements from OMI average over a much larger area in comparison to HAIDI's nadir scanner. For this reason the smaller emission plume of Indianapolis cannot be observed by the OMI measurements.

7.3. Flight on 25th October

The measurement flight from 25th of October can be found in Appendix A.2.

8. Results of the BROMEX Campaign (2012)

During the BROMEX campaign a total of 11 measurement flights were undertaken, from which four are presented and discussed in detail in the following chapter. Especially on these days, large scale BrO distributions with partially strong horizontal gradients could be observed around Barrow. The flight to Prudhoe Bay on 31st March 2012 furthermore shows some interesting anti-correlations between the spatial distributions of BrO and NO_2. Measurements on the remaining days showed generally lower column densities of BrO or very similar results (see e. g. 19th and 24th March). Maps and time series with the data of these flights can be found in Appendix A.3.

8.1. Flight on 13th March

The first measurement flight of the BROMEX campaign started on 13th March at about 19:50 UTC (11:50 LT, change to Alaska Daylight Time was on 11th March). Generally clear-sky conditions could be seen on that day and also the Arctic sea ice cover around Barrow was still intact (see also Fig. 5.9a). A map with the flight track from 13th March can be found in Fig. 5.8. The track basically ran between the position of the two IceLanders, which were deployed on the sea ice eastern (IceLander-1) and western (IceLander-2) of Barrow by the University of Alaska Fairbanks (UAF). The IceLanders are solar powered mobile instrument packages that are able to measure BrO, O_3 and meteorological parameters like temperature, wind speed, wind direction, relative humidity and atmospheric pressure (UAF, 2012). Data from the IceLanders was transmitted via two-way Iridium satellite connection for more than a month, before Icelander-1 was returned and Icelander-2 drifted away with the melting sea ice.

A time series with the measurement data from 13th March can be found in Fig. 8.1. As one can seen here, the nadir scanner could measure BrO dSCDs of up to 2.3×10^{14} molec/cm^2, but no significant NO_2 column densities. The highest dSCDs of BrO were thereby observed close to Barrow, shortly after takeoff. Similar observations were made by the forward-looking telescope. Interestingly, a split-up between the different viewing directions can be seen here. For flight altitudes above $\sim$ 1000 m the downward looking viewing directions detected considerably higher column densities, so that most of the BrO was probably below this altitude. The spatial distribution of BrO (Fig. 8.2) furthermore reveals that there was a strong gradient along the east-west direction on that day. For a better comparability with satellite data, the map shows tropospheric VCDs, which were calculated from measured dSCDs using Eq. (4.11).

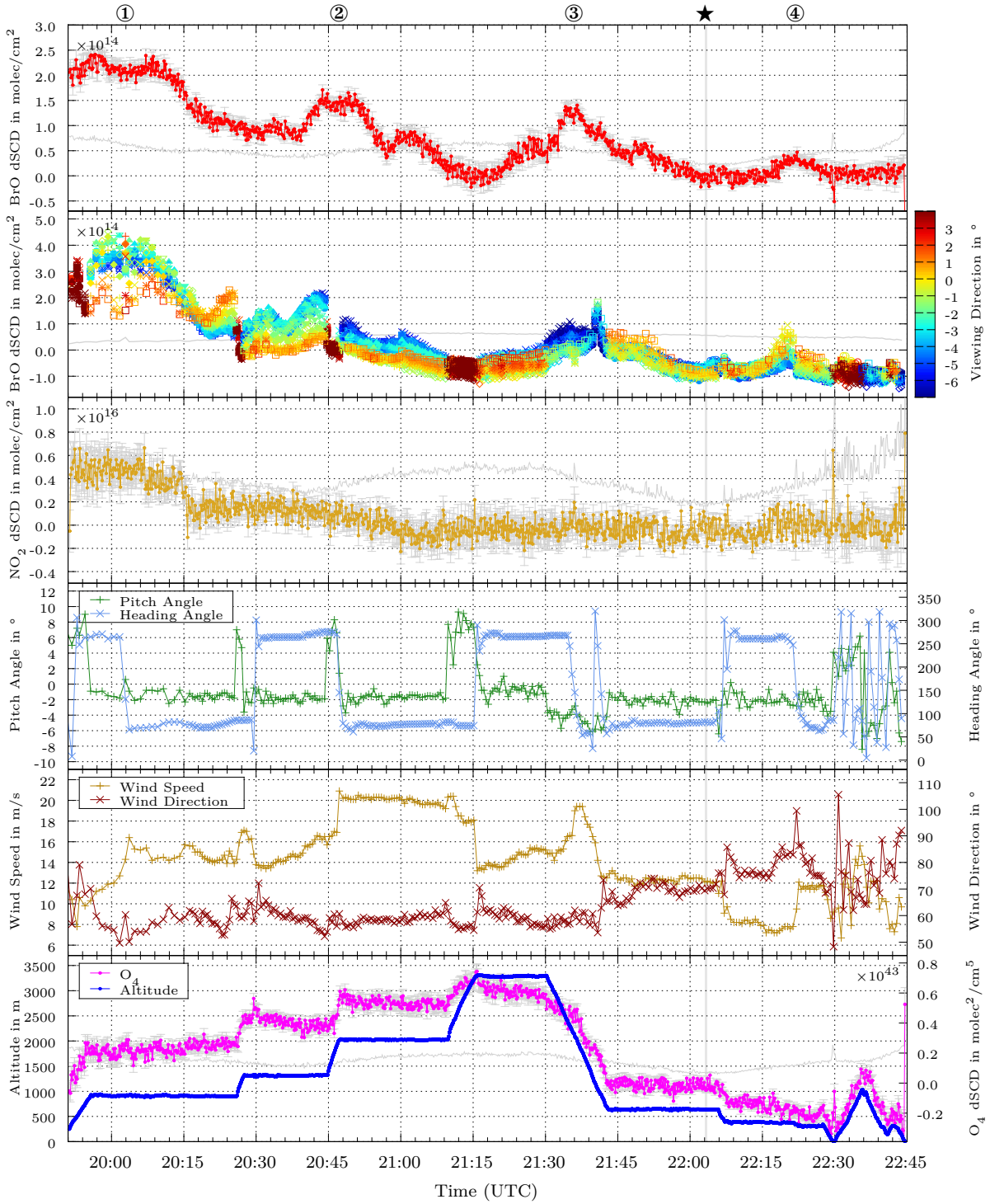

Figure 8.1.: Time series of measurement data from the flight on 13$^{\text{th}}$ March 2012. Errors and detection limits are plotted in gray. ★: Recording period of nadir scanner in-flight FRS. ①–④: western about-turns, also shown in Figs. 8.2 and 8.3.

The stratospheric VCD of BrO was assumed to be 5×10^{13} molec/cm^2 (Choi, 2010) for this conversion. Since the visibility of the data in the map is limited by overlapping flight sections, Fig. 8.3 illustrates the data from the nadir scanner in a slightly different way. Here the measured BrO dSCDs are plotted in a longitude versus time diagram. For a better orientation the western about-turns are marked by numbers from ① to ④ in chronological order in the map and the raw data plot as well. The plot shows high BrO VCDs of about 3.5×10^{13} molec/cm^2 directly above the airport and during the first flight to the west (①). In the subsequent flight to the east a strong horizontal BrO gradient was found. Within a range of 10 km the measured BrO VCDs declined nearly by a factor of 2. When the aircraft returned to the west (②) approximately 45 min later, to almost the same coordinates as before (157.8° W), the measured column density had dropped to around 2.8×10^{13} molec/cm^2 but also the observed BrO gradient has shifted by about 20 km to the west in the meantime. Another 45 min later ($\sim$ 102 min after takeoff) the aircraft flew a third time to the area western of Barrow (③) where the BrO gradient has again shifted to the west by a similar distance. These observations suggest, that the detected BrO distribution was part of a larger BrO plume, which propagates in western direction with the wind.

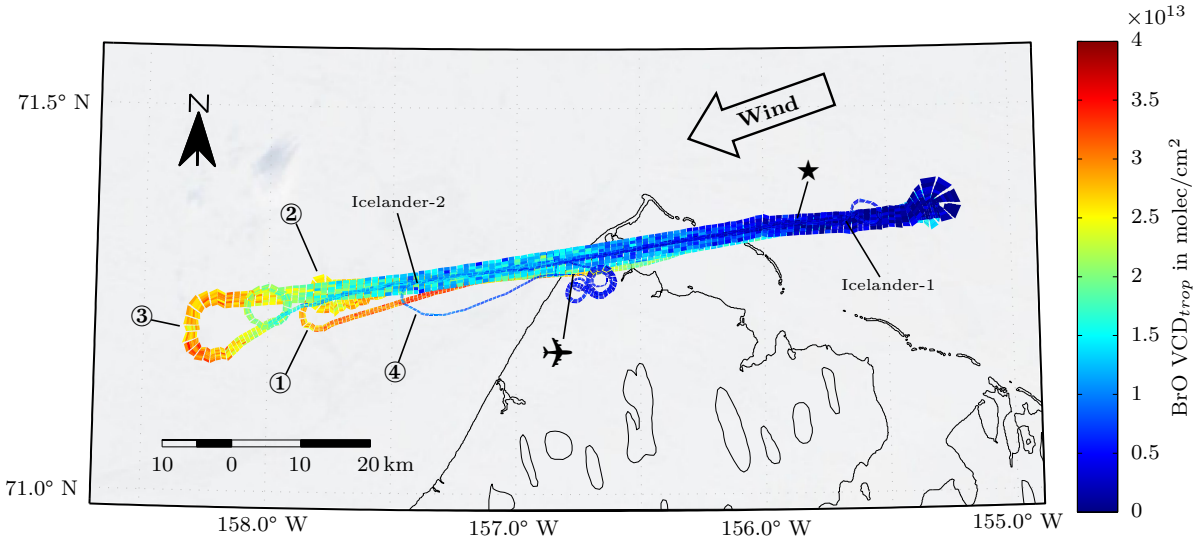

Figure 8.2.: Map showing the spatial distribution of BrO around Barrow, measured by HAIDI's nadir scanner on 13th March 2012. In the background a true color satellite image from MODIS (Terra), taken on the same day with a resolution of 250 m, is shown (NASA, 2012). The encircled numbers indicate the western about-turns, which are also marked in Figs. 8.3 and 8.1. ✈: Location of Barrow airport, ★: Recording position of nadir scanner in-flight FRS.

8.1.1. Calculation of Plume Age and Speed

The approximate speed at which the observed BrO distribution was moving westward could be estimated by fitting a straight line trough points where the BrO gradient reaches a column

density of 2.5×10^{13} molec/cm^2 in Fig. 8.3. The fit yields a slope of about (61 ± 4) min/° W, which corresponds to a speed of (9.8 ± 0.6) m/s for the given latitude. This agrees with the meteorological data taken by the BAT probe of the aircraft during flight. For altitudes below 1000 m an average wind direction of (70 ± 10)° and a wind speed of (11.6 ± 2.4) m/s were measured (Tab. 5.6). Hence, air masses move to the west with an average rate of (10.9 ± 3.0) m/s, which matches the calculated speed of the plume within the error.

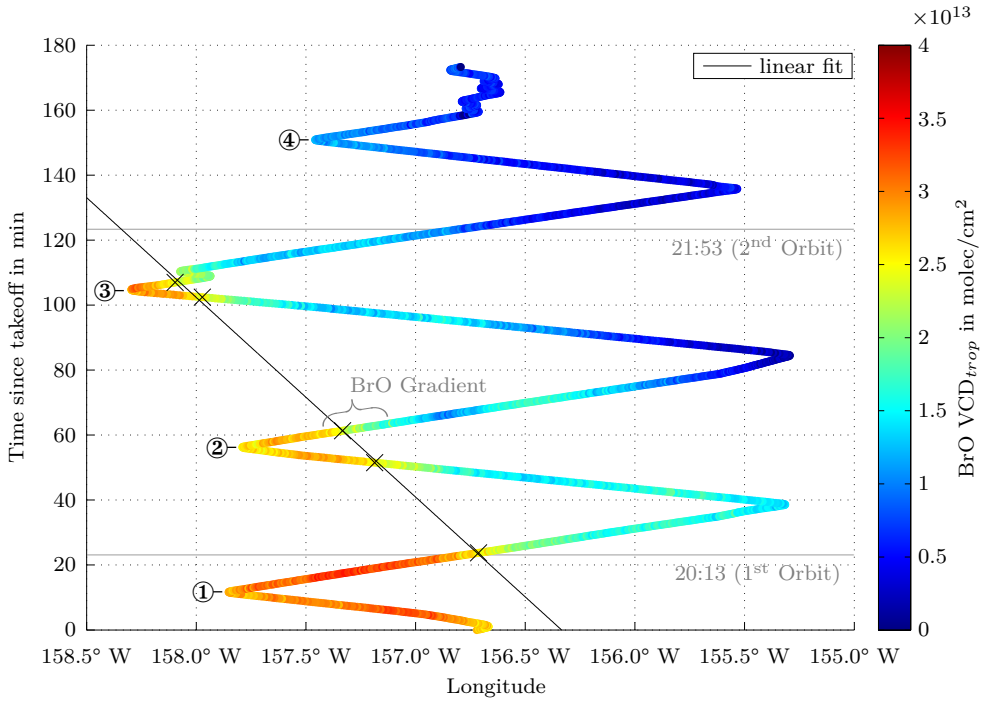

Figure 8.3.: BrO VCDs measured on 13$^{\text{th}}$ March 2012 by HAIDI's nadir scanner. For a better overview the data is plotted in a longitude versus time diagram. At the beginning of the flight (19:50 UTC) high column densities could be observed close to Barrow. Later during flight strong horizontal BrO gradients along the east-west direction were detected. These gradients make a change in BrO column density by a factor of 2 within a distance of 10 km (indicated by the width of the bracket). As time passed, the BrO distribution seemed to move to the west with the wind. Also shown are the times where GOME-2 passed over the area.

From the observed BrO gradients also a rough plume age t_{plume} can be derived via the turbulent diffusion equation (Roedel, 2000):

$$t = \frac{\Delta x^2}{2K_x} \,. \tag{8.1}$$

Here, Δx is the mean square distance of the gradient, which is about the distance after which the column density has dropped to half, and K_x is the turbulent diffusion coefficient. For a plume with $\Delta x = 1 \times 10^4$ m the turbulent diffusion coefficient K_x is approximately 5×10^7 cm^2/s:

$$\Rightarrow t_{plume} \approx \frac{(10^4\,\mathrm{m})^2}{10^4\,\mathrm{m^2\,s^{-1}}} = 10^4\,\mathrm{s} \approx 3\,\mathrm{h}$$

Thus, the observed BrO plume was relatively young and most likely still actively recycling to support the strong gradients.

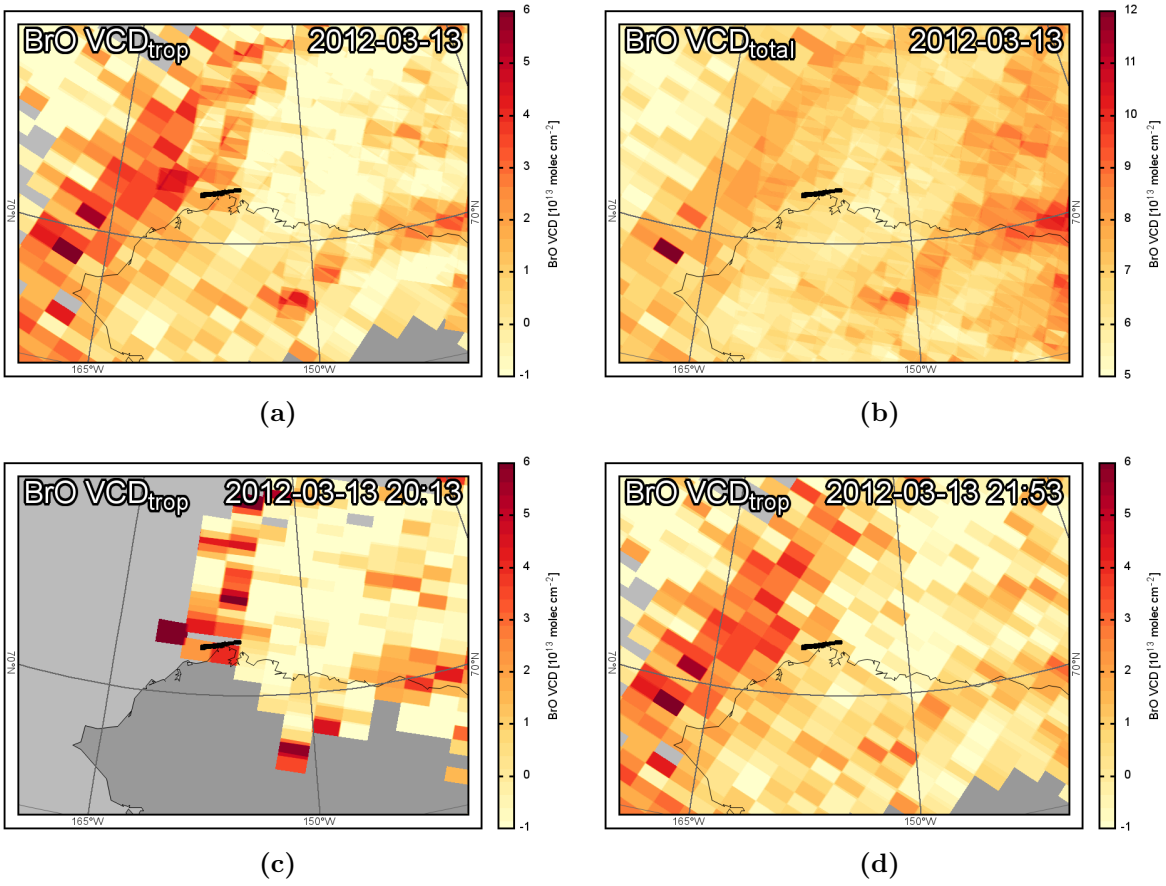

Figure 8.4.: GOME-2 satellite images showing the BrO distribution around Barrow on 13th March 2012 (H. Sihler, personal communication, 2013): (a) Tropospheric BrO VCD from a combination of two orbits. (b) Total BrO VCD from a combination of two orbits. (c) Tropospheric BrO VCD from a single orbit, taken during the start of the measurement flight. High BrO concentrations can be seen close to Barrow. (d) Tropospheric BrO VCD from the successive orbit, showing the BrO plume propagated to the west.

8.1.2. Comparison with Satellite Data

Satellite images from that day seem to confirm the measurements made by HAIDI. A series of satellite images from GOME-2 (MetOP) can be found in Fig. 8.4. The GOME-2 instrument orbits the Earth in a mean altitude of 817 km with an orbital period of approximately 101 min and takes spectral images with a spatial resolution (footprint size) of about 80 × 40 km (EUMETSAT,

2013). Particularly interesting are Figs. 8.4c and 8.4d, which show tropospheric BrO VCDs of the region around Barrow, derived from two consecutive orbits. The data in Fig. 8.4c was taken at 20:13 UTC, thus shortly after takeoff, and displays high BrO VCDs of around 4×10^{13} molec/cm^2 over Barrow. This agrees very well with the data from the nadir scanner, where tropospheric BrO VCDs of up to 3.5×10^{13} molec/cm^2 could be measured close to Barrow at the beginning of the flight. The next image (Fig. 8.4d) shows data from the subsequent orbit (21:53 UTC). At that time the BrO column density over Barrow has already declined to 1–2 $\times 10^{13}$ molec/cm^2 and higher VCDs were only seen further to the west, outside the area covered by the measurement flight from that day. HAIDI's instruments could also not observe higher BrO VCDs after 21:53 UTC (see also Fig. 8.3).

8.2. Flight on 15th March

The second measurement flight during the BROMEX campaign was performed on 15th March 2012 and started at about 20:39 UTC from Barrow airport. First cracks in the Arctic sea ice cover west of Barrow could be seen on satellite images from that day (Fig. 5.9b). However, the flight track on 15th March mainly led towards the inland and not above any leads. Apart from that, the weather conditions were similar to the flight on 13th March with no visible clouds in the sky. A map with the flight track from that day can be found in Fig. 5.8. The BAT probe of the aircraft measured a relatively constant wind direction of about $(70 \pm 7)°$ and a wind speed of (13.1 ± 2.1) m/s for altitudes below 1000 m (Tab. 5.9). For higher altitudes the wind direction changes northwards and reaches 30° at 3300 m.

At the beginning of the flight (20:39–21:22 UTC) the aircraft circled up to an altitude of approximately 3300 m in order to take a vertical profile. During all that time HAIDI's nadir scanner measured high BrO column densities directly over Barrow (Fig. 8.5). The spatial distribution of BrO (Fig. 8.6) furthermore shows that there was a gradient between the north-west and the south-east of Barrow. All data in the map was again converted to tropospheric VCDs using Eq. (4.11) and assumed stratospheric BrO VCDs of 5×10^{13} molec/cm^2 (Choi, 2010). This gradient also shows up as a zig-zag-pattern in the raw data from the nadir scanner at the beginning of the flight. Similar observations can be seen in the raw data from the forward-looking telescope, especially after 20:57 UTC, when the aircraft's pitch angle had returned to normal values for horizontal flight. In addition, the data from the forward-looking telescope suggests that BrO was located somewhere below 500 m in the vicinity to Barrow, since the highest column densities were observed at the beginning (20:39 UTC) and the end (21:21 UTC) of the vertical profile. After finishing the vertical profile, the aircraft returned to a normal flight level of about 700 m and headed in eastern direction towards the position of IceLander-1 (②). Here, only low BrO dSCDs were observed. The same was true for the location of IceLander-2 (③). At around 22:24 UTC the aircraft started to fly inland, in south-west direction. Over the tundra the measured BrO column densities increased again and strong gradients were found (④,

⑥). For example, at location ④ the tropospheric VCDs increased from about 2×10^{13} molec/cm^2 to 4×10^{13} molec/cm^2 within a distance of 10 km. This is comparable to the gradients seen on the flight before (13th March). The highest BrO column densities over the tundra were seen at about 22:43 UTC (⑤), 70 km to the south of Barrow. When the aircraft returned to Barrow airport no enhanced BrO could be detected any more. So within three hours the observed BrO dSCDs over Barrow dropped by about an order of magnitude, from 3.0×10^{14} molec/cm^2 ($VCD_{trop} = 5.6 \times 10^{13}$ molec/cm^2) to 2.5×10^{13} molec/cm^2 ($VCD_{trop} = 7.8 \times 10^{12}$ molec/cm^2), indicating high dynamics in the BrO distribution.

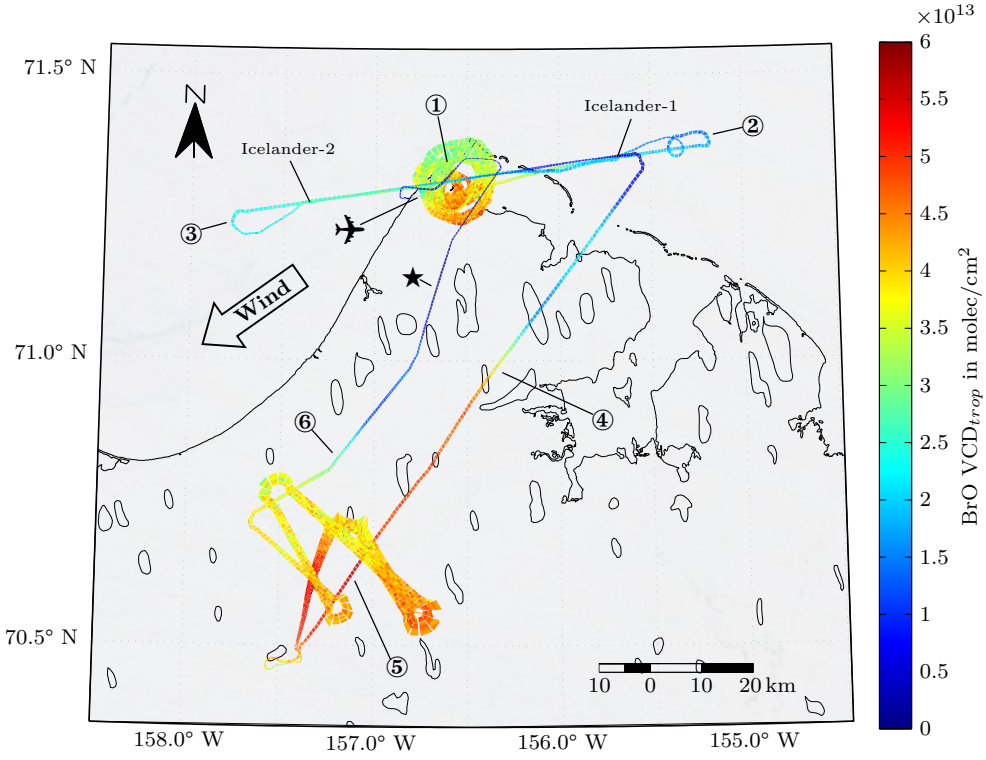

Figure 8.6.: Map showing the spatial distribution of BrO around Barrow, measured by HAIDI's nadir scanner on 15th March 2012. In the background a true color satellite image from MODIS (Terra) taken on the same day with a resolution of 250 m is shown (NASA, 2012). ①–⑥: characteristic points, also shown in Fig. 8.5. ✈: Location of Barrow airport, ★: Recording position of nadir scanner in-flight FRS.

8.2.1. Comparison with Satellite Data

The satellite images from 15th March show a BrO distribution which is in good agreement with the observations from HAIDI. In Fig. 8.7 a series of images from GOME-2 can be found. The data for the tropospheric VCD is thereby split into separate overpasses again (Figs. 8.7c and 8.7d) to get a better temporal resolution. The first overpass was taken at 19:31 UTC, about one hour before the flight. Here, one can see enhanced BrO column densities eastern, southern and western of Barrow. On the basis of wind speed and direction from that day the plume could

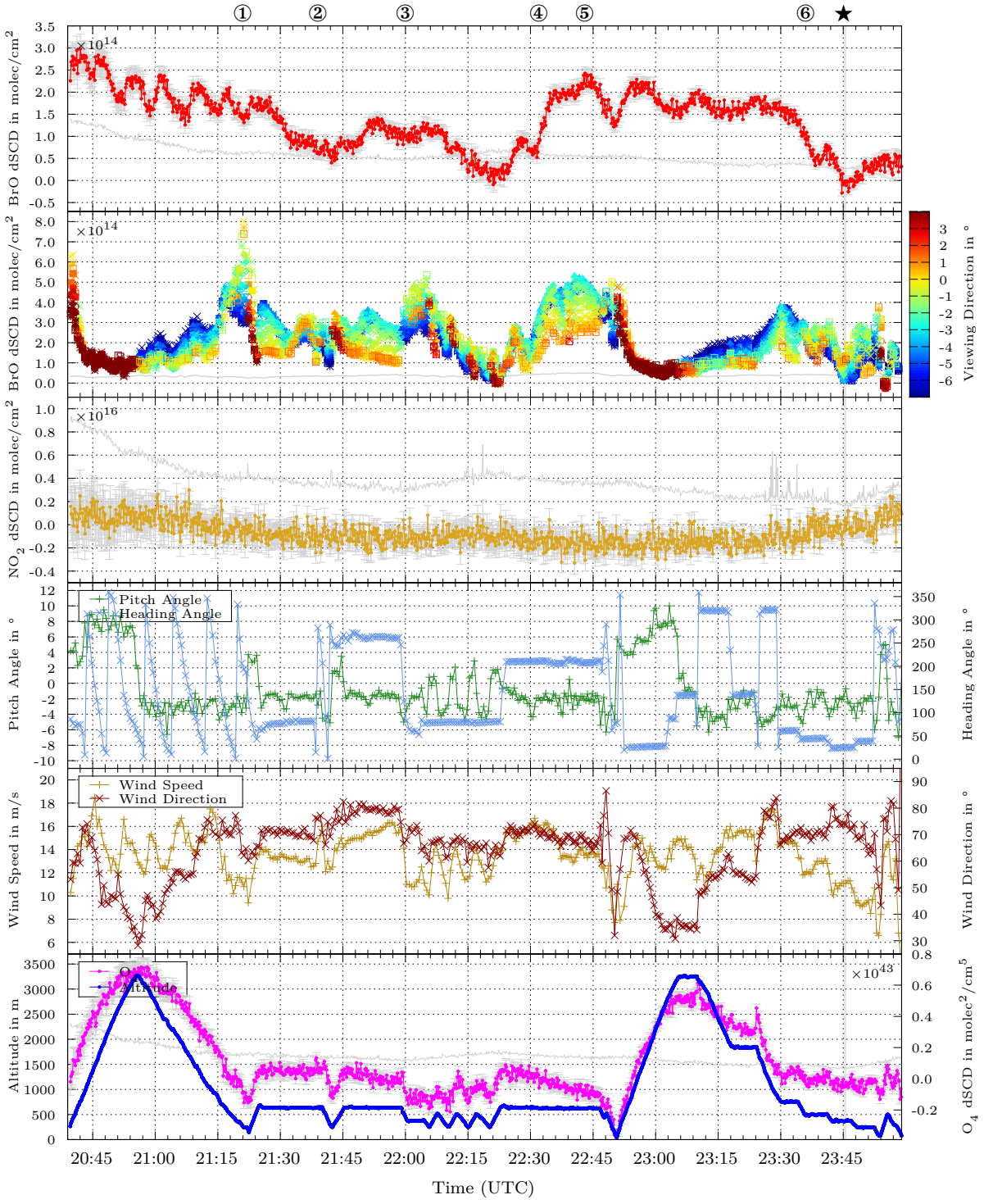

Figure 8.5.: Time series of measurement data from the flight on 15th March 2012. Errors and detection limits are plotted in gray. ★: Recording period of nadir scanner in-flight FRS. ①–⑥: characteristic points, also shown in Fig. 8.6.

have reached Barrow to the beginning of the flight. This would explain the high BrO column densities measured by HAIDI's nadir scanner close to Barrow and maybe also the observed gradient, because further to the north the column densities measured by GOME-2 where close to zero. Also the measured column densities agree with the satellite data. The nadir scanner showed peak VCDs of about 5.6×10^{13} molec/cm^2 over Barrow during the initial phase of the flight, which matches the 5.2×10^{13} molec/cm^2 from GOME-2 very well. The next overpass was taken at 21:12 UTC, to the time where the aircraft took the vertical profile. Higher VCDs of BrO ($\sim 4.5 \times 10^{13}$ molec/cm^2) were now observed mostly over the tundra to the south of Barrow. Similar observations were made by HAIDI's nadir scanner, that showed enhanced BrO over the tundra approximately 80 min later. Furthermore, in accordance with the data taken by HAIDI, measurements from GOME-2 showed only low column densities of BrO at the locations of Icelander-1 and 2.

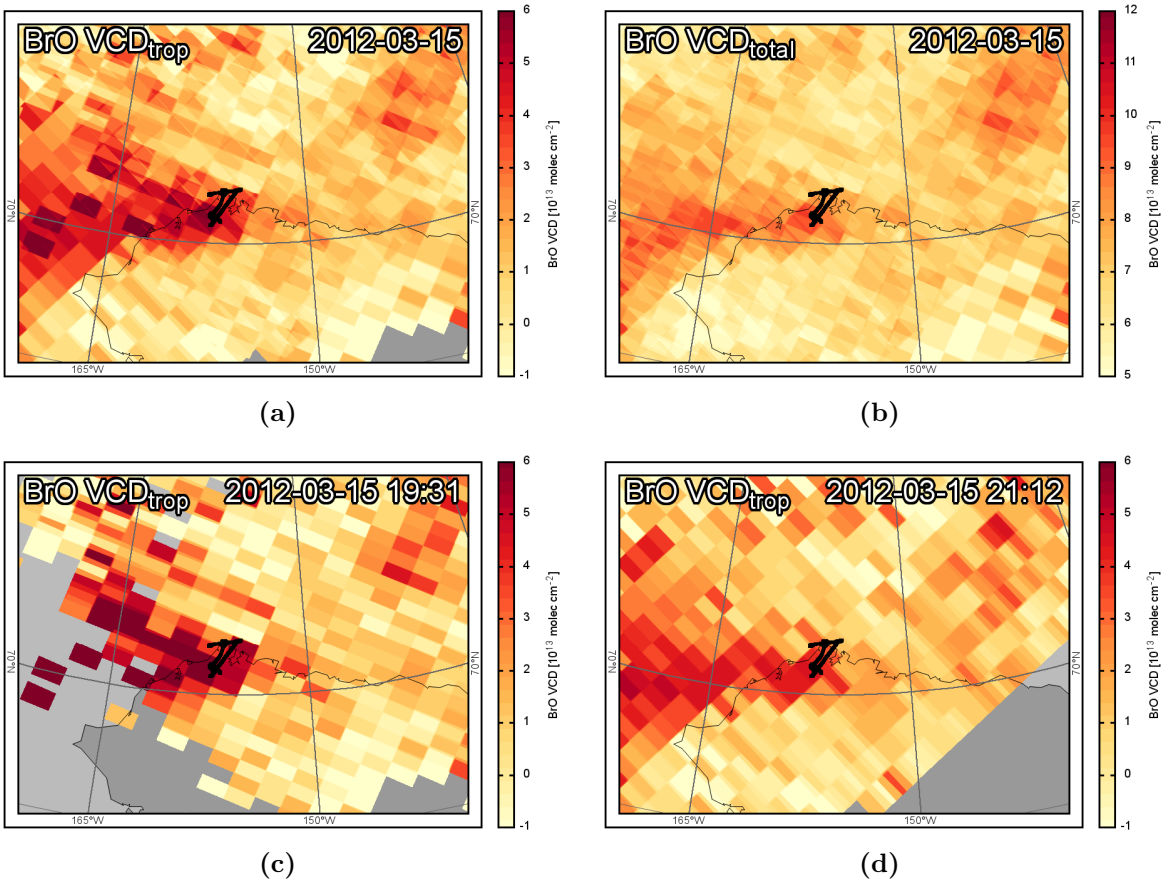

Figure 8.7.: GOME-2 satellite images showing the BrO distribution around Barrow on 15th March 2012 (H. Sihler, personal communication, 2013): (a) Tropospheric BrO VCD from a combination of two orbits. (b) Total BrO VCD from a combination of two orbits. (c) Tropospheric BrO VCD from a single orbit, taken about one hour before the measurement flight. High BrO concentrations can be seen around Barrow in western, eastern and southern direction. (d) Tropospheric BrO VCD from the successive orbit, showing generally lower BrO VCDs but still high concentrations over the tundra.

8.3. Flights on 19th–22nd March

The measurement flights from 19th, 20th and 22nd of March can be found in Appendix A.3.

8.4. Flight on 24th March

The sixth measurement flight of the BROMEX campaign was realized on 24th March and started at about 19:56 UTC from Barrow airport. As can be seen in Fig. 8.10 the lead western of Barrow had opened to a width of several kilometers in the meantime. Thus, it was too dangerous to cross it and the flight track could only go as far as to the edge of the lead. Therefore, the position of IceLander-2 could not be reached anymore, because IceLander-2 had already started to drift away with the sea ice from its initial position. A map with the flight track from that day can be found in Fig. 5.8. Weather conditions still show a clear sky above Barrow, but over the open lead and above the tundra some cloud layers could be seen on that day (see Figs. 5.9c and 8.8b). The average wind direction for flight altitudes below 1000 m was measured to be $(82 \pm 6)°$, with a wind speed of (17.3 ± 1.5) m/s (Tab. 5.9). Also for greater altitudes these values did not change much on 24th March (see Fig. 8.9).

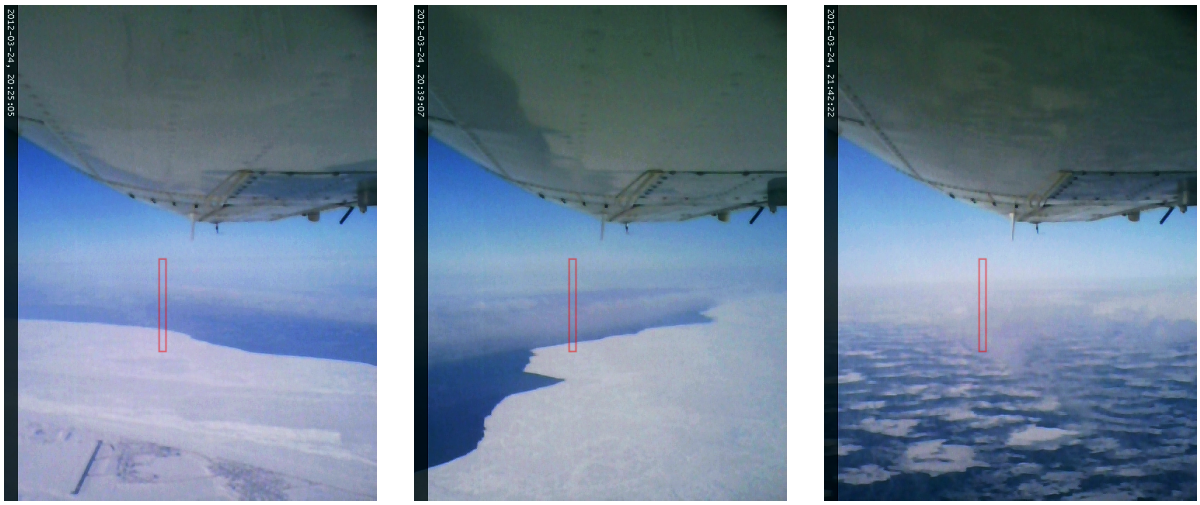

(a) (b) (c)

Figure 8.8.: Approaching the open lead on 24th March 2012, recorded by HAIDI's forward webcam. The FOV of the forward-looking telescope is indicated by the red rectangle: (a) The open lead at 20:25 UTC with Barrow airport and village in the foreground. (b) Flying along the open lead at 20:39 UTC. A dense cloud layer, formed by water vapor, arose from the open lead. (c) Above the open water at 21:42 UTC, showing drift ice in the lead.

As on the days before, also on 24th March enhanced BrO column densities could be observed. A time series with the data from that day can be found in Fig. 8.9. However, in contrast to the previous measurements the spatial distribution (Fig. 8.10) shows that no enhanced BrO could be detected close to Barrow. Along the path between Icelander-1 and the initial position

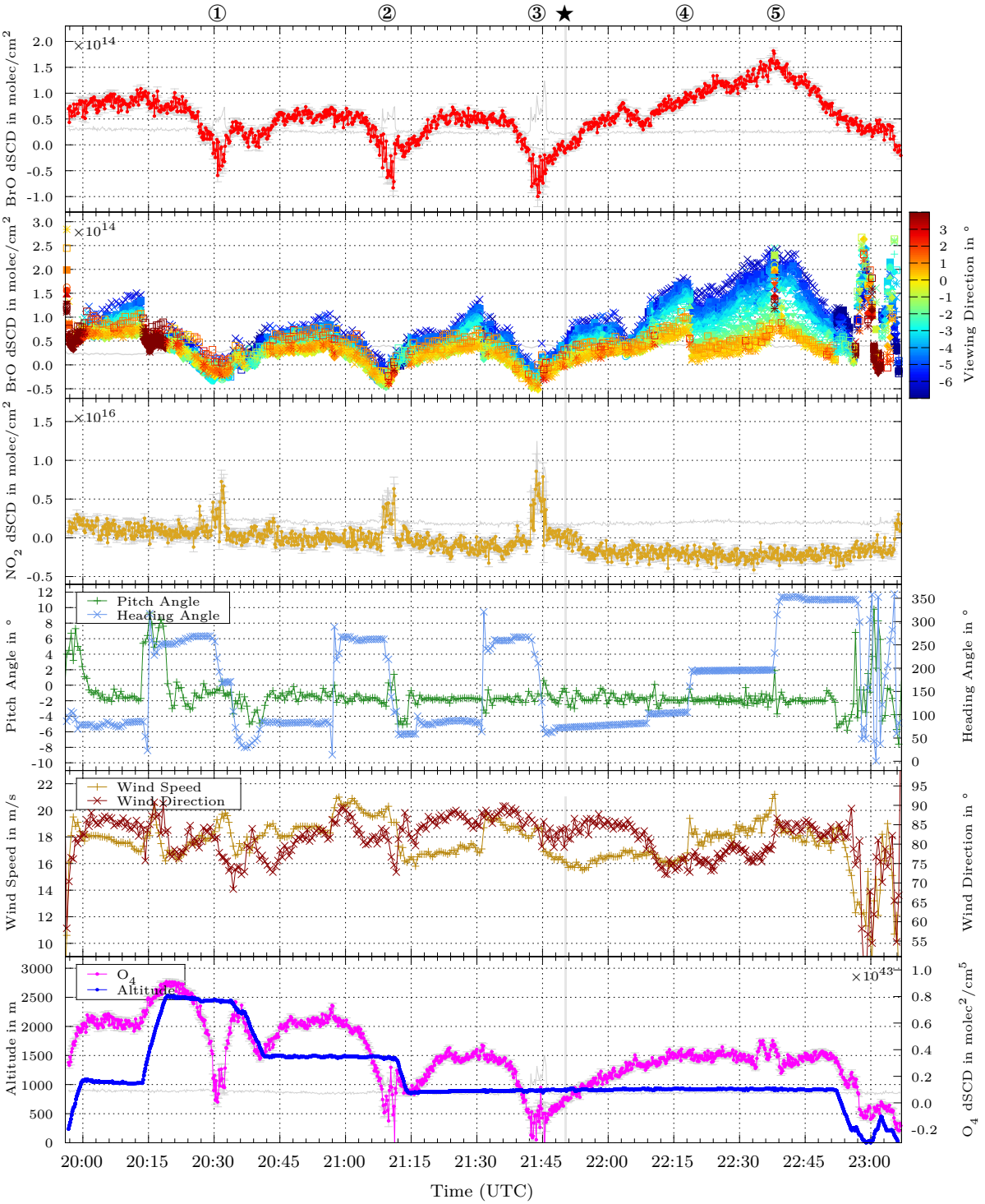

Figure 8.9.: Time series of measurement data from the flight on 24th March 2012. Errors and detection limits are plotted in gray. Directly above the open lead (①–③) the light intensity received by the nadir scanner dropped to very low values, which results in a noticeable higher detection limit. ★: Recording period of nadir scanner in-flight FRS.

of Icelander-2 relatively constant tropospheric VCDs of 1.3×10^{13} molec/cm^2 were observed. Particularly low values were measured when the aircraft approached the open lead (①–③). This is probably due to the fact that in these cases most of the light received by the nadir scanner is scattered on top of a cloud layer, which reduces the length of the instrument's light path. A strong indication for this are also the decreasing O_4 column densities, measured at the corresponding locations. Thus, most of the BrO must be located below the cloud layer. This is supported by the measurements from the forward-looking telescope, which shows generally higher column densities for the downward looking viewing directions, even at flight altitudes of around 500 m (22:54 UTC).

Higher column densities of BrO were only seen above the tundra on 24th March. At about 22:18 UTC (④) the aircraft headed south in order to fly inland. Starting from here the measured BrO column densities from both instruments increased the further the aircraft moved to the south. The highest values were seen at about 22:37 UTC (⑤), with tropospheric VCDs of approximately 5.2×10^{13} molec/cm^2. However, the observed gradients were lower than those seen on 13th and 15th March, indicating a higher plume age. The fact that enhanced bromine oxide levels were often seen at low altitudes above the tundra, like e. g. on 15th, 19th (Appendix A.3: Fig. A.13) and 24th March, or seem to originate from areas close to snow-covered first-year

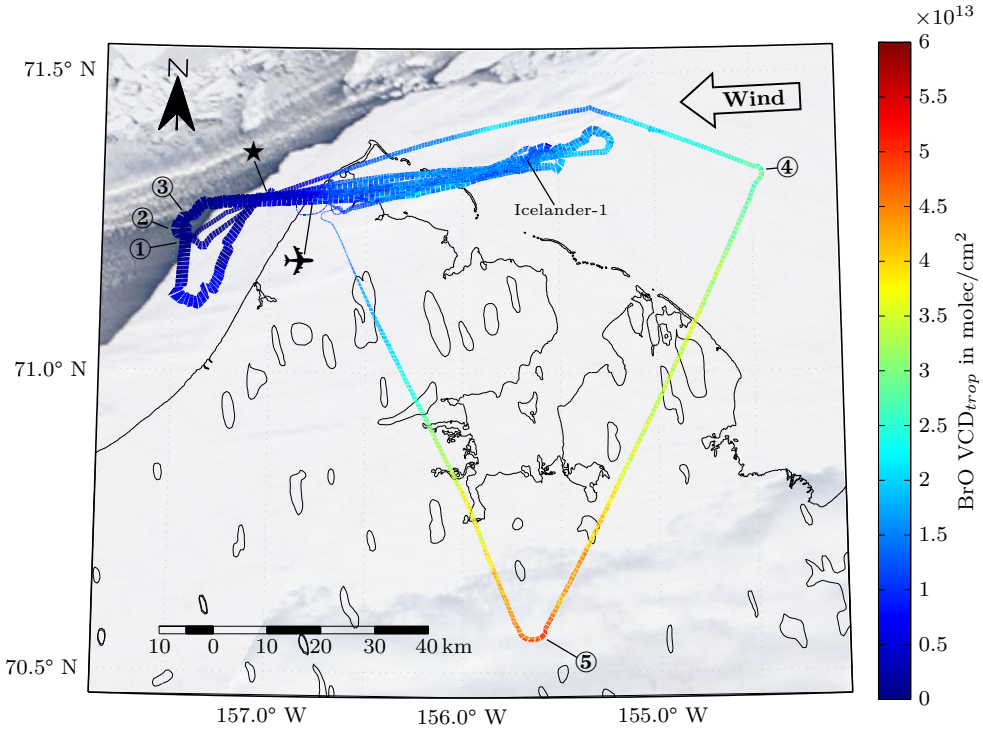

Figure 8.10.: Map showing the spatial distribution of BrO around Barrow, measured by HAIDI's nadir scanner on 24th March 2012. In the background a true color satellite image from MODIS (Terra) taken on this day with a resolution of 250 m is shown (NASA, 2012). ①–③: Measurements above the open lead. ✈: Location of Barrow airport, ★: Recording position of nadir scanner in-flight FRS.

sea ice, like e. g. on 13th and 31st March, suggests that surface snow serves as one major source of reactive bromine in the Arctic springtime as stated by Pratt et al. (2013).

8.4.1. Comparison with Satellite Data

Satellite images from GOME-2, that were recorded around the time of the measurement flight, can be found in Fig. 8.11. The first overpass (Fig. 8.11c) was taken at 19:45 UTC, around 10 min before the start of the measurement flight, and shows generally low levels of bromine oxide around Barrow and at the location of the open lead. This is consistent with later measurements from HAIDI in the same area. Higher levels of bromine oxide were seen by GOME-2 over the tundra instead. The next overpass (Fig. 8.11d) was at 21:26 UTC, while the aircraft was still cruising between the positions of Icelander-1 and 2. The column densities measured by GOME-2 around Barrow have not changed much in the meantime. Both instruments reported similar

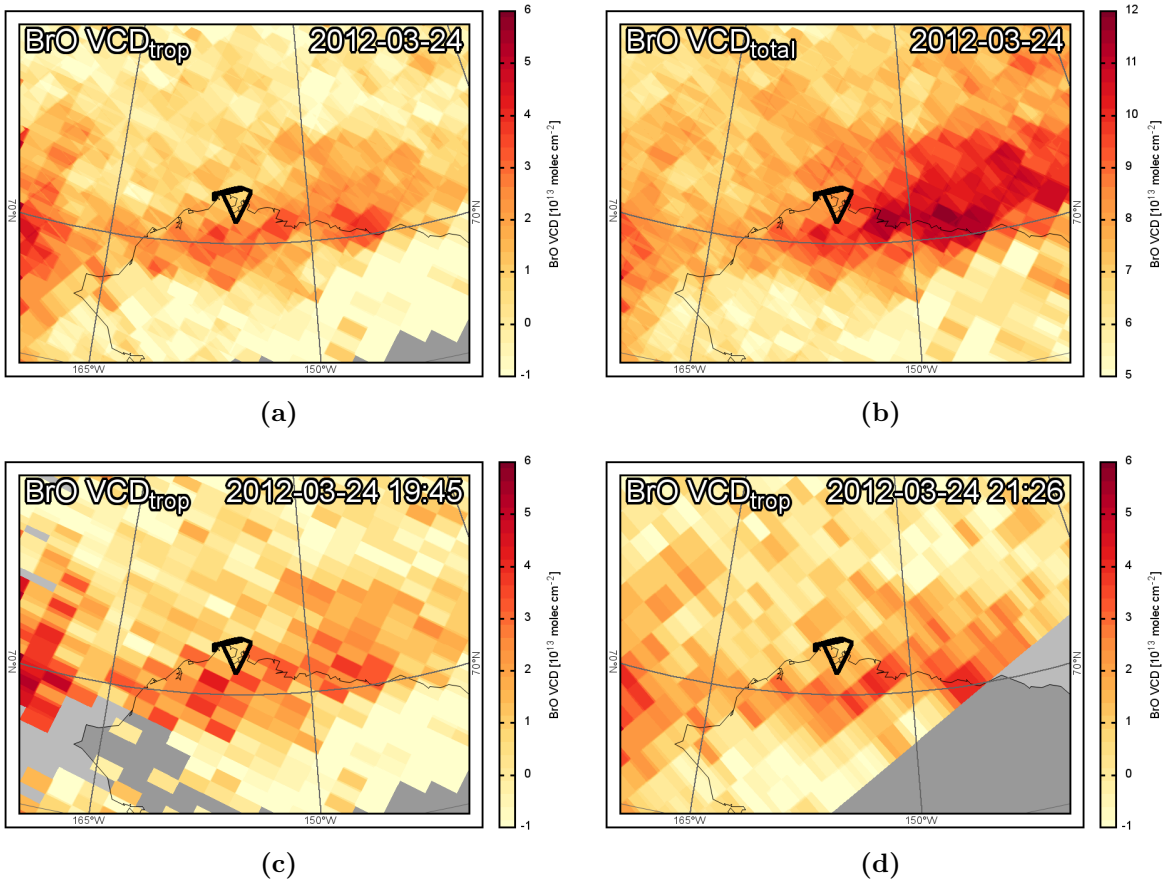

Figure 8.11.: GOME-2 satellite images showing the BrO distribution around Barrow on 24th March 2012 (H. Sihler, personal communication, 2013): (a) Tropospheric BrO VCD from a combination of two orbits. (b) Total BrO VCD from a combination of two orbits. (c) Tropospheric BrO VCD from a single orbit, taken shortly before the measurement flight. BrO enhancements can be seen over the tundra, south of Barrow, but not over the surrounding sea ice or at the open lead. (d) Tropospheric BrO VCD from the successive orbit. At this time BrO values in the south have declined, but another plume with enhanced BrO has formed in the east.

results from this area. While GOME-2 measured a VCD of 1.5×10^{13} molec/cm^2, HAIDI shows an average value of 1.3×10^{13} molec/cm^2 at the same time. However, the tropospheric VCDs observed by GOME-2 over the tundra during the second overpass have declined significantly. Enhanced BrO ($\sim 4.0 \times 10^{13}$ molec/cm^2) was detected more to the east at that time, about 70 km away from the later flight track of the aircraft. HAIDI passed the area with enhanced BrO approximately 70 min after the overpass of GOME-2. Due to the wind direction and wind speed from that day, the BrO plume could have reached the area overflown by the aircraft within this time. Because of the strong horizontal gradients measured by the nadir scanner in this area and the much larger pixel size of GOME-2, measurements from HAIDI have to be averaged in order to compare them with the satellite data. The average tropospheric VCD detected by HAIDI over the tundra is $\sim 4.5 \times 10^{13}$ molec/cm^2. This roughly agrees with the column density measured by GOME-2 in the east ($\sim 4.0 \times 10^{13}$ molec/cm^2).

8.5. Flights on 26th–28th March

The measurement flights from 26th and 28th of March can be found in Appendix A.3.

8.6. Flight on 31st March

The eleventh and last measurement flight of the BROMEX campaign was conducted on 31st March 2012. Compared with the previous flights, it started relatively late, at about 00:25 UTC, from Barrow airport. Only the flight on 19th March (Appendix A.3: Fig. A.12) was performed at a comparable time. Due to the late time of day both flights show high SZAs (up to 82°/85°, see Tab. 5.7) and therefore low light conditions in the later flight phase. The reason for the late takeoff on that day was, that another flight was conducted earlier. For the earlier flight, however, no GPS data is available and therefore no measurement data from that flight is presented here. Apart from the late flight time, the track from 31st March also led to a different region. While most of the previous flights went to the south of Barrow (see Fig. 5.8), the flight on 31st March led towards Prudhoe Bay, about 350 km eastern of Barrow. Prudhoe Bay is adjacent to the biggest oil field in North America and also hosts one of the world's largest industrial complexes with an approximate annual NO_x emission of $(12 \pm 4) \times 10^3$ t (Jaffe et al., 1995).

The weather conditions had slightly declined in the days before, so that there was a thin cloud layer above Barrow on 31st March. Also above the open lead clouds have formed again and satellite images from that day show larger cloud formations over the western part of Prudhoe Bay (Fig. 5.9d). The aircraft's instruments measured an average wind direction of 70° at Prudhoe Bay and a wind speed of about 9 m/s.

Due to the large expansion of the flight track in east-west direction, the maps in Fig. 8.13 show only a part of the flight with the area of Prudhoe Bay. The data in these maps was taken in the period between 1:31 and 2:30 UTC (gray shaded section in Fig. 8.12). A set of

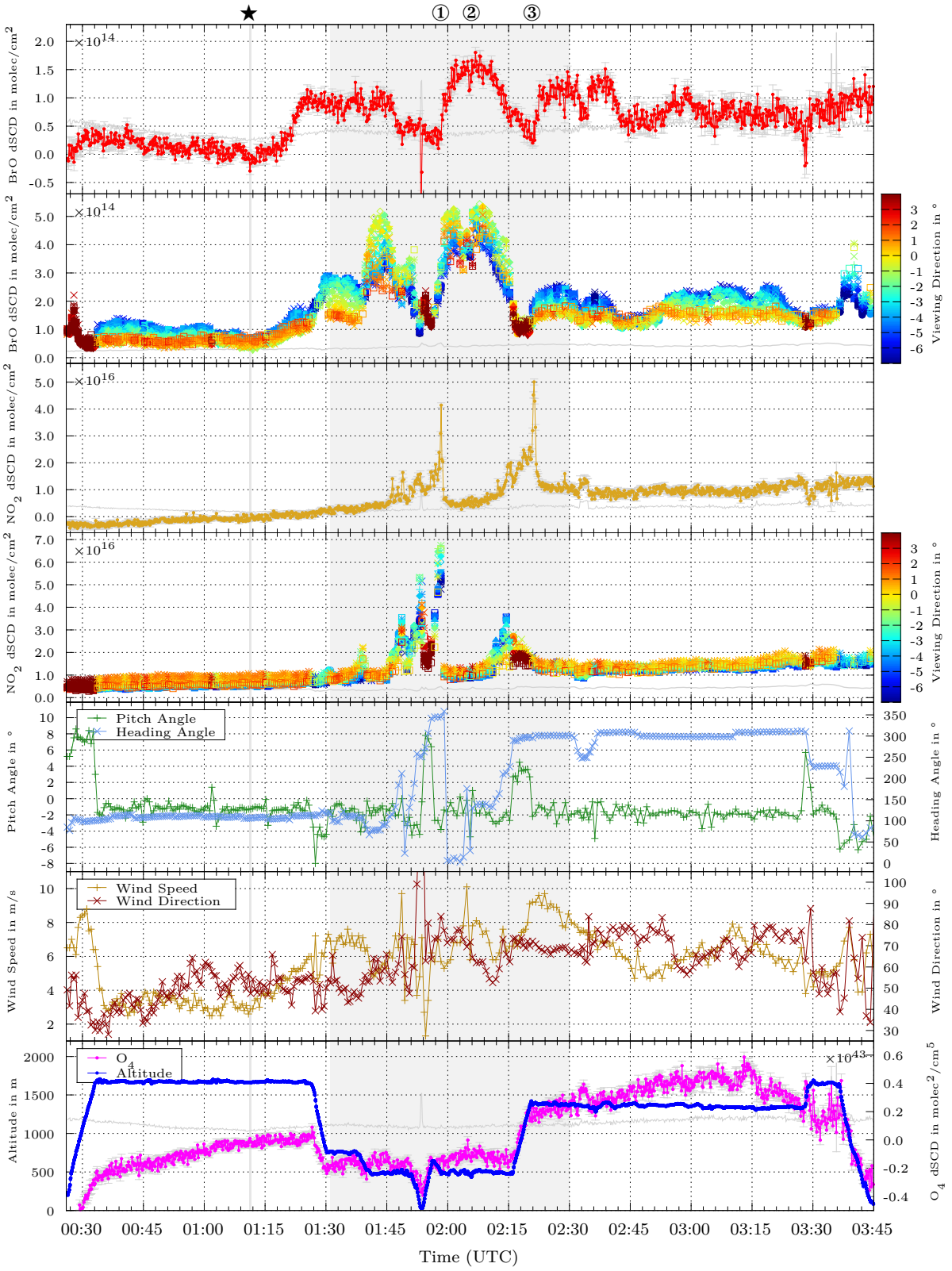

Figure 8.12.: Time series of measurement data from the flight on 31st March 2012. Shaded in gray is the section of the flight around Prudhoe Bay, Alaska, which is also shown in Fig. 8.13. Errors and detection limits are also plotted in gray. ★: Recording period of nadir scanner in-flight FRS.

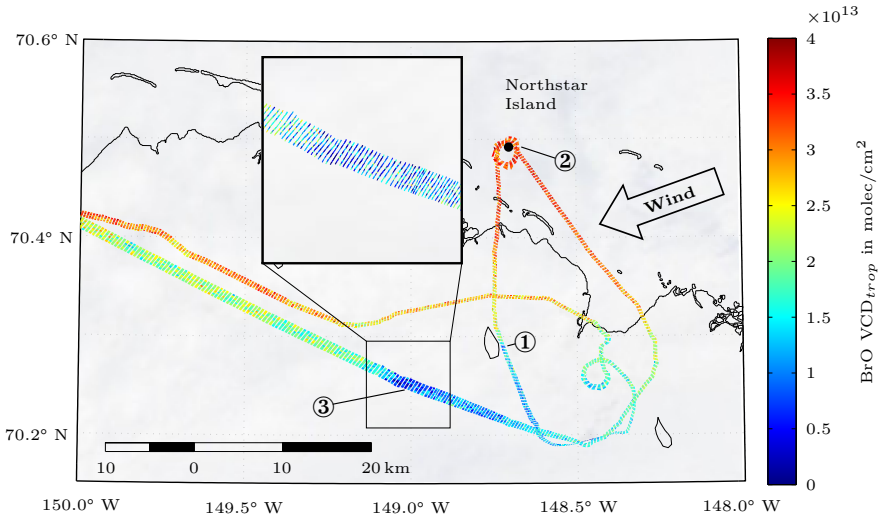

(a) BrO distribution

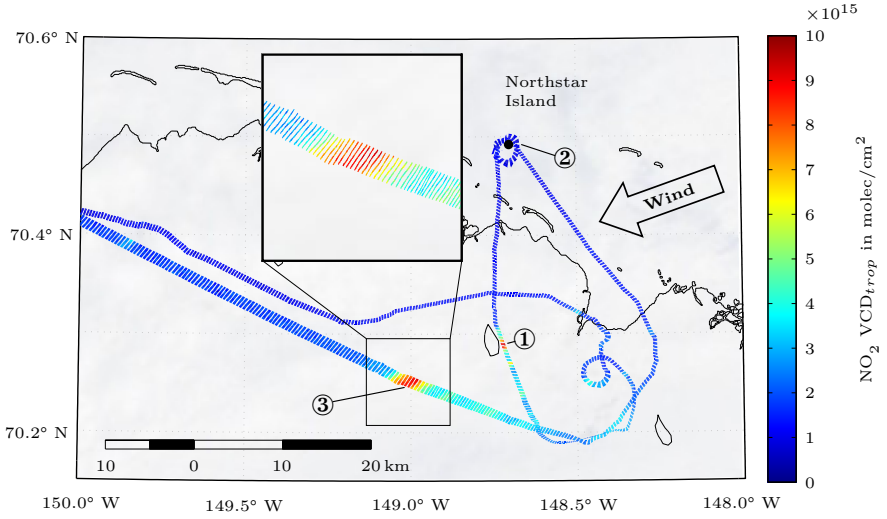

(b) NO_2 distribution

Figure 8.13.: Maps showing a part of the flight to Prudhoe Bay on 31st March 2012. The displayed distributions of BrO and NO_2 were measured by HAIDI's nadir scanner between 1:31 and 2:30 UTC (gray shaded section in Fig. 8.12). Noticeable in the observed trace gas distribution is an anti-correlation between BrO and NO_2 column densities (①, ②, ③). The background shows a true color satellite image taken by MODIS (Aqua) on the same day with a resolution of 250 m (NASA, 2012).

maps showing data from the whole flight can be found in Appendix A.3: Fig. A.27. As can be seen with reference to the spatial distribution, the highest BrO column densities were observed offshore on that day, while flying in vicinity of the coastline (②). The nadir scanner measured BrO dSCDs of up to 1.7×10^{14} molec/cm^2 ($VCD_{trop} \approx 3.7 \times 10^{13}$ molec/cm^2) in this area and also the data from the forward-looking telescope shows clearly increasing column densities at the same location. Due to the combustion of fossil fuels by the industrial complex of Prudhoe Bay, the flight on 31st March is the only one during the BROMEX campaign where significant column

densities of NO_2 could be observed. NO_2 acts as a sink for BrO by forming $BrONO_2$, thus some interesting anti-correlations between the distribution of BrO and NO_2 could be observed close to Prudhoe Bay. At the location of enhanced BrO, the observed NO_2 column densities were always close to zero. The opposite effect occurred further to the south of Prudhoe Bay (③), where high NO_2 dSCDs of about 5.0×10^{16} molec/cm^2 ($VCD_{trop} \approx 8.2 \times 10^{15}$ molec/cm^2) could be seen by the nadir scanner, together with a local BrO minimum. This location is also shown with a higher spatial resolution (binning: $1 \times 8 \Rightarrow$ resolution: 39×137 m) in the magnification view of Fig. 8.13. Here, one can clearly see that the NO_2 plume extended along the ENE-WSW direction. A second but smaller NO_2 distribution can be seen more to the northeast (①). Both can be connected with a straight line whose orientation corresponds approximately to the wind direction. Therefore, it can be assumed that both NO_2 distributions belong to a contiguous exhaust plume, which propagates with the wind from the industrial complexes of Prudhoe Bay. The general increase that can be seen in the measured slant column densities of NO_2 (Fig. 8.12), is most likely due to an increasing SZA (69–82°) during the flight, which enhances the stratospheric AMF.

8.6.1. Comparison with Satellite Data

The satellite images taken by GOME-2 on 31st March 2012 unfortunately do not show any information about the spatial distribution of BrO in the area covered by the measurement flight (Fig. 8.14). However, NO_2 satellite data from GOME-2 is available for comparison. As can be seen in Fig. 8.15, the NO_2-enriched air masses originating from Prudhoe Bay were also seen by GOME-2, which passed over the area only a few hours before HAIDI. Despite this temporal offset measurements from GOME-2 and HAIDI show a very good agreement in the spatial distribution of NO_2.

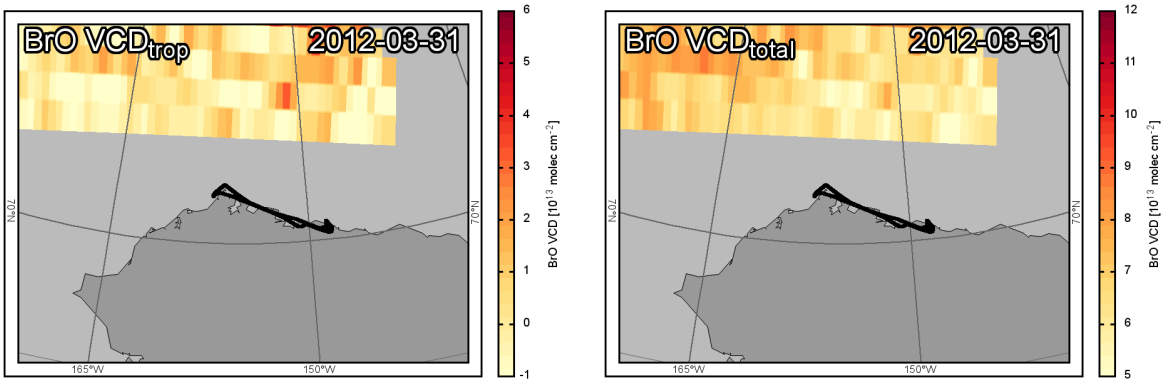

(a) **(b)**

Figure 8.14.: GOME-2 satellite images showing the BrO distribution around Barrow on 31st March 2012 (H. Sihler, personal communication). Unfortunately there is no data for the area of the flight on this day: (a) Tropospheric BrO VCD from a combination of two orbits. (b) Total BrO VCD from a combination of two orbits.

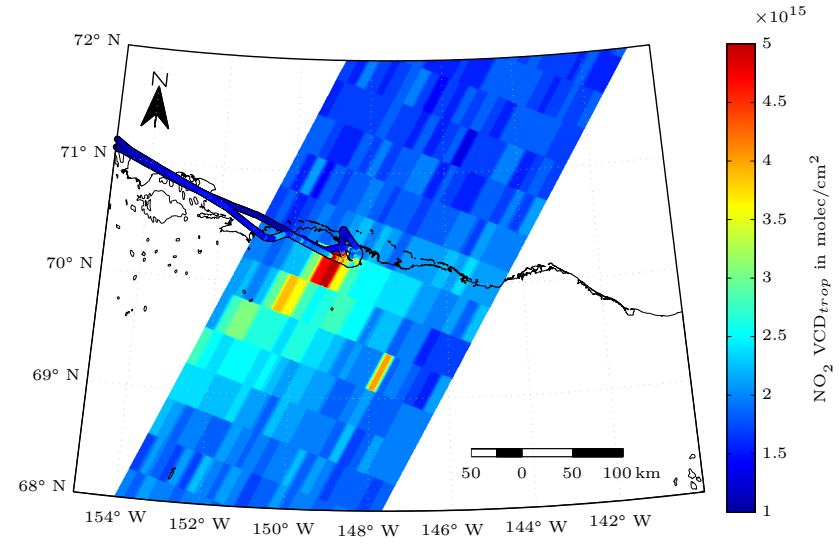

(a)

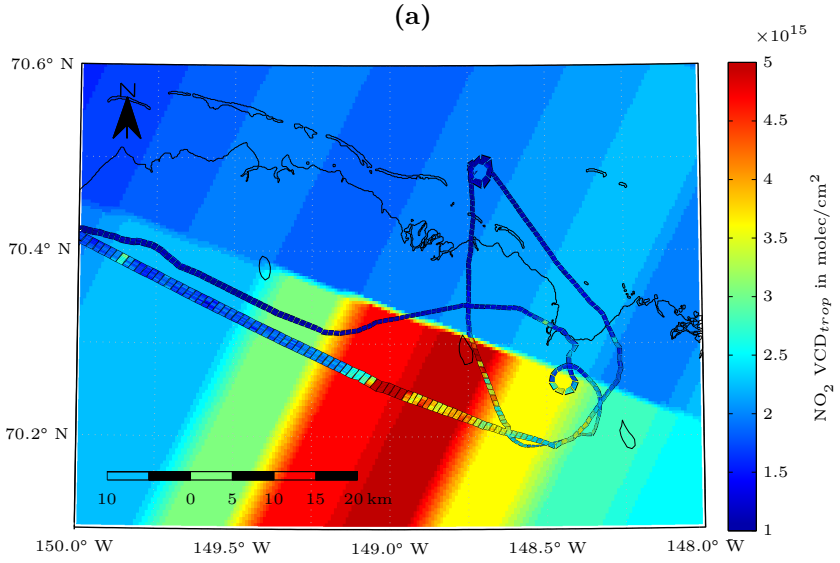

(b)

Figure 8.15.: Comparison of NO_2 VCDs around Prudhoe Bay, measured by GOME-2 (DLR, 2012) and HAIDI: (a) The GOME-2 satellite swath covered Prudhoe Bay on 30th March at 21:02 UTC, 4.5 hours prior to the measurements with HAIDI. As can be seen, the satellite data shows a large NO_2 plume propagating in wind direction. Measurements from HAIDI are indicated by color-coded dots. (b) The enlarged view shows that enhanced NO_2 was only seen onshore. Due to favorable pixel positions in the satellite swath this can also be confirmed by the GOME-2 measurements, which have a much lower resolution.

9. Conclusion and Outlook

The focus of this thesis was the development and testing of a novel remote sensing device for spatial and temporal high resolved measurements of various atmospheric trace gases on the basis of the differential optical absorption spectroscopy, the **H**eidelberg **A**irborne **I**maging **D**OAS **I**nstrument (HAIDI). HAIDI is primarily intended for future usage on the German research aircraft HALO, but can also be operated on smaller aircraft. Due to various restrictions, the operation on such aircraft usually requires a very compact system with low power consumption. Therefore, HAIDI uses a modular concept. It can either be operated with a single whiskbroom scanner (only 2-dimensional hyperspectral images) or, if vertical trace gas profiles are desired, with up to three whiskbroom scanners or a combination of whiskbroom and pushbroom scanners. Furthermore, several main components of the system, like e. g. spectrographs and CCD cameras, are custom-built in order to adapt them to the particular requirements of airborne imaging DOAS measurements.

9.1. Characteristics of the HAIDI System

As a result of the aforementioned efforts, the entire system (except the entrance optics) with three imaging spectrographs and CCD cameras requires only about 9 rack units ($\sim 40\,\mathrm{cm}$) in a standard 19-inch rack. In this configuration the system has an approximate power consumption of 100 W and a total weight around 50 kg including the entrance optics. Platforms like ultralight aircraft, that require a lower weight or power consumption, can accordingly use a configuration with less scanners.

In addition to being compact and energy efficient, test measurements presented in this thesis showed that the custom-built components enable high quality measurements of several species in the spectral range between 300 and 450 nm (instantaneous spectral coverage: 107 nm), e. g. NO_2, SO_2, BrO, IO, HCHO, $C_2H_2O_2$, H_2O, O_3 and O_4. Key characteristics of the spectrographs are an almost constant spectral resolution of 0.5 nm over the usable wavelength range and a stray light ratio of less than 0.5 % in a typical signal. Due to the small f-number of the spectrographs ($f/\# = 3.2$), the overall system furthermore features a high light throughput, resulting in usual integration times below 50 ms (in full vertical binning mode) for a pixel saturation of 50 % and thus low signal to noise ratio ($R \approx 10^4$, for 100 scans with a total int. time of $\sim 5\,\mathrm{s}$). Another important component of the system is the entrance optics. While the forward-looking telescope offers the possibility to retrieve vertical profiles of absorbers close to the flight altitude, the

nadir scanner is capable of recording horizontal distributions with high spatial resolution. Even at a flight altitude of 10 000 m the diameter of the nadir scanner's GIFOV is still below 300 m, whereas the typical swath width covers an area of almost 10 km at the same time. Together with the precise control of the servo motors and the presented algorithm to transform the position of the nadir scanner's GFOV to a geographic system, horizontal trace gas distributions can be mapped with high spatial accuracy (see Fig. 3.18).

Beside test measurements under laboratory conditions, HAIDI was also operated on two different research aircraft. Up to now, three campaigns with a total of 18 measurement flights could be conducted. During these campaigns the HAIDI system could yield first measurement results which gave new insights into chemical processes. In the following, the most important findings of the respective campaigns are briefly summarized.

9.2. BrO/SO_2 and $OClO/SO_2$ Ratios in the Plume of Mt. Etna

During the campaign on Sicily, Italy, in July 2011, spatial distributions of BrO, OClO and SO_2 were determined in the volcanic emissions of Mt. Etna. The measurements showed slant column densities (SCDs in units of molec/cm^2) of up to 4.2×10^{14} for BrO, 1.5×10^{14} for OClO and 4.6×10^{18} for SO_2, with corresponding detection limits (2σ) of about 3.6×10^{13}, 4.0×10^{13} and 1.2×10^{16}, respectively. Although measured SCDs depend on the actual light path in the atmosphere and may therefore slightly vary for different measurement geometries, it can be said that the observed SO_2, BrO and OClO column densities are within the range of previous measurements performed by e. g. Bobrowski and Platt (2007) and Vogel (2011) at Mt. Etna. The determined ratios of BrO and OClO with SO_2 are generally more comparable, because here the influence of different light paths is almost canceled out. During a two hour flight around Mt. Etna on 8$^{\text{th}}$ July 2011, plume ages of 10–34 min could be investigated, showing a fairly constant BrO/SO_2 ratio of about 1.4×10^{-4} along the centerline of the plume. This agrees with average ratios measured by Bobrowski and Giuffrida (2012) in the years 2006 to 2009 at Mt. Etna. No initial increase in the BrO/SO_2 ratio was seen, possibly because the formation of BrO reached an equilibrium state already within the very first minutes after emission (Bobrowski and Giuffrida, 2012; Platt and Bobrowski, 2014), which are not covered by the measurements. However, plume cross sections from 8$^{\text{th}}$ and 9$^{\text{th}}$ July show a significant increase of about a factor of 2–3 in the BrO/SO_2 ratio towards the edges of the plume. Similar increases were already observed by Louban et al. (2009) and are probably due to the limited transport of O_3 towards the plume's center.

In contrast to the flight on 8$^{\text{th}}$ July 2011, an increasing BrO/SO_2 ratio up to a plume age of 31 min appeared to be present on 9$^{\text{th}}$ July. A significant part of this increase turned out to be induced by a gradual drop in the BrO/SO_2 ratio over time, with an average rate of -1.6×10^{-6}/min. This change may be caused by an increasing volcanic activity during the time of the flight and is an highly interesting finding. The increasing activity could be accompanied

by a change in the emitted gas composition or a reduced transformation of the emitted bromine into BrO due to insufficient O_3 supply and therefore lead to a smaller BrO/SO_2 ratio. Potential dependencies between the BrO/SO_2 ratio and the volcanic activity were already reported by e. g. Bobrowski and Giuffrida (2012) and Lübcke et al. (2013), stating decreasing BrO/SO_2 ratios shortly before and during the initial phase of eruptive activities. Considering this time depending variation the differences in the BrO/SO_2 ratios, observed by traversing the plume in various distances to the crater, disappear (Fig. 6.5b). Unfortunately there are no traverses of the plume for distances exceeding 10 km, which preclude a reliable distinction of plume edge and plume center measurements more than 16.5 min downwind. Various signs indicate, however, that the measurement locations deviated from the centerline of the plume with increasing distance to the source. So, for example, only low SO_2 dSCDs were seen for measurements in larger distances to the summit. Moreover, the total observed increase in the BrO/SO_2 ratio between measurements in 5 km and 19 km distance to the summit would agree with the variation seen from the center of the plume towards the edges (factor of 2–3).

Even though HAIDI's detection limit was still affected by technical problems with the CCD camera during the flights on Sicily, weak absorbers like OClO could successfully be detected. Due to the imaging capabilities of the system, measurements from 9th July 2011 are furthermore one of the first to show the spatial distribution of OClO within the volcanic plume of Mt. Etna. Measurements along the centerline of the plume revealed relatively constant $OClO/SO_2$ and OClO/BrO ratios of about 0.3×10^{-4} and 0.2, respectively, with slightly higher values close to the crater (distance of 2 km, see Fig. 6.8). From the measured OClO/BrO ratios also ClO mixing ratios could be derived. The calculated mixing ratios are between 80 and 300 ppt, which agrees with calculations by Gliß (2013) and recent model studies (e. g. Roberts et al., 2009). However, because of the technical problems the measurement sensitivity was insufficient for a more detailed investigation of the OClO evolution in the plume and increasing $OClO/SO_2$ ratios with plume age or towards the edges of the plume could not be determined reliably.

9.3. Spatial Distribution of NO_2 in Urban Areas

The second campaign was conducted in Indiana, USA, at the end of October 2011. Several flights to the metropolitan area of Indianapolis were performed in order to map the spatial distribution of NO_2 and thus to investigate the air pollution in urban areas due to the combustion of fossil fuels. The NO_2 SCDs measured by the nadir scanner reached a value of 2.4×10^{16} molec/cm^2 downwind of the city core, with a detection limit of about 3.2×10^{15} molec/cm^2. In contrast to the measurements at Mt. Etna, also the forward-looking telescope could be applied this time, because of an improved mechanical shutter. However, both instruments were still suffering from the electronic noise of the CCD cameras.

Nonetheless, the measurements clearly demonstrated the usefulness of an airborne system. HAIDI could map the NO_2 distribution along several traverses downwind of the city within

a few minutes, which would not be possible with a car-based instrument. The measurements allowed on the one hand to determine the total NO_2 emission flux of Indianapolis. Data from 24th October (working day, 13:00–13:25 LT), for example, yielded a value of approximately 4 t/h. This value seems to be reasonable when comparing it to the total NO_x emission of the Mannheim/Ludwigshafen area that was determined to be about 2 t/h (Ibrahim et al., 2010). On the other hand, such measurements can be used to complement global satellite observations with high resolution trace gas distributions on a regional scale. While simultaneous measurements from OMI could not resolve the emission plume of Indianapolis due to the low spatial resolution at the ends of the swath ($\sim 13 \times 150$ km, Levelt et al. (2006)), it can be clearly seen in the NO_2 maps generated by the HAIDI system (see e. g. Fig. 7.3). The plume measured on 24th October had a width of approximately 18 km in a distance of 22 km from the city core. Structures with such dimensions can only be resolved by OMI in the Spatial Zoom-In Observation Mode, which has a resolution of about 13×12 km in nadir direction (Levelt et al., 2006).

9.4. Spatial Distribution of BrO and NO_2 during polar ODEs

With a total of 11 measurement flights, the BROMEX field study performed during March 2012 in Alaska, USA, was the most extensive campaign conducted with the HAIDI system to date. Throughout the entire month, ground-level ozone mixing ratios measured at the Barrow Observatory (see Fig. 5.10) were almost regularly depleted from about 40 ppb to near zero. Accordingly, large scale BrO distributions could be observed during most of the flights. A comparison with GOME-2 satellite measurements showed generally good agreement with the data from HAIDI. The highest values of BrO, with vertical column densities of about 6.0×10^{13} molec/cm^2 and 4.9×10^{13} molec/cm^2 (SCDs of 2.5×10^{14} molec/cm^2 and 1.8×10^{14} molec/cm^2), were seen over the tundra on 15th and 24th of March, respectively. Often, the measured spatial distributions of BrO exhibited strong horizontal gradients (change of $\sim 1.3 \times 10^{13}$ molec/cm^2 in VCD within 10 km), which suggests an observation at young plume ages with regard to the turbulent diffusion in the atmosphere. Together with measured wind speeds and directions, this allows a backtracking of the bromine-enriched air masses and therefore rough conclusions about the origin of a plume. As the strongest BrO gradients were measured on 13th and 15th of March, close to the coast or downwind of it (see Figs. 8.2 and 8.6), the backtracking points to regions of snow-covered first-year sea ice as possible place of origin. This would be in line with previous assumptions for the sources of reactive bromine in the atmosphere (e. g. Simpson et al., 2007a; Pratt et al., 2013). Compared to the measurements on Sicily, the detection limit for BrO could be improved to $\sim 2.9 \times 10^{13}$ molec/cm^2 by a revised CCD camera readout electronics.

Significant levels of NO_2 were only seen during the flight to Prudhoe Bay on 31st March. Measurements from HAIDI's nadir scanner showed an extended NO_2 plume originating from the industrial complexes of Prudhoe Bay, with peak VCDs of about 8.0×10^{15} molec/cm^2 (SCD: 5.0×10^{16} molec/cm^2). Also the detection limit for NO_2 has slightly improved since the flights in

Indiana. Despite less co-added scans (64 instead of 128), it was only about 3.1×10^{15} molec/cm^2 during the BROMEX campaign.

9.5. Further Development and possible Improvements

Based on the results presented in this work, the HAIDI system could prove to be a suitable tool for the investigation of tropospheric trace gas distributions from smaller aircraft. For the near future it is planned to operate HAIDI not only on similar platforms, but also on the German research aircraft HALO. First measurements on HALO are scheduled for 2016 in the context of the EMerGe[1] project. As the name suggest, the project addresses the influence of selected European and Asian megacities on the atmospheric chemistry. The HAIDI system, with its capability to detect several atmospheric species simultaneously with high spatial resolution in two and potentially three dimensions, can make an important contribution to this mission. The considerably higher flight altitude and faster cruise speed of HALO in comparison to the previously used aircraft will furthermore allow the HAIDI system to cover much larger areas in future measurements. This is especially important for the validation and supplementation of global satellite measurements.

However, for operation on HALO the system first has to pass through a certification process. Even if the hardware for HALO is mostly completed, minor changes to the system may be necessary as part of the certification process. In order to fully exploit the possibilities of the system, it is moreover required to apply radiative transfer models (e. g. McArtim or SCIATRAN) in future data evaluations and to set-up a suitable tomographic inversion model for the three-dimensional reconstruction of the measured trace gas distributions.

[1] Effect of megacities on the transport and transformation of pollutants on the regional and global scale

A. Additional Data

A.1. Etna Campaign (2011)

A.1.1. Vogel-Sihler-Plots

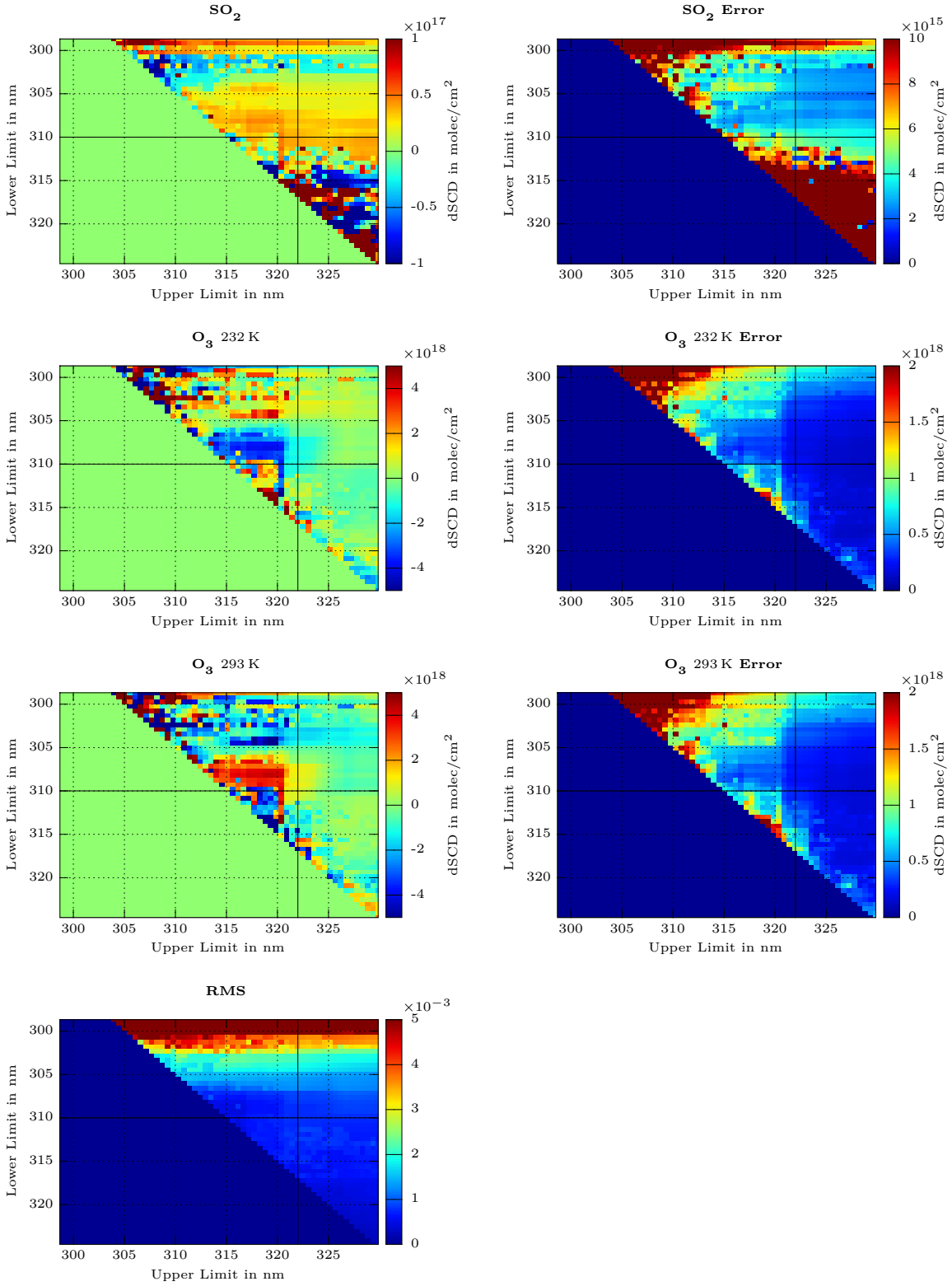

Figure A.1.: Vogel-Sihler-plot of a spectrum with low SO_2 column density, measured during the flight on 9th July 2011. The intersecting lines indicate the wavelength interval that was finally chosen for the evaluation of low SO_2 column densities ($< 5 \times 10^{17}$) during the campaign at Mt. Etna.

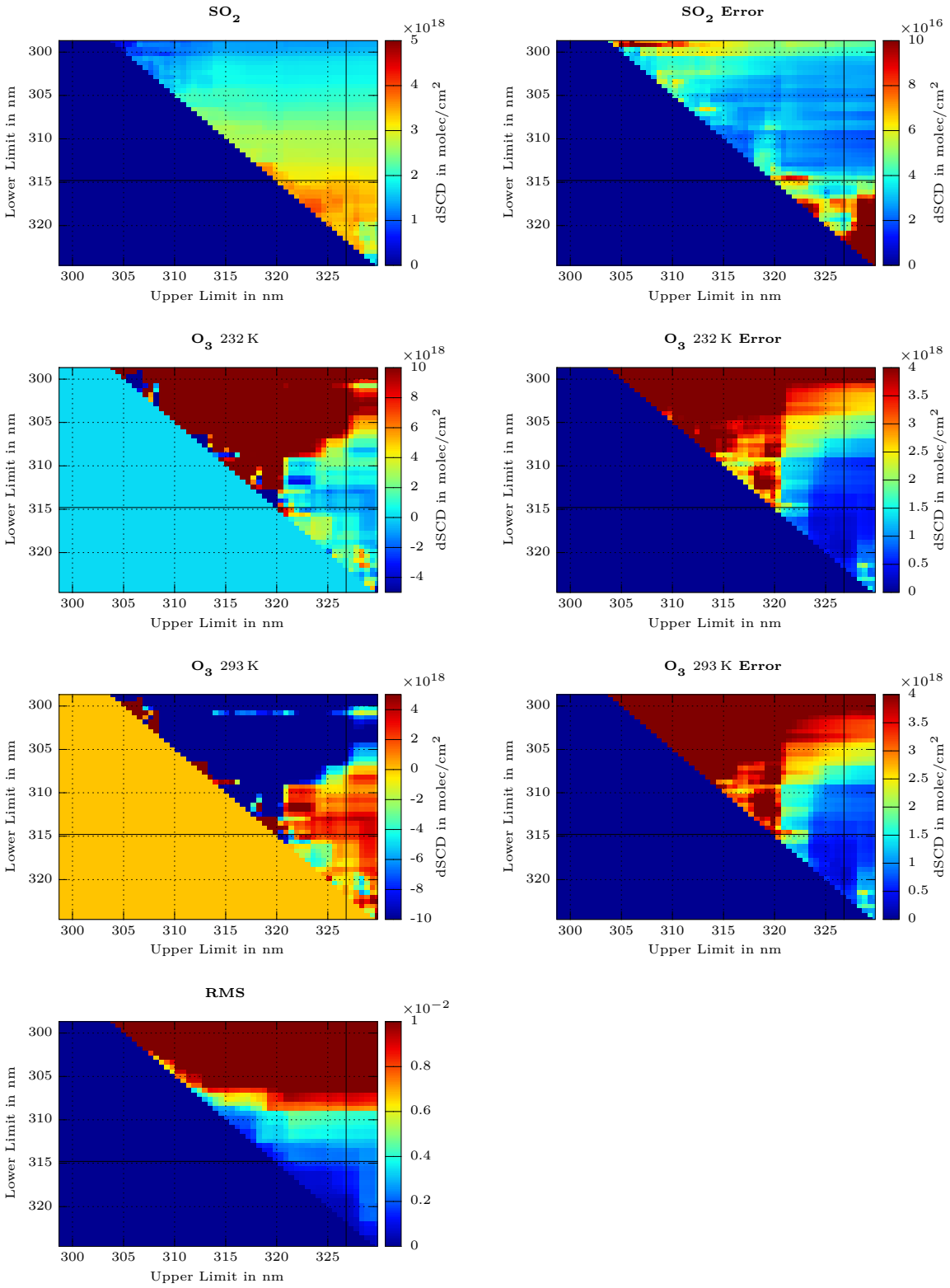

Figure A.2.: Vogel-Sihler-plot of a spectrum with high SO_2 column density, measured during the flight on 9th July 2011. The intersecting lines indicate the wavelength interval that was finally chosen for the evaluation of high SO_2 column densities ($\geq 5 \times 10^{17}$) during the campaign at Mt. Etna.

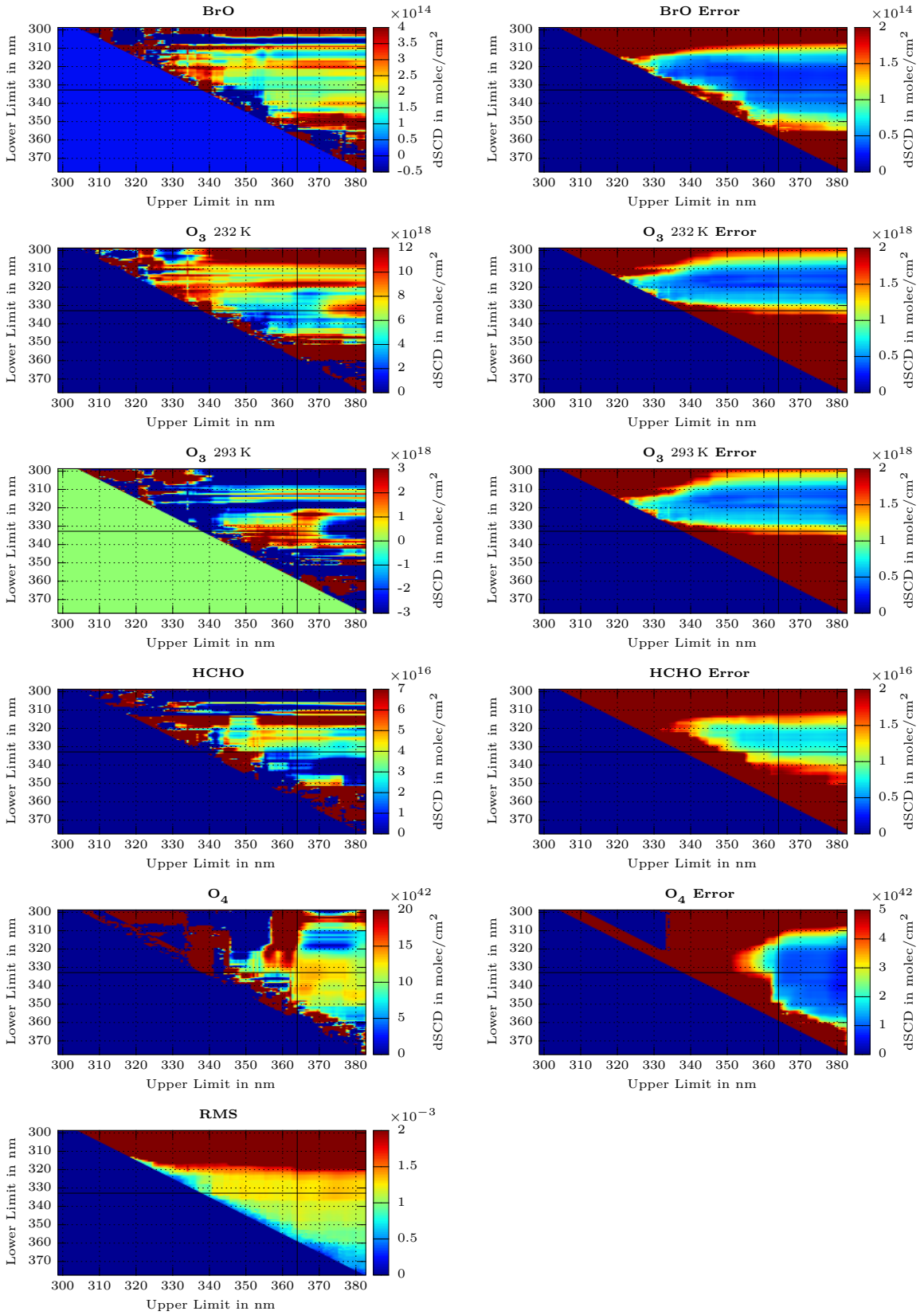

Figure A.3.: Vogel-Sihler-plot of a spectrum which was measured on 9th July 2011 and evaluated with the BrO fit scenario. The intersecting lines indicate the wavelength interval that was finally chosen for the evaluation of BrO during the campaign at Mt. Etna.

A.2. Indiana Campaign (2011)

A.2.1. Vogel-Sihler-Plots

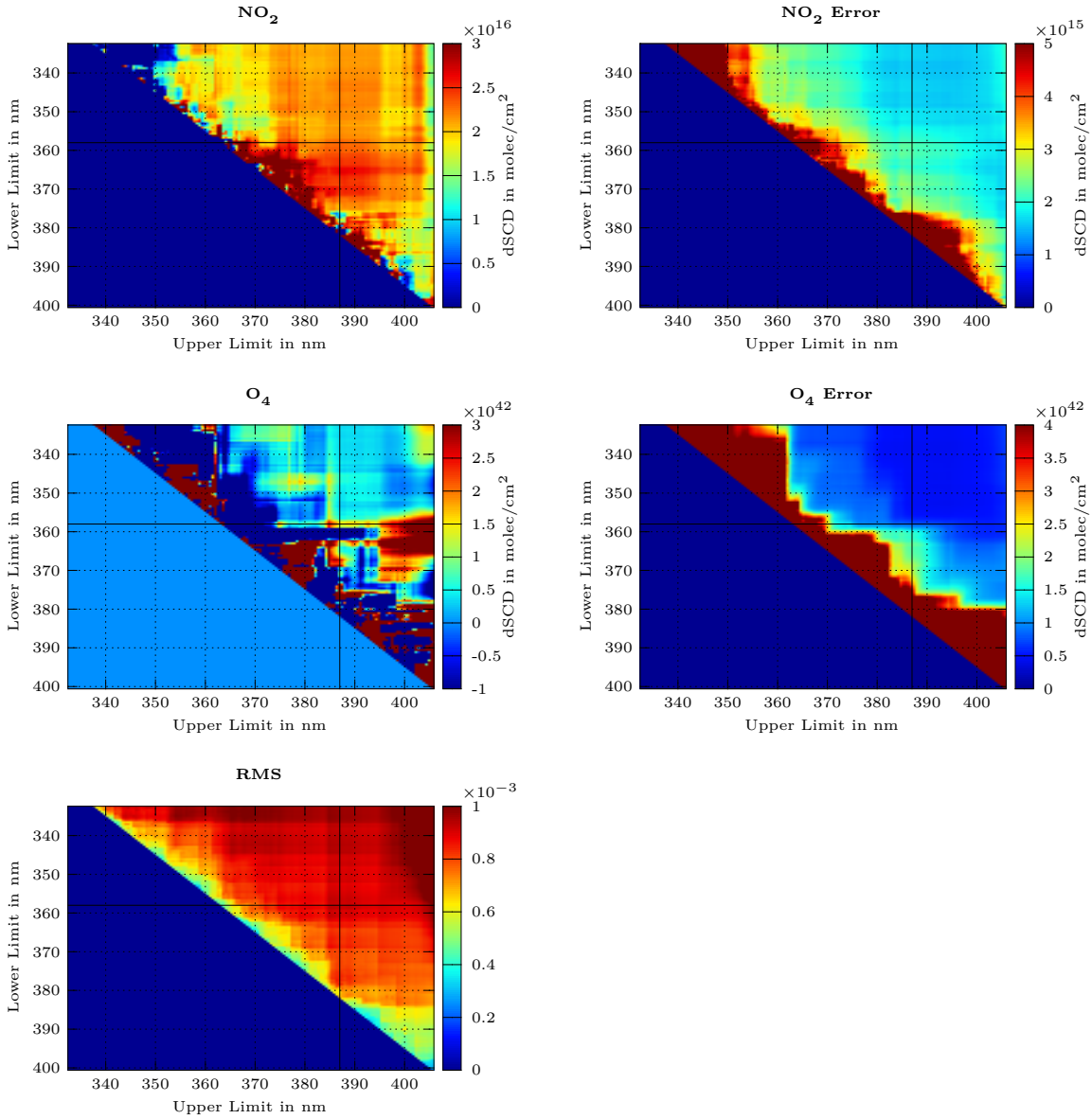

Figure A.4.: Vogel-Sihler-plot of a spectrum which was measured on 24th October 2011 and evaluated with the NO_2 fit scenario. The intersecting lines indicate the wavelength interval that was finally chosen for the evaluation of NO_2 during the campaign in Indiana.

A.2.2. Flight on October 23rd, 2012

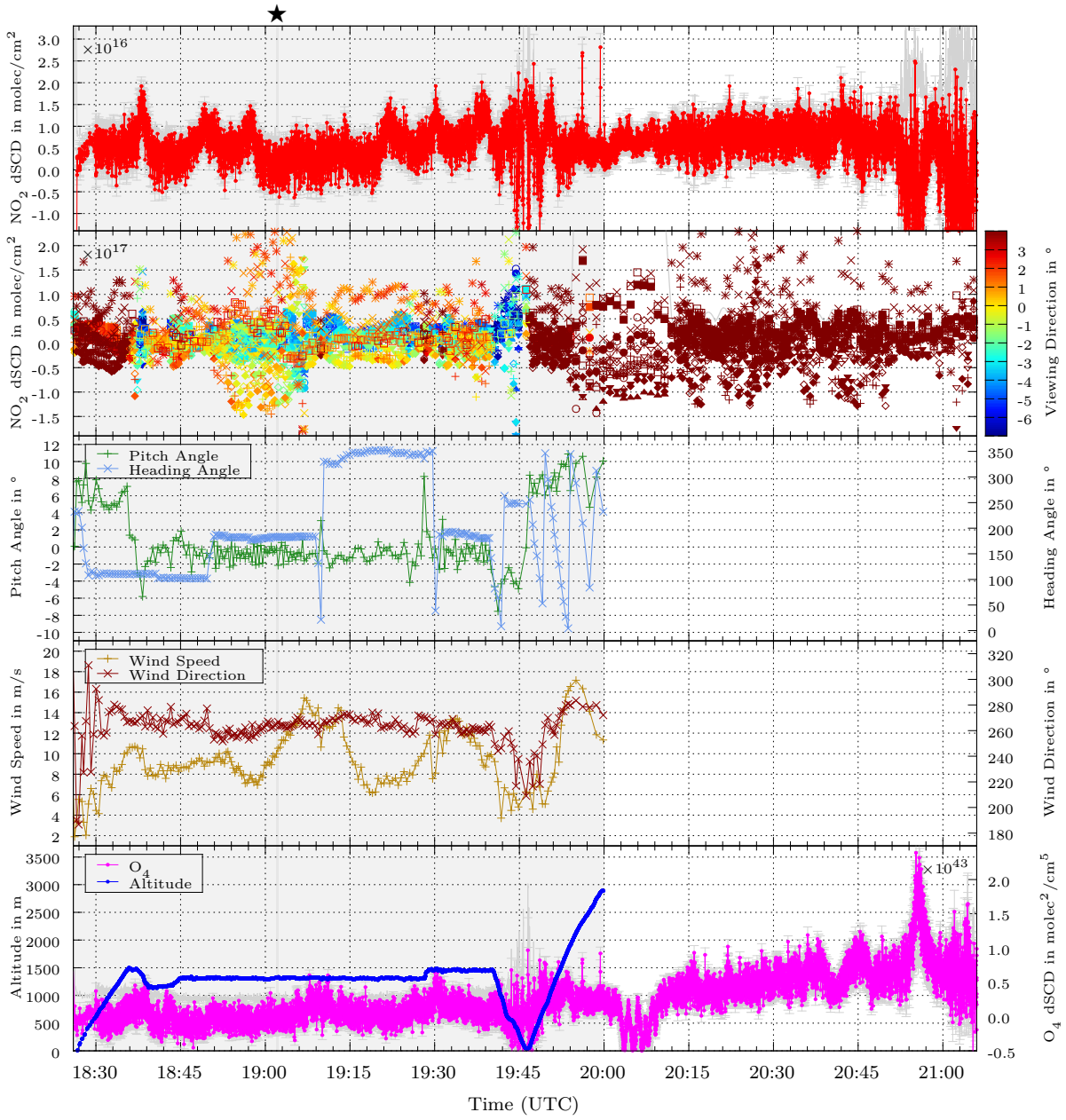

Figure A.5.: Time series of measurement data from 23rd October 2011. GPS data from this day is only available prior to 20:00 UTC (gray shaded section). Errors and detection limits are also plotted in gray. ★: Recording period of nadir scanner in-flight FRS.

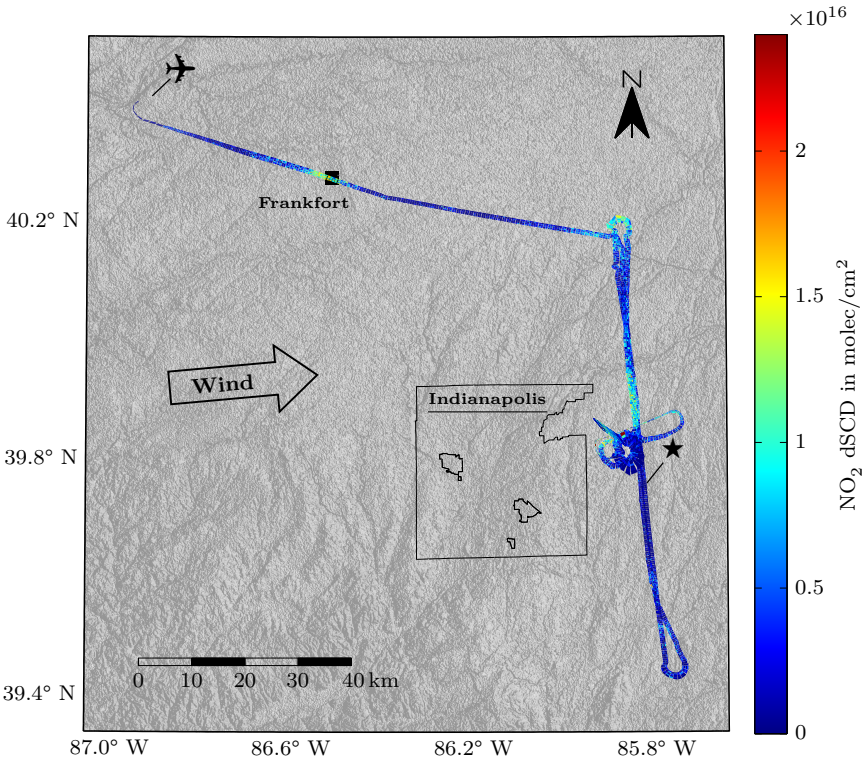

Figure A.6.: Topographic map showing measured NO_2 column densities from the flight to Indianapolis on 23rd October 2011 (SRTM data taken from USGS (2012)). Only measurements prior to 20:00 UTC (gray shaded section in Fig. A.5) are depicted as GPS logging failed afterwards. ✈: Location of Purdue University Airport, ★: Recording position of nadir scanner in-flight FRS.

A.2.3. Flight on October 24th, 2012

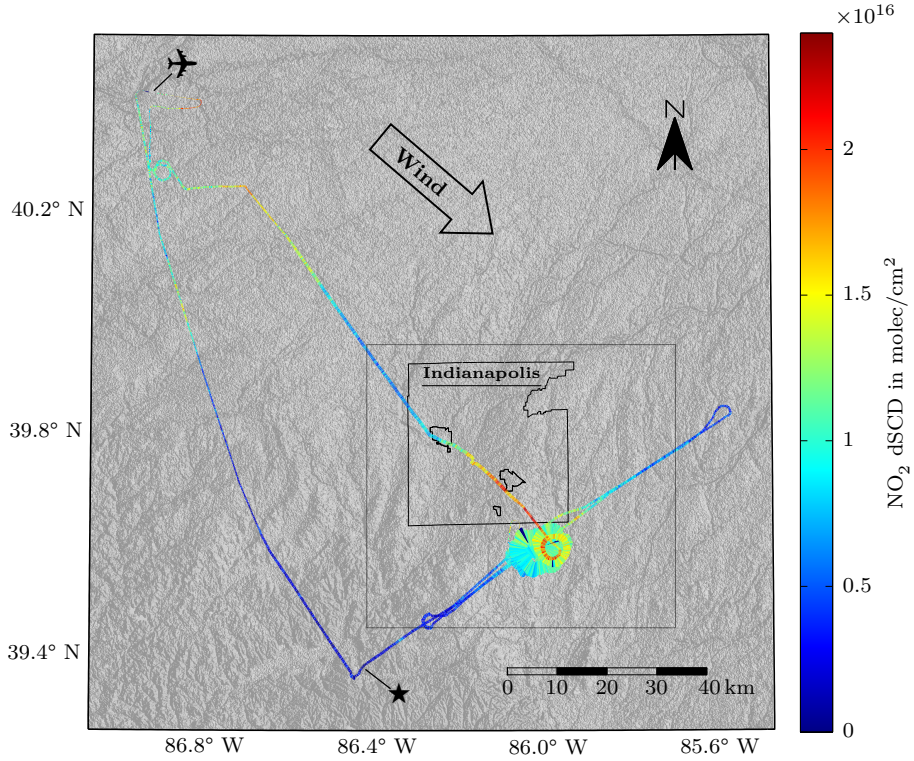

Figure A.7.: Topographic map showing measured NO_2 column densities from the flight to Indianapolis on 24th October 2011 (SRTM data taken from USGS (2012)). The box around Indianapolis indicates the section of the map, which is also shown in Fig. 7.2. ✈: Location of Purdue University Airport, ★: Recording position of nadir scanner in-flight FRS.

A.2.4. Flight on October 25th, 2012

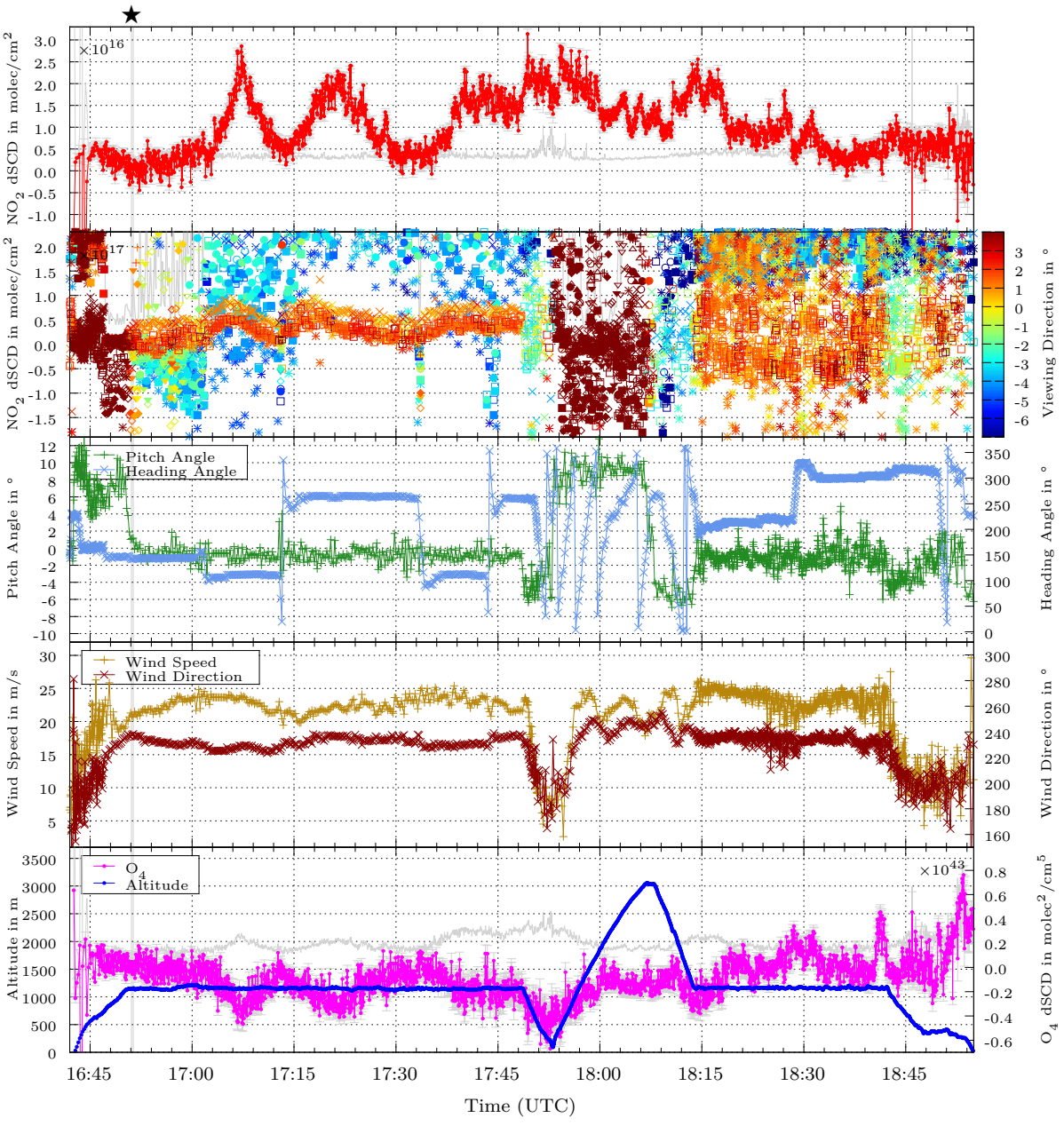

Figure A.8.: Time series of measurement data from 25th October 2011. Errors and detection limits are plotted in gray. ★: Recording period of nadir scanner in-flight FRS.

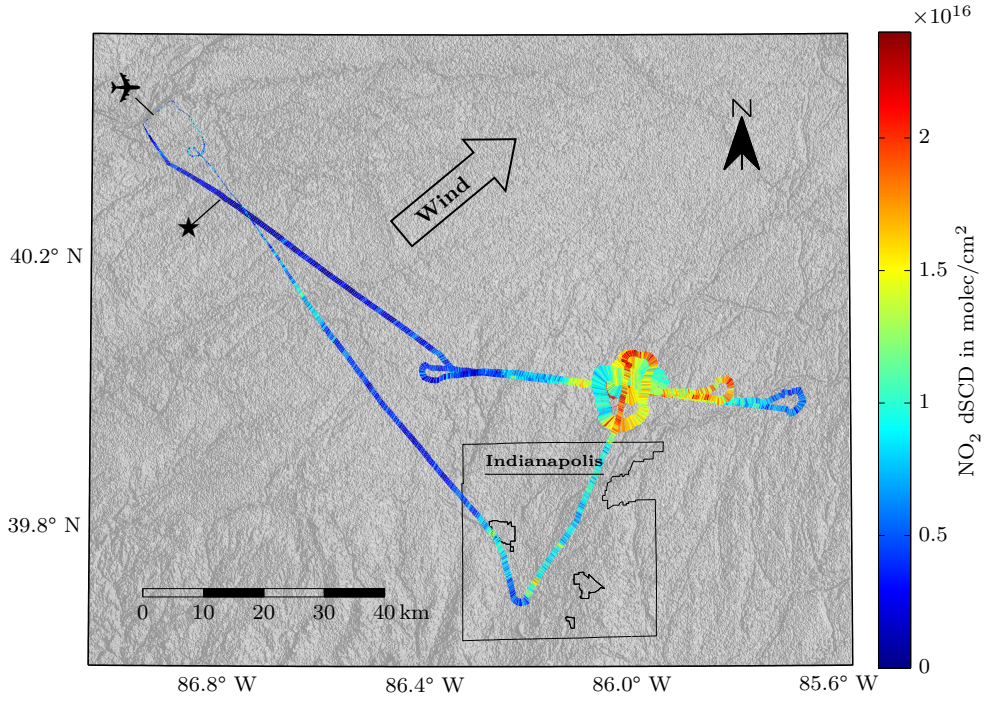

Figure A.9.: Topographic map showing measured NO_2 column densities from the flight to Indianapolis on 25$^{\text{th}}$ October 2011 (SRTM data taken from USGS (2012)). ✈: Location of Purdue University Airport, ★: Position of inflight reference.

A.3. BROMEX Campaign (2012)

A.3.1. Vogel-Sihler-Plots

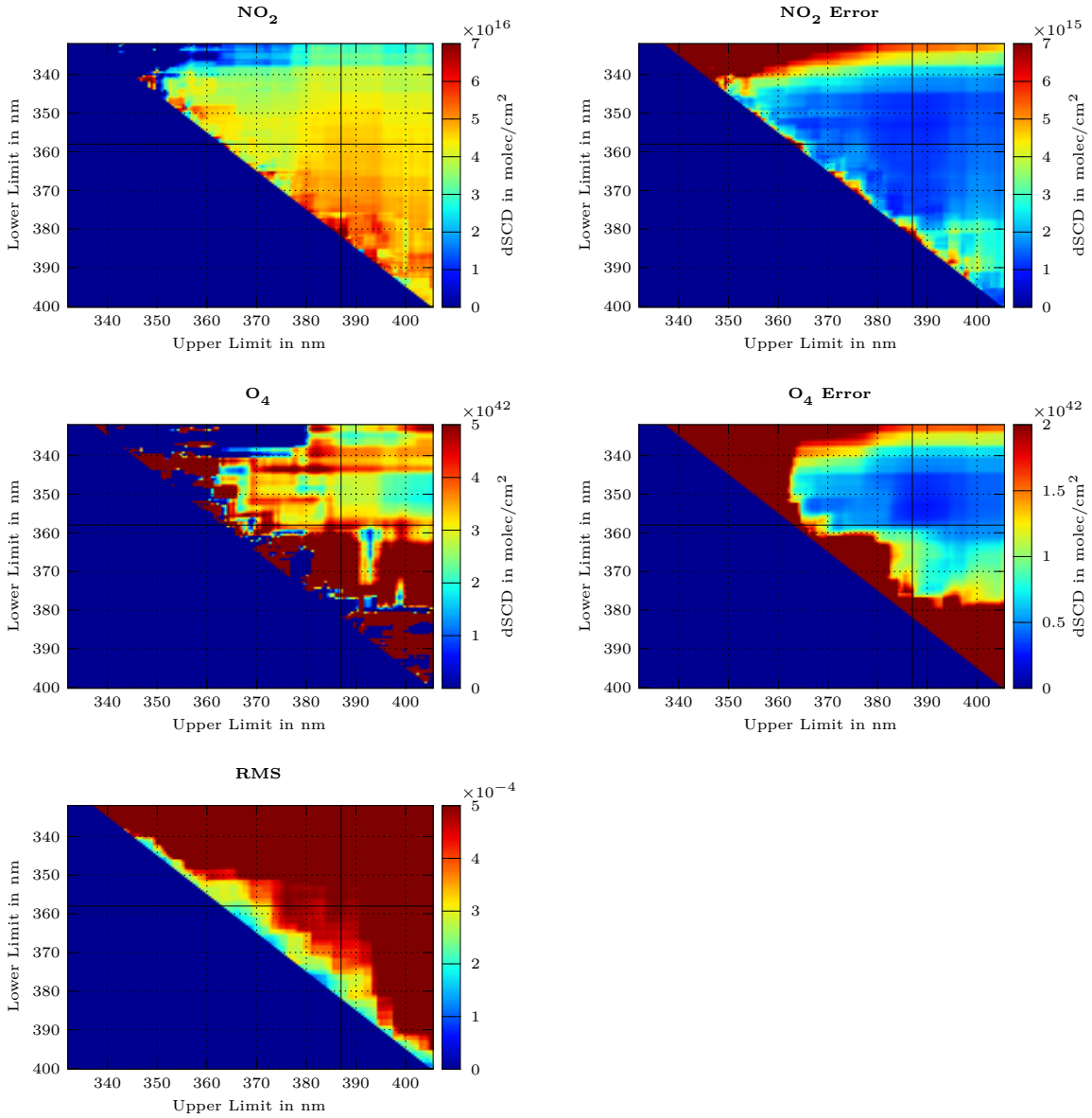

Figure A.10.: Vogel-Sihler-plot of a spectrum which was measured on 31st March 2012 and evaluated with the NO_2 fit scenario. The intersecting lines indicate the wavelength interval that was finally chosen for the evaluation of NO_2 during the BROMEX campaign.

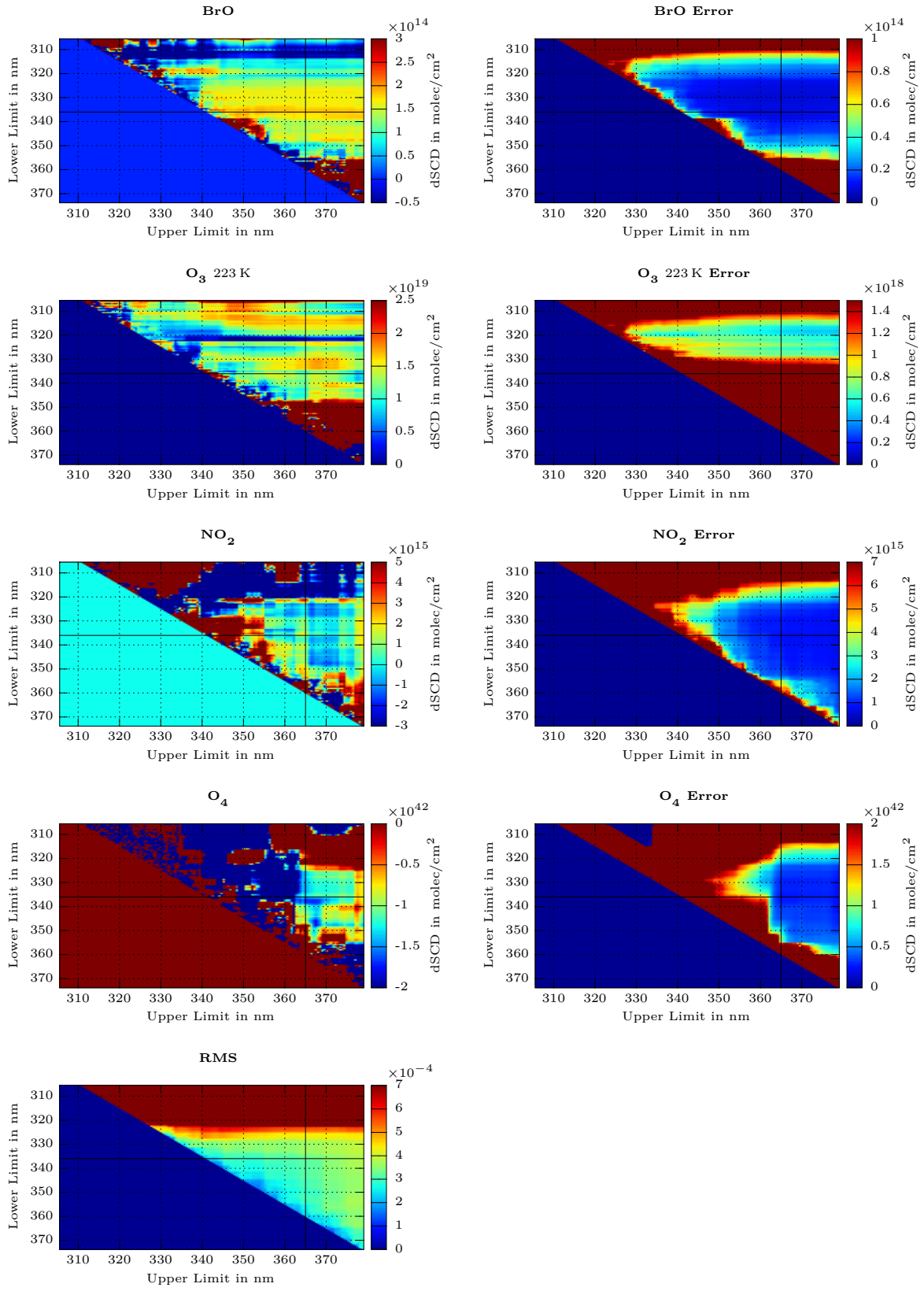

Figure A.11.: Vogel-Sihler-plot of a spectrum which was measured on 31st March 2012 and evaluated with the BrO fit scenario. The intersecting lines indicate the wavelength interval that was finally chosen for the evaluation of BrO during the BROMEX campaign.

A.3.2. Flight on March 19th, 2012

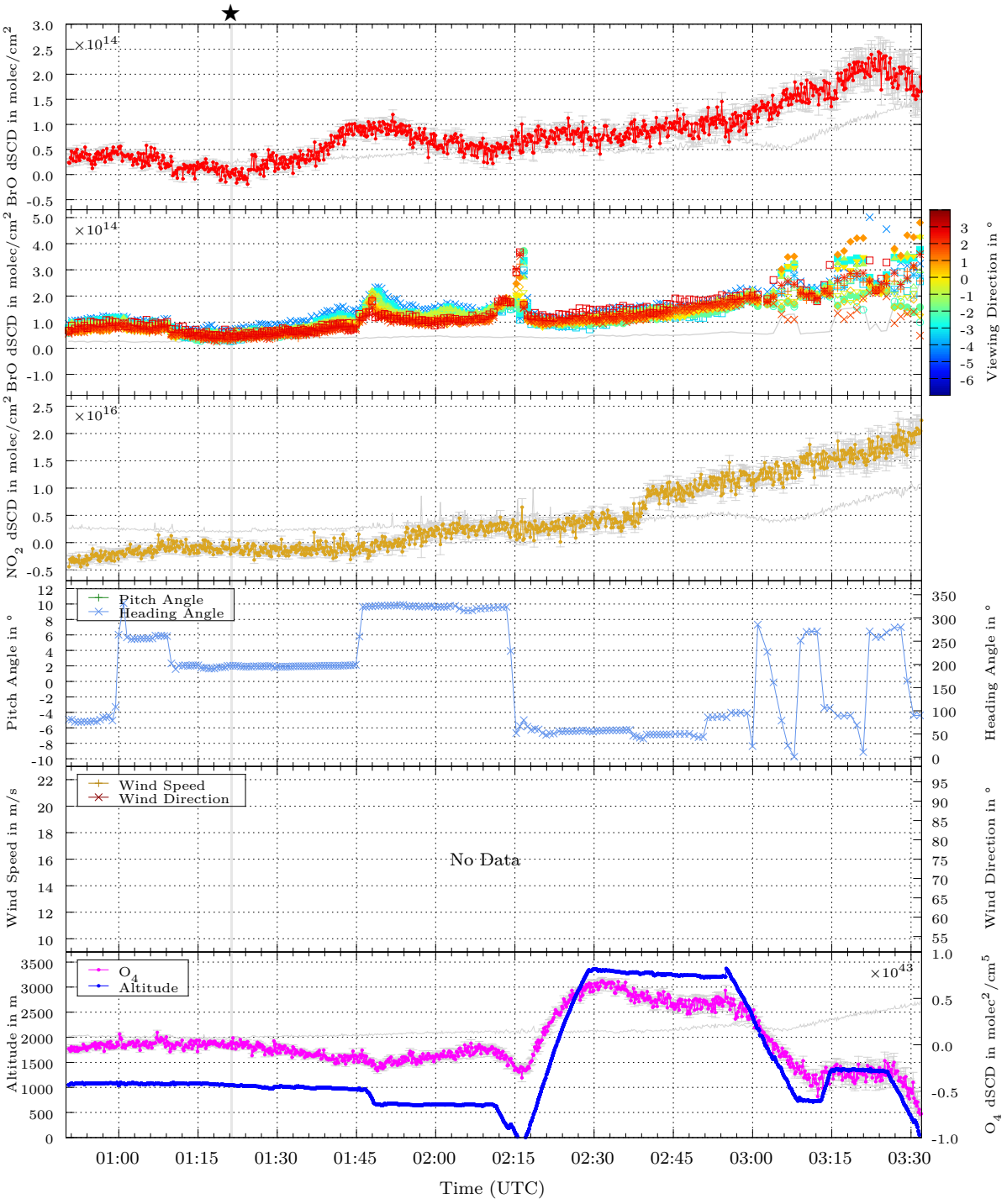

Figure A.12.: Time series of measurement data from the flight on 19th March 2012. No GPS data is available for the first 3 min of the flight. Errors and detection limits are plotted in gray. ★: Recording period of nadir scanner in-flight FRS.

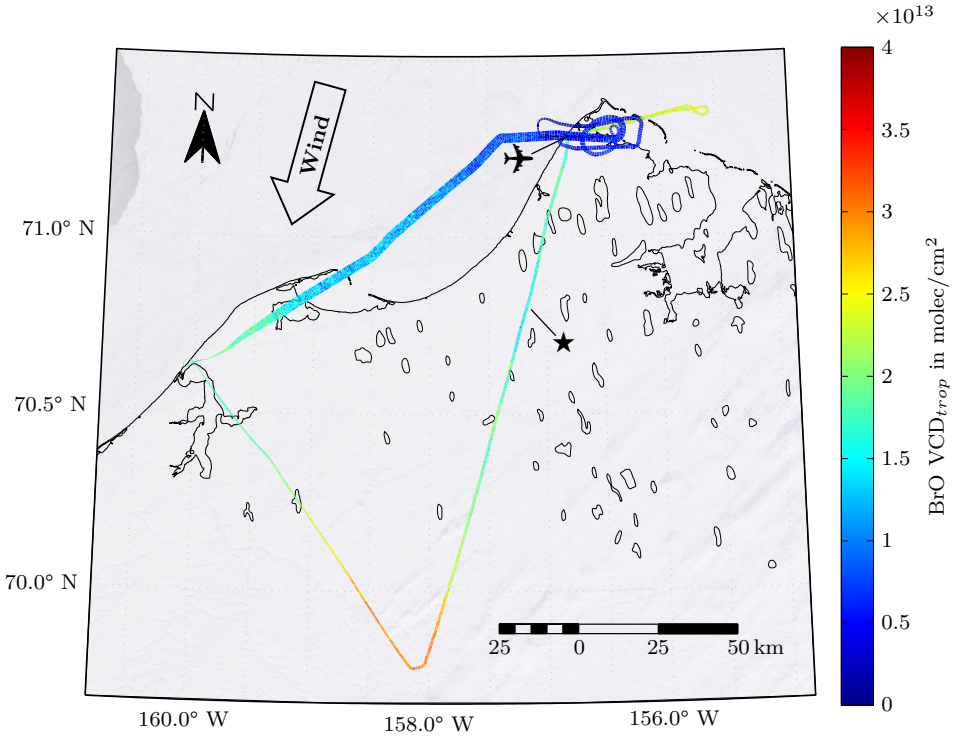

Figure A.13.: Spatial distribution of BrO around Barrow, measured by HAIDI's nadir scanner on 19th March 2012. The background shows a true color satellite image taken by MODIS (Aqua) on the same day with a resolution of 250 m (NASA, 2012). ✈: Location of Barrow airport, ★: Recording position of nadir scanner in-flight FRS.

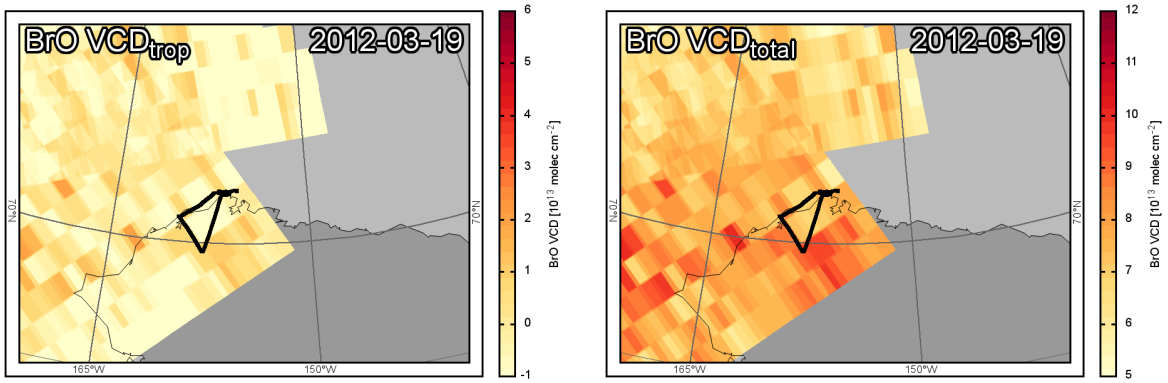

(a) tropospheric VCD **(b)** total VCD

Figure A.14.: GOME-2 satellite images showing the BrO distribution around Barrow on 19th March 2012 (H. Sihler, pers. comm.)

A.3.3. Flight on March 20th, 2012

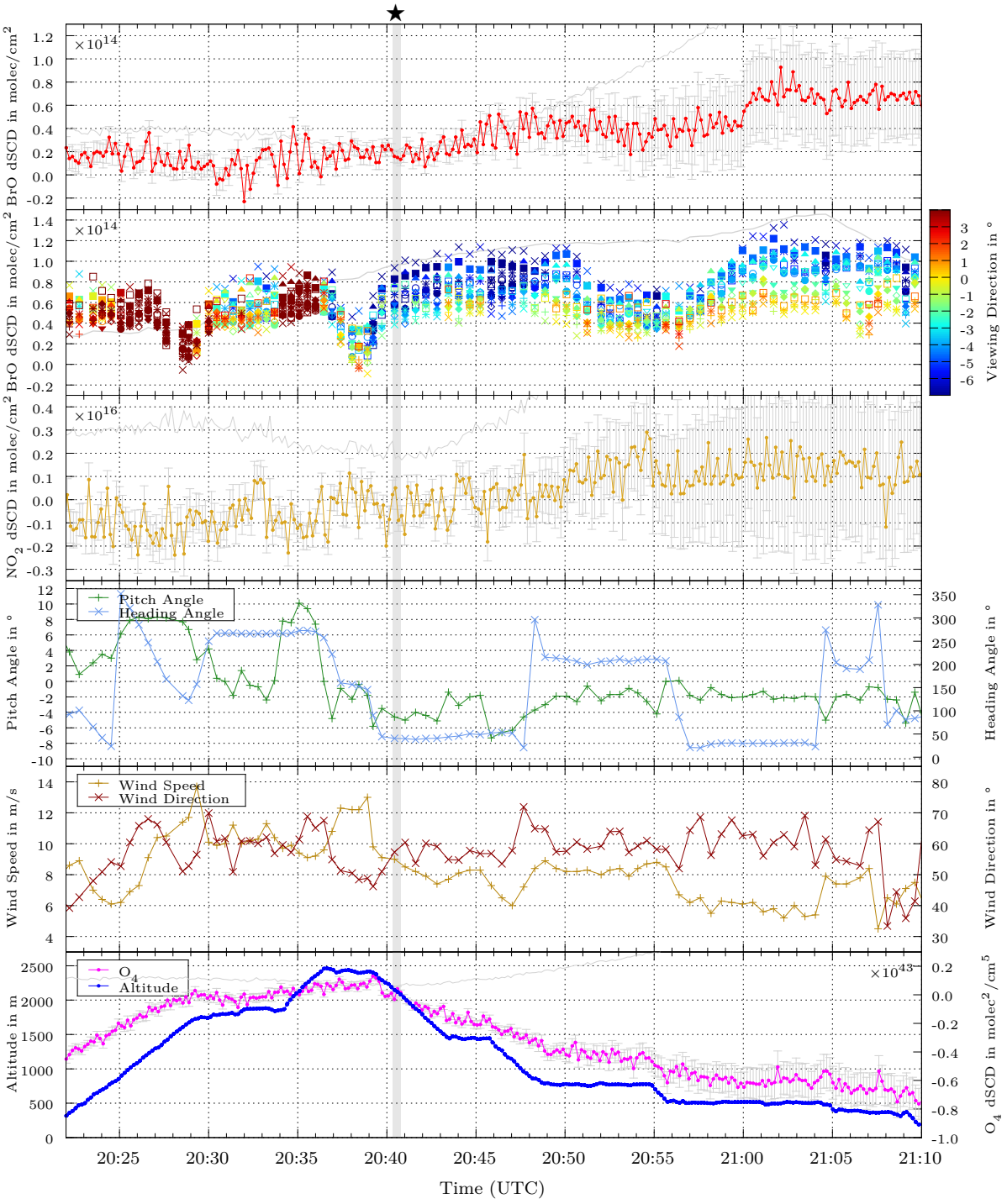

Figure A.15.: Time series of measurement data from the flight on 20th March 2012. The flight was aborted shortly after takeoff due to problems with the heating of the cockpit. Errors and detection limits are plotted in gray. ★: Recording period of nadir scanner in-flight FRS.

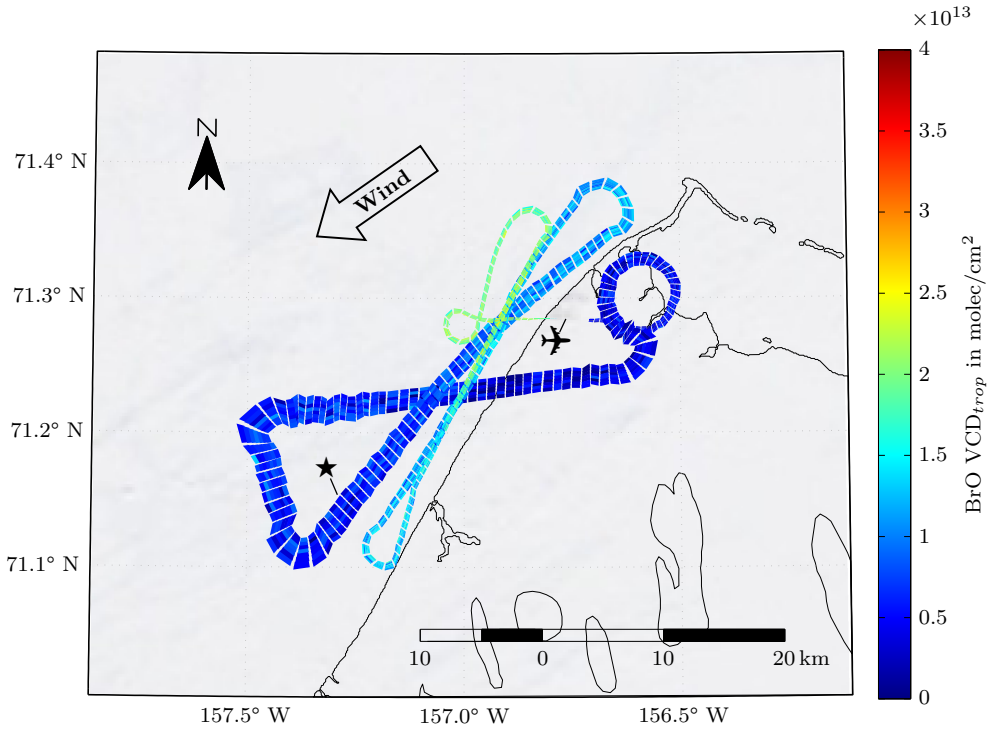

Figure A.16.: Spatial distribution of BrO around Barrow, measured by HAIDI's nadir scanner on 20th March 2012. The background shows a true color satellite image taken by MODIS (Aqua) on the same day with a resolution of 250 m (NASA, 2012). ✈: Location of Barrow airport, ★: Recording position of nadir scanner in-flight FRS.

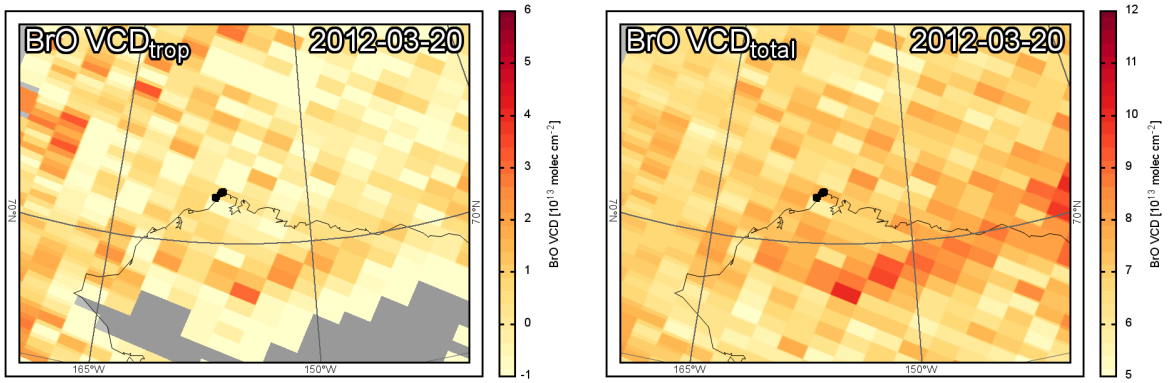

(a) tropospheric VCD **(b)** total VCD

Figure A.17.: GOME-2 satellite images showing the BrO distribution around Barrow on 20th March 2012 (H. Sihler, pers. comm.)

A.3.4. Flight on March 22nd, 2012

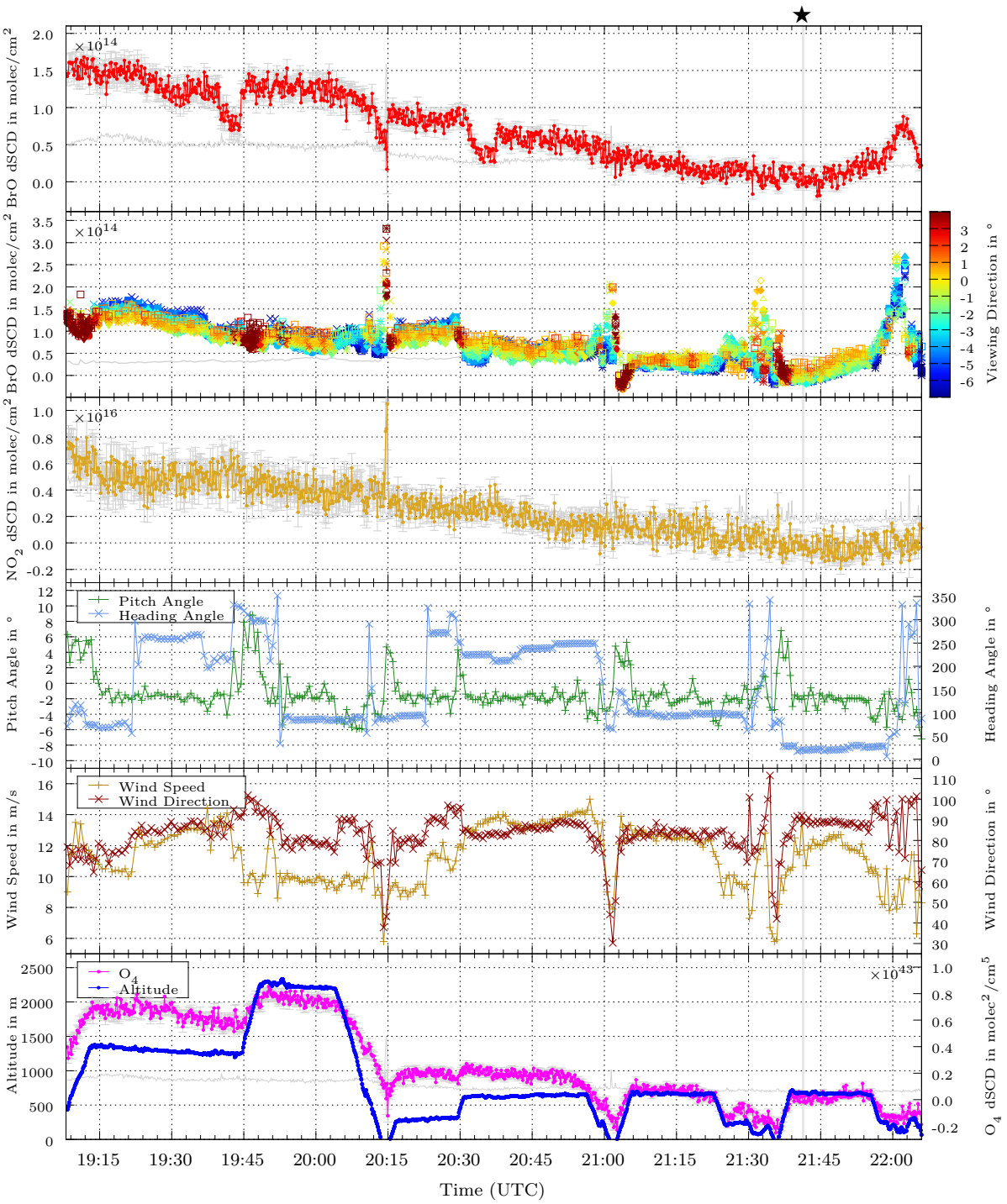

Figure A.18.: Time series of measurement data from the flight on 22nd March 2012. Errors and detection limits are plotted in gray. ★: Recording period of nadir scanner in-flight FRS.

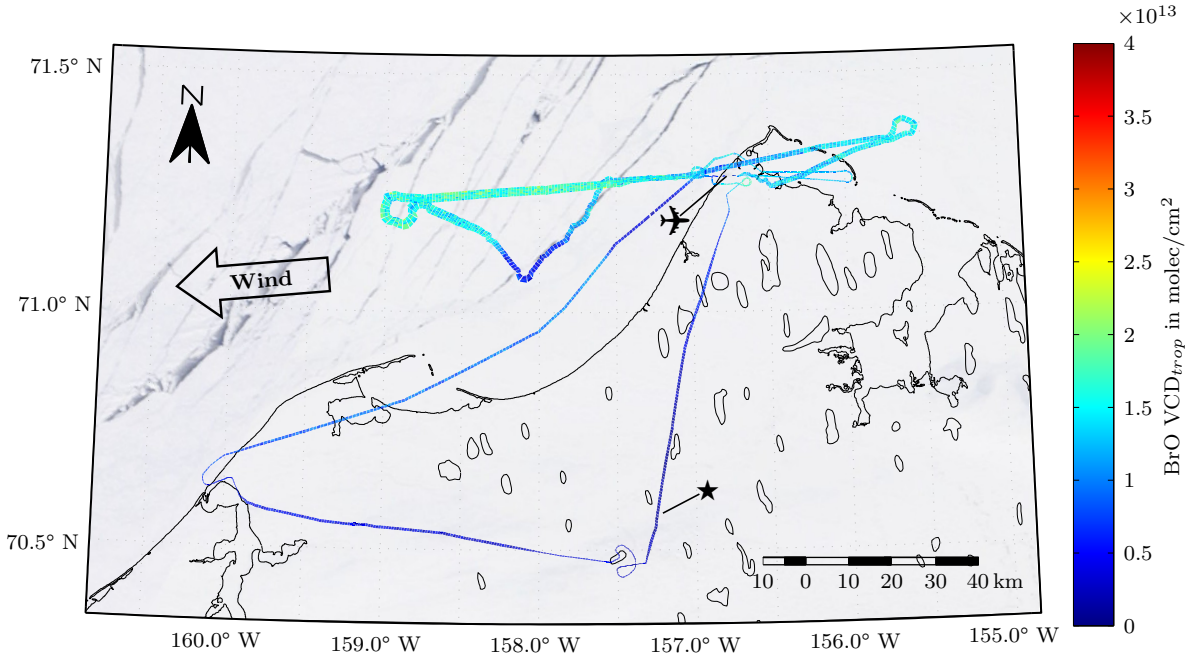

Figure A.19.: Spatial distribution of BrO around Barrow, measured by HAIDI's nadir scanner on 22nd March 2012. The background shows a true color satellite image taken by MODIS (Aqua) on the same day with a resolution of 250 m (NASA, 2012). ✈: Location of Barrow airport, ★: Recording position of nadir scanner in-flight FRS.

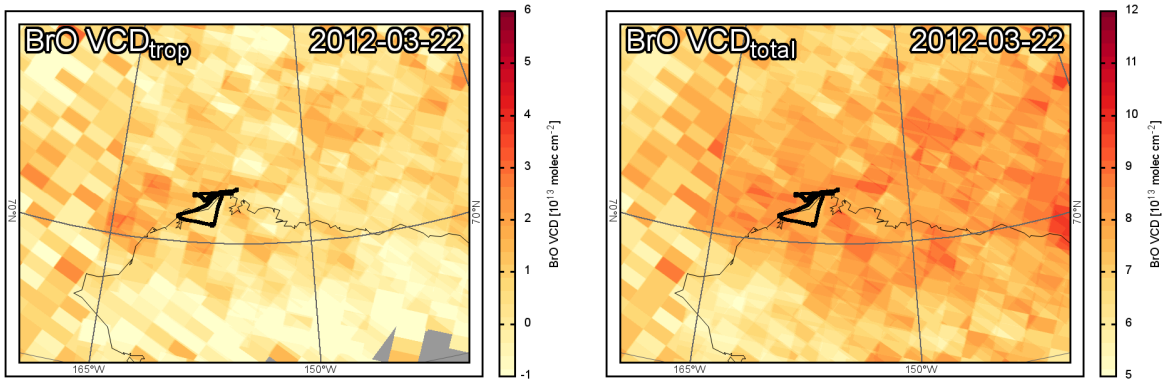

(a) tropospheric VCD **(b)** total VCD

Figure A.20.: GOME-2 satellite images showing the BrO distribution around Barrow on 22nd March 2012 (H. Sihler, pers. comm.).

A.3.5. Flight on March 26th, 2012

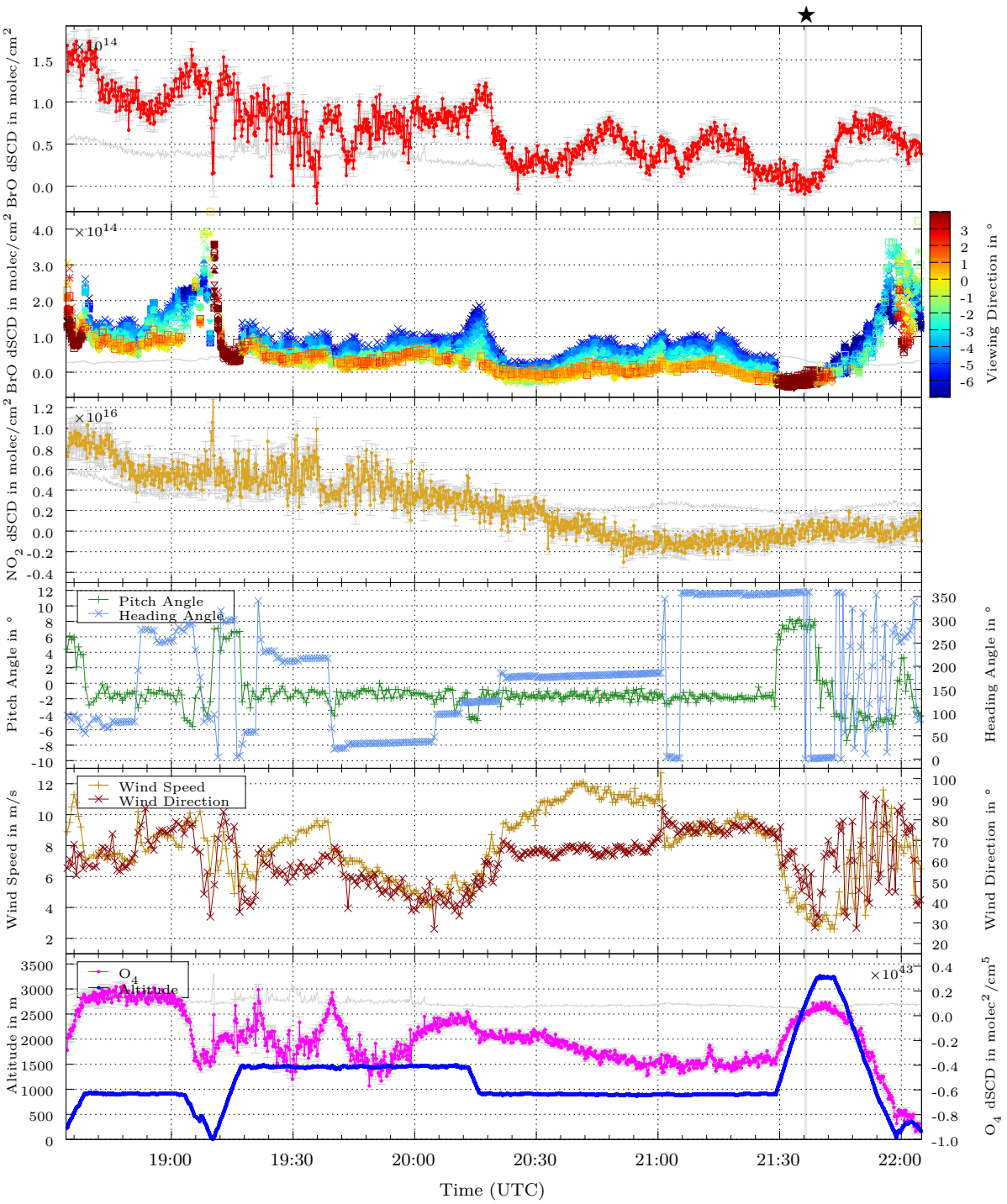

Figure A.21.: Time series of measurement data from the flight on 26th March 2012. Errors and detection limits are plotted in gray. ★: Recording period of nadir scanner in-flight FRS.

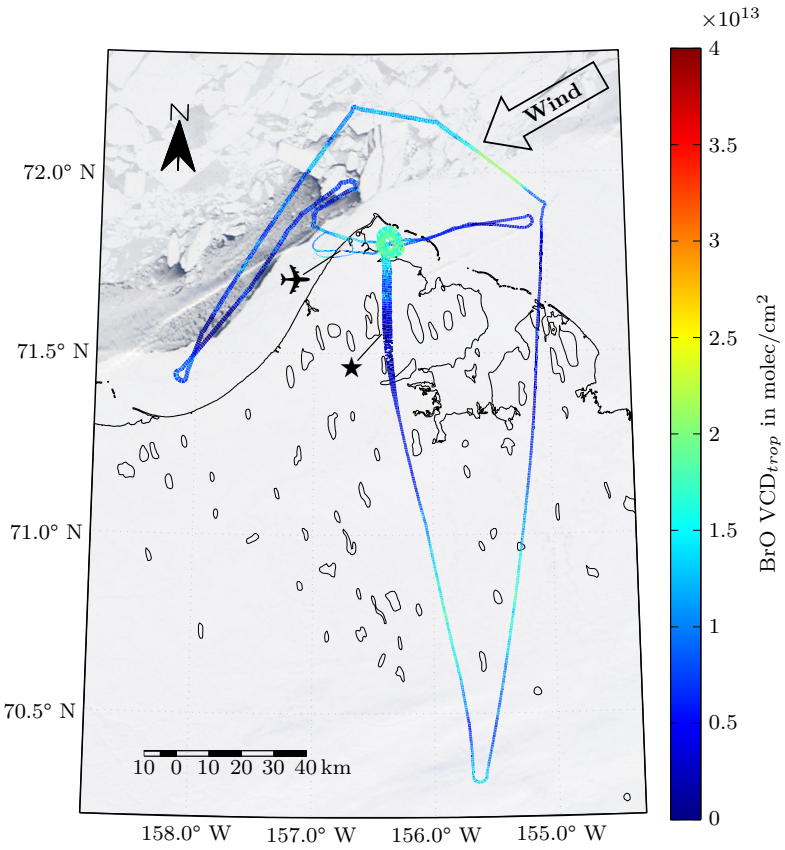

Figure A.22.: Spatial distribution of BrO around Barrow, measured by HAIDI's nadir scanner on 26th March 2012. The background shows a true color satellite image taken by MODIS (Aqua) on the same day with a resolution of 250 m (NASA, 2012). ✈: Location of Barrow airport, ★: Recording position of nadir scanner in-flight FRS.

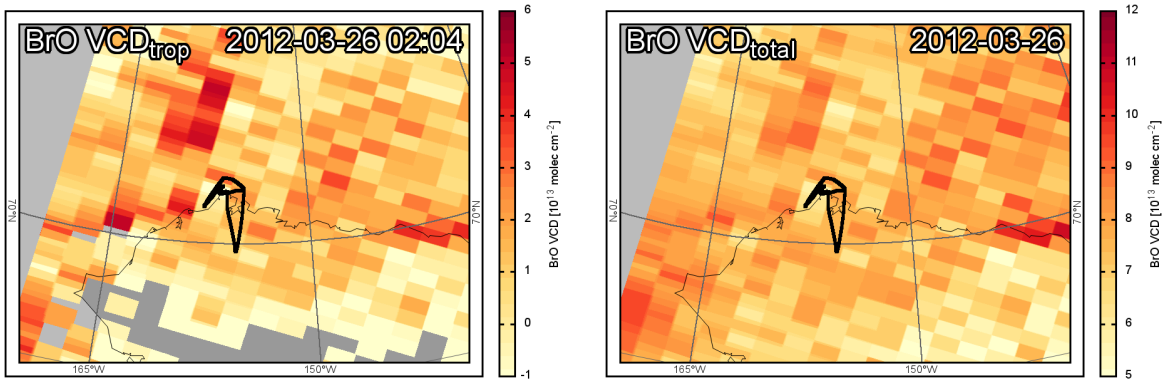

(a) tropospheric VCD **(b)** total VCD

Figure A.23.: GOME-2 satellite images showing the BrO distribution around Barrow on 26th March 2012 (H. Sihler, pers. comm.).

A.3.6. Flight on March 28th, 2012

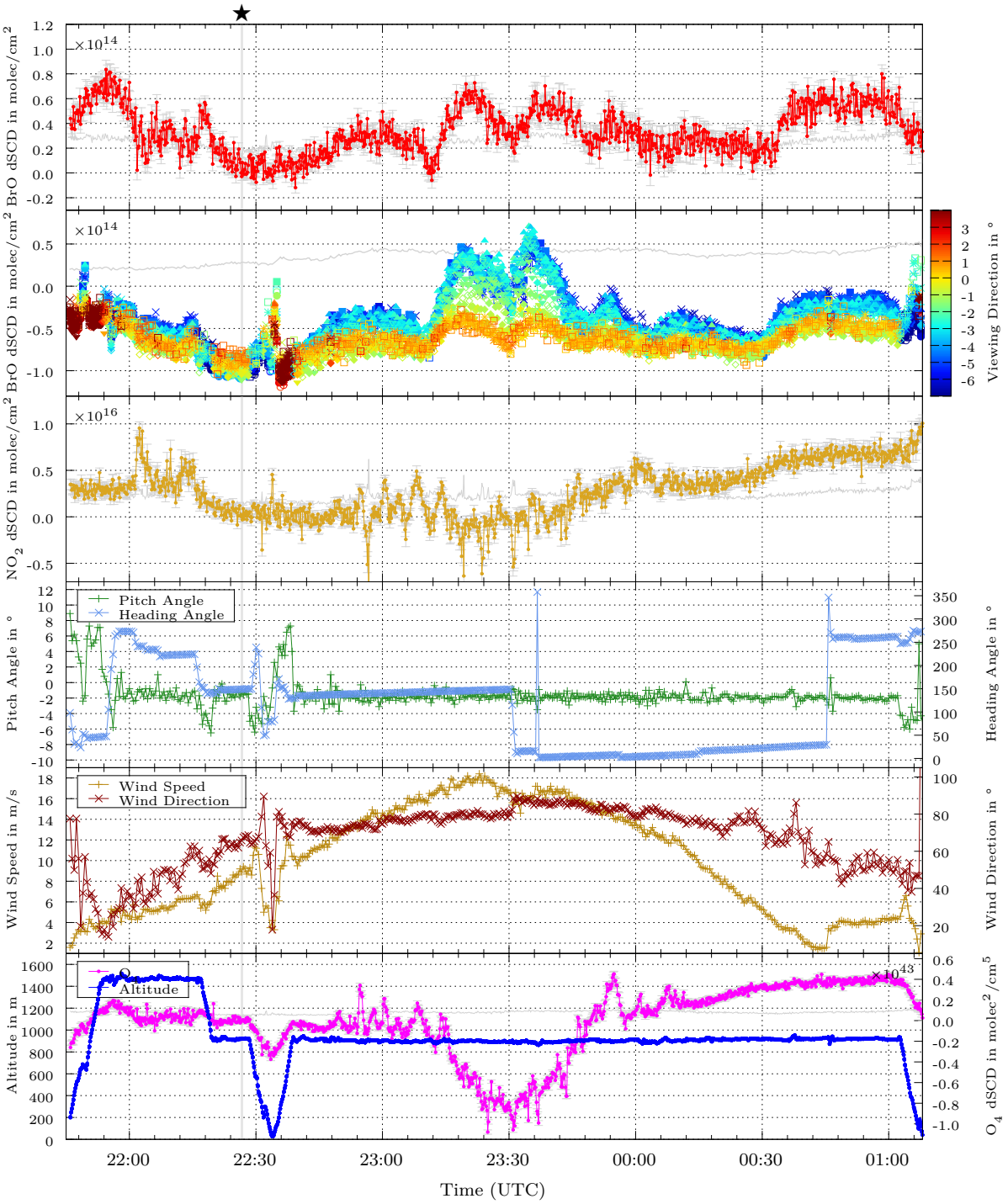

Figure A.24.: Time series of measurement data from the flight on 28th March 2012. Errors and detection limits are plotted in gray. ★: Recording period of nadir scanner in-flight FRS.

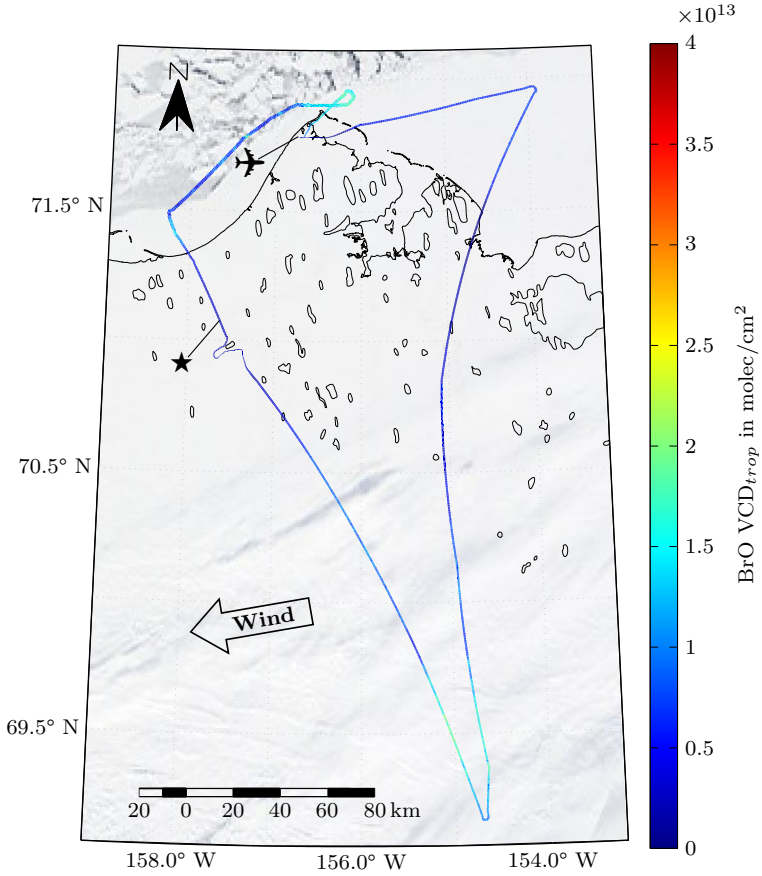

Figure A.25.: Spatial distribution of BrO around Barrow, measured by HAIDI's nadir scanner on 28$^{\text{th}}$ March 2012. The background shows a true color satellite image taken by MODIS (Aqua) on the same day with a resolution of 250 m (NASA, 2012). ✈: Location of Barrow airport, ★: Recording position of nadir scanner in-flight FRS.

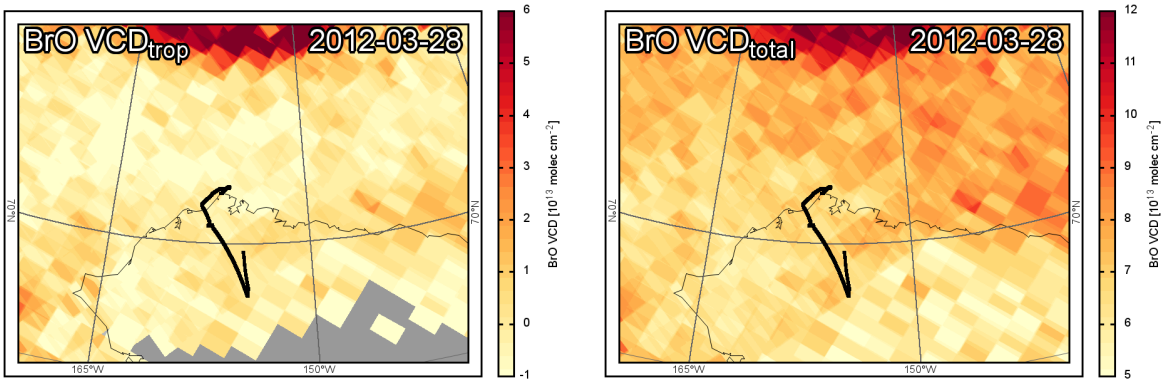

(a) tropospheric VCD **(b)** total VCD

Figure A.26.: GOME-2 satellite images showing the BrO distribution around Barrow on 28$^{\text{th}}$ March 2012 (H. Sihler, pers. comm.).

A.3.7. Flight on March 31st, 2012

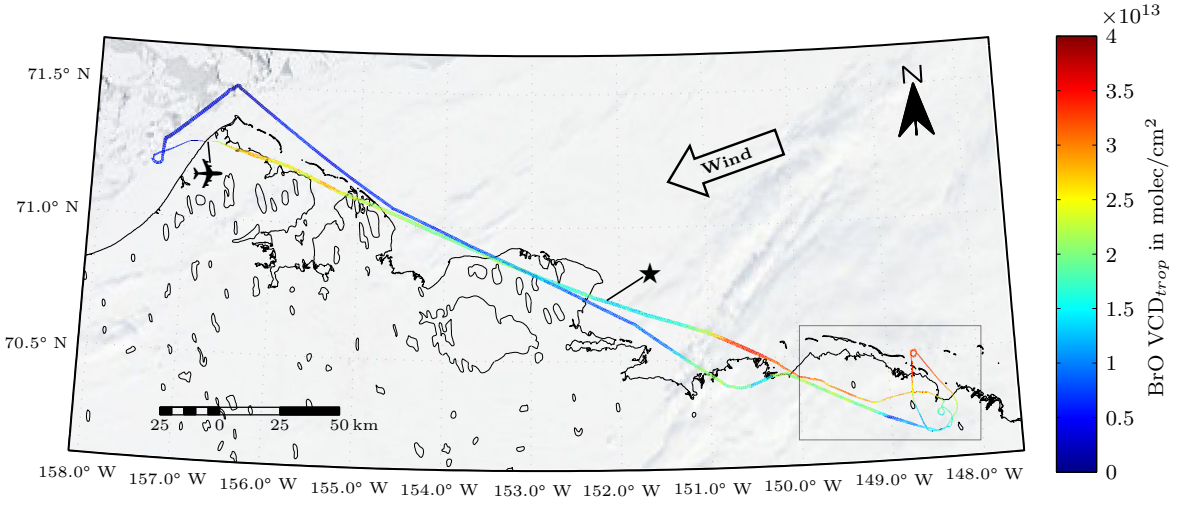

(a) BrO distribution

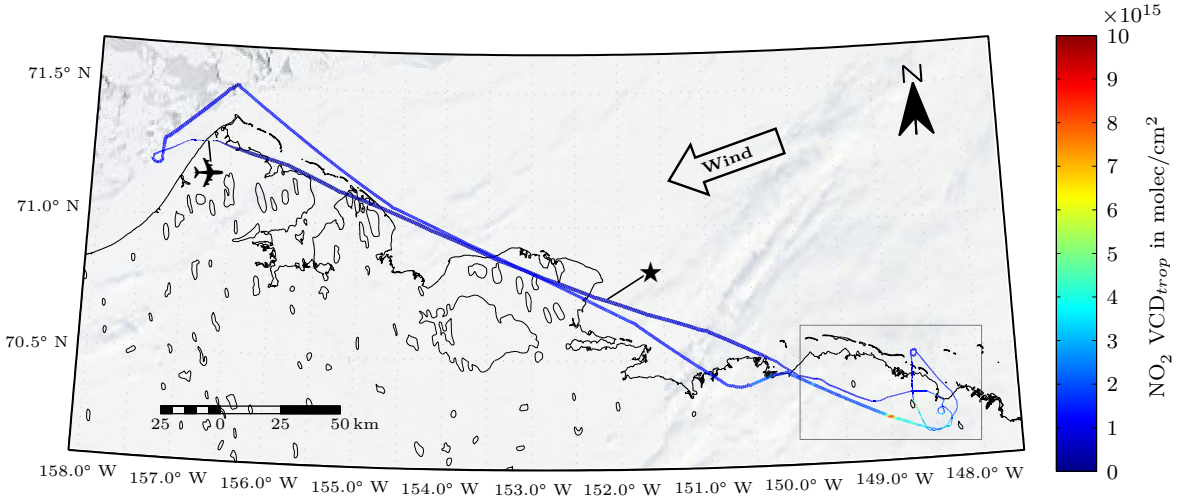

(b) NO_2 distribution

Figure A.27.: Maps of the flight to Prudhoe Bay on 31st March 2012. The box in the lower right corner indicates the section of the map, which is illustrated in Fig. 8.13. The background shows a true color satellite image taken by MODIS (Aqua) on the same day with a resolution of 250 m (NASA, 2012). ✈: Location of Barrow airport, ★: Recording position of nadir scanner in-flight FRS.

Bibliography

Aliwell, S. R., M. Van Roozendael, P. V. Johnston, A. Richter, T. Wagner, D. W. Arlander, J. P. Burrows, D. J. Fish, R. L. Jones, K. K. Tørnkvist, J.-C. Lambert, K. Pfeilsticker, and I. Pundt (2002). "Analysis for BrO in zenith-sky spectra: An intercomparison exercise for analysis improvement." *J. Geophys. Res.* 107.

Allègre, C., G. Manhès, and E. Lewin (2001). "Chemical composition of the Earth and the volatility control on planetary genetics." *Earth Planet. Sci. Lett.* 185, pp. 49–69.

Andor Technology (2013). *CCD Spectral Response (QE) - Defining the QE of a CCD*. URL: http://www.andor.com/learning-academy/ccd-spectral-response-(qe)-defining-the-qe-of-a-ccd.

Atkinson, R., D. L. Baulch, R. A. Cox, J. N. Crowley, R. F. Hampson, R. G. Hynes, M. E. Jenkin, M. J. Rossi, and J. Troe (2004). "Evaluated kinetic and photochemical data for atmospheric chemistry: Volume I - gas phase reactions of O_x, HO_x, NO_x and SO_x species." *Atmos. Chem. Phys.* 4, pp. 1461–1738.

Baidar, S., H. Oetjen, S. Coburn, B. Dix, I. Ortega, R. Sinreich, and R. Volkamer (2013). "The CU Airborne MAX-DOAS instrument: vertical profiling of aerosol extinction and trace gases." *Atmospheric Measurement Techniques* 6, pp. 719–739.

Barrie, L.A., J. W. Bottenheim, R. C. Schnell, P. J. Crutzen, and R. A. Rasmussen (1988). "Ozone destruction and photochemical reactions at polar sunrise in the lower Arctic atmosphere." *Nature* 334, pp. 138–141.

Beirle, S. (2004). "Estimating source strength and lifetime of Nitrogen Oxides from satellite data." Doctoral dissertation. University of Heidelberg.

Beirle, S., U. Platt, M. Wenig, and T. Wagner (2004). "Highly resolved global distribution of tropospheric NO_2 using GOME narrow swath mode data." *Atmos. Chem. Phys.* 4, pp. 1913–1924.

Berresheim, H., P. H. Wine, and D. D. Davis (1995). In: *Composition, Chemistry, and Climate of the Atmosphere*. Ed. by H. B. Singh. John Wiley & Sons. Chap. Sulfur in the atmosphere, pp. 251–307.

Beutler, H. G. (1945). "The Theory of the Concave Grating." *J. Opt. Soc. Am.* 35, pp. 311–350.

Bhartia, Pawan K. (2009). In: *Twenty Years of Ozone Decline*. Springer-Verlag Berlin Heidelberg. Chap. Role of Satellite Measurements in the Discovery of Stratospheric Ozone Depletion, pp. 183–189.

Bobrowski, N. and G. Giuffrida (2012). "Bromine monoxide/sulphur dioxide ratios in relation to volcanological observations at Mt. Etna 2006–2009." *Solid Earth Discussions* 4, pp. 475–505.

Bobrowski, N., G. Hönninger, B. Galle, and U. Platt (2003). "Detection of bromine monoxide in a volcanic plume." *Nature* 423(6937), pp. 273–276.

Bobrowski, N., C. Kern, U. Platt, C. Hörmann, and T. Wagner (2010). "Novel SO_2 spectral evaluation scheme using the 360–390 nm wavelength range." *Atmos. Meas. Tech.* 3, pp. 879–891.

Bobrowski, N. and U. Platt (2007). "SO_2/BrO ratios studied in five volcanic plumes." *Journal of Volcanology and Geothermal Research* 166, pp. 147–160.

Bobrowski, N., R. von Glasow, A. Aiuppa, S. Inguaggiato, I. Louban, O. W. Ibrahim, and U. Platt (2007). "Reactive halogen chemistry in volcanic plumes." *Journal of Geophysical Research: Atmospheres* 112.

Bonaccorso, A., A. Bonforte, S. Calvari, C. Del Negro, G. Di Grazia, G. Ganci, M. Neri, A. Vicari, and E. Boschi (2011). "The initial phases of the 2008–2009 Mount Etna eruption: A multidisciplinary approach for hazard assessment." *Journal of Geophysical Research* 116.

Bottenheim, J. W., J. D. Fuentes, D. W. Tarasick, and K. G. Anlauf (2002). "Ozone in the Arctic lower troposphere during winter and spring 2000 (ALERT2000)." *Atmos. Environ.* 36(15/16), pp. 2535–2544.

Boudries, H. and J. W. Bottenheim (2000). "Cl and Br Atom Concentrations During a Surface Boundary Layer Ozone Depletion Event in the Canadian High Arctic." *Geophys. Res. Lett.* 27, pp. 517–520.

Boyle, W. S. and G. E. Smith (1970). "Charge Coupled Semiconductor Devices." *Bell System Technical Journal* 49, pp. 587–593.

Brady, David J. (2009). *Optical Imaging and Spectroscopy.* John Wiley & Sons.

Bras, G. Le and U. Platt (1995). "A possible mechanism for combined chlorine and bromine catalyzed destruction of tropospheric ozone in the Arctic." *Geophys. Res. Lett.* 22, pp. 599–602.

Brasseur, G., J. Orlando, and G. Tyndall (1999). *Atmospheric chemistry and global change.* Oxford University Press, New York.

Brückner, Volkmar (2003). *Optische Nachrichtentechnik - Grundlagen und Anwendungen.* Teubner.

Bruns, M., S. A. Buehler, J. P. Burrows, K.-P. Heue, U. Platt, I. Pundt, A. Richter, A. Rozanov, T. Wagner, and P. Wang (2004). "Retrieval of profile information from airborne multiaxis UV-visible skylight absorption measurements." *Appl. Opt.* 43.22, pp. 4415–4426. DOI: 10.1364/AO.43.004415.

Bruns, M., S. A. Buehler, J. P. Burrows, A. Richter, A. Rozanov, P.Wang, K. P. Heue, U. Platt, I. Pundt, and T. Wagner (2006). "NO_2 Profile retrieval using airborne multi axis UV-visible skylight absorption measurements over central Europe." *Atmos. Chem. Phys.* 6, pp. 3049–3058.

Buat-Ménard, P. and M. Arnold (1978). "The heavy metal chemistry of atmospheric particulate matter emitted by Mount Etna volcano." *Geophys. Res. Lett.* 5, pp. 245–248.

Burton, M. R., C. Oppenheimer, L. A. Horrocks, and P. W. Francis (2001). "Diurnal changes in volcanic plume chemistry observed by lunar and solar occultation spectroscopy." *Geophys. Res. Lett.* 28, pp. 843–846.

Bussemer, M. (1993). "Der Ring-Effekt: Ursachen und Einfluß auf die spektroskopische Messung stratosphärischer Spurenstoffe." Master's thesis. University of Heidelberg.

Carroll, M. A. and A. M. Thompson (1995). *Progress and Problems in Atmospheric Chemistry*. Ed. by J. R. Baker. Singapore: World Scientific.

Carroll, M. R. and J. R. Holloway, eds. (1994). *Volatiles in magmas*. Vol. 30. Reviews in Mineralogy. Mineralogical Society of America.

Ceamanos, X. and S. Doute (2010). "Spectral Smile Correction of CRISM/MRO Hyperspectral Images." *Trans. Geosci. Remote Sensing* 48, pp. 3951–3959.

Center for Aerospace Structures - University of Colorado Boulder (2013). URL: http://www.colorado.edu/engineering/CAS/courses.d/AFEM.d/AFEM.Ch20.d/AFEM.Ch20.pdf.

Chance, K. V. and R. J. D. Spurr (1997). "Ring effect studies: Rayleigh scattering, including molecular parameters for rotational Raman scattering, and the Fraunhofer spectrum." *Appl. Opt.* 36, pp. 5224–5230.

Chance, K. and R. L. Kurucz (2010). "An improved high-resolution solar reference spectrum for Earth's atmosphere measurements in the ultraviolet, visible, and near infrared." *J. Quant. Spectrosc. Ra.* 111, pp. 1289–1295.

Choi, S. (2010). "Estimating Stratospheric and Tropospheric BrO columns using Ozone Monitoring Instrument." In: *NASA Goddard/Graduate Student Summer Program in Earth System Science*.

Ciddor, Philip E. (1996). "Refractive index of air: new equations for the visible and near infrared." *Appl. Opt.* 35, pp. 1566–1573.

Clémer, K., M. Van Roozendael, C. Fayt, F. Hendrick, C. Hermans, G. Pinardi, R. Spurr, P. Wang, and M. De Mazière (2010). "Multiple wavelength retrieval of tropospheric aerosol optical properties from MAXDOAS measurements in Beijing." *Atmos. Meas. Tech.* 3, pp. 863–878. DOI: 10.5194/amt-3-863-2010.

Coltelli, Mauro, Paola Del Carlo, and Luigina Vezzoli (1998). "Discovery of a Plinian basaltic eruption of Roman age at Etna volcano, Italy." *Geology* 26, pp. 1095–1098.

Crutzen, P. J. (1970). "The influence of nitrogen oxides on the atmospheric ozone content." *Quarterly Journal of the Royal Meteorological Society* 96(408), pp. 320–325.

Davidson, Michael W., Mortimer Abramowitz, Kenneth R. Spring, John C. Long, and Kirill I. Tchourioukanov (2012). *Concepts in Digital Imaging Technology*. URL: http://www.micro.magnet.fsu.edu/primer/digitalimaging/concepts/concepts.html.

Dentener, F. J. and P. J. Crutzen (1993). "Reaction of N_2O_5 on tropospheric aerolsols: impact an the global distribution of NO_x, O_3 and OH." *Journal of Geophysical Research* 98, pp. 7149–7163.

Deutschmann, T., S. Beirle, U. Frieß, M. Grzegorski, C. Kern, L. Kritten, U. Platt, C. Prados-Roman, J. Pukite, T. Wagner, B. Werner, and K. Pfeilsticker (2011). "The Monte Carlo atmospheric radiative transfer model McArtim: Introduction and validation of Jacobians and 3D features." *J. Quant. Spec. Rad. Trans.* 112, pp. 1119–1137. ISSN: 0022-4073. DOI: 10.1016/j.jqsrt.2010.12.009.

Dix, B., S. Baidar, J. F. Bresch, S. R. Hall, K. S. Schmidt, S. Wang, and R. Volkamer (2013). "Detection of iodine monoxide in the tropical free troposphere." *Proc. Natl. Acad. Sci. USA* 110.6, pp. 2035–2040. DOI: 10.1073/pnas.1212386110.

Dix, B., C. A. M. Brenninkmeijer, U. Frieß, T. Wagner, and U. Platt (2009). "Airborne multi-axis DOAS measurements of atmospheric trace gases on CARIBIC long-distance flights." *Atmos. Meas. Tech.* 2.2, pp. 639–652. ISSN: 1867-1381. DOI: 10.5194/amt-2-639-2009.

DLR (2012). Deutsches Zentrum für Luft- und Raumfahrt. URL: http://atmos.eoc.dlr.de/gome2/.

– (2013a). Deutsches Zentrum für Luft- und Raumfahrt. URL: http://www.dlr.de/dlr/desktopdefault.aspx/tabid-10630/.

– (2013b). Deutsches Zentrum für Luft- und Raumfahrt. URL: http://www.halo.dlr.de/protected/technical-notes/HALO-TN-2008-005-E-Racks.pdf.

– (2013c). Deutsches Zentrum für Luft- und Raumfahrt. URL: http://www.halo.dlr.de/protected/technical-notes/HALO-TN-2008-001-B.pdf.

– (2013d). *Technical Note HALO-TN-2007-003-B*. Deutsches Zentrum für Luft- und Raumfahrt. URL: http://www.halo.dlr.de/protected/technical-notes/HALO-TN-2007-003-B.pdf.

e2v (2013). URL: http://www.eureca.de/pdf/optoelectronic/e2v/ccd30-11-bi-high.pdf.

Edmund Optics (2012). URL: http://www.edmundoptics.com/techsupport/resource_center/product_docs/prnt_48284.pdf.

EUMETSAT (2013). European Organisation for the Exploitation of Meteorological Satellites. URL: http://www.eumetsat.int/website/home/Satellites/CurrentSatellites/Metop/MetopDesign/GOME2/index.html.

Fan, S.-M. and D.J. Jacob (1992). "Surface ozone depletion in Arctic spring sustained by bromine reactions on aerosols." *Nature* 359, pp. 522–524.

Fickert, S., J.W. Adams, and J.N. Crowley (1999). "Activation of Br_2 and BrCl via uptake of HOBr onto aqueous salt solutions." *J. Geophys. Res.* 104, pp. 23719–23727.

Frieß, U., J. Hollwedel, G. König-Langlo, T. Wagner, and U. Platt1 (2004). "Dynamics and chemistry of tropospheric bromine explosion events in the Antarctic coastal region." *J. Geophys. Res.* 109.

Frieß, U., P.S. Monks, J.J. Remedios, A. Rozanov, R. Sinreich, T. Wagner, and U. Platt (2006). "MAX-DOAS O_4 measurements: A new technique to derive information on atmospheric aerosols: 2. Modeling studies." *J. Geophys. Res.* 111, p. D14203. DOI: 10.1029/2005JD006618.

Frieß, U., H. Sihler, R. Sander, D. Pöhler, S. Yilmaz, and U. Platt (2011). "The vertical distribution of BrO and aerosols in the Arctic: Measurements by active and passive differential optical absorption spectroscopy." *J. Geophys. Res.* 116, D00R04. ISSN: 0148-0227. DOI: 10.1029/2011JD015938.

Frieß, U., T. Wagner, I. Pundt, K. Pfeilsticker, and U. Platt (2001). "Spectroscopic measurements of tropospheric iodine oxide at Neumayer station, Antarctica." *Geophys. Res. Lett.* 28, pp. 1941–1944.

Gardiner, W. C. Jr. (2000). *Gas-Phase Combustion Chemistry*. Springer-Verlag Berlin Heidelberg.

General, S., D. Pöhler, H. Sihler, N. Bobrowski, U. Frieß, J. Zielcke, P. Shepson, B. Stirm, W. Simpson, K. Weber, C. Fischer, and U. Platt (2014). "The Heidelberg Airborne Imaging DOAS Instrument (HAIDI): A Novel Imaging DOAS Device for 2-D and 3-D Imaging of Trace Gases." Manuscript submitted for publication.

Gerlach, T. M. (2004). "Volcanic sources of tropospheric ozone-depleting trace gases." *Geochem. Geophys. Geosyst.* 5(9).

Gliß, Jonas (2013). "MAX-DOAS measurements of chlorine and bromine compounds in the volcanic plume of Mt. Etna." Master's thesis. University of Heidelberg.

Google (2013). URL: https://maps.google.de/.

Grainger, J. and J. Ring (1962). "Anomalous Fraunhofer Line Profiles." *Nature* 193, p. 762.

Grote, Karl-Heinrich and Jörg Feldhusen (2011). *Dubbel - Taschenbuch für den Maschinenbau*. Springer-Verlag Berlin Heidelberg.

Gvirtzman, Zohar and Amos Nur (1999). "The formation of Mount Etna as the consequence of slab rollback." *Nature* 401, pp. 782–785.

Hartl, A., B. C. Song, and I. Pundt (2006). "2-D reconstruction of atmospheric concentration peaks from horizontal long path DOAS tomographic measurements: parametrisation and geometry within a discrete approach." *Atmospheric Chemistry and Physics* 6, pp. 847–861.

Hausmann, M. and U. Platt (1994). "Spectroscopic measurement of bromine oxide and ozone in the high Arctic during Polar Sunrise Experiment 1992." *Journal of Geophysical Research* 99, pp. 25399–25413.

Heraeus Quarzglas (2012). URL: http://heraeus-quarzglas.com/media/webmedia_local/downloads/broschren_mo/dataandproperties_optics_fusedsilica.pdf.

Heue, K.-P. (2005). "Airborne Multi AXis DOAS instrument and measurements of two-dimensional tropospheric trace gas distributions." Doctoral dissertation. University of Heidelberg.

Heue, K.-P., C. A. M. Brenninkmeijer, A. K. Baker, A. Rauthe-Schöch, D. Walter, T. Wagner, C. Hörmann, H. Sihler, B. Dix, U. Frieß, U. Platt, B. G. Martinsson, P. F. J. van Velthoven, A. Zahn, and R. Ebinghaus (2011). "SO_2 and BrO observation in the plume of the Eyjafjallajökull

volcano 2010: CARIBIC and GOME-2 retrievals." *Atmos. Chem. Phys.* 11, pp. 2973–2989. DOI: 10.5194/acp-11-2973-2011.

Heue, K.-P., A. Richter, M. Bruns, J. P. Burrows, C. v. Friedeburg, U. Platt, I. Pundt, P. Wang, and T. Wagner (2005). "Validation of SCIAMACHY tropospheric NO_2-columns with AMAXDOAS measurements." *Atmospheric Chemistry and Physics* 5, pp. 1039–1051.

Heue, K.-P., T. Wagner, S. P. Broccardo, D. Walter, S. J. Piketh, K. E. Ross, S. Beirle, and U. Platt (2008). "Direct observation of two dimensional trace gas distributions with an airborne Imaging DOAS instrument." *Atmospheric Chemistry and Physics* 8, pp. 6707–6717.

Hinkley, T. K., P. J. Lamothe, S. A. Wilson, D. L. Finnegan, and T. M. Gerlach (1999). "Metal emissions from Kilauea, and a suggested revision of the estimated worldwide metal output by quiescent degassing of volcanoes." *Earth Planet. Sci. Lett.* 170, pp. 315–325.

HiTEC (2014). URL: http://hitecrcd.com/products/servos/ultra-premium-digital-servos/hs-7940th-high-voltage-high-speed-titanium-gear-coreless-/product.

Hofmann, D., P. Bonasoni, M. De Maziere, F. Evangelisti, G. Giovanelli, A. Goldman, F. Goutail, J. Harder, R. Jakoubek, P. Johnston, J. Kerr, T. McElroy, R. McKenzie, G. Mount, U. Platt, J.-P. Pommereau, A. Sarkissian, P. Simon, S. Solomon, J. Stutz, A. Thomas, M. Van Roosendael, and E. Wu (1995). "Intercomparison of UV/visible spectrometers for measurement of stratospheric NO_2 for the Network for the Detection of Stratospheric Change." *Journal of Geophysical Research* 100, pp. 16765–16791.

Hönninger, G., H. Leser, O. Sebastián, and U. Platt (2004). "Ground-based measurements of halogen oxides at the Hudson Bay by active longpath DOAS and passive MAX-DOAS." *Geophys. Res. Lett.* 31, p. L04111.

Horbanski, Martin (2010). "A Compact Resonator Based Instrument for DOAS Measurements of Ambient Nitrogen Dioxide." Master's thesis. University of Heidelberg.

Horrocks, L., C. Oppenheimer, M. Burton, and H. Duffell (2003). In: *Volcanic degassing.* Vol. 213. Geological Society Special Publications. Chap. Compositional variation in tropospheric volcanic gas plumes: Evidence from ground-based remote sensing, pp. 349–369.

Hung, H., P. Blanchard, C. J. Halsall, T. F. Bidleman, G. A. Stern, P. Fellin, D. C. G. Muir, L. A. Barrie, L. M. Jantunen, P. A. Helm, J. Ma, and A. Konoplev (2005). "Temporal and spatial variabilities of atmospheric polychlorinated biphenyls (PCBs), organochlorine (OC) pesticides and polycyclic aromatic hydrocarbons (PAHs) in the Canadian Arctic: Results from a decade of monitoring." *Science of The Total Environment* 342(1-3), pp. 119–144.

Ibrahim, O., R. Shaiganfar, R. Sinreich, T. Stein, U. Platt, and T. Wagner (2010). "Car MAX-DOAS measurements around entire cities: quantification of NO_x emissions from the cities of Mannheim and Ludwigshafen (Germany)." *Atmos. Meas. Tech.* 3, pp. 709–721.

IJIS (2013). URL: http://www.ijis.iarc.uaf.edu/en/index.htm.

INGV (2011). Istituto Nazionale di Geofisica e Vulcanologia. URL: http://www.ct.ingv.it/en/.

Irie, H., Y. Kanaya, H. Akimoto, H. Iwabuchi, A. Shimizu, and K. Aoki (2008). "First retrieval of tropospheric aerosol profiles using MAX-DOAS and comparison with lidar and sky radiometer measurements." *Atmos. Chem. Phys.* 8, pp. 341–350. ISSN: 1680-7316. DOI: 10.5194/acp-8-341-2008.

Jaffe, D. A., R. E. Honrath, D. Furness, T. J. Conway, E. Dlugokencky, and L. P. Steele (1995). "A determination of the CH_4, NO_x and CO_2 emissions from the Prudhoe Bay, Alaska oil development." *Journal of Atmospheric Chemistry* 20, pp. 213–227.

Joiner, J. and P. K. Bhartia (1995). "The determination of cloud pressures from rotational Raman scattering in satellite backscatter ultraviolet measurements." *J. Geophys. Res.* 100, pp. 23019–23026.

Junkermann, W., U. Platt, and A. Volz-Thomas (1989). "A photoelectric detector for the measurement of photolysis frequencies of ozone and other atmospheric molecules." *J. Atmos. Chem.* 8, pp. 203–227.

Kaleschke, L., A. Richter, J. Burrows, O. Afe, G. Heygster, J. Notholt, A. M. Rankin, H. K. Roscoe, J. Hollwedel, T. Wagner, and H.-W. Jacobi (2004). "Frost flowers on sea ice as a source of sea salt and their influence on tropospheric halogen chemistry." *Geophys. Res. Lett.* 31(16).

Keil, A. D. and P. B. Shepson (2006). "Chlorine and bromine atom ratios in the springtimes Arctic troposphere as determined from measurements of halogenated volatile organic compounds." *J. Geophys. Res.* 111.

Kern, C., T. Deutschmann, L. Vogel, M. Wöhrbach, T. Wagner, and U. Platt (2010). "Radiative transfer corrections for accurate spectroscopic measurements of volcanic gas emissions." *Bull. Volcanol.* 72, pp. 233–247.

Kidger, Michael J. (2002). *Fundamental Optical Design*. SPIE Press.

Kowalewski, M. G. and S. J. Janz (2009). "Remote sensing capabilities of the Airborne Compact Atmospheric Mapper." In: *Proc. SPIE*. Vol. 7452. Earth Observing Systems XIV, 74520Q.

Kramer, Herbert J. (2001). *Observation of the Earth and its Environment: Survey of Missions and Sensors*. Springer-Verlag Berlin Heidelberg.

Kraus, Stefan (2006). "DOASIS - A Framework Design for DOAS." Doctoral dissertation. University of Mannheim.

Kuchling, Horst (2001). *Taschenbuch der Physik*. Fachbuchverlag Leipzig.

Kunze, Hans-Joachim (2009). *Introduction to Plasma Spectroscopy*. Springer-Verlag Berlin Heidelberg.

Laepple, T., V. Knab, K.-U. Mettendorf, and I. Pundt (2004). "Longpath DOAS tomography on a motorway exhaust gas plume: numerical studies and application to data from the BAB II campaign." *Atmospheric Chemistry and Physics* 4, pp. 1323–1342.

Lampel, J. (2010). "Ship-borne MAX-DOAS Measurements of Tropospheric Halogen Oxides on Atlantic Transects." Master's thesis. University of Heidelberg.

Lee, C., Y. Kim, H. Tanimoto, N. Bobrowski, U. Platt, T. Mori, K. Yamamoto, and C. Hong (2005). "High ClO and ozone depletion observed in the plume of Sakurajima volcano, Japan." *Geophys. Res. Lett.* 32.

Lee, D. S., I. Kohler, E. Grobler, F. Rohrer, R. Sausen, L. Gallardo-Klenner, J. G. J. Olivier, F. J. Dentener, and A. F. Bouwman (1997). "Estimations of global NO_x emissions and their uncertainties." *Atmos. Environ.* 31, pp. 1735–1749.

Lehrer, E., G. Hönninger, and U. Platt (2004). "A one dimensional model study of the mechanism of halogen liberation and vertical transport in the polar troposphere." *Atmos. Chem. Phys.* 4, pp. 2427–2440.

Leighton, P. A. (1961). *Photochemistry of air pollution*. Academic Press, New York.

LEONI (2013). URL: http://www.leoni-fiber-optics.com/Transmission-tool.11883.0.html?&L=1.

Levelt, P. F., G. H. J. van den Oord, M. R. Dobber, A. Mälkki, H. Visser, J. de Vries, P. Stammes, J. O. V. Lundell, and H. Saari (2006). "The Ozone Monitoring Instrument." *Trans. Geosci. Remote Sensing* 44, pp. 1093–1101.

Levenberg, K. (1944). "A method for the solution of certain non-linear problems in least squares." *Quart. Appl. Math.* 2, pp. 164–168.

Lewis, Ian R. and Howell G. M. Edwards (2001). *Handbook of Raman Spectroscopy: From the Research Laboratory to the Process Line*. Marcel Dekker, Inc.

Lindberg, S. E., S. Brooks, C. J. Lin, K. J. Scott, M. S. LANDIS, R. K. STEVENS, M. Goodsite, and A. Richter. (2002). "Dynamic Oxidation of Gaseous Mercury in the Arctic Troposphere at Polar Sunrise." *Environ. Sci. Technol.* 36(6), pp. 1245–1256.

Liou, K. N. (2002). *An Introduction to Atmospheric Radiation (2nd Edition)*. Academic Press.

Loewen, Erwin G. and Evgeny Popov (1997). *Diffraction Gratings and Applications*. Marcel Dekker Inc.

Louban, I., N. Bobrowski, D. Rouwet, S. Inguaggiato, and U. Platt (2009). "Imaging DOAS for volcanological applications." *B. Volcanol.* 71, pp. 753–765.

Lübcke, P., N. Bobrowski, S. Arellano, B. Galle, G. Garzón, L. Vogel, and U. Platt (2013). "BrO/SO_2 molar ratios from scanning DOAS measurements in the NOVAC network." *Solid Earth Discuss.* 5, pp. 1845–1870.

Malitson, I. H. (1965). "Interspecimen Comparison of the Refractive Index of Fused Silica." *J. Opt. Soc. Am.* 55, pp. 1205–1208.

Marcuse, D. (1973). "Coupled Mode Theory of Round Optical Fibres." *Bell Syst. Tech J.* 52, pp. 817–842.

Marquardt, D. W. (1963). "An algorithm for least-squares estimation of non-linear parameters." *J. Soc. Indust. Appl. Math.* 11, pp. 431–441.

Martin, R. S., J. C. Wheeler, E. Ilyinskaya, C.F. Braban, and C. Oppenheimer (2012). "The uptake of halogen (HF, HCl, HBr and HI) and nitric (HNO_3) acids into acidic sulphate particles in quiescent volcanic plumes." *Chem. Geol.* 296–297, pp. 19–25.

Martin, R. V., C. E. Sioris, K. Chance, T. B. Ryerson, T. H. Bertram, P. J. Wooldridge, R. C. Cohen, J. A. Neuman, A. Swanson, and F. M. Flocke (2006). "Evaluation of space-based constraints on global nitrogen oxide emissions with regional aircraft measurements over and downwind of eastern North America." *J. Geophys. Res.* 111, p. D15308.

Martinez, M., T. Arnold, and D. Perner (1999). "The role of bromine and chlorine chemistry for arctic ozone depletion events in Ny-Ålesund and comparison with model calculations." *Ann. Geophys.* 17, pp. 941–956.

Mather, T. A., A. G. Allen, C. Oppenheimer, D. M. Pyle, and A. J. S. McGonigle (2003). "Size-Resolved Characterisation of Soluble Ions in the Particles in the Tropospheric Plume of Masaya Volcano, Nicaragua: Origins and Plume Processing." *J. Atm. Chem.* 46, pp. 207–237.

Mayer, B. and A. Killing (2005). "Technical note: The libRadtran software package for radiative transfer calculations - description and examples of use." *Atmos. Chem. Phys.* 4, pp. 1255–1263.

McElroy, C. T., C. A. McLinden, and J. C. McConnell (1999). "Evidence for bromine monoxide in the free troposphere during the Arctic polar sunrise." *Nature* 397, pp. 338–341.

McGonigle, A. J. S., P. Delmelle, C. Oppenheimer, V. I. Tsanev, T. Delfosse, G. Williams-Jones, K. Horton, and T. A. Mather (2004). "SO_2 depletion in tropospheric volcanic plumes." *Geophys. Res. Lett.* 31.

Melamed, M. L., S. Solomon, J. S. Daniel, A. O. Langford, R. W. Portmann, T. B. Ryerson, D. K. Nicks Jr., and S. A. McKeen (2003). "Measuring reactive nitrogen emissions from point sources using visible spectroscopy from aircraft." *Journal of Environmental Monitoring* 5, pp. 29–34.

Mentel, T. F., D. Bleilebens, and A. Wahner (1996). "A study of nitrogen oxide oxidation in a large reaction chamber - The fate of NO_2, N_2O_5, HNO_3 and O_3 at different humidities." *Atmos. Environ.* 30, pp. 4007–4020.

Merlaud, A., M. Van Roozendael, J. van Gent, C. Fayt, J. Maes, X. Toledo-Fuentes, O. Ronveaux, and M. De Maziére (2012). "DOAS measurements of NO_2 from an ultralight aircraft during the Earth Challenge expedition." *Atmos. Meas. Tech.* 5, pp. 2057–2068. DOI: 10.5194/amt-5-2057-2012.

Merlaud, A., M. Van Roozendael, N. Theys, C. Fayt, C. Hermans, B. Quennehen, A. Schwarzenboeck, G. Ancellet, M. Pommier, J. Pelon, J. Burkhart, A. Stohl, and M. De Mazière (2011). "Airborne DOAS measurements in Arctic: vertical distributions of aerosol extinction coefficient and NO_2 concentration." *Atmos. Chem. Phys.* 11.17, pp. 9219–9236. DOI: 10.5194/acp-11-9219-2011.

Mickle, R. E., J. W. Bottenheim, W. R. Leaitch, and W. Evans (1989). "Boundary layer ozone depletion during AGASP-II." *Atmos. Environ.* 23(11), pp. 2443–2449.

NASA (2011). National Aeronautics and Space Administration. URL: http://www.nasa.gov/mission_pages/aura/spacecraft/omi.html.

– (2012). National Aeronautics and Space Administration. URL: http://lance-modis.eosdis.nasa.gov/imagery/subsets/?subset=BROMEX.

Neri, M. and V. Acocella (2007). "Structural evolution of the South-East Crater at Mt. Etna (Italy) during the 2004–2006 period." *Geophysical Research Abstracts* 9, p. 02206.

Neumann, Wilfried (2013). URL: http://www.spectra-magic.de.

NOAA (2013). National Oceanic and Atmospheric Administration. URL: http://www.esrl.noaa.gov/gmd/obop/brw/.

Oltmans, S. J. (1981). "Surface ozone measurements in clean air." *Journal of Geophysical Research* 86, pp. 1174–1180.

Oppenheimer, C. (2003). *Volcanic Degassing*. Ed. by D. M. Pyle and J. Barclay. Geol. Soc. London, U. K.

Oppenheimer, C., P. Bani, J. A. Calkins, M. R. Burton, and G. M. Sawyer (2006a). "Rapid FTIR sensing of volcanic gases released by Strombolian explosions at Yasur volcano, Vanuatu." *Appl. Phys.* B 85, pp. 453–460.

Oppenheimer, C., P. Francis, and J. Stix (1998). "Depletion rates of sulfur dioxide in tropospheric volcanic plumes." *Geophys. Res. Lett.* 25, pp. 2671–2674.

Oppenheimer, C., V. I. Tsanev, C. F. Braban, R. A. Cox, J. W. Adams, A. Aiuppa, N. Bobrowski, P. Delmelle, J. Barclay, and A. J.S. McGonigle (2006b). "BrO formation in volcanic plumes." *Geochim. Cosmochim. Acta* 70, pp. 2935–2941.

Palmer, Christopher and Erwin Loewen (2005). *Diffraction Grating Handbook*. Newport Corporation.

Parrish, D. D., M. Trainer, E. J. Williams, D. W. Fahey, G. Hübler, C. S. Eubank, S. C. Liu, P. C. Murphy, D. L. Albritton, and F. C. Fehsenfeld (1986). "Measurements of the NO_x-O_3 photostationary state at Niwot Ridge, Colorado." *Journal of Geophysical Research* 91, pp. 5361–5370.

Perner, D., D. H. Ehhalt, H. W. Pätz, U. Platt, E. P. Röth, and A. Volz (1976). "OH - Radicals in the lower troposphere." *Geophys. Res. Lett.* 3, pp. 466–468.

Petritoli, A., F. Ravegnani, G. Giovanelli, D. Bortoli, U. Bonafè, I. Kostadinov, and A. Oulanovsky (2002). "Off-axis measurements of atmospheric trace gases by use of an airborne ultraviolet-visible spectrometer." *Applied Optics* 41, pp. 5593–5599.

Pfeilsticker, K. and U. Platt (1994). "Airborne measurements during the Arctic stratospheric experiment: Observation of O_3 and NO_2." *Geophys. Res. Lett.* 21, pp. 1375–1378.

Platt, U. and N. Bobrowski (2014). In: *Volcanism and Global Environmental Change*. Manuscript submitted for publication. Cambridge University Press. Chap. Quantification of volcanic reactive halogen emissions.

Platt, U. and E. Lehrer (1997). *Arctic Tropospheric Ozone Chemistry (ARCTOC) - Final Report of the EU-Project EV5V-CT93-0318*. Heidelberg.

Platt, U., L. Marquard, T. Wagner, and D. Perner (1997). "Corrections for zenith scattered light DOAS." *Geophys. Res. Lett.* 24, pp. 1759–1762.

Platt, U., D. Perner, and H. W. Pätz (1979). "Simultaneous measurement of atmospheric CH_2O, O_3 and NO_2 by differential optical absorption." *J. Geophys. Res.* 84, pp. 6329–6335.

Platt, U. and J. Stutz (2008). *Differential Optical Absorption Spectroscopy*. Springer-Verlag Berlin Heidelberg.

Pöhler, D. (2010). "Determination of two dimensional trace gas distributions using tomographic LP-DOAS measurements in the city of Heidelberg, Germany." Doctoral dissertation. University of Heidelberg.

Pöhler, Denis, Leif Vogel, Udo Frieß, and Ulrich Platt (2009). "Observation of halogen species in the Amundsen Gulf, Arctic, by active long-path differential optical absorption spectroscopy." *Proceedings of the National Academy of Sciences* 107, pp. 6582–6587.

Popp, C., D. Brunner, A. Damm, M. Van Roozendael, C. Fayt, and B. Buchmann (2012). "High-resolution NO_2 remote sensing from the Airborne Prism EXperiment (APEX) imaging spectrometer." *Atmos. Meas. Tech.* 5, pp. 2211–2225.

Prados-Roman, C., A. Butz, T. Deutschmann, M. Dorf, L. Kritten, A. Minikin, U. Platt, H. Schlager, H. Sihler, N. Theys, M. Van Roozendael, T. Wagner, and K. Pfeilsticker (2011). "Airborne DOAS limb measurements of tropospheric trace gas profiles: case studies on the profile retrieval of O_4 and BrO." *Atmos. Meas. Tech.* 4, pp. 1241–1260. DOI: 10.5194/amt-4-1241-2011.

Pratt, Kerri A., Kyle D. Custard, Paul B. Shepson, Thomas A. Douglas, Denis Pöhler, Stephan General, Johannes Zielcke, William R. Simpson, Ulrich Platt, David J. Tanner, L. Gregory Huey, Mark Carlsen, and Brian H. Stirm (2013). "Photochemical production of molecular bromine in Arctic surface snowpacks." *Nature Geoscience* 6, pp. 351–356.

Rankin, A. M., E. W. Wolff, and S. Martin (2002). "Frost flowers: Implications for tropospheric chemistry and ice core interpretation." *J. Geophys. Res.* 107(D23).

Richter, A., J. P. Burrows, H. Nüß, C. Granier, and U. Niemeier (2005). "Increase in tropospheric nitrogen dioxide over China observed from space." *Nature* 437, pp. 129–132.

Rizzo, A. L., A. Caracausi, M. Liotta, A. Paonita, J. D. Barnes, R. A. Corsaro, and M. Martelli (2013). "Chlorine isotope composition of volcanic gases and rocks at Mount Etna (Italy) and inferences on the local mantle source." *Earth and Planetary Science Letters* 371–372, pp. 134–142.

Roberts, T. J., C. F. Braban, R. S. Martin, C. Oppenheimer, J. W. Adams, R. A. Cox, R. L. Jones, and P. T. Griffiths (2009). "Modelling reactive halogen formation and ozone depletion in volcanic plumes." *Chem. Geo.* 263, pp. 151–163.

Robock, A. (2000). "Volcanic eruptions and climate." *Rev. Geophys.* 38, pp. 191–219.

Rodgers, C. D. (2000). *Inverse methods for atmospheric sounding, theory and practice*. Series on Atmospheric, Oceanic and Planetary Physics. World Scientific.

Roedel, Walter (2000). *Physik unserer Umwelt - Die Atmosphäre*. Springer-Verlag Berlin Heidelberg.

Roscoe, H. K., D. J. Fish, and R. L. Jones (1996). "Interpolation errors in UV-visible spectroscopy for stratospheric sensing: implications for sensitivity, spectral resolution, and spectral range." *Appl. Opt.* 35, pp. 427–432.

Roy, D.P., M.A.Wulder, T.R. Loveland, C.E.Woodcock, R.G. Allen, M.C. Anderson, D. Helder, J.R. Irons, D.M. Johnson, R. Kennedy, T.A. Scambos, C.B. Schaaf, J.R. Schott, Y. Sheng, E.F. Vermote, A.S. Belward, R. Bindschadler, W.B. Cohen, F. Gao, J.D. Hipple, P. Hostert, J. Huntington, C.O. Justice, A. Kilic, V. Kovalskyy, Z.P. Lee, L. Lymburner, J.G.Masek, J.McCorkel, Y. Shuai, R. Trezza, J. Vogelmann, R.H.Wynne, and Z. Zhu (2014). "Landsat-8: Science and product vision for terrestrial global change research." *Remote Sensing of Environment* 145, pp. 154–172.

Rozanov, A., V. Rozanov, and J.P. Burrows (2001). "A numerical radiative transfer model for a spherical planetary atmosphere: combined differential-integral approach involving the Picard iterative approximation." *J. Quant. Spec. Rad. Trans.* 69, pp. 491–512. ISSN: 0022-4073. DOI: 10.1016/S0022-4073(00)00100-X.

Saiz-Lopez, A., A. S. Mahajan, R. A. Salmon, S. J.-B. Bauguitte, A. E. Jones, H. K. Roscoe, and J. M. C. Plane (2007). "Boundary layer halogens in coastal Antarctica." *Science* 317, pp. 348–351.

Sander, S. P., R.R. Friedl, D. M. Golden, M. J. Kurylo, G. K. Moortgat, H. Keller-Rudek, P. H. Wine, A. R. Ravishankara, C. E. Kolb, M. J. Molina, B. J. Finlayson-Pitts, R. E. Huie, and V. L. Orkin (2006). *Chemical Kinetics and Photochemical Data for Use in Atmospheric Studies - Evaluation Number 15*. JPL Publication 06-2, Jet Propulsion Laboratory, Pasadena, CA.

Schmidt, A., K. S. Carslaw, G. W. Mann, A. Rap, K. J. Pringle, D. V. Spracklen, M. Wilson, and P. M. Forster (2012). "Importance of tropospheric volcanic aerosol for indirect radiative forcing of climate." *Atmos. Chem. Phys.* 12, pp. 7321–7339.

Schowengerdt, Robert A. (2006). *Remote Sensing: Models and Methods for Image Processing*. Academic Press.

Schroeder, W. H., K. G. Anlauf, L. A. Barrie, J. Y. Lu, A. Steffen, D. R. Schneeberger, and T. Berg (1998). "Arctic springtime depletion of mercury." *Nature* 394, pp. 331–332.

Scollo, S., A. Boselli, M. Coltelli, G. Leto, G. Pisani, N. Spinelli, and X. Wang (2012). "Monitoring Etna volcanic plumes using a scanning LiDAR." *Bulletin of Volcanology* 74(10), pp. 2383–2395.

Sebastián Müller de Vries, Oliver (2004). "The relative contribution of free radicals to the oxidation chain of Dimethylsulphide in the marine boundary layer." Doctoral dissertation. University of Heidelberg.

Seinfeld, John H. (1986). *Atmospheric Chemistry and Physics of Air Pollution*. John Wiley & Sons.

Shefov, N. N. (1959). "Spectroscopic, Photoelectric, and Radar Investigations of Aurorae and the Nightglow." *Izd. Akad. Nauk* 1.

Sihler, Holger (2007). "Light-Emitting Diodes as Light Sources in Spectroscopic Measurements of Atmospheric Trace Gases." Master's thesis. University of Heidelberg.

Sihler, Holger, Thomas Wagner, Lars Kaleschke, Hella Riede, Steffen Beirle, Steffen Dörner, Udo Frieß, Rolf Sander, and Ulrich Platt (2011). "Arctic tropospheric bromine activation as seen

from space and how it is related to meteorology, sea ice properties and surface observations." *Geophysical Research Abstracts* 13.

Simpson, W. R., D. Carlson, G. Hoenninger, T. A. Douglas, M. Sturm, D. Perovich, and U. Platt (2007a). "First-year sea-ice contact predicts bromine monoxide (BrO) levels better than potential frost flower contact." *Atmos. Chem. Phys.* 7, pp. 621–627.

Simpson, W. R., R. von Glasow, K. Riedel, P. Anderson, P. Ariya, J. Bottenheim, J. Burrows, L. J. Carpenter, U. Frieß, M. E. Goodsite, D. Heard, M. Hutterli, H.-W. Jacobi, L. Kaleschke, B. Neff, J. Plane, U. Platt, A. Richter, H. Roscoe, R. Sander, P. Shepson, J. Sodeau, A. Steffen, Wagner, and E. Wolff (2007b). "Halogens and their role in polar boundary-layer ozone depletion." *Atmos. Chem. Phys.* 7, pp. 4375–4418.

Sinreich, R., U. Frieß, and U. Platt (2005). "Multi axis differential optical absorption spectroscopy (MAX-DOAS) of gas and aerosol distributions." *Faraday Discuss.* 130, pp. 153–164. DOI: 10.1039/b419274p.

Skyum, Sven (1991). "A simple algorithm for computing the smallest enclosing circle." *Inf. Process. Lett.* 37, pp. 121–125.

Solomon, S., R. R. Garcia, and A. R. Ravishankara (1994). "On the role of iodine in ozone depletion." *J. Geophys. Res.* 99, pp. 20491–20499.

Solomon, S., G. Mount, R. W. Sanders, and A. Schmeltekopf (1987). "Visible spectroscopy at McMurdo station, Antarctica: 2. Observation of OClO." *J. Geophys. Res.* 92, pp. 8329–8338.

SSEC (2011). Space Science and Engineering Center - University of Wisconsin-Madison. URL: http://www.ssec.wisc.edu/gallery/modis/.

Stutz, J. (1996). "Messung der Konzentration troposphärischer Spurenstoffe mittels Differentieller-Optischer-Absorptionsspektroskopie: Eine neue Generation von Geräten und Algorithmen." Doctoral dissertation. Institute of Environmental Physics, Heidelberg University.

Stutz, J. and U. Platt (1996). "Numerical analysis and estimation of the statistical error of differential optical absorption spectroscopy measurements with least-squares methods." *Appl. Opt.* 35, pp. 6041–6053.

Su, Yushan, Hayley Hung, Pierrette Blanchard, Gregory W. Patton, Roland Kallenborn, Alexei Konoplev, Phil Fellin, Henrik Li, Charles Geen, Gary Stern, Bruno Rosenberg, and Leonard A. Barrie (2006). "Spatial and Seasonal Variations of Hexachlorocyclohexanes (HCHs) and Hexachlorobenzene (HCB) in the Arctic Atmosphere." *Environ. Sci. Technol.* 40(21), pp. 6601–6607.

Sumner, A. L. and P. B. Shepson (1999). "Snowpack production of formaldehyde and its impact on the Arctic troposphere." *Nature* 398, pp. 230–233.

Tanskanen, A. and T. Manninen (2007). "Effective UV surface albedo of seasonally snow-covered lands." *Atmos. Chem. Phys.* 7, pp. 2759–2764.

TEMIS (2013). Tropospheric Emission Monitoring Internet Service. URL: http://www.temis.nl/airpollution/no2col/no2regioomi_v2.php.

Textor, C., H.-F. Graf, C. Timmreck, and A. Robock (2004). In: *Emissions of Atmospheric Trace Compounds*. Ed. by C. Granier, P. Artaxo, and C. Reeves. Kluwer, Dordrecht. Chap. Emissions from volcanoes, pp. 269–303.

Thornton, J. A., P. J. Wooldridge, R. C. Cohen, M. Martinez, H. Harder, W. H. Brune, E. J. Williams, J. M. Roberts, F. C. Fehsenfeld, S. R. Hall, R. E. Shetter, B. P. Wert, and A. Fried (2002). "Ozone production rates as a function of NOx abundances and HOx production rates in the Nashville urban plume." *J. Geophys. Res.* 107, pages.

Trick, Sebastian (2004). "Formation of nitrous acid on urban surfaces: a physical-chemical perspective." Doctoral dissertation. Heidelberg University.

Tuckermann, M., R. Ackermann, C. Gölz, H. Lorenzen-Schmidt T. Senne, J. Stutz, B. Trost, W. Unold, and U. Platt (1997). "DOAS-observation of halogen radical-catalysed arctic boundary layer ozone destruction during the ARCTOC-campaigns 1995 and 1996 in Ny-Ålesund, Spitsbergen." *Tellus B* 49, pp. 533–555.

UAF (2012). University of Alaska Fairbanks. URL: http://www.uaf.edu/files/cnsm/CNSM_2012_spring_newsletter.pdf.

USGS (2012). United States Geological Survey. URL: http://earthexplorer.usgs.gov/.

UW (2012). University of Washington - Applied Physics Laboratory. URL: http://seaice.apl.washington.edu/AirChemistry/index.html.

UWYO (2011). University of Wyoming - Department of Atmospheric Science. URL: http://weather.uwyo.edu/upperair/sounding.html.

Veefkind, J. Pepijn, Johan F. de Haan, Ellen J. Brinksma, Mark Kroon, and Pieternel F. Levelt (2006). "Total Ozone From the Ozone Monitoring Instrument (OMI) Using the DOAS Technique." *Trans. Geosci. Remote Sensing* 44, pp. 1239–1244.

Vogel, L. (2011). "Volcanic plumes: Evaluation of spectroscopic measurements, early detection, and bromine chemistry." Doctoral dissertation. University of Heidelberg.

Vogel, L., B. Galle, C. Kern, H. Delgado Granados, V. Conde, P. Norman, S. Arellano, O. Landgren, P. Lübcke, J. M. Alvarez Nieves, L. Cárdenas Gonzáles, and U. Platt (2011). "Early in-flight detection of SO_2 via Differential Optical Absorption Spectroscopy: a feasible aviation safety measure to prevent potential encounters with volcanic plumes." *Atmos. Meas. Tech.* 4, pp. 1785–1804.

Vogel, L., H. Sihler, J. Lampel, T. Wagner, and U. Platt (2013). "Retrieval interval mapping: a tool to visualize the impact of the spectral retrieval range on differential optical absorption spectroscopy evaluations." *Atmos. Meas. Tech.* 6, pp. 275–299.

Vogt, R., P.J. Crutzen, and R. Sander (1996). "A mechanism for halogen release from sea-salt aerosol in the remote marine boundary layer." *Nature* 383, pp. 327–330.

Voigt, C., P. Jessberger, T. Jurkat, S. Kaufmann, R. Baumann, H. Schlager, N. Bobrowski, G. Salerno, and G. Giuffrida (2014). "Evolution of CO_2, SO_2, HCl and HNO_3 in the volcanic plumes from Etna." *Geophys. Res. Lett.* 41, pp. 2196–2203.

Volz, A. and D. Kley (1988). "Evaluation of the Montsouris series of ozone measurements made in the nineteenth century." *Nature* 332, pp. 240–242.

von Glasow, R. (2010). "Atmospheric chemistry in volcanic plumes." *PNAS* 107(15), pp. 6594–6599.

von Glasow, R., N. Bobrowski, and C. Kern (2009). "The effects of volcanic eruptions on atmospheric chemistry." *Chemical Geology* 263(1-4), pp. 131–142.

Vountas, M., V.V. Rozanov, and J.P. Burrows (1998). "Ring effect: Impact of rotational Raman scattering on radiative transfer in earth's atmosphere." *J. Quant. Spectrosc. Radiat. Transf.* 60.6, pp. 943–961.

Wagner, T., S. Beirle, T. Brauers, T. Deutschmann, U. Frieß, C. Hak, J.D. Halla, K.-P. Heue, W. Junkermann, X. Li, U. Platt, and I. Pundt-Gruber (2011). "Inversion of tropospheric profiles of aerosol extinction and HCHO and NO_2 mixing ratios from MAX-DOAS observations in Milano during the summer of 2003 and comparison with independent data sets." *Atmos. Meas. Tech.* 4, pp. 2685–2715. DOI: 10.5194/amt-4-2685-2011.

Wagner, T., S. Beirle, and T. Deutschmann (2009). "Three-dimensional simulation of the Ring effect in observations of scattered sun light using Monte Carlo radiative transfer models." *Atmospheric Measurement Techniques* 2, pp. 113–124.

Wagner, T., B. Dix, C. von Friedeburg, U. Frieß, S. Sanghavi, R. Sinreich, and U. Platt (2004). "MAX-DOAS O_4 measurements: A new technique to derive information on atmospheric aerosols - principles and information content." *J. Geophys. Res.* 109, p. D22205. DOI: 10.1029/2004JD004904.

Wagner, T., C. Leue, M. Wenig, K. Pfeilsticker, and U. Platt (2001). "Spatial and temporal distribution of enhanced boundary layer BrO concentrations measured by the GOME instrument aboard ERS-2." *J. Geophys. Res.* 106(D20), pp. 24225–24235.

Wahner, A., J. Callies, H.-P. Dorn, U. Platt, and C. Schiller (1990). "Near UV Atmospheric Absorption Measurements of Column Abundances During Airborne Arctic Stratospheric Expedition, Jan. - Feb. 1989: 1. Technique and NO_2 Observations." *Geophys. Res. Lett.* 17, pp. 497–500.

Wan, Zhengming, Yulin Zhang, Xialin Ma, Michael D. King, Jeffrey S. Myers, and Xiaowen Li (1999). "Vicarious calibration of the Moderate-Resolution Imaging Spectroradiometer Airborne Simulator thermal-infrared channels." *Applied Optics* 38, pp. 6294–6306.

Wang, P., A. Richter, M. Bruns, J. P. Burrows, R. Scheele, W. Junkermann, K.-P. Heue, T. Wagner, U. Platt, and I. Pundt (2006). "Airborne multi-axis DOAS measurements of tropospheric SO_2 plumes in the Po-valley, Italy." *Atmos. Chem. Phys.* 6.2, pp. 329–338. ISSN: 1680-7316. DOI: 10.5194/acp-6-329-2006.

Wang, P., A. Richter, M. Bruns, V. V. Rozanov, J. P. Burrows, K.-P. Heue, T. Wagner, I. Pundt, and U. Platt (2005). "Measurements of tropospheric NO_2 with an airborne multi-axis DOAS instrument." *Atmospheric Chemistry and Physics* 5.2, pp. 337–343. DOI: 10.5194/acp-5-337-2005.

Wenig, M., S. Kühl, S. Beirle, E. Bucsela, B. Jähne, U. Platt, J. Gleason, and T. Wagner (2004). "Retrieval and analysis of stratospheric NO_2 from the Global Ozone Monitoring Experiment." *J. Geophys. Res.* 109.

Williams, Ed (2012). *Aviation Formulary*. URL: http://williams.best.vwh.net/avform.htm#LL.

Williams, M. D. (1982). "Laser reflection from oxide-coated aluminum." *Appl. Opt.* 21.4, pp. 747–750. DOI: 10.1364/AO.21.000747.

Yienger, J. J. and H. Levy (1995). "Empirical model of global soil-biogenic NO_x emissions." *Journal of Geophysical Research* 100(D6), pp. 11447–11464.

Zel'dovich, Y. B. (1946). "The oxidation of nitrogen in combustion and explosions." *Acta Physicochimica U.R.S.S.* 21, pp. 577–628.

Zelenski, M. and Y. Taran (2012). "Volcanic emissions of molecular chlorine." *Geochimica et Cosmochimica Acta* 87, pp. 210–226.

Zielcke, Johannes (2010). "Direct moonlight studies of volcanic plumes using differential optical absorption spectroscopy." Master's thesis. University of Heidelberg.

Acknowledgements

At the end, I would like to express my sincere thanks to the following people and institutions:

- my advisor Prof. Dr. Ulrich Platt for accepting me to his research group, for introducing me to the challenging world of research and for the opportunity to participate in a number of very exciting measurement campaigns.
- Prof. Dr. Thomas Wagner for kindly being co-referee of this thesis.
- Dr. Denis Pöhler for always being on hand with help and advice. His guidance and encouragement was a great support for my work and the undertaken measurement campaigns.
- Dr. Nicole Bobrowski for the great cooperation in the context of the Etna campaign, for many useful comments on my work and also for her friendly manner.
- all members of the Heidelberg "Luftchemie" group and of the other research groups at the IUP for the pleasant working atmosphere. Especially Dr. Thomas Reichel and Martin Horbanski for non-work-related activities, Sabrina Niebling as former member of our office team, Katja Großmann for proofreading parts of this thesis, Johannes Lampel for the trip to Bremerhaven as well as sense and nonsense discussions, Dr. Holger Sihler for providing useful satellite data, Dr. Sebastian Kreycy for endless conversations about smartphones, movies and the fate of the world, Peter Lübcke, Johannes Zielcke and Tobias Tröndle.
- the staff of the IUP workshop for working overtime in case of emergency and for converting my confused ideas into an actually working instrument.
- the Deutsche Forschungsgemeinschaft (DFG) for funding the development of HAIDI within the Priority Program (SPP) No. 1294 "HALO" (DFG PF-384 7/1 and 7/2).
- Prof. Paul B. Shepson and all members of his Atmospheric Chemistry Group for the kind invitation to the measurement campaigns in Indiana and Alaska.
- my parents, my brother, the rest of the family and also my friends for supporting me in many respects during the whole time of this dissertation.
- last but not least, I want to thank a very special person in my life, my girlfriend Ulrike. Although I had to sacrifice a lot of time for this work that I would have otherwise spent with her, she was always behind me and encouraged me to complete the thesis. So, this is for her...